

# Material properties of copper alloys containing arsenic, antimony, and bismuth

The material of Early Bronze Age ingot torques

Von der Fakultät für Werkstoffwissenschaft und Werkstofftechnologie  
der Technischen Universität Bergakademie Freiberg

genehmigte

## **DISSERTATION**

zur Erlangung des akademischen Grades

Doktor-Ingenieur

Dr.-Ing.

vorgelegt

von Dipl.-Ing. Margrit Junk

geboren am 17.01.1973 in Dresden

Gutachter.: Prof. Dr. Ernst Pernicka, Freiberg  
Prof. Dr. Horst Biermann, Freiberg  
Dr. Peter Northover, Oxford

Tag der Verleihung: 16.05.2003



## Acknowledgements

I would like to thank Prof. Ernst Pernicka for the possibility to work on this project and for his support.

For providing archaeological material I am grateful to Dr. Stephan Möslein (Bad Tölz), Dr. Hans-Peter Uenze (Prähistorische Staatssammlung München), Werner Haberland (Neuhaus b. Schliersee), Dr. Rüdiger Krause (Landesdenkmalamt Baden-Württemberg, Stuttgart) and Dr. Oldrich Kotyza (Okresní vlastivedné muzeum Litoměřice). The sampling and restoration of the ingot torques and fragments was carried out by the author in the restoration workshop of the Staatlicher Mathematisch-Physikalischer Salon Dresden. For their support and hints I would like to thank Andreas Holfert, Lothar Haselmeyer and Johannes Eulitz.

The copper for the reference material was provided by the Institut für NE-Metallurgie, arsenic by the faculty for chemistry and physics and by Freiburger Compound Materials GmbH. Antimony and bismuth were provided by the Institut für Gießereitechnik. The sand moulds were made by ACTech (Advanced Casting Technologies), Freiberg. The pattern for the mould was provided by the Institut für Gießereitechnik (Dr. Klaus Peukert, Reiner Rabe). The graphite mould was made in the mechanical workshop of the faculty for material science, as well as the specimens for material testing. The reference material was cast by Dr. Hans-Peter Heller, Peter Neuhold and Günter Franke in the Institut für Stahltechnologie.

For X-raying the cast rods and for carrying out the tensile tests I would like to thank Reinald Weber (Institut für Werkstofftechnik). The notched bar impact tests were carried out by Dr. Peter Trubitz (Institut für Werkstofftechnik) and Dr. Andreas Weiß (Institut für Stahltechnologie), the torsion tests by Dr. Marlene Spittel, Dr. Werner Jungnickel, and Dagmar Schmidt (Institut für Metallformung). The rods were forged by Uwe Heinze (Institut für Metallformung). With the hardness measurements I was supported by Gudrun Bittner (Institut für Werkstofftechnik), with the stereo microscope by Birgit Liebscher (Institut für Werkstofftechnik). The EPMA and SEM investigations were carried out by Dr. Dietrich Heger, Dr. Hartmut Baum, and Brigitte Bleiber (Institut für Metallkunde). I am indebted to Gudrun Wolf (Institut für Metallkunde) for the support in metallographic preparation.

The photographs of the artefacts were taken by Peter Müller (Staatlicher Mathematisch-Physikalischer Salon Dresden). The slides were scanned to files by Maik Böhme (Institut für Archäometrie).

I would like to thank Amanda Crain and Dr. Daniel Müller (Departement Erdwissenschaften, ETH Zürich) for language and proof correction of the manuscript. Finally, and most importantly, I am indebted to my husband and my parents for their patience to discuss about the work and for the support in all stages of the project.



# Abstract

This work deals with Early Bronze Age ingot torques, their composition, and material properties. The aim was to decide whether and how a choice of materials by composition or properties was possible during the Early Bronze Age.

Early Bronze Age ingot torques were analysed and artefacts from several hoard finds and working stages were investigated metallographically. On the basis of these data the production technology was reconstructed. For the determination of mechanical and technological properties, reference alloys were produced and investigated. The production process was simulated by forging experiments.

The investigations revealed that ingot torques were produced by a standardised technology, independent of their composition. The results of the material testing show that it is possible to distinguish the composition of the Early Bronze Age alloys by their mechanical and technological properties.

---

Die Arbeit befaßt sich mit frühbronzezeitlichen Ösenringbarren, ihrer Zusammensetzung und ihren Werkstoffeigenschaften. Es sollte untersucht werden, ob und wie in der Frühbronzezeit eine Materialauswahl auf der Basis von Zusammensetzung oder Eigenschaften möglich war.

Frühbronzezeitliche Ösenringbarren wurden analysiert und Artefakte unterschiedlicher Herkunft und Fertigungsstufen metallographisch untersucht. Auf der Grundlage dieser Ergebnisse wurde die Herstellung der Ringe rekonstruiert. Zur Bestimmung der mechanischen und technologischen Eigenschaften wurden Referenzlegierungen hergestellt und untersucht. Der Herstellungsprozeß wurde durch Schmiedeversuche simuliert.

Die Untersuchungen ergaben, daß die Ösenringbarren unabhängig von ihrer Zusammensetzung nach einer einheitlichen Technologie hergestellt wurden. Die Ergebnisse der Werkstoffprüfung zeigen, daß eine Unterscheidung frühbronzezeitlichen Legierungen anhand ihrer mechanischen und technologischen Eigenschaften möglich ist.



# Contents

<b>List of Tables</b>	<b>XI</b>
<b>List of Figures</b>	<b>XIII</b>
<b>Symbols and abbreviations</b>	<b>XIX</b>
<b>1 Introduction</b>	<b>1</b>
<b>2 Ingot torques and ingot torque metal</b>	<b>3</b>
2.1 An archaeological view on materials . . . . .	4
2.1.1 Alloys in prehistory . . . . .	4
2.1.2 Estimates for material classification . . . . .	5
2.2 Ingot torques . . . . .	11
2.2.1 General remarks and typology . . . . .	11
2.2.2 Technology . . . . .	13
2.2.3 The material of ingot torques . . . . .	13
2.2.4 Archaeological and archaeometallurgical interpretation of ingot torques . . . . .	17
<b>3 The influence of arsenic, antimony, and bismuth on the properties of copper</b>	<b>19</b>
3.1 The influence of arsenic on copper . . . . .	19
3.1.1 The copper-arsenic equilibrium phase diagram . . . . .	19
3.1.2 Casting properties . . . . .	20
3.1.3 Mechanical properties . . . . .	22
3.1.4 Working properties . . . . .	23
3.2 The influence of antimony on copper . . . . .	26
3.2.1 The copper-antimony equilibrium phase diagram . . . . .	26

---

3.2.2	Casting properties . . . . .	26
3.2.3	Mechanical properties . . . . .	27
3.2.4	Working properties . . . . .	28
3.3	The influence of bismuth on copper . . . . .	29
3.3.1	The copper-bismuth equilibrium phase diagram . . . . .	29
3.3.2	Casting properties . . . . .	29
3.3.3	Mechanical properties . . . . .	29
3.3.4	Working properties . . . . .	30
3.4	The combined influence of the alloying elements . . . . .	31
3.4.1	Combined influence of arsenic and antimony on copper . .	31
3.4.2	The influence of arsenic and antimony on copper contain- ing oxygen . . . . .	32
3.4.3	The influence of arsenic and antimony on copper contain- ing bismuth . . . . .	33
<b>4</b>	<b>Methods used for sampling, analysis and material testing</b>	<b>35</b>
4.1	Sampling of archaeological material . . . . .	35
4.1.1	Drill shavings for X-ray fluorescence analysis . . . . .	35
4.1.2	Samples for metallography . . . . .	35
4.2	Analysis . . . . .	36
4.2.1	Energy dispersive X-ray fluorescence analysis . . . . .	36
4.2.2	Scanning electron microscopy and electron microprobe analysis . . . . .	38
4.3	Metallography . . . . .	39
4.4	Material testing . . . . .	40
4.4.1	Macroscopic X-ray analysis (radiography) . . . . .	40
4.4.2	Vickers hardness test . . . . .	40
4.4.3	Tensile test . . . . .	42
4.4.4	Notched bar impact test . . . . .	43
4.4.5	Torsion test . . . . .	44
<b>5</b>	<b>X-ray fluorescence analyses of Early Bronze Age ingot torques</b>	<b>47</b>
5.1	Andechs-Erling, Kr. Starnberg . . . . .	48
5.2	Piding, Kr. Berchtesgadener Land . . . . .	48
5.3	Sicharting, Kr. Traunstein . . . . .	52
5.4	Staudach-Egerndach, Kr. Traunstein . . . . .	52
5.5	Unterwössen, Kr. Traunstein . . . . .	55
5.6	Valley, Kr. Miesbach . . . . .	56



---

5.7	Summary . . . . .	59
<b>6</b>	<b>Metallographic investigation of Early Bronze Age ingot torques</b>	<b>61</b>
6.1	Aschering, Kr. Starnberg . . . . .	61
6.1.1	Fragment Asch1 . . . . .	62
6.1.2	Fragment Asch2 . . . . .	65
6.2	Bernhaupten, Kr. Traunstein . . . . .	67
6.2.1	Fragment Ber1 . . . . .	68
6.2.2	Fragment Ber3 . . . . .	68
6.3	Gammersham, Kr. Wasserburg am Inn . . . . .	70
6.3.1	Fragment Gam1 . . . . .	72
6.3.2	Fragment Gam2 . . . . .	75
6.4	Hechendorf am Pilsensee, Kr. Starnberg . . . . .	77
6.4.1	Fragment Hech1 . . . . .	77
6.4.2	Fragment Hech2 . . . . .	78
6.5	Hohenlinden-Mühlhausen, Kr. Ebersberg . . . . .	80
6.5.1	Fragment Hoh1 . . . . .	81
6.6	Mühldorf am Inn, Kr. Mühldorf . . . . .	84
6.6.1	Fragment Müh1 . . . . .	84
6.7	Pfedelbach-Untersteinbach, Hohenlohekreis . . . . .	86
6.7.1	Ingot torque Pfe10 . . . . .	86
6.7.2	Ingot torque Pfe14 . . . . .	90
6.8	Radostice, okr. Litomeřice . . . . .	93
6.8.1	Ingot torque Rad2 . . . . .	93
6.8.2	Ingot torque Rad4 . . . . .	94
6.9	Thailing, Kr. Ebersberg . . . . .	98
6.9.1	Fragment Tha1 . . . . .	98
6.10	Valley, Kr. Miesbach . . . . .	101
6.10.1	Ingot torque Val1 . . . . .	101
6.10.2	Fragment Val2 . . . . .	104
6.10.3	Fragment Val3 . . . . .	110
6.10.4	Fragment Val4 . . . . .	115
6.10.5	Ingot torque Val5 . . . . .	119
6.10.6	Ingot torque Val6 . . . . .	122
6.11	Summary . . . . .	126

---

<b>7</b>	<b>Reference material and material testing</b>	<b>129</b>
7.1	Preparation of reference materials . . . . .	129
7.2	Metallographic investigation and analysis of the cast material . . .	131
7.2.1	X-ray fluorescence analysis . . . . .	131
7.2.2	Copper . . . . .	132
7.2.3	Cu As <sub>0.25</sub> Sb <sub>0.25</sub> Bi <sub>0.1</sub> . . . . .	132
7.2.4	Cu As <sub>0.5</sub> Sb <sub>0.5</sub> Bi <sub>0.1</sub> . . . . .	135
7.2.5	Cu As <sub>1</sub> Sb <sub>1</sub> Bi <sub>0.1</sub> . . . . .	137
7.2.6	Cu As <sub>2</sub> Sb <sub>2</sub> Bi <sub>0.1</sub> . . . . .	137
7.2.7	Cu As <sub>3</sub> Sb <sub>3</sub> Bi <sub>0.1</sub> . . . . .	140
7.2.8	Cu As <sub>4</sub> Sb <sub>4</sub> Bi <sub>0.1</sub> . . . . .	141
7.2.9	Comparison of the reference materials with Early Bronze Age material . . . . .	144
7.3	Mechanical properties . . . . .	144
7.3.1	Vickers hardness test . . . . .	144
7.3.2	Tensile test . . . . .	146
7.3.3	Notched bar impact test . . . . .	148
7.3.4	Torsion test . . . . .	150
7.3.5	Interpretation of the material tests . . . . .	152
7.4	Cold working properties . . . . .	154
7.4.1	Cold working . . . . .	154
7.4.2	Vickers hardness . . . . .	155
7.4.3	Metallographic investigation of cold worked material . . .	158
7.4.4	Summary . . . . .	167
<b>8</b>	<b>Discussion</b>	<b>169</b>
	<b>Bibliography</b>	<b>177</b>
<b>A</b>	<b>X-ray fluorescence analyses of ingot torques</b>	<b>189</b>
<b>B</b>	<b>Metallographic investigations of ingot torques</b>	<b>205</b>
<b>C</b>	<b>Material Testing</b>	<b>233</b>

# List of Tables

4.1	EDXRF parameter sets . . . . .	37
4.2	Etchants used for the metallographic sections . . . . .	41
7.1	EDXRF analyses of reference material . . . . .	132
7.2	Deformation steps for cold working . . . . .	155
A.1	XRF analyses Andechs, Sicherting, Unterwössen . . . . .	191
A.2	XRF analyses Piding . . . . .	192
A.3	XRF analyses Staudach-Egerndach . . . . .	195
A.4	XRF analyses Valley . . . . .	196
A.5	Average analyses of material class FA . . . . .	198
A.6	Average analyses of material class C2 . . . . .	198
A.7	Typology of the ingot torques from Piding . . . . .	199
A.8	Typology of the ingot torques from Valley . . . . .	202
B.1	Provenance of investigated ingot torques . . . . .	206
B.2	XRF analyses of metallographic sections . . . . .	207
B.3	Vickers hardness HV0.2 . . . . .	209
B.4	Asch1, EPMA of inclusions . . . . .	212
B.5	Asch2, EPMA of inclusions . . . . .	213
B.6	Gam1, EPMA of inclusions . . . . .	214
B.7	Hech1, EPMA of inclusions . . . . .	215
B.8	Hoh1, EPMA of inclusions . . . . .	216
B.9	Pfe10, EPMA of inclusions . . . . .	217
B.10	Pfe14, EPMA of inclusions . . . . .	220
B.11	Rad4, EPMA of inclusions . . . . .	222
B.12	Val1b, EPMA of inclusions . . . . .	224
B.13	Val2b, EPMA of inclusions . . . . .	225

---

B.14	Val3b, EPMA of inclusions . . . . .	226
B.15	Val4a, EPMA of inclusion . . . . .	227
B.16	Val5b, EPMA of inclusions . . . . .	228
B.17	Val6a, EPMA of inclusions . . . . .	229
B.18	Metallographic investigation of ingot torques . . . . .	230
C.1	Casting parameters . . . . .	234
C.2	Cu, EPMA of inclusions . . . . .	235
C.3	CuAs <sub>0.25</sub> Sb <sub>0.25</sub> Bi <sub>0.1</sub> , EPMA of inclusions . . . . .	236
C.4	CuAs <sub>0.5</sub> Sb <sub>0.5</sub> Bi <sub>0.1</sub> , EPMA of inclusions . . . . .	238
C.5	Cu As <sub>1</sub> Sb <sub>1</sub> Bi <sub>0.1</sub> , EPMA of inclusions . . . . .	240
C.6	Cu As <sub>2</sub> Sb <sub>2</sub> Bi <sub>0.1</sub> , EPMA of inclusions . . . . .	242
C.7	Cu As <sub>3</sub> Sb <sub>3</sub> Bi <sub>0.1</sub> , EPMA of inclusions . . . . .	244
C.8	Cu As <sub>4</sub> Sb <sub>4</sub> Bi <sub>0.1</sub> , EPMA of inclusions . . . . .	246
C.9	Tensile test . . . . .	248
C.10	Notched bar impact test . . . . .	250
C.11	Torsion test . . . . .	252
C.12	Vickers hardness test . . . . .	253

# List of Figures

2.1	Material classification according to Junghans et al. (1968a) . . . . .	8
2.2	Typological variations of ingot torques . . . . .	12
2.3	Composition of ingot torques . . . . .	14
3.1	Cu-As equilibrium phase diagram . . . . .	20
3.2	Cu-Sb equilibrium phase diagram . . . . .	27
3.3	Cu-Bi equilibrium phase diagram . . . . .	30
5.1	XRF-analyses of the Andechs ingot torques . . . . .	49
5.2	XRF-analyses of the Piding ingot torques . . . . .	51
5.3	XRF-analyses of the Sickingen neckrings . . . . .	53
5.4	XRF-analyses of the Staudach ingot torques . . . . .	54
5.5	XRF-analyses of the Unterwössen ingot torques . . . . .	55
5.6	Typology of the Valley ingot torques . . . . .	57
5.7	XRF-analyses of the Valley ingot torques . . . . .	58
6.1	Ingot torque fragment Asch1 . . . . .	62
6.2	Asch1, metallographic section . . . . .	63
6.3	Asch1, metallographic section etched with $\text{NH}_3/\text{H}_2\text{O}_2$ . . . . .	64
6.4	Asch1, metallographic section etched with $\text{K}_2\text{Cr}_2\text{O}_7$ solution . . . . .	64
6.5	Ingot torque fragment Asch2 . . . . .	66
6.6	Asch2, metallographic section . . . . .	67
6.7	Ingot torque fragment Ber1 . . . . .	68
6.8	Ber1, metallographic section . . . . .	69
6.9	Ber1, metallographic section etched with $\text{NH}_3/\text{H}_2\text{O}_2$ . . . . .	69
6.10	Ingot torque fragment Ber3 . . . . .	70
6.11	Ber3, metallographic section . . . . .	71
6.12	Ber3, metallographic section etched with $(\text{NH}_4)_2\text{S}_2\text{O}_8$ solution . . . . .	71

---

6.13	Ingot torque fragment Gam1 . . . . .	72
6.14	Gam1, metallographic section . . . . .	74
6.15	Gam1, metallographic section etched with $(\text{NH}_4)_2\text{S}_2\text{O}_8$ solution . . . . .	74
6.16	Ingot torque fragment Gam2 . . . . .	75
6.17	Gam2, metallographic section . . . . .	76
6.18	Gam2, metallographic section etched with $\text{K}_2\text{Cr}_2\text{O}_7$ solution . . . . .	76
6.19	Ingot torque fragment Hech1 . . . . .	78
6.20	Hech1, metallographic section . . . . .	79
6.21	Hech1, metallographic section etched with $\text{NH}_3/\text{H}_2\text{O}_2$ . . . . .	79
6.22	Ingot torque fragment Hech2 . . . . .	80
6.23	Hech2, metallographic section etched with $\text{NH}_3/\text{H}_2\text{O}_2$ . . . . .	81
6.24	Neckring fragment Hoh1 . . . . .	82
6.25	Hoh1, metallographic section . . . . .	83
6.26	Hoh1, metallographic section etched with $\text{K}_2\text{Cr}_2\text{O}_7$ solution . . . . .	83
6.27	Ingot torque fragment Müh1 . . . . .	84
6.28	Müh1, metallographic section . . . . .	85
6.29	Müh1, metallographic section etched with $\text{K}_2\text{Cr}_2\text{O}_7$ solution . . . . .	85
6.30	Ingot torque Pfe10 . . . . .	87
6.31	Ingot torque Pfe10, detail . . . . .	87
6.32	Pfe10, metallographic section . . . . .	88
6.33	Pfe10, metallographic section etched with $\text{NH}_3/\text{H}_2\text{O}_2$ . . . . .	89
6.34	Pfe10, metallographic section etched with $\text{K}_2\text{Cr}_2\text{O}_7$ solution . . . . .	89
6.35	Ingot torque Pfe14 . . . . .	91
6.36	Pfe14, metallographic section . . . . .	92
6.37	Pfe14, metallographic section etched with $\text{K}_2\text{Cr}_2\text{O}_7$ solution . . . . .	92
6.38	Ingot torque Rad2 . . . . .	93
6.39	Rad2, metallographic section . . . . .	95
6.40	Rad2, metallographic section etched with $\text{K}_2\text{Cr}_2\text{O}_7$ solution . . . . .	95
6.41	Ingot torque Rad4 . . . . .	96
6.42	Rad4, metallographic section . . . . .	97
6.43	Rad4, metallographic section $\text{K}_2\text{Cr}_2\text{O}_7$ solution . . . . .	97
6.44	Ingot torque fragment Tha1 . . . . .	98
6.45	Tha1, metallographic section . . . . .	99
6.46	Tha1, metallographic section etched with $(\text{NH}_4)_2\text{S}_2\text{O}_8$ solution . . . . .	100
6.47	Tha1, metallographic section etched with $\text{K}_2\text{Cr}_2\text{O}_7$ solution . . . . .	100
6.48	Ingot torque Val1 . . . . .	101
6.49	Val1a, metallographic section . . . . .	102
6.50	Val1a, metallographic section etched with $\text{NH}_3/\text{H}_2\text{O}_2$ . . . . .	103

---

6.51	Val1a, metallographic section etched with $(\text{NH}_4)_2\text{S}_2\text{O}_8$ solution	103
6.52	Val1b, metallographic section	105
6.53	Val1b, metallographic section etched with $(\text{NH}_4)_2\text{S}_2\text{O}_8$ solution	105
6.54	Ingot torque fragment Val2	106
6.55	Val2a, metallographic section	107
6.56	Val2a, metallographic section etched with $\text{NH}_3/\text{H}_2\text{O}_2$	107
6.57	Val2b, metallographic section	108
6.58	Val2b, metallographic section etched with $(\text{NH}_4)_2\text{S}_2\text{O}_8$ solution	108
6.59	Val2c, metallographic section	109
6.60	Val2c, metallographic section	109
6.61	Ingot torque fragment Val3	111
6.62	Val3a, metallographic section	112
6.63	Val3a, metallographic section etched with $(\text{NH}_4)_2\text{S}_2\text{O}_8$ solution	112
6.64	Val3b, metallographic section	113
6.65	Val3b, metallographic section etched with $\text{NH}_3/\text{H}_2\text{O}_2$	113
6.66	Val3c, metallographic section	114
6.67	Val3c, metallographic section etched with $(\text{NH}_4)_2\text{S}_2\text{O}_8$ solution	114
6.68	Ingot torque fragment Val4	115
6.69	Val4a, metallographic section	117
6.70	Val4a, metallographic section etched with $\text{NH}_3/\text{H}_2\text{O}_2$	117
6.71	Val4b, metallographic section	118
6.72	Val4b, metallographic section etched with $(\text{NH}_4)_2\text{S}_2\text{O}_8$ solution	118
6.73	Ingot torque Val5	119
6.74	Val5a, metallographic section	120
6.75	Val5a, metallographic section etched with $\text{NH}_3/\text{H}_2\text{O}_2$	120
6.76	Val5b, metallographic section	121
6.77	Ingot torque Val6	122
6.78	Val6a, metallographic section	124
6.79	Val6a, metallographic section	124
6.80	Val6b, metallographic section	125
6.81	Val6b, metallographic section etched with $\text{NH}_3/\text{H}_2\text{O}_2$	125
6.82	Comparison of bulk and matrix analyses	127
7.1	Composition of reference alloys	130
7.2	Cu, metallographic section	133
7.3	Cu As0.25 Sb0.25 Bi0.1, metallographic section	134
7.4	Cu As0.25 Sb0.25 Bi0.1, metallographic section	134
7.5	Cu As0.5 Sb0.5 Bi0.1, metallographic section	136

7.6	Cu As0.5 Sb0.5 Bi0.1, metallographic section etched with NH <sub>3</sub> /H <sub>2</sub> O <sub>2</sub> . . . . .	136
7.7	Cu As1 Sb1 Bi0.1, metallographic section . . . . .	138
7.8	Cu As1 Sb1 Bi0.1, metallographic section etched with NH <sub>3</sub> /H <sub>2</sub> O <sub>2</sub> . . . . .	138
7.9	Cu As2 Sb2 Bi0.1, metallographic section . . . . .	139
7.10	Cu As2 Sb2 Bi0.1, metallographic section etched with NH <sub>3</sub> /H <sub>2</sub> O <sub>2</sub> . . . . .	139
7.11	Cu As3 Sb3 Bi0.1, metallographic section . . . . .	142
7.12	Cu As3 Sb3 Bi0.1, metallographic section etched with NH <sub>3</sub> /H <sub>2</sub> O <sub>2</sub> . . . . .	142
7.13	Cu As4 Sb4 Bi0.1, metallographic section . . . . .	143
7.14	Cu As4 Sb4 Bi0.1, metallographic section etched with NH <sub>3</sub> /H <sub>2</sub> O <sub>2</sub> . . . . .	143
7.15	Reference material, comparison of bulk and matrix analyses . . . . .	145
7.16	Vickers hardness HV0.2 of cast reference material . . . . .	145
7.17	Tensile test, 0.2% offset yield strength . . . . .	147
7.18	Tensile test, tensile strength . . . . .	147
7.19	Tensile test, percentage elongation after fracture . . . . .	148
7.20	Notched bar impact test, notch impact work . . . . .	149
7.21	Notched bar impact test, lateral spreading . . . . .	149
7.22	Torsion test, maximum reference amount of deformation . . . . .	151
7.23	Torsion test, reference stress for $\phi_v=0.1$ . . . . .	151
7.24	Torsion test, hardening exponent . . . . .	152
7.25	Cold working, stepwise cold worked specimen . . . . .	154
7.26	Cold working, work hardening . . . . .	156
7.27	Cold working, percentage hardness increase . . . . .	157
7.28	Cu, 23 % cold worked, metallographic section . . . . .	159
7.29	Cu, 86 % cold worked, metallographic section . . . . .	159
7.30	Cu As0.25 Sb0.25 Bi0.1, 20 % cold worked, metallographic section . . . . .	160
7.31	Cu As0.25 Sb0.25 Bi0.1, 83 % cold worked, metallographic section . . . . .	160
7.32	Cu As0.5 Sb0.5 Bi0.1, 23 % cold worked, metallographic section etched with NH <sub>3</sub> /H <sub>2</sub> O <sub>2</sub> . . . . .	161
7.33	Cu As0.5 Sb0.5 Bi0.1, 83 % cold worked, metallographic section etched with NH <sub>3</sub> /H <sub>2</sub> O <sub>2</sub> . . . . .	161
7.34	Cu As1 Sb1 Bi0.1, 23 % cold worked, metallographic section etched with NH <sub>3</sub> /H <sub>2</sub> O <sub>2</sub> . . . . .	163
7.35	Cu As1 Sb1 Bi0.1, 83 % cold worked, metallographic section etched with NH <sub>3</sub> /H <sub>2</sub> O <sub>2</sub> . . . . .	163
7.36	Cu As2 Sb2 Bi0.1, 20 % cold worked, metallographic section etched with NH <sub>3</sub> /H <sub>2</sub> O <sub>2</sub> . . . . .	164



---

7.37	Cu As <sub>2</sub> Sb <sub>2</sub> Bi <sub>0.1</sub> , 83 % cold worked, metallographic section etched with NH <sub>3</sub> /H <sub>2</sub> O <sub>2</sub> . . . . .	164
7.38	Cu As <sub>3</sub> Sb <sub>3</sub> Bi <sub>0.1</sub> , 20 % cold worked, metallographic section etched with NH <sub>3</sub> /H <sub>2</sub> O <sub>2</sub> . . . . .	165
7.39	Cu As <sub>3</sub> Sb <sub>3</sub> Bi <sub>0.1</sub> , 83 % cold worked, metallographic section etched with NH <sub>3</sub> /H <sub>2</sub> O <sub>2</sub> . . . . .	165
7.40	Cu As <sub>4</sub> Sb <sub>4</sub> Bi <sub>0.1</sub> , 23 % cold worked, metallographic section etched with NH <sub>3</sub> /H <sub>2</sub> O <sub>2</sub> . . . . .	166
7.41	Cu As <sub>4</sub> Sb <sub>4</sub> Bi <sub>0.1</sub> , 83 % cold worked, metallographic section etched with NH <sub>3</sub> /H <sub>2</sub> O <sub>2</sub> . . . . .	166
8.1	Manufacturing stages of ingot torques . . . . .	171
8.2	Work hardening . . . . .	172
8.3	Vickers hardness HV0.2 of ingot torques . . . . .	173
A.1	Locations of the investigated hoards . . . . .	190
B.1	Fracture appearance of ingot torque fragments I . . . . .	210
B.2	Fracture appearance of ingot torque fragments II . . . . .	211
B.3	Asch1, metallographic section . . . . .	212
B.4	Asch2, metallographic section . . . . .	213
B.5	Gam1, metallographic section . . . . .	214
B.6	Hech1, metallographic section . . . . .	215
B.7	Hoh1, metallographic section . . . . .	216
B.8	Pfe10, metallographic section . . . . .	217
B.9	Pfe10, SEM image of a two phase inclusion . . . . .	218
B.10	Pfe10, EPMA of a two phase inclusion . . . . .	218
B.11	Pfe10, EPMA line scan of the sample cross section . . . . .	219
B.12	Pfe14, metallographic section . . . . .	220
B.13	Pfe10, Vickers hardness HV0.2 . . . . .	221
B.14	Pfe14, Vickers hardness HV0.2 . . . . .	221
B.15	Rad4, metallographic section . . . . .	222
B.16	Rad4, SEM image . . . . .	223
B.17	Rad4, distribution of elements . . . . .	223
B.18	Val1b, metallographic section . . . . .	224
B.19	Val2b, metallographic section . . . . .	225
B.20	Val3b, metallographic section . . . . .	226
B.21	Val4a, metallographic section . . . . .	227

---

B.22	Val5b, metallographic section . . . . .	228
B.23	Val6a, metallographic section . . . . .	229
C.1	Cu, metallographic section . . . . .	235
C.2	CuAs <sub>0.25</sub> Sb <sub>0.25</sub> Bi <sub>0.1</sub> , metallographic section . . . . .	236
C.3	CuAs <sub>0.25</sub> Sb <sub>0.25</sub> Bi <sub>0.1</sub> , EPMA line scan of the sample cross-section . . . . .	237
C.4	CuAs <sub>0.5</sub> Sb <sub>0.5</sub> Bi <sub>0.1</sub> , metallographic section . . . . .	238
C.5	CuAs <sub>0.5</sub> Sb <sub>0.5</sub> Bi <sub>0.1</sub> , EPMA line scan of the sample cross-section . . . . .	239
C.6	Cu As <sub>1</sub> Sb <sub>1</sub> Bi <sub>0.1</sub> , metallographic section . . . . .	240
C.7	Cu As <sub>1</sub> Sb <sub>1</sub> Bi <sub>0.1</sub> , EPMA line scan of the sample cross-section . . . . .	241
C.8	Cu As <sub>2</sub> Sb <sub>2</sub> Bi <sub>0.1</sub> , metallographic section . . . . .	242
C.9	Cu As <sub>2</sub> Sb <sub>2</sub> Bi <sub>0.1</sub> , EPMA line scan of the sample cross-section . . . . .	243
C.10	Cu As <sub>3</sub> Sb <sub>3</sub> Bi <sub>0.1</sub> , metallographic section . . . . .	244
C.11	Cu As <sub>3</sub> Sb <sub>3</sub> Bi <sub>0.1</sub> , EPMA line scan of the sample cross-section . . . . .	245
C.12	Cu As <sub>4</sub> Sb <sub>4</sub> Bi <sub>0.1</sub> , metallographic section . . . . .	246
C.13	Cu As <sub>4</sub> Sb <sub>4</sub> Bi <sub>0.1</sub> , EPMA line scan of the sample cross-section . . . . .	247
C.14	Fracture appearance of tensile test specimens . . . . .	249
C.15	Fracture appearance of notched bar impact specimens . . . . .	251

# Symbols and abbreviations

$A$	pyramid indentation area in Vickers hardness test; percentage elongation after fracture in the tensile test
$A_f$	final cross-sectional area in forging experiments
$A_o$	original cross-sectional area in forging experiments
$A_v$	notch impact work
$a_k$	notch impact strength
$D$	diameter of specimen in the torsion test
$d$	pyramid diagonals in Vickers hardness test
$d_f$	final diameter of specimen in forging experiments
$d_o$	original diameter of specimen in forging experiments
$F$	force
$G$	weight of the hammer in the notched bar impact test
$H$	starting elevation of the hammer in the notched bar impact test
$h$	final elevation of the hammer in the notched bar impact test
$HV$	Vickers hardness number
$HV0.2$	low load Vickers hardness number
$L$	length of the specimen in the tensile and in the torsion test
$L_0$	initial length of the specimen in the tensile test
$L_u$	length of the specimen after fracture in the tensile test
$LB$	lateral spreading of the sample in the notched bar impact test
$M_D$	torsion moment in the torsion test
$n$	number of twists in the torsion test; fraction of analyses in each histogram class
$P$	hardening exponent in the torsion test
$R$	radius of the specimen in the torsion test
$R_{p0.2}$	offset yield strength
$R_m$	tensile strength

---

$r$	distance
$S_0$	initial cross-section of the specimen in the tensile test
$S_u$	cross-section of the specimen after fraction in the tensile test
$SB$	lateral spreading of the specimen in the notched bar impact test
$t$	Celsius temperature
$w$	mass fraction of an element
$\bar{w}$	average mass fraction of an element
$x$	amount fraction of an element
$Z$	percentage reduction of area after fraction in the tensile test
$\Delta(HV0.2)$	percentage increase in low load Vickers hardness number
$\gamma$	shear strain in the torsion test
$\gamma_N$	shear strain after Nadei in the torsion test
$\varepsilon$	strain
$\phi$	amount of deformation in the forging experiments
$\phi_v$	reference amount of deformation in the torsion test
$\phi_{v,max}$	maximum reference amount of deformation in the torsion test
$\sigma$	stress
$\sigma_v$	reference stress in the torsion test
$\tau$	shear stress in the torsion test
EDXRF	energy dispersive X-ray fluorescence
EPMA	electron probe microanalysis
Kr.	district (Germany)
okr.	district (Czech republic)
SAM	Studien zu den Anfängen der Metallurgie (Studies on the beginning of metallurgy)
SEM	scanning electron microscope
SMAP	Stuttgarter Metallanalysenprojekt (Stuttgart metal analysis project)

# Chapter 1

## Introduction

This study began with the Early Bronze Age ingot hoard from Valley in Upper Bavaria. The 60 ingot torques found *in situ* were deposited on a tiny space in bundles of five ingots each (Winghart, 1990). Additionally, the rings in this hoard could be divided into two groups: rough cast ingots and reworked items with forging seams (priv. comm. S. Möslein). Similar typological variations were found e.g. in the Mauthausen hoard, where Menke (1982) interpreted them as different working stages of the ingot torques. In contrast to the Mauthausen hoard, the chemical analyses of the Valley ingot torques revealed the presence of two groups: low-impurity copper and copper containing significant amounts of arsenic and antimony. But the most distinctive feature of these ingot torques was the strong correlation between their typology and composition, which has not been documented before. Without any exception, the rough-cast ingots were made of low-impurity copper, and the reworked ones of the alloyed material. The Valley ingot torques and their 'labelling' are not unique. A similar correlation between typology and composition could be observed in an ingot hoard from Piding.

Neuninger and Pittioni (1962) suggested that different kinds of copper were produced and worked systematically by a few people, i.e. in a few workshops. This suggestion combined with the observations in Valley and Piding begs the question if there was any conscious choice of metal composition or properties during the Early Bronze Age. Or was it just coincidence? During the Early Bronze Age a large variety of copper based materials was used, depending both on origin and function of the artefacts. The majority of ingot torques is made of a distinct copper type with significant amounts of arsenic and antimony, which seems to be less used for other artefacts. Again the question arises whether materials were used intentionally. Therefore, different materials have to be available and it is

necessary to distinguish between them. Gowland (1912) noticed that alloys of definite composition could not be ensured by the early practice of smelting mixtures of ores. He suggested, if weapons or implements of suitable composition for their intended use are found, some physical tests must have been applied. Decades later, Coghlan (1960) suspected that the ancient smith had ample skill and experience to enable him to detect any variation, improved working qualities or the reverse in his metal. As main factors, he suggested the suitability of the metal for casting, its behaviour under forging, and the hardness and strength of the metal in the finished product.

Even if it is difficult to find any proof of material testing in the Early Bronze Age, there may be indicators. Pietsch (1964) suggested that the ingot torques probably represented selected 'pure' castings which could form the basis for other artefacts. The shape of the ingot torques was not regarded as arbitrary but chosen for technological reasons. Therefore it is necessary to know how ingot torques were produced. Another question was the possibility for the ancient metalworker to distinguish between different copper types by their properties. How do changes in composition influence the mechanical and technological behaviour of the material? The goal was to describe the relationship between the composition, the working process with the resulting microstructure, and the properties of certain Early Bronze Age metals.

To answer the above questions, ingot torques from Bavaria, Baden-Wuerttemberg and Bohemia were investigated. The majority was analysed by XRF in order to determine the metals used. Several ingot torques from different hoard finds and working stages were investigated metallographically to obtain information about the microstructure. On the basis of these data the technology of ingot torque production was reconstructed. The chemical analyses of the ingot torques were used to prepare reference alloys similar to the ancient material. Standard material tests were applied to determine the mechanical properties of the material. Several investigations concerning material properties of the finished products are available (Budd, 1991; Lechtman, 1996; Ravič and Ryndina, 1984). Since it was presumed that in the Early Bronze Age material testing, if at all, has been applied during working, in this work the focus was placed on the properties in the as-cast state, as the ancient metalworker started to work the metal. Forging experiments were used to simulate the production process and to provide further information about the working properties.

The main aim of this work was to decide whether and how a choice of materials by composition or properties was possible during the Early Bronze Age.

## Chapter 2

# Ingot torques and ingot torque metal

The use of copper not only for jewellery but also for tools began during the transition from the late Neolithic to the Early Bronze Age. In southern Germany, the knowledge of metal working appeared during the 4th millennium BC. Regular metal production in the Alps began at the end of the third and the beginning of the second millennium BC. During this time, the large copper ore deposits in the Alps, especially in the Salzburg and Graubünden provinces were exploited (Krause, 1988).

The main ores used for the copper production in the Alpine area were chalcopyrite ( $\text{CuFeS}_2$ ) and fahlores, i.e. ores of the tetrahedrite ( $\text{Cu}_{12}\text{Sb}_4\text{S}_{13}$ )/tennantite ( $\text{Cu}_{12}\text{As}_4\text{S}_{13}$ ) series<sup>1</sup>. Finds of smelting sites with roasting beds and furnaces confirm the smelting of sulfidic copper ores (Preßlinger and Eibner, 1989). Experiments have shown, that smelting of such ores was possible with Early Bronze Age technology (Böhne, 1968).

The above-mentioned fahlore metals and other arsenic containing alloys were wide-spread and very intensively used during the Early Bronze Age. In the Middle Bronze Age they were replaced by tin bronzes. The exact reason for this is not known, but there are several possibilities. Smelting of arsenic-bearing ores, as well as melting and working arsenical copper may lead to the evaporation of highly toxic arsenic oxides. It is not certain if the Bronze Age metal-workers recognised this danger. But Selimchanov (1982) certainly goes too far when stating, that in the course of smelting copper and arsenical minerals not only the smelter, but all life in the vicinity deceased. However, Charles (1967) noted that the persistent use of the arsenical copper for a period of 300 to 400 years must

---

<sup>1</sup>For further information on ores see e.g. Rösler (1991).

mean that some kind of control was developed in order to control the risks. Surely the ancient metalworker noticed the characteristic garlic-like smell, which results from the evaporation of arsenic oxides. It seems that some consequences of arsenic metallurgy were noticed and described in ancient myths. Acute and chronic intoxication by arsenic is accompanied by arsenic-neuritis and often leads to permanent paralysis of the legs, which may explain the limping smiths of the ancient myths, like Hephaistos and Wieland (Schubert, 1981). Another reason for the replacement of copper-arsenic alloys may be the control of the metallurgical process and product. In contrast to arsenical bronzes smelted from the related ores, tin bronzes may be easier controlled by adding tin to the copper melt. Tin bronzes show a much more obvious correlation between composition, colour and mechanical properties than arsenical copper and fahlore metals. Hence their production and working has been more reproducible even by less experienced metal-workers. Besides such technological reasons, there may have been aesthetic ones, like the colour of the alloys and prestige aspects as the high value of tin due to its rarity (Moorey, 1985; Pernicka, 1990).

## 2.1 An archaeological view on materials

### 2.1.1 Alloys in prehistory

In general, alloys<sup>2</sup> are combinations of at least two components of which one has to be a metal, that enhance the general characteristics of metals (Askeland, 1994; Gräfen, 1991; Falbe and Regitz, 1995). In this sense, arsenical copper and the fahlore metals are alloys. In the narrow sense, the term alloy is used if there is an intentional addition to a metal in order to provide, modify or improve the properties of the material (Northover, 1988). The intentional smelting of ores which result in 'high-impurity' copper is something between both definitions.

In this work the term alloy will be used for high-impurity copper, if its properties are obviously different from those of the pure metal. There will be no distinction between 'natural' and 'intentionally produced' alloys, between 'dirty copper' and 'chosen alloy', as Lechtman (1996) called it. In most cases, such a distinction is neither possible nor useful. The main question is rather to find out whether the ancient metal-workers used metals and alloys intentionally. As mentioned by Sangmeister (1971), the advantages of the arsenical copper were surely recognised and used. Even if alloying in the narrow sense was not known, the result may have

---

<sup>2</sup>from lat. *ligare*: to bind, combine



been a selective mining of special ores and the preferred use of copper from a specific provenance (Sangmeister, 1971; Hauptmann, 1991). Ottaway (1994) applied statistical analysis to answer the question of whether the improved properties of arsenical copper were noticed and used by the prehistoric metal-worker. It was found that in Europe arsenical copper was mainly used for cutting tools. The use for prestige objects was regarded as a further sign of intentional production of arsenical copper.

There are several hypotheses concerning the discovery of alloys, ranging from unintentional smelting of arsenic-bearing ores to intentional alloying with native arsenic (Pernicka, 1990). Sometimes the first alloys were interpreted as shamanism. As Spiridonov (1986) wrote, the red realgar and the golden auripigment may have been added to the copper melt as an offering to the ‘magic keeper’ of the fire. Obviously it was successful: the ‘ritual’ copper was better and harder than the usual one. It was also suggested that oxidic or carbonatic copper ores like malachite were mixed up and smelted together with similarly coloured arsenic minerals like olivenite (Ottaway, 1994). Otto and Witter (1952) suggested that copper alloys containing more than 1 % arsenic would be intentional products. Sangmeister (1971) mentioned smelted copper with up to 6 % arsenic.

### 2.1.2 Estimates for material classification

The classical archaeological method to describe artefacts is typology. But already in the 19th century researchers were interested in the composition of ancient materials<sup>3</sup>. Hamilton (1991) stated that the central assumption behind the work of most researchers in archaeometallurgy is that the elemental composition of metal artefacts has meaning; a specific composition is characteristic of a certain time period, culture, or artefact type. So the analyses were seen as ‘internal’ typology (Sperl, 1975), an ‘objective’ method to classify artefacts. For instance, Otto (1949) defined a technological Bronze Age besides the typological one, but he also strongly warned to base a chronological classification only on analyses.

#### Otto and Witter

In 1932 Otto and Witter began with chemical and metallurgical investigations in order to solve the disputed problems of prehistoric extractive metallurgy in Central Europe and the use of the first metals with scientific methods from a geological

---

<sup>3</sup>A detailed introduction to the history of material classification is given by Härke (1978).

and metallurgical point of view. Their primary aims were to establish the possibility of copper mining in ancient times in mining areas of Central Germany and to determine the exploited ores by studies of the metal (Otto and Witter, 1952). The work is based on the assumption that impurities in ancient copper directly reflect those in the ores from which they were smelted (Witter, 1953).

In the course of their investigations, samples of Bronze Age metal objects were analysed with optical emission spectroscopy and the quantities of tin, lead, silver, gold, nickel, cobalt, arsenic, antimony, bismuth, iron, zinc, and sulfur were determined. Otto and Witter classified their analyses using technological and mineralogical aspects. The so-called alloy types ('Leitlegierungen') were described already by Otto (1949). Beside pure and crude copper ('Rohkupfer'), Otto and Witter (1952) defined copper-arsenic alloys, fahlore metals with and without silver, and copper-tin alloys.

Eckel (1992) noticed that the material groups of Otto and Witter were not defined on the basis of analyses, but the analyses were sorted into material combinations set in advance by knowledge of certain mineral associations. But the main criticism of this work concerns the so-called provenance postulate (Budd et al., 1996), the use of artefacts for provenancing ores, and the lack of slag and ore analyses (Härke, 1978).

Nevertheless, the conclusions of Otto and Witter (1952) were confirmed by Eibisch (1992), who classified their results with statistical frequency analysis. He stated that the statistical grouping is in accordance both with the empirical alloy types and technological properties.

### **Neuninger and Pittioni**

The Vienna group of Neuninger, Pittioni and Preuschen tried to relate finished products and ore deposits to answer the question from which area the artefacts derive (Pittioni, 1957). Similar to the work of Otto and Witter (1952), their investigations base on the assumption that the impurity patterns in metals are similar to those in the related ores. But in contrast to Otto and Witter (1952) the Vienna group included ore analyses.

The large number of analyses were grouped on the basis of their impurity patterns. Since semi-quantitative analyses were used, they are not really comparable to other investigations. In summary, five copper types related to ore deposits were defined (Neuninger and Pittioni, 1962; Neuninger et al., 1960, 1969). The East Alpine copper from Mitterberg-Kelchalm is characterised by very low amounts of impurities, with about 0.1 % nickel. Another so-called Eastern copper, which

was regarded to be probably of Hungarian-Slovakian origin contains appreciable amounts of arsenic, antimony and silver. Other types are the North Tyrolean copper from the Alte-Zeche-Bertagrube near Schwaz, Transylvanian copper, and copper from 'southern ore deposits'. Since the composition of ores is changed in the smelting process, slags were analysed to derive possible metal compositions. The impurity pattern of analysed artefacts was compared with those copper types and related to the assumed mining areas.

According to Pernicka (1999), three major complications have to be considered in such provenance studies: the inhomogeneity of ores, alterations due to the smelting process, and the treatment of the copper to produce the finished object. Sperl (1970) pointed out that silver, gold, selenium, tellurium, nickel and cobalt have similar smelting behaviour to copper and their ratios in the metallic end-product would be the same as in the ore. The amounts of arsenic, antimony and bismuth are more altered, while the amounts of tin, zinc, lead, iron and sulfur are significantly reduced (Sperl, 1970). The concentration of volatile elements, like arsenic, antimony, and zinc depends on the ore roasting process. The amount of arsenic in the final metal further depends on the smelting temperature (Pollard et al., 1989).

### **The Stuttgart analyses (SAM)**

The most extensive and perhaps most discussed analyses of Bronze Age material were carried out by the Stuttgart group of Junghans, Sangmeister, Schröder, Klein and Scheufele. They began their 'studies on the beginning of metallurgy' ('Studien zu den Anfängen der Metallurgie': SAM) in 1952, and published about 22,000 analyses. The aim was to establish in which regions copper was mined and worked for the first time, in which direction and period of time the technology spread, whether the same material was used for the whole lifetime of a culture or was modified and if there were any differences in the material depending on its purpose (Junghans et al., 1960). The sources of the material, i.e. the related ores, were not determined. According to Sangmeister (1998), this was not necessary to answer the questions.

For the classification of the analyses, the Stuttgart group used arsenic, antimony, nickel, silver, and bismuth, which can be found also in the ores. Since tin and lead may be added to copper, they were determined but not used for classification. The classification itself was a statistical one resulting in a 'decision tree' of material groups which aimed to include all materials made during the same process with the same raw materials. With the growing database the initial twelve

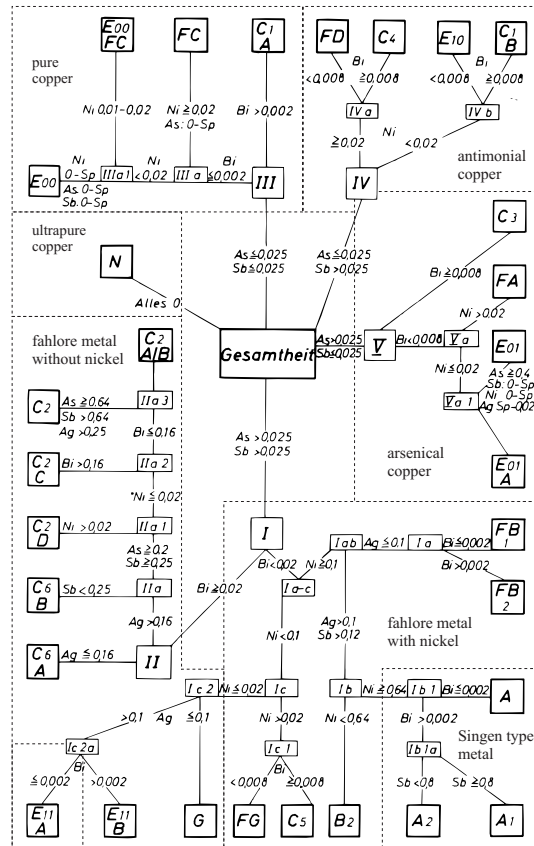


**Figure 2.1:** Material classification according to Junghans et al. (1968a). The ‘branches’, representing different ore types, were defined by Pernicka (1990).

groups of Junghans et al. (1960) were further divided so that in Junghans et al. (1968a,b) twenty-nine material groups were established (Fig. 2.1, p. 8). The main problem with this classification is the use of fixed concentration ranges for the elements. Some of them were close to the detection limit, most of them do not represent metallurgical or technological markers (as maximum solubility, remarkable changes in properties)

Eckel (1992) criticised the use of beads for spectral analysis, because during melting of the drill chips some of volatile elements may be lost. Comparative studies by Pernicka (1984) have shown that this effect can be ignored. Slater and Charles (1970) stated that segregations within castings have to be considered if the analyses were of a single sample removed from each object. However, in their

investigations they found bismuth segregations of no importance in relation to analyses performed for most archaeological purposes, but of significance for the classification based on trace elements (Slater and Charles, 1970).

The main doubts about the Stuttgart classification are based on the statistical interpretation of the data. Menke (1982) criticised the interpretation of statistical groups of analyses as real kinds of metal and that the chronology of the material types is mainly based on grave finds. Budd et al. (1996) criticised that the Stuttgart group assumed that artefacts which were statistically associated in terms of their impurity patterns must derive from the same source.

### **Butler's material classification based on SAM**

Butler (1978) reinterpreted the analyses of ingot torques and rib-shaped ingots given by Junghans et al. (1968a,b) to answer the question of which copper the hoards consist. For the classification he used cluster analysis combined with logarithmic percentage histograms. As Butler (1978) wrote, he tried to obtain clues on the differences in the metal composition of the 'ingots', differences within individual hoards, between different types of ingots, and variations from region to region.

Butler (1978) stated that ingot torques were made of many different types of copper and that it is uncommon to find a hoard consisting entirely of one kind of copper. Most of the examined hoards contained a mixture of two or more distinct copper types. This assessment strongly depends on the material classification used. In his study of Austrian and Moravian ingot torques Butler found that 85 % to 90 % of the rings consisted of one distinctive metal type, that he called 'classical *Ösenring* metal'. This material is nearly identical with the copper type C2 in the Stuttgart tree. The remaining rings were found to consist of almost pure copper, with nickel and/or arsenic as the major impurities. In the Bavarian hoards the classical ingot torque metal was important, but more so in the Lower Austrian–Southern Moravian province (Butler, 1978). In the Bernhaupten hoard Butler (1978) determined a third cluster with an intermediate copper type besides ingot torque metal and low-impurity copper.

### **Material groups according to Menke and Eckel**

As that of Butler, the material classifications of Menke and Eckel are based on the Stuttgart analyses. Menke (1982) raised doubts about whether the Stuttgart material groups represented different metal types which could be distinguished

by the prehistoric metal worker. He focused on hoard finds and tried to evaluate different material groups without using a mathematical-statistical approach. As a result of his work, Menke defined material groups on the basis of the large Bavarian hoards. For classification he mainly used arsenic and tin. However, since the groups should be comparable to the Stuttgart grouping, the elements antimony, silver, nickel, bismuth and cobalt were also considered (Menke, 1982). The material groups are defined by what he called limiting values (as Pernicka (1995) noted, the term 'ranges' would be more exact) where the margins between minimum and maximum values of the elements are determined.

However, Menke's material grouping based on the investigated hoard finds can be misleading. For instance, the arsenical bronze type 'Grubmoos' is neither found only in Aschering (Grubmoos), nor does the material necessarily originate from Aschering. The primary question, if the different material groups could be distinguished by the prehistoric metal-worker was not answered by Menke (1982).

Eckel (1992) also tried to locate the origin of the ores. Furthermore he wanted to find out whether such material classes are noticeable in different ingot shapes. His main criticism of previous analyses concerned the allocation and classification of materials on the basis of trace elemental composition. He stated that the composition of ores is not constant and the trace element composition of a metal depends on the smelting technology which surely changes with time and location (Eckel, 1992). Furthermore he stated that in the case of minimal amounts of trace elements the differences between the material classes become small and some uncertainties would lead to a wrong classification of the analyses.

Eckel reinterpreted the data published by Junghans et al. (1968a), and set up material classes based on so-called analyses of variance. Therefore, the relation of arsenic to antimony, the silver to nickel ratio and, in some cases, the bismuth to antimony ratio were investigated. As Pernicka (1995) stated, the disadvantages of this classification are the use of linear instead of logarithmic diagrams and that only two elements can be considered in one step. Although the investigated hoard finds are not identical to those used by Menke, their classifications are very similar.

### **The new Stuttgart metal analysis project (SMAP)**

The new Stuttgart metal analysis project aimed to complete and reevaluate the available analyses of Neolithic and Early Bronze Age metal objects in Central Europe (Krause and Pernicka, 1996). Krause and Pernicka (1996) used the SAM data and additional regional studies to determine significant copper types. The

silver, nickel, antimony and arsenic contents were used for the calculations and grouping. Some of the initial material classes from Junghans et al. (1960, 1968a) could be confirmed, others like the fahlore metals (like C2 and C2A/B, C2C) were combined (Pernicka, 1990; Krause and Pernicka, 1996).

The Stuttgart material groups were divided into ultrapure and pure copper, arsenical and antimonial copper and fahlore metal with and without nickel (Pernicka, 1990) (Fig. 2.1, p. 8). These ‘branches’ in the decision tree represent different ore types, while the ‘twigs’, i.e. subgroups, represent different ore deposits/workshops. At the beginning of the Early Bronze Age, artefacts were made of significantly different copper alloys, while in the later period of the Early Bronze Age large metal groups characterised mainly by fahlore metal with and without nickel predominated (Krause and Pernicka, 1998a).

## 2.2 Ingot torques

### 2.2.1 General remarks and typology

The distribution of the ingot torques is closely related to the copper mining districts of the northeastern Alps (Hell, 1952). Most of them were found in the northern foothills of the Alps, i.e. in south-east Bavaria, in southern, central and western Bohemia, in Lower Austria and in southern and central Moravia. According to Bath-Bílková (1973) about 80 to 90 % of the hoard finds in these regions consist of ingot torques.

Ingot torques<sup>4</sup> are neckring-size rings with flattened and bent ends, which are usually dated as transitional from Early Bronze Age A1 to A2, i.e. about 2000 BC (several chronological schemes have been suggested, see e.g. Menke (1982)). The typological features within this artefact group range from as-cast state to roughly or carefully reworked items with faceted or smooth surfaces (Neugebauer et al., 1999). The cross-sections vary from rounded, roundish or triangular to quadrilateral, the ends can be curled into loops, slightly rolled or only flattened (Fig. 2.2, p. 12). Menke (1982) interpreted such typological features as different working stages. In some hoards only rough cast ingots were found (e.g. Gammersham), other hoards contain several types (e.g. Mauthausen) (Lernerz-deWilde, 1995).

Butler (1978) pointed out that the ingot torques have a shape which is convenient for storage, transport, and division in other units of size, weight, or value

---

<sup>4</sup>In this work the terminus ingot torque (Ösenringbarren) is used for hoard finds. Similar torques from graves are considered as neckrings (Ösenhalsringe).



**Figure 2.2:** Typological variations of ingot torques (from the top): rough cast ingot with casting groove and flattened end (fragment Müh1), reworked ingot torque with rounded cross-section and hook-shaped end (fragment Tha1), neckring with rounded cross-section and curled end (fragment Hoh1). (Photo: P. Müller)

for purposes of counting, or further manipulation, such as melting, alloying, casting, or forging. This would mean that they are ‘real’ ingots, i.e. semi-finished products. This assumption is supported by the more or less standardised shape and weight. For 1020 ingot torques from southern Germany Lenerz-deWilde (1995) reported weights between 115 and 255 g with smaller variations within the individual hoards. More than 70 % of the 600 ingot torques in the Mauthausen hoard were found to have weights between 180 and 220 g (Menke, 1982). This was interpreted as gearing to fixed weight averages, showing an ingot function by material value (Innerhofer, 1997). In contrast, Budd and Taylor (1995) postulated that the occurrence of a large number of closely similar artefacts, such as ingot torques, may be the result of the multiple use of moulds and the use of previously cast items as patterns for new moulds. Similarities may also be a function of cultural norms so that ‘ingots’ were expected to take a certain form in a particular time.



### 2.2.2 Technology

The large scale production of ingot torques led to the supposition that casting in lost moulds was known in the Early Bronze Age (Otto, 1949). However, Otto (1949) further stated that only a few workshops may have mastered this sophisticated technology. The simplest mould, according to Smith (1968), is the open groove, pressed into clay. This technology is comparable to sand-casting as suggested by Goldmann (1981). For semi-permanence the mould may be cut into stone, like e.g. the Late Bronze Age moulds from Heilbronn-Neckargartach (Paret, 1954). Both casting technologies leave one face of the casting flat and unfinished (Smith, 1968). Evidence for casting in open moulds was reported by Hell (1952).

Transverse hammer tracks on the inner surface of the Viehausen ingot torques show that they were rounded by hammering over two supports (Hell, 1952). According to Coghlan (1960) the material was cold hammered and annealed when it became too hard to work. However, Voce (1961) pointed out that the cold-working properties of cast tough-pitch copper are rather poor. He suggested hot-working at least during the early stages of fabrication.

### 2.2.3 The material of ingot torques

Large scale investigations like the Stuttgart analyses (Junghans et al., 1960, 1968a) have shown that ingot torques were mainly made of two materials: low-impurity copper and a specific copper alloy (see Fig. 2.3, p. 14). The second one, the so-called ingot torque metal, contains between 1 and 3 % arsenic and antimony, up to 2 % silver, 0.1 % bismuth and negligible amounts of nickel and tin.

#### Low-impurity copper

About 8 % of the ingot torques are made of low-impurity copper (SMAP database, 1999), including material with different impurity patterns, which seem to be characteristic for the provenance of the material. Copper with about 0.1 % nickel, called FC in the Stuttgart analyses, is characteristic for the ingot torques in Lower Austria and Southern Moravia (Junghans et al., 1968b). About 88 % of the low-impurity copper used for ingot torques belongs to this material type. In the Bavarian hoards the low-impurity copper was found to be almost 99.9 % pure, with a lower nickel content than that from the Lower Austrian-Southern Moravian area (Butler, 1978).

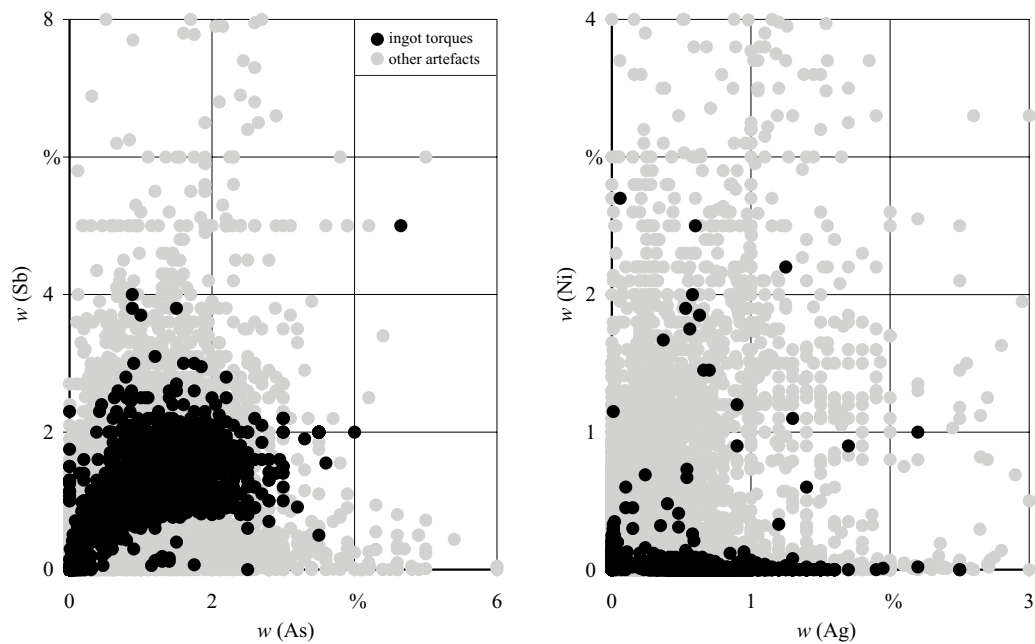


**Figure 2.3:** Composition of ingot torques (black dots) compared with Early Bronze Age artefacts as a whole (grey dots). Data are taken from the SMAP database (1999), including artefacts from South and East Germany, Switzerland, Austria, Bohemia, and Moravia.

Menke (1982) and Eckel (1992) defined similar types of low-impurity copper on the basis of the Gammersham and Hodonín hoard finds. While the copper type Gammersham is characterised by up to 0.95 % arsenic, 0.49 % antimony and 0.6 % nickel (Menke, 1982), the material type B contains only minimal amounts of trace elements (Eckel, 1992).

Besides pure copper Krause and Pernicka (1998a) defined a group of East Alpine coppers, which are comparable with the low-impurity copper of Butler (1978). Based on ore and artefact analyses already Neuninger et al. (1960) suggested that the East Alpine copper was smelted from ores of type Mitternberg-Kelchalm.

While most of the researchers paid attention to the nickel content of the material, Otto and Witter (1952) distinguished between a so-called crude copper (total amount of impurities of about 1 %) with higher and lower silver content and with natural tin content. As they stated, pure and the so-called crude copper were either derived from native copper or smelted from oxidic or sulfidic copper ores.

### Ingot torque metal

The majority of ingot torques (86 %) is made of copper containing arsenic, antimony, silver, bismuth, and in some cases nickel. On the basis of the composition Witter (1953) pointed out that these metals can be considered as alloys in the narrow sense which should have very good properties, like an excellent castability. From the impurity pattern it was concluded by Otto (1949), Otto and Witter (1952) that this metal was smelted from fahlores.

Comparing the composition of ingot torques from Danubian areas and Central Germany, Witter (1953) stated, that all these finds have the same origin. Even if there was no evidence for this hypothesis, later analyses have shown that about 67 % of the ingot torques are made of a specific fahlore metal (SMAP database, 1999). Junghans et al. (1968b) called this material C2, Butler (1978) coined the name 'classical *Ösenring* metal' (ingot torque metal) for this material and minor related types in the Stuttgart system (C2A/B and C2C). The main impurities in the ingot torque metal, i.e. arsenic, antimony and silver, are usually present in an average ratio approximating 2:2:1 (Butler, 1978). Bismuth is present at a level of 0.05 to 0.1 %, nickel is typically absent (Butler, 1978). Christoforidis et al. (1988) state that this metal is identical with the so-called 'Ostkupfer' (Eastern copper) by Pittioni (1957). Sperl (1975) equates C2 with the copper type 'Bertagrube' ('Volderer' copper) by Neuninger et al. (1960). A type of nickel containing ingot torque metal was called by Liversage and Liversage (1991) 'modified *Ösenring* metal'. On the basis of the Aschering hoard find (in the older literature called Grubmoos) Menke (1982) defined a copper type which is nearly identical with the ingot torque metal. The material class A according to Eckel (1992) shows a similar composition.

The classical ingot torque metal was mainly found in the Alpine foothills in southern Bavaria, and it is wide spread in Lower Austria, Moravia and Bohemia (Krause and Pernicka, 1998a). Based on the main distribution of this copper type (which cannot be separated from the distribution of ingot torques) Junghans et al. (1960) regarded it as 'Bavarian-Austrian group'. Butler (1978) suggested that the classical ingot torque metal has its origin between the Slovakian ore mountains and the Salzburg area. According to Krause and Pernicka (1996) any further compositional differentiation of ingots is impossible. As they stated, the composition of the ingot torque metal might be rather determined by the production process, because the compositional range is narrower than it would be expected from the ore body.

As described in the following chapter (see 3, p. 19ff.) copper alloys with

about 4 to 5 % arsenic represent the optimal compositional range in terms of cold working and hardening. However, the majority of ancient arsenical copper objects contain less than 4 to 5 % arsenic (Northover, 1998). Ravič and Ryndina (1984) noted that most of the Circumpontic artefacts only contain 1 to 2 % arsenic. Nevertheless it has to be considered that many Early Bronze Age artefacts, including ingot torques, were made of copper containing not only arsenic but also antimony. The sum of arsenic and antimony often reaches 4 to 5 %, which would mean that the used alloys are within the optimal compositional range.

Rittershofer (1983) pointed out that the material of ingot torques contains high amounts of bismuth which would lead to brittleness. This material would not be suitable for weapons or tools, but is found mostly in jewellery. I think, a material which is regarded as 'poor quality' will not be used for prestige objects like jewellery. Furthermore, a brittle material is not suitable for objects made of thin or sheet metal (like pendants or spirals). The problem of the bismuth content will be further discussed in the following chapter (3.4.3, p. 33).

### **Mixed groups**

Menke (1982) interpreted 18 ingot torques of the Bernhaupten hoard which he could not relate to one of the groups as mixed copper, he called type Bernhaupten. Although using a different classification system, Eckel (1992) came to the same conclusions. He explained 22 remaining analyses within the Bernhaupten find as a mixture of material.

Already Neuninger and Pittioni (1962) supposed that copper of different provenance was mixed for the production of objects. Other authors suggest a production of copper by cosmelting of sulfidic and oxidic ores (Lechtman, 1985; Lechtman and Klein, 1999; Rostoker and Dvorak, 1991) or cosmelting of copper-arsenic-antimony-ores, domeykite and arsenopyrite with copper (Earl and Adriaens, 2000; Rostoker et al., 1989; Zwicker, 1991; Zwicker et al., 1992). Such processes will also result in 'mixed copper'. If it is further taken into consideration, that the amount of arsenic in the metal depends on the smelting process (Pollard et al., 1990, 1989), it is difficult to identify real, i.e. intentional mixtures of metals. Pernicka (1995) stated that the so-called mixed groups are rather superposing material groups which may be based on different ores.

### **2.2.4 Archaeological and archaeometallurgical interpretation of ingot torques**

Based on the Stuttgart analyses and the distribution of material groups, Butler (1978) excluded the possibility that the shape of the ingots (ingot torque or rib-shaped ingot) served to identify the copper type present. Some years later, Eckel (1992) stated that differences in the shape of the rings – rough cast ingot torques, reworked neckrings and stages in between – are not related to the composition of the material. On the other hand, Butler (1978) pointed out that to some extent the technique of manufacture would have had to be adjusted to the type of material used. And by comparing objects of different composition a visible differentiation by colour was possible (Rittershofer, 1983). This is in accordance with Otto (1949), who defined a typological and a technological Bronze Age. If the material is different then different production and working technologies have to be considered. Low-impurity copper yielded very porous castings, which required a lot of hammer work to rectify. By contrast, castings of high-impurity copper are compact (Butler, 1978).

Since ingot torques were made of material of different provenance, Junghans et al. (1954) regarded them as an ‘international’ shape for raw material. Butler (1978) suspected, that the ingot torques were the rough-outs for the manufacture of neckrings, Junghans et al. (1960) suggested, that the ingot torques represent raw material for the production of pins, spirals and sheet metal. The main problem concerning these interpretations is the discrepancy between the number of ingot torques and final products (Krause and Pernicka, 1998b). About 29 % of the analysed artefacts were ingot torques and only 2 % were described as neckrings (SMAP database, 1999). If one presumes, that neckrings went out of fashion in a very short time, the material of their rough-outs would have been used for something else. However, about 69 % of the analysed artefacts made of the so-called ingot torque metal are ingot torques, about 15 % are rib-shaped ingots, and only 6 % of the artefacts are spirals and ring-headed pins (SMAP database, 1999). Furthermore it has to be considered, that this statistics represent only the number of objects, not the real amount, i.e. mass of metal. Krause and Pernicka (1998b) therefore questioned the general interpretation of the ingot torques as trading forms of raw copper. They noted that, if the ingot torques were indeed an intermediate product in the metallurgical chain, one would rather expect a smaller chance of preservation for them than for the finished products.

The peculiar chemical composition of the ingot torques compared to most other finished objects was interpreted as an indication of their specialised use.

Lenerz-deWilde (1995) suggested their use as premonetary payment or ‘special purpose money’. Innerhofer (1997) interpreted the numerous ingot finds to be the result of religious overcoming with the increase of ‘industrially’ organised bronze metallurgy. The careful deposition of the ingots was taken as an argument against profane interpretation, e.g. as trade deposits. Nevertheless, one can assume that a metal-worker or tradesman will hide his stock carefully for easier recovery.

## **Chapter 3**

# **The influence of arsenic, antimony, and bismuth on the properties of copper**

As shown in the previous chapter, ingot torques were mainly made of two copper types: low-impurity copper and ingot torque metal. The latter one was smelted from fahlores and is characterised by higher amounts of arsenic, antimony, and silver. The properties of such a material will be different from those of pure copper. This may be one reason, why fahlore metals were produced in the Early Bronze Age.

Coghlan (1960) stated, that mainly three factors were important for the ancient metalworker: the suitability of the metal for casting, its behaviour under hot and cold forging, and the hardness and strength of the metal in the finished product. The following chapter describes, how the properties of copper are altered by arsenic, antimony and bismuth and how the above-mentioned factors are influenced.

### **3.1 The influence of arsenic on copper**

#### **3.1.1 The copper-arsenic equilibrium phase diagram**

In the solid state copper and arsenic are only partially soluble within each other. At the eutectic temperature of 685 °C 6.83 % ( $w=7.8$  %) arsenic dissolves in copper (Fig. 3.1, p. 20) (Dies, 1967). At lower temperatures the solubility decreases to 6.5 % ( $w=6.9$  %) at room temperature (Dies, 1967).

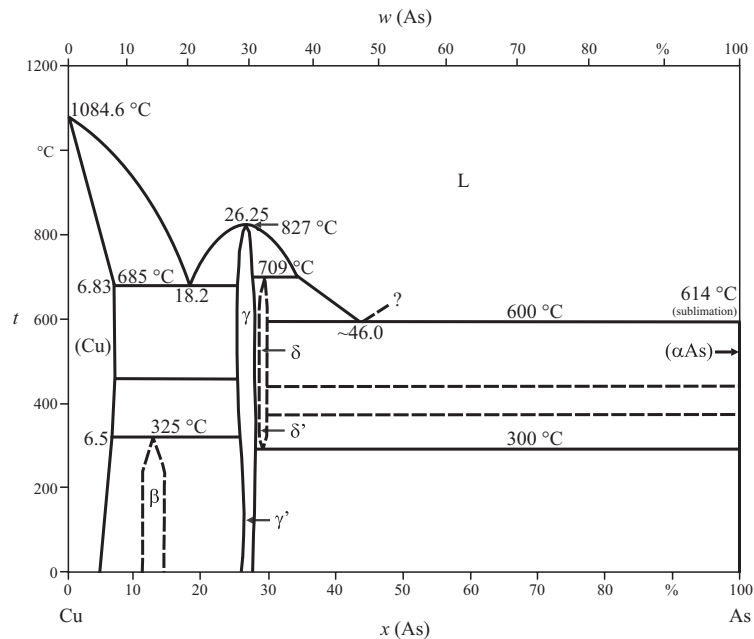


**Figure 3.1:** Equilibrium phase diagram of copper and arsenic. Drawing modified after Subramanian and Laughlin (1994a).

The copper-rich part of the equilibrium phase diagram shows an eutectic at 18.2 % ( $w=21$  %) arsenic and two intermetallic compounds. The copper-rich  $\beta$ -phase  $\text{Cu}_8\text{As}$  is peritectically formed between 300 and 350 °C (Subramanian and Laughlin, 1994a). The  $\gamma$ -phase  $\text{Cu}_3\text{As}$  is congruently formed at 827 °C and exists almost independently of temperature in a compositional range between 25.5 and 27.8 % arsenic. The naturally occurring mineral with the composition  $\text{Cu}_3\text{As}$  is known as domeykite.

### 3.1.2 Casting properties

Compared with pure copper the copper-arsenic alloys offer some advantages in casting. With an increasing amount of arsenic the melting temperature of the metal is decreasing. Spigatis (1876) mentioned the addition of a ‘Secretfluß’<sup>1</sup> containing arsenic, bismuth and lead, to cannon metal after the Thirty Years’ War.

<sup>1</sup>Secret from lat. *secretum*: secret, seldom, secret substance; according to Grimm and Grimm (1905) the term Secret was used in seafaring also for the ignition hole of cannons  
Fluß: flux



As Zwicker (1991) reported, the addition of 0.5 % arsenic to copper prevented porosity even when casting under oxidising conditions. Nevertheless, Hanson and Marryat (1927) reported difficulties to obtain perfectly sound castings of copper alloys with 1 % arsenic and a very low oxygen content. With increasing oxygen content this difficulty disappears to a large extent. The problem of soundness was also observed by Budd (1991). He found that particularly his sand cast copper alloys containing up to 11.7 % arsenic were porous (Budd, 1991). The pores showed a spherical and semi-spherical shape which is characteristic for steam-porosity. In addition, Budd (1991) could not observe a relationship between the amount of arsenic and the overall soundness of the castings. In this case the problem may rather be attributed to a decomposition of the binder in the used sand moulds. As Hanson and Marryat (1927) reported, a slight amount of unsoundness in the casting did not appear to have any harmful effects on the working properties of the metal, however it will influence its mechanical properties.

If copper-arsenic alloys are melted under oxidising conditions evaporative loss of arsenic may occur. McKerrell and Tylecote (1972) found an arsenic loss of about 1 % (absolute) after two times of melting and cooling of an alloy with 9.7 % arsenic. By contrast, in a non-oxidising atmosphere no arsenic loss was measured. Budd and Ottaway (1991) recorded that melting and alloying under a charcoal layer results in highly reducing conditions so that in their experiments no evidence of arsenic loss was found. During casting the molten metal is in contact with the air and the conditions are more oxidising, making arsenic loss more likely (Budd and Ottaway, 1991). In their experiments with copper alloys containing 8.01 % and 11.7 % arsenic, the solidification was accompanied by the evolution of a white vapour of arsenic oxide (Budd, 1991; Budd and Ottaway, 1991). But analytical data of the alloys suggested that the arsenic loss was negligible (Budd and Ottaway, 1991). McKerrell and Tylecote (1972) interpreted the arsenic loss as the solution of oxygen in the metal followed by reaction with arsenic and subsequent volatilisation of arsenic trioxide. The volatilisation of arsenic itself was not considered to be the main rate-determining process.

Another problem in casting copper-arsenic alloys is their segregation tendency. The copper-arsenic equilibrium phase diagram (Fig. 3.1, p. 20) shows that solidification takes place during a large temperature interval, suggesting a non-equilibrium, often dendritic, solidification. In the case of segregations or coring, the centre of the formed dendrites is enriched in the higher melting component, i.e. copper. The zones between the dendrites contain more of the lower melting component. Schimmel (1930) reported that it is possible to distinguish between copper with more than 0.2 % arsenic and arsenic-free copper in metallographic

sections, because the first one forms zoned crystals. Due to the slow diffusion of arsenic in copper the dendrites are still visible even after several annealing cycles (Schimmel, 1930).

Several authors reported the formation of the intermetallic phase  $\text{Cu}_3\text{As}$  between copper-rich dendrites. Hanson and Marryat (1927) found that cast specimens with 2.52 up to 7.25 % arsenic and free of copper oxides contained a light blue constituent, which they termed  $\beta$ . Ravič and Ryndina (1984) found a non-equilibrium eutectic of  $\text{Cu}_3\text{As}$  in copper containing 3 % arsenic. Northover (1989) recorded the first appearance of the  $\gamma$ -phase at about 2% arsenic and Budd (1990) observed this phase already in alloys containing about 1 % arsenic.

### 3.1.3 Mechanical properties

Budd (1991) stated that, although the effect of solid solution strengthening by arsenic in copper would be minimal in arsenical copper of the bulk compositions reported from European Eneolithic artefacts, it should not be entirely disregarded. At higher amounts a significant effect might be expected (Budd, 1991). Hanson and Marryat (1927) found an arsenic content of 1 % not to increase the Brinell hardness of the copper alloy. For copper with 2 % arsenic a hardness of 53 HV was measured, which is only a slight increase compared to the copper with about 50 HV (Lechtman, 1996). The main increase in hardness has been recorded by Lechtman (1996) at about 7 % As. Above 8 % arsenic the alloys became brittle. Hence, Lechtman (1996) concluded, that up to the solid solubility limit, the solid solution hardening of copper by arsenic is not significant.

Budd (1991) reported that in his experiments the more slowly cooled sand castings were subject to greater solution hardening than the chill cast billets. He concluded, that the cooling of the sand casts would be closer to the equilibrium and, therefore, a greater proportion of arsenic would be expected in the solid solution (Budd, 1991). Hence, he took not account of the fact, that a faster cooling would result in smaller grains and according to the Hall-Petch equation smaller grains would result in a higher strength or hardness (see Askeland (1994); Hummel (1997)).

Hanson and Marryat (1927) found arsenic to reduce the crystal size in castings. This may lead to an increase of the tensile strength, since it increases with decreasing grain size. Up to 1 % arsenic the formation of a solid solution slightly increases the tensile strength, whereas the ductility of the material was not influenced (Hanson and Marryat, 1927). The increase of tensile strength of cast alloys with the arsenic content was also reported by Pazuchin (1964). But he noticed

that the elongation and the reduction in area after fracture decreased markedly with higher arsenic contents, i.e. the improved strength of the alloyed copper is reached at the expense of its ductility (Pazuchin, 1964). Lechtman (1996) noticed that copper-arsenic alloys rolled to a 50 and 75 % reduction in thickness were highly ductile. The tensile strength of the alloys was increased with increasing arsenic content and degree of working. In accordance with Hanson and Marryat (1927) she reported that up to the solid solubility limit, with increasing arsenic concentrations the material becomes stronger with no sacrifice in ductility (Lechtman, 1996).

With increasing arsenic contents the absorbed energy in the notched-bar impact test was increased for the rolled and annealed specimens (Hanson and Marryat, 1927).

### 3.1.4 Working properties

#### Cold Working

The increase of the work hardenability, i.e. the influence of cold working, is one of the most regarded and investigated properties of copper-arsenic alloys.

Cold working is the deformation of a metal below its recrystallisation temperature. With cold working the desired final shape is produced and the metal is simultaneously strengthened. The strengthening or work hardening is the result of the increasing number of dislocations. When the applied stress exceeds the yield strength, the dislocations in the metal start to slip. The traces of this movement can be seen in metallographic section as so-called slip traces. Further increase of the applied stress, and thus the deformation, leads to a visible distortion of the grains. The metallographic evidence is a deformed, fibrous microstructure. The dislocations interact with each other and with grain boundaries and inclusions. At a certain degree of deformation the motion of the dislocations is impeded. This leads to an increased material's resistance to deformation which is known as work hardening. If the material is further deformed its structure will be destroyed by cracks until the material fails.

Böhne (1965) compared pure copper and a copper alloy containing 1.5 % arsenic both hammered to a wedge shape. Although there is a hardening effect, Böhne (1965) found no influence of the arsenic content. He interpreted the hardening only as an effect of cold working. In contrast to other researchers (Budd and Ottaway, 1991; Budd, 1991; Northover, 1989) he stated that with an arsenic content of 2 % the alloys would become markedly brittle.

Ravič and Ryndina (1984) used compression tests to simulate forging. Alloys with up to 5 % arsenic were found to be forgeable up to a 70 to 80 % reduction in thickness. The higher alloyed material with 6 to 8 % arsenic was less ductile with the first cracks occurring at a 60 to 40 % deformation. Alloys with arsenic contents exceeding 10 % were hardly cold deformable (Ravič and Ryndina, 1984). In this case, first cracks were found at a deformation of 20 %.

Budd and Ottaway (1991) reported that pure copper could be cold rolled to reductions of more than 75 %. By contrast, copper alloys with 8.1 and 11.7 % arsenic work hardened very rapidly and were comparatively brittle. These alloys showed surface cracking at a deformation of 5 % and the alloys fractured after 31 % reduction in thickness (Budd, 1991).

Lechtman (1996) pointed to the difference in hardening of a hammered and a rolled material. Under both kinds of deformation copper-arsenic alloys work-harden rapidly, according to Lechtman (1996) particularly in the 0 to 50 % thickness reduction range. Both, rolled and hammered alloys, reach the same hardness at a reduction in thickness between 75 and 87.5 % (Lechtman, 1996). However, in the compositional range of 0.5 to 5 % arsenic the hammered material was found to work-harden more rapidly than its rolled counterpart (Lechtman, 1996).

It was noted that alloys with 2 to 6 % arsenic represent the most successful range of composition in terms of cold working, being sufficiently ductile to be rolled to reductions in width of 60 to 80 % without cracking (Budd and Ottaway, 1991). As for the rolled alloys the most suitable compositional range for forging and hardening was found to be a 4 to 5 % arsenic content (Ravič and Ryndina, 1984).

### **Annealing**

The improved work hardenability of copper-arsenic alloys can be an advantage over pure copper if hard edges should be produced. But it will be a disadvantage if high deformation rates are required.

As described previously, cold working increases the number of dislocations in the material. If the motion of the dislocations is impeded at a certain amount of deformation, cracks may form and the material finally fails. If a material is to be deformed to a higher degree, the work hardening effects have to be eliminated and the ductility has to be restored. Annealing at moderate temperatures leads to the elimination of residual stresses introduced during cold deformation while the strength of the material is not affected. At temperatures of about 0.4 times the absolute melting temperature, the movement of dislocations begins and new grain

boundaries may be formed. The nucleation and growth of new grains is called recrystallisation. Since most of the dislocations are eliminated by this process, the recrystallised material has a lower strength.

Alloys recrystallise at higher temperatures than pure metals, because assimilated elements in the solid solution or other phases impede the movement of the dislocations. Pure copper will recrystallise at about 200 to 270 °C, while arsenical copper recrystallises at temperatures ranging from 300 to 400 °C (Northover, 1989). Budd (1990) noted that even after annealing at temperatures of 682 °C the specimens of copper with up to 6.06 % arsenic were characterised by the survival of the cast-in segregations with partly distorted copper-rich dendrites interspersed with islands of  $\text{Cu}_3\text{As}$ . He recorded that the recrystallisation of the copper-rich areas takes place at temperatures as low as 300 °C, but the complete recrystallisation of the whole microstructure is not apparent below about 600 °C (Budd, 1990). At the beginning of the 20th century the higher recrystallisation temperature of arsenical copper was one of the reasons for its use for steam locomotive fireboxes, staybolts and other heat-exchange equipment.

The metallographic evidence for recrystallisation are equiaxed grains instead of deformed, elongated grains. Small recrystallised grains are formed if the initial grain sizes were small and the amount of deformation was high. Short annealing times, lower temperatures and a second phase prevents grain growth. Particularly in cubic face-centred materials like copper annealing twins occur and may be used in metallographic sections as evidence for recrystallisation. Another evidence for recrystallisation is the decreased strength and hardness of the annealed material, which can be determined by hardness measurements.

### Hot working

Hot working takes place at temperatures above the recrystallisation temperature. The deformation energy absorbed during working is immediately released by recrystallisation.

According to Ravič and Ryndina (1984) copper alloys with up to 18 % arsenic were found to be very ductile in hot working at 500 and 600 °C. Arsenical bronzes hot rolled and hot hammered at 625 °C were found to be extremely ductile, with elongation levels for high arsenic contents approaching those of copper (Lechtman, 1996). Even an alloy with 13 % arsenic remained plastic and malleable, although it showed edge cracks.

One problem in hot working copper-arsenic alloys in air, i.e. under oxidising conditions, may be the loss of arsenic. McKerrell and Tylecote (1972) observed a

decrease of the initial arsenic content of 8.7% to 7.3 % on hot working the material twice. A period of 10 min hot working reduced the arsenic content from 2.9 to 0.8 % arsenic (McKerrell and Tylecote, 1972). Lechtman (1996) noticed a minimal oxidative arsenic loss with copper containing 7 % arsenic, and a noticeable loss with the 10 and 13 % alloys.

According to Northover (1989) there is little, if any, conclusive metallographic evidence for hot working of prehistoric copper-arsenic alloys. Elongated inclusions cannot be taken as indicators because both sulfides and oxides are also cold deformable.

## **3.2 The influence of antimony on copper**

### **3.2.1 The copper-antimony equilibrium phase diagram**

In the solid state antimony is partially soluble in copper, decreasing with temperature. The maximum solubility of 5.8 % ( $w=11$  %) antimony in copper is reached at a temperature of 645 °C (Dies, 1967). At lower temperatures the solubility decreases rapidly. The copper-rich part of the equilibrium phase diagram (Fig. 3.2, p. 27) shows an eutectic point at 19 % ( $w=31$  %) antimony (Dies, 1967; Subramanian and Laughlin, 1994b). The  $\delta$ -phase ( $\text{Cu}_9\text{Sb}_2$ ) with 18.5 to 20 % antimony is formed peritectically at 462 °C (Subramanian and Laughlin, 1994b). As Archbutt and Prytherch (1937a) stated, antimony occurs in copper only partly in solution, and partly as an insoluble compound with oxygen.

### **3.2.2 Casting properties**

Like arsenic, antimony lowers the melting temperature of copper. Hence, copper-antimony alloys should have some casting advantages over pure copper.

Difficulties to obtain sound castings as mentioned by Hanson and Marryat (1927) for copper-arsenic alloys are not reported for copper-antimony alloys. This might be explained by the casting technology. Archbutt and Prytherch (1937a) prepared copper alloys with up to 0.75 % antimony in a vacuum furnace. The billets were cast in machined graphite moulds. An effect of antimony on the microstructure of the alloys was not determined (Archbutt and Prytherch, 1937a).

As with copper-arsenic alloys antimony is partially lost during melting. The antimony removal from copper melts by evaporation and slagging is reported to be similar to that of arsenic, but slower (Stahl, 1918). At first, a small amount

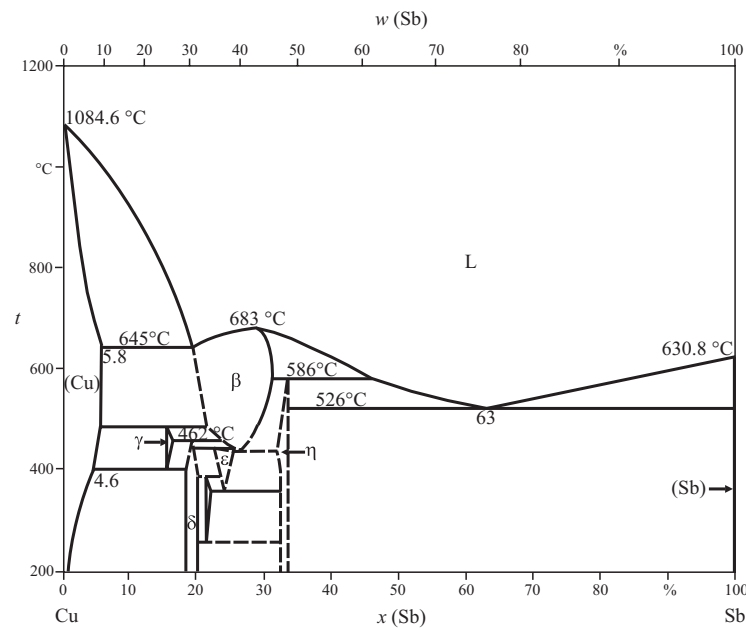


**Figure 3.2:** Equilibrium phase diagram of copper and antimony. Drawing modified after Subramanian and Laughlin (1994b).

evaporates, while another part evaporates after reaction with oxygen. The major part forms antimonates with other impurities and copper. (Stahl, 1918).

Copper-antimony alloys have a large solidification interval. Similar to copper-arsenic alloys they have a pronounced shrinkage tendency and show crystal segregations. Discontinuous precipitation was reported for antimony amounts of 9 to 10 % and temperatures below 410 °C (below this temperature the solubility of antimony in copper rapidly decreases, see Fig. 3.2, p. 27) (Dies, 1967). The segregation temperatures are quite low, so that even at temperatures below 300 °C coarse-lamellar segregation was observed (Dies, 1967).

### 3.2.3 Mechanical properties

In 1912, Lewis stated that there would be a future for antimonial copper when the correct proportions between antimony and oxygen would become known (Archbutt and Prytherch, 1937a). By contrast, several years later, Dies (1967) reported that the bad influence of antimony on copper is so significant that it could be considered as a harmful alloying element.

As Dies (1967) stated, the solution hardening effect of antimony on copper is comparably low. Archbutt and Prytherch (1937a) noted, that with equal percentages, antimony produces alloys which are as tough and ductile as arsenic-copper alloys, but slightly harder. This effect can be explained by the larger difference of the atomic radii compared to the copper and arsenic. The larger atoms of antimony cause higher strain in the lattice, so that the material becomes harder.

According to Dies (1967) the elastic modulus strongly decreases with increasing antimony contents, independent of the formation of the intermetallic compounds  $\text{Cu}_3\text{Sb}$  and  $\text{Cu}_2\text{Sb}$ . Compared with pure copper, both yield and tensile strength of copper-antimony alloys increase between  $-100$  and  $500$  °C (Dies, 1967). Fine-grained copper-antimony alloys obtain a significant yield point behaviour with increasing antimony content, which is absent in the copper stress-strain diagram.

Archbutt and Prytherch (1937a) found that up to an antimony content of 0.47 % there is no pronounced effect on the toughness of copper. Since they investigated the copper-antimony alloys mostly in the hot/cold rolled and annealed state, their results are not comparable to investigations of alloys in the cast state.

### **3.2.4 Working properties**

#### **Cold Working and annealing**

Since copper-antimony and copper-arsenic alloys show both similarities in the phase equilibrium diagram and in their mechanical properties, one would expect similar technological properties.

Dies (1967) reported, that the  $\alpha$ -solid solution of the copper-antimony system shows a good cold deformability. Archbutt and Prytherch (1937a) found antimony to increase the hardness of copper both in the rolled state and under annealed conditions. The effect was found to be more distinct in the rolled state (Archbutt and Prytherch, 1937a). The work hardening was found to increase with rising antimony content.

Similar to copper-arsenic alloys the recrystallisation temperature of copper-antimony alloys increases with the alloying content (Dies, 1967).

#### **Hot working**

Archbutt and Prytherch (1937a) reported that an alloy with 1 % antimony was extremely hot-short, but withstood a fair amount of cold working. According to



experiments carried out by Hampe, copper with 0.5 % antimony was reported to be as tough as electrolytic copper, but tends to red-fracture (breaking at red-heat). Copper with the same antimony content bound as cuproantimonate showed neither cold- nor red-fracturing (Stahl, 1918). With the recrystallisation temperature of copper-antimony alloys the warm-deformation resistance is increased (Dies, 1967).

Hot working of copper-antimony alloys in air results in oxidative loss of the alloying element. McKerrell and Tylecote (1972) have shown that the initial antimony content of 4.3 % is reduced to 2.6 % by triple remelting and hot working. Remelting and hot working of 10 min lowered the antimony content of this alloy to 0.9 % (McKerrell and Tylecote, 1972).

### **3.3 The influence of bismuth on copper**

#### **3.3.1 The copper-bismuth equilibrium phase diagram**

In the solid state about 0.001 % bismuth can be dissolved in copper (Dies, 1967). The copper-bismuth equilibrium diagram shows an eutectic point at about 99.5 % bismuth and 270.6 °C (Fig. 3.3, p. 30) (Chakrabarti and Laughlin, 1994).

#### **3.3.2 Casting properties**

Hanson and Ford (1927) reported difficulties in obtaining a sound casting with the desired oxygen content of 0.015 %, probably due to excessive oxidation.

Stahl (1925) explained the harmful effect of bismuth on copper by the solidification of the metal. At high temperatures copper solidifies, while liquid bismuth is distributed at the edges of the copper crystals and solidifies at 269 °C (Stahl, 1925). By this process a separating layer of bismuth is formed between the copper crystals. Hanson and Ford (1927) found such layers along the grain boundaries of their cast alloys. A further damage is caused by the expansion of bismuth during its solidification which further separates the copper crystals (Stahl, 1925).

#### **3.3.3 Mechanical properties**

Hanson and Ford (1927) found that bismuth contents of up to 0.1 % had no beneficial effect on the tensile properties of rolled copper. The tensile strength of

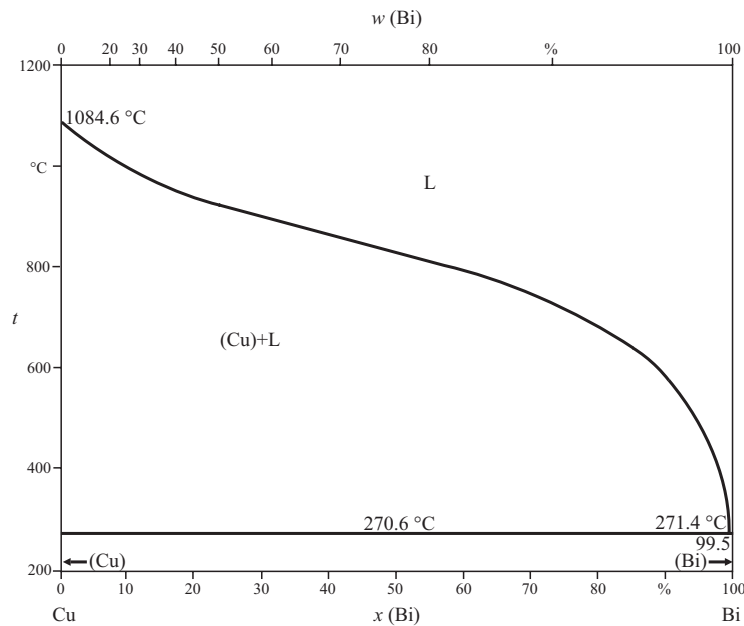


**Figure 3.3:** Equilibrium phase diagram of copper and bismuth. Drawing modified after Chakrabarti and Laughlin (1994).

rolled copper containing bismuth was slightly higher than that of copper containing oxygen only (Hanson and Ford, 1927). Elongation and reduction of area were slightly reduced, i.e. the copper was embrittled. For the cold rolled material a distinct reduction in its elongation was observed (Hanson and Ford, 1927).

Dies (1967) reported that the notch impact strength of copper is decreased at bismuth amounts above 0.0005 %. The fractures of the alloys were found to be intercrystalline both at low and high temperatures (Dies, 1967). He pointed out that the fewer grain boundaries were available for the distribution of bismuth, the more distinct was the embrittlement (Dies, 1967).

### 3.3.4 Working properties

#### Cold working

As Dies (1967) stated, the small solubility of bismuth in solid copper reduces the workability of copper even at low concentrations. Stahl (1925) cited an earlier work of Hampe, who found that already 0.05 % bismuth cause cold fracturing of copper. Copper with 0.1 % bismuth was regarded as unusable for technical

purposes because it showed edge cracking during hammering (Stahl, 1925). Hanson and Ford (1927) reported that copper containing up to 0.047 % bismuth was cold rollable without cracking. However, the higher alloyed copper with 0.999 % bismuth cracked at the first pass of rolling (Hanson and Ford, 1927).

### Hot working

Hanson and Ford (1927) found small quantities of bismuth to affect adversely the rolling properties of copper, particular during hot rolling.

According to Stahl (1918) 0.05 % of bismuth make copper cold- and strongly red-short, while only 0.02 % bismuth lead to red-fracturing of copper (Stahl, 1925). Dies (1967) stated, that a bismuth content in excess of 0.005 % leads to hot-shortness of copper. Stahl (1925) explained this with the melting of the bismuth layer along the grain boundaries destroying the internal structure of the copper.

## 3.4 The combined influence of the alloying elements

### 3.4.1 Combined influence of arsenic and antimony on copper

A pronounced effect of antimony and arsenic has not been observed in the macrostructure of cast alloys with up to 0.5 % antimony and 0.53 % arsenic (Archbutt and Prytherch, 1937b). The microstructure of annealed rolled rod showed a small quantity of a second constituent, which was not further described. Hein and Bombach (1980) reported that in copper containing arsenic and antimony no binary phases such as  $\text{Cu}_3\text{As}$  or  $\text{Cu}_3\text{Sb}$  were found. Several authors mentioned a ternary phase  $\text{Cu}_6\text{AsSb}$  ( $\text{Cu}_{72.4}\text{As}_{12.8}\text{Sb}_{14.8}$ ) (Tedenac, 1994). Northover (1998) recorded two phases close to  $\text{Cu}_3(\text{As,Sb})$  and  $\text{Cu}_2(\text{As,Sb})$  in copper-arsenic-antimony alloys from Arbedo (Switzerland). They may be ternary intermetallic compounds with compositions such as  $\text{Cu}_9\text{AsSb}_2$  and  $\text{Cu}_9\text{As}_2\text{Sb}$  (Northover, 1998).

According to Archbutt and Prytherch (1937b) the addition of antimony to arsenic containing copper increases the ultimate stress (tensile strength) and the elongation in the tensile test, particularly for annealed material. A striking result of their investigations was the fact that the effect of antimony on copper alloys with a specific arsenic content was much more distinct than that of arsenic on copper containing a specific amount of antimony (Archbutt and Prytherch, 1937b). It was proposed that antimony improves the mechanical properties of copper to a

greater extent than arsenic does. The combined effect of both is greater than that of either antimony or arsenic alone (Archbutt and Prytherch, 1937b).

Oxygen-free copper containing arsenic and antimony was found to have better cold-rolling properties than copper containing only antimony (Archbutt and Prytherch, 1937b). Copper alloys with up to 0.5 % antimony and arsenic could be hot rolled without difficulty. It appeared that arsenic assists the hot rolling of antimony-copper alloys (Archbutt and Prytherch, 1937b).

A significant softening of cold worked material was not observed below a temperature of 350 °C and is complete in most cases at 400 °C (Archbutt and Prytherch, 1937b). It was found that arsenic does not appear to rise the softening temperature range of copper-antimony alloys. Hence, this range is considerably higher than that of copper-arsenic alloys (Archbutt and Prytherch, 1937b).

### **3.4.2 The influence of arsenic and antimony on copper containing oxygen**

Johnson (1910) found in his investigations of tough-pitch copper that the arsenical copper showed improved mechanical properties when compared with the arsenic free specimen. The reason for this improvement is the deoxidising effect of arsenic on copper.

If the copper melt contains oxygen, a copper-copper oxide eutectic can be formed at the grain boundaries. This eutectic decreases the ductility of the copper and, due to its lower melting point, influences the hot workability. Altwicker (1925) reported that the tensile strength increases with oxygen content, while the elongation and the reduction of area after fracture rapidly decrease. This means, that the copper embrittles with increasing oxygen content. It was further noted that with increasing amount of oxygen the amount of rolling energy has to be increased (Altwicker, 1925).

In copper alloys with low oxygen and high arsenic contents Ruhrmann (1925) observed the reduction of  $\text{Cu}_2\text{O}$  by arsenic. Copper containing less than 0.31 % arsenic and less than 0.38 % oxygen showed a copper-copper oxide eutectic. Hanson and Marryat (1927) reported copper oxides in copper-arsenic alloys with up to 1.87 % arsenic. If the copper contained about 0.38 % oxygen (the eutectic composition), arsenic amounts below 4.73 % did not lead to significant deoxidation (Ruhrmann, 1925). Instead, new dark blue inclusions were formed, while the eutectic disappeared. As Ruhrmann (1925) noted, they cannot consist of  $\text{As}_2\text{O}_3$  and  $\text{As}_2\text{O}_5$ , because these compounds evaporate at low temperatures. Thus, he

concluded that the segregations may consist of a compound of  $\text{As}_2\text{O}_5$  and  $\text{Cu}_2\text{O}$ , best described by the formula  $\text{Cu}_2\text{O}\cdot\text{As}_2\text{O}_5$  (Ruhrmann, 1925). Keesmann and Moreno Onorato (1999) described a similar oxidic phase within arsenic rich copper from Los Millares with the formula  $4\text{Cu}_2\text{O}\cdot 3(\text{As,Sb})_2\text{O}_3$  (see also Keesmann et al. (1997)). Charles (1967) reported that during solidification arsenic may copper oxide cause to form discrete particles, rather than the eutectic grain boundary network. Budd and Ottaway (1991) stated that it seems unlikely that deoxidation by arsenic could be sufficiently thorough to remove oxygen from the melt as rapidly as it would be dissolved. In contrast to the relatively high affinity of arsenic to oxygen, Budd (1991) reported that its deoxidising function during solidification is not straightforward.

Deoxidising effects of antimony on copper are not reported. According to Stahl (1918) the usual amount of antimony in copper refining melts is not sufficient to reduce cuprite, but he reported the removal of absorbed  $\text{SO}_2$  from the melt.

Even if the investigations of Stan et al. (1998) do not concern copper containing antimony and oxygen, but ceramics of the Sn-Sb-Cu-O system, the observations for the phase equilibrium system Cu-Sb-O can be taken as a clue for the processes occurring in copper metal. In the above-mentioned system the formation of different oxides, depending on the temperature was observed.  $\text{Sb}_2\text{O}_3$  undergoes oxidation to  $\text{Sb}_2\text{O}_4$  and  $\text{Sb}_2\text{O}_5$  while  $\text{CuO}$  reduces to  $\text{Cu}_2\text{O}$  at temperatures above  $500^\circ\text{C}$  (Stan et al., 1998). Also the formation of  $\text{CuSb}_2\text{O}_6$  and  $\text{Cu}_4\text{SbO}_{4.5}$  binary compounds was observed whereby  $\text{CuSb}_2\text{O}_6$  was interpreted as  $\text{CuO}\cdot\text{Sb}_2\text{O}_5$  and  $\text{Cu}_4\text{SbO}_{4.5}$  as  $4\text{Cu}_2\text{O}\cdot\text{Sb}_2\text{O}_5$ .

As a further effect of deoxidation and oxide formation Northover (1989) reported that about 25 % of the arsenic in the alloys may be bound as oxides. This part of arsenic will not contribute to the properties of the copper-arsenic solid solution. The same should be true for antimony suggesting that the properties of the alloy can hardly be estimated by bulk analyses alone.

### **3.4.3 The influence of arsenic and antimony on copper containing bismuth**

Dies (1967) stated that if bismuth is bound in oxides or as high-melting intermetallic compounds concentrations higher than in unalloyed copper are permissible. In this case, oxygen and phosphorus as well as additions of arsenic, cadmium and tin are effective (Dies, 1967).

From rolling and bending experiments Lewis concluded that arsenic neutralised the injurious effect of bismuth to a certain extent. Copper with 0.1 % bismuth was found to crack very badly at the edges in the rolling test and could not be bent. With the addition of 0.6 % arsenic the cracks were less severe than without arsenic and the sheet bent fairly well (Johnson, 1910). Copper with 0.05 % bismuth and 0.6 % arsenic was found to roll fairly well and to bend well.

Johnson (1910) found the effect of bismuth on the mechanical properties of rolled tough-pitch arsenical copper not to be serious up to 0.1 % bismuth. Bismuth raises the tensile strength, but it lowers the elastic limit and resistance to alternating stress (Johnson, 1910). Hence, he stated that no commercial arsenical copper could be regarded as fit for working at a red-heat which contained so much bismuth. As Johnson (1910) further wrote, any crude copper containing over 0.01 % of bismuth should be regarded with suspicion, since the copper might contain other impurities. It was concluded that arsenic and oxygen both aid in improving the mechanical properties of copper containing bismuth (Johnson, 1910). As possible cause he mentioned the 'quick-setting' properties of arsenical copper. The pure copper solidifies more slowly and any bismuth will be given more time to separate out and find its way to the grain boundaries (Johnson, 1910).

Stahl (1925) reported that bismuth arsenate was found to be less harmful for copper than bismuth. Furthermore he noted that copper with some hundredth percent of bismuth bound as arsenate was suitable for different mechanical working (Stahl, 1925). If 0.05 or 0.06 % of bismuth occurs in copper as antimonate, the material was found to be neither red- nor cold-brittle (Stahl, 1918). He concluded that antimony in sufficient quantity will counteract the effect of bismuth on copper. However, if the bismuth contents exceed 0.2 % even the antimonate can not prevent copper from red-fracture (Stahl, 1918).

# **Chapter 4**

## **Methods used for sampling, analysis and material testing**

### **4.1 Sampling of archaeological material**

#### **4.1.1 Drill shavings for X-ray fluorescence analysis**

In order to analyse archaeological metal artefacts, it is often necessary to take samples to obtain the bulk composition. In most cases drill shavings are taken. This sampling method is destructive, but it is possible to keep the damage of the artefact relatively small.

For the analyses of this study the sampling of the ingot torques was performed by S. Möslein. The samples were taken with a HSS-spiral drill bit of 1.5 mm diameter (in some cases 1.0 mm diameter) with a small Proxxon drilling machine. After removal of the corrosion layer the drilling went as deep as possible, mostly intersecting the object. The drill was cleaned after each sample and changed after 5 to 8 applications.

For XRF analysis the drill shavings were transferred into small polyethylene containers with 8 mm diameter and fixed between weighing paper on the upper and a mylar thin-film on the lower side.

#### **4.1.2 Samples for metallography**

The samples for metallographic investigations of the ingot torques were cut with a jeweller's saw. On the one hand, samples should be as representative as necessary to answer the questions. On the other hand, the damage to an artefact should be as

small as possible. In most cases the samples were taken from the heavily deformed zone near the loops of the ingot torques. This ensures that the investigated parts are comparable and provide as much information about the working process as possible. In some cases broken ends and loops were sampled.

After metallographic investigations the unmounted samples were inserted into the original positions and fixed into the ingot torques with epoxy resin. The same resin was used to fill the gaps from cutting and grinding. A brass wire hammered to the desired thickness was used as a spacer. Besides the cuts, this wire is detectable by X-raying in order to determine the sample location. Finally, the cuts were retouched with oil paint.

## **4.2 Analysis**

### **4.2.1 Energy dispersive X-ray fluorescence analysis**

X-ray fluorescence is the excitation of emission lines in the X-ray spectrum by X-rays (Böcker, 1997). Electrons on a level close to the atomic nucleus are excited. As they return to their initial level, the energy difference is emitted as characteristic X-radiation. This radiation is analysed by the detector system for intensity and spectral distribution (Hahn-Weinheimer et al., 1984). In this work energy dispersive X-ray fluorescence analysis (EDXRF) was used allowing simultaneous determination of different elements.

For the investigations a TX-5000 spectrometer (Spectrace Instruments Inc.) was used. This spectrometer is equipped with a conventional, nitrogen-cooled Si(Li)-detector with a resolution of 150 eV at 5.9 keV. The auto-sampler allows the measurement of 10 samples in one run. For calibration, pure element standards were used. The elements which are determined in ancient copper artefacts can be divided into two groups based on the energy of their characteristic radiation. The used X-ray energies of Fe, Co, Ni, Cu, Zn, As, Au, Pb, and Bi are between 6.4 and 15.2 keV, that of Ag, Sn, and Sb between 22.1 and 31 keV (Lutz and Pernicka, 1998). Hence, for each analysis two spectra were measured. Copper as the main component was used as an internal standard, i.e. the copper signal was measured in both analysing runs.

Both sample types, metallographic sections and drill shavings, were measured with the same parameter sets (Table 4.1, p. 37). The measurements were finished if the preset count rate for copper or the maximum measuring time was reached. A control sample (plane sample of reference alloy Cu As<sub>2</sub> Sb<sub>2</sub> Bi<sub>0.1</sub>) was measured



**Table 4.1:** EDXRF parameter sets for metallographic sections and drill shavings

	1st parameter set	2nd parameter set
spectral lines determined	Fe $K_{\alpha}$ , Co $K_{\alpha}$ , Ni $K_{\alpha}$ , Cu $K_{\alpha}$ , Zn $K_{\alpha}$ , As $K_{\alpha}$ , Se $K_{\alpha}$ , Au $L_{\alpha}$ , Pb $L_{\alpha}$ , Bi $L_{\alpha}$	Ag $K_{\alpha}$ , Sn $K_{\alpha}$ , Sb $K_{\alpha}$ , Te $K_{\alpha}$
tube voltage	35 kV	50 kV
tube current	0.25 mA	0.25 mA
filter	Rh2	Cu
max. measuring time	3000 s	3000 s
preset count rate for Cu	740,000	50,000
atmosphere	air	air

regularly to ensure that the measurement was in statistical control, i.e. that the values for arsenic, antimony, bismuth and iron lay within the range defined by the two sigma limits of the mean (see e.g. Freiser and Nancollas (1987)).

The measured spectra were analysed in two steps. For qualitative analysis and the first quantification the internal software of the TX-5000 EDXRF version 1.35b was used. The elemental contents were calculated with the method of fundamental parameters (see e.g. Hahn-Weinheimer et al. (1984)). For the special composition of ancient copper alloys the internal quantification routine was not sufficient. Further problems arose with the use of drill shavings as samples.

Iron and nickel represent important impurities in prehistoric copper. In previous investigations it was found that iron below 1 % and nickel below 0.1 % are difficult to determine with high precision, because the main lines partly overlap with the copper  $K_{\alpha}$  and escape peak (Lutz and Pernicka, 1996, 1998). Small blank values for iron, nickel and cobalt were determined in previous investigations (Lutz and Pernicka, 1996). These values were subtracted from the analyses.

One of the major impurities in Early Bronze Age copper is arsenic. There are no problems with the analysis as long as the lead content in the sample is low. At high lead concentrations, arsenic amounts below 0.5% are difficult to determine accurately, since the arsenic  $K_{\alpha}$  line and the lead  $L_{\alpha}$  line have identical energies (Lutz and Pernicka, 1996).

Small amounts of lead and bismuth are often found in prehistoric copper. Since both metals do not dissolve in copper, they are inhomogeneously distributed.

This leads to an overestimation in drill shaving samples, which has to be considered (Lutz and Pernicka, 1998).

Silver, tin and antimony belong to the important elements in Early Bronze Age copper alloys. There are no analytical problems for plane samples, but for drill shavings. For silver, tin, and antimony the information depth of the fluorescence radiation and, hence, the analysed volume is greater than for the elements with low X-ray energies (Lutz and Pernicka, 1996). If the samples are thicker than the information depth then there are no problems. However, this condition is not met for drill shavings and small sample weights. As a consequence, for small sample weights the amounts of silver, tin and antimony are underestimated. The geometry of drill shavings leads to the opposite effect. The excitation of the characteristic spectral lines is better for drill shavings than for flat samples. That means that silver, tin and antimony are overestimated (Lutz and Pernicka, 1996).

The above-mentioned effects of over- and underestimation of elemental contents were corrected with an empirical evaluation routine by Lutz and Pernicka (1996). For this work, the initial SAS code was rewritten for PERL in order to simplify the evaluation of the data.

#### **4.2.2 Scanning electron microscopy and electron microprobe analysis**

In scanning electron microscopy, the sample surface is scanned with a highly focused electron beam. The secondary electrons emitted have their origin in small depths of the sample and are used for imaging the surface topography. The resolution is limited by the diameter of the electron beam (Schumann, 1991). The backscattered electrons provide information about the atomic number of the elements in the sample. This image is used for element contrast. Similar to the X-ray beam in X-ray fluorescence analysis the electron beam can be used for excitation of emission lines in the X-ray spectrum. The characteristic X-rays emitted are used for qualitative and quantitative elemental analysis. The electron microprobe can be considered as a combination of X-ray spectral microanalysis and a scanning electron microscope (Hunger, 1995; Schumann, 1991). It is a highly localised analysing technique with a diameter of the excited volume of about 1  $\mu\text{m}$ .

Scanning electron microscopy combined with energy dispersive X-ray analysis (EDX) was used for the determination of the elemental distribution in the samples. The measurements were carried out on a DSM 960 SEM (CARL ZEISS Oberkochen) with an EDX facility. The analyses of inclusions were made with

a JXA 8900RL microprobe (JEOL) by wavelength dispersive spectrometry. For standardisation, pure copper, silver, antimony, bismuth, and iron were used. For the determination of arsenic gallium arsenide GaAs was used as standard, for sulfur marcasite FeS<sub>2</sub>, and for oxygen cuprite Cu<sub>2</sub>O (priv. comm. D. Heger). Since the microprobe is equipped with five crystal spectrometers, only five elements can be determined simultaneously. In the first run arsenic, sulfur, silver, and antimony, in the second run oxygen, iron, bismuth, and copper were measured. In both runs an accelerating voltage of 20 kV was used. The main disadvantage of this method is that during the first and the second run two different areas may be analysed. In a few cases this problem occurred with the mounted samples, although the non-conductive resin was covered with conducting silver paint. In such cases the sum of the mass fractions is rather different from the ideal 100 %. When very small inclusions had to be analysed, some matrix material was also measured. This had to be considered in the interpretation of the results.

For the determination of the matrix composition an EPMA line scan with 41 single points was measured. The line over the sample cross-section was selected to contain as few inclusions as possible. Since it was not possible in every case, analyses with more than 1 % oxygen were considered as inclusions and were not used for the calculation of the matrix composition. The average of the remaining single analyses was taken as matrix composition.

### 4.3 Metallography

The most obvious information from a metallographic section are the types and the distribution of phases and inclusions. The appearance of dendrites provides information about the casting process. The smaller the dendrites and the dendrite arm spacings are, the faster was the cooling of the material. Elongated grains and slip traces indicate cold working. Recrystallised grains with annealing twins are indicators both for annealing after cold working and for hot working (Scott, 1991). The total amount of deformation can be determined by the elongation of ductile inclusions or phases.

Prior to metallographic preparation the samples were mounted in synthetic resin. In order to enable simple unmounting for the restoration of the prehistoric objects, a brittle UV-setting resin was chosen. The mounted samples were ground on wet SiC-paper up to grid 4000, and polished with 3  $\mu\text{m}$  followed by 1  $\mu\text{m}$  diamond suspension on a Struers MOL-cloth. In order to obtain an optimal surface the samples were finally polished with Struers OP-U-Suspension (SiO<sub>2</sub> with grid

40  $\mu\text{m}$  and pH 9.8) on a DP-Chem-cloth. This combination of mechanical removal and chemical attack provided a scratch- and deformation-free sample surface and a slight etching.

In order to highlight the structure and make more details visible, the metallographic sections were etched (Table 4.2, p. 41). The grain surfaces were mainly etched with an ammonia/hydrogen peroxide mixture. In some cases, already a slight grain boundary etching occurred. The dendritic structure was etched with an ammonium persulfate solution. Grain boundaries and annealing twins were made visible with a potassium dichromate solution or ferric chloride solution. If the etching was not sufficient to highlight the structure, a so-called three acid mixture (Table 4.2, p. 41) was used for preetching. This etchant caused a chemical polishing of the sample surface.

The metallographic sections were investigated with a Nikon Eclipse ME600 microscope equipped with a camera. Mainly bright-field illumination was used, dark-field illumination and polarised light were used in order to determine inclusion types.

## **4.4 Material testing**

### **4.4.1 Macroscopic X-ray analysis (radiography)**

Macroscopic X-ray analysis was used in order to control the quality of the cast rods. The material of rods with larger defects like shrinkage and pores was not used for material testing specimen. Such charges were remelted and cast again. If only small parts of the material were not sound, the remaining parts were used to produce the specimen for material testing.

### **4.4.2 Vickers hardness test**

The hardness is one of the most obvious material properties. Not only the working properties are influenced by the hardness, but also the use of the material. If a thin sheet of metal should be produced, i.e. for ornaments, a soft material which does not work harden very quickly will be used. When a good wear resistance is required, a hard material is chosen.

The hardness of a material was defined by Martens as its resistance against the penetration of the surface by a harder object (Blumenauer, 1994). The hardness is not measured directly, but is derived from primary data, like force and indentation

**Table 4.2:** Etchants used for the metallographic sections. The chemicals were p.a. quality, the water was deionised.

etchant	composition	etching time
ammonia/hydrogen peroxide	50 ml NH <sub>3</sub> 5 ml H <sub>2</sub> O <sub>2</sub>	1 – 5 s
ammonium persulfate solution	5 g (NH <sub>4</sub> ) <sub>2</sub> S <sub>2</sub> O <sub>8</sub> 50 ml H <sub>2</sub> O 2 ml HCl	3 – 8 s
potassium dichromate solution	5 g K <sub>2</sub> Cr <sub>2</sub> O <sub>7</sub> 50 ml H <sub>2</sub> O 1 ml H <sub>2</sub> SO <sub>4</sub>	10 s
ferric chloride solution	1.5 g FeCl <sub>3</sub> 50 ml H <sub>2</sub> O 1 ml HCl	10 s
three acid mixture	63 ml CH <sub>3</sub> COOH 27 ml H <sub>3</sub> PO <sub>4</sub> 10 ml HNO <sub>3</sub>	2 s

depth. Hardness values can only be compared if the same method with identical parameters is used. Such parameters are the definition of hardness number, geometry and material of the indenter, the type, value and application time of the force, and sample character (GMA, 1994).

Vickers hardness (DIN 50 133) is determined by indenting a diamond pyramid into the material. After indentation the residual pyramid diagonals  $d_1$  and  $d_2$  are measured. The Vickers hardness number  $HV$  is proportional to the quotient of the force  $F$  and the surface  $A$  of the indentation:

$$HV = 0.102 \frac{F}{A} = 0.1891 \frac{F}{d^2} \quad (4.1)$$

There are three ranges of Vickers hardness, depending on the load used. The macrohardness HV5 to HV100 is tested with a force between 49.03 and 980.7 N. Low load hardness is defined by a test force of up to 1.961 N, i.e. HV0.2. Below

1.961 N microhardness is measured.

The hardness measurements were carried out with the M-400-PC3 hardness tester (LECO instruments). Since some of the samples in this work were very small and the damage should be kept as small as possible for the investigation of the Bronze Age material, low load Vickers hardness HV0.2 was chosen. To guarantee the comparability of the hardness values the reference alloys were tested with the load of 200g, too.

### 4.4.3 Tensile test

If a material should be selected for a specific purpose, both its strength and deformability play important roles. On the one hand, it is difficult to make rivets of a very strong and brittle material which shows nearly no plastic deformation before breaking. On the other hand, a material which deforms plastically at low loads will not be suitable for axes.

According to Lechtman (1996) tensile testing is valuable because it provides a reliable measure not only of the strength of a material when subjected to stress in tension, but also of the ductility of the material. In contrast, Northover (1989) pointed out that in Bronze Age metallurgy the ultimate tensile stress of a material is only rarely of interest while other properties, such as wear resistance and toughness, are extremely important.

The tensile test (DIN 50 145) provides the main material characteristics for strength and deformability, measuring the resistance of a material to a static or slowly applied uniaxial force (Askeland, 1994; Gräfen, 1991). A specimen is placed in the testing machine and a unidirectional load is applied by means of the movable crosshead. Usually, the sample is stretched until fracturing and the related tension force  $F$  is measured. From this force and the initial cross-section of the specimen  $S_0$  the stress  $\sigma$  is calculated:

$$\sigma = \frac{F}{S_0} \quad (4.2)$$

The strain  $\varepsilon$  is calculated with the initial specimen length  $L_0$  and the measured length  $L$ :

$$\varepsilon = \frac{L - L_0}{L_0} \cdot 100 \quad (4.3)$$

The 0.2% offset yield strength  $R_{p0.2}$  is defined as the material's permanent elongation of 0.2 %, i.e. the transition from elastic to plastic deformation. It is de-

terminated from the stress-strain-diagram. The tensile strength  $R_m$  is the maximum stress which the material sustains. With further stretching, the material undergoes a localised reduction of its cross-section until breaking.

Besides the strength parameters the deformation parameters were also determined. The percentage elongation after fracture  $A$  is defined as the elongation of the sample after breaking in relation to the length of the sample before testing:

$$A = \frac{L_u - L_0}{L_0} \cdot 100 = \frac{\Delta L_r}{L_0} \cdot 100 \quad (4.4)$$

The percentage reduction of area after fracture  $Z$  is the largest permanent reduction of the area after breaking in relation to the initial area:

$$Z = \frac{S_u - S_0}{S_0} \cdot 100 = \frac{\Delta S}{S_0} \cdot 100 \quad (4.5)$$

The tensile tests were carried out on a Zwick 1476 universal testing machine at room temperatures with a testing rate of  $0.001 \text{ s}^{-1}$  using round specimens with thread (shape B, according to DIN 50 125).

#### 4.4.4 Notched bar impact test

If a material is subjected to a sudden intense blow, it often shows a much more brittle behaviour than observed during slow deformation. If, for instance, a hammer should be produced this change in properties needs to be considered.

The notched bar impact test (DIN 50 115) is a mechanical-technological test to determine the toughness of a material and its tendency to brittle fracture. It does not provide data for strength calculation.

In the test, a specimen is placed on two supports and two abutments. It is broken with one stroke by the pendulum of the impact machine. The impact energy, i.e. the energy absorbed by the specimen during its failure is measured. The notch impact work  $A_v$  is calculated from the weight of the hammer  $G$ , its starting elevation  $H$  and the final elevation  $h$

$$A_v = G(H - h) \quad (4.6)$$

The impact work in relation to the cross-section  $S$  is called notch impact strength  $a_k$ :

$$a_k = \frac{A_v}{S} \quad (4.7)$$

Besides the above-mentioned parameters, the deformation of the specimen after testing was analysed. The lateral spreading  $SB$  is the difference between the maximum width of the broken sample and its initial width. Furthermore, the appearance of the fracture (ductile, brittle) was recorded.

The notched bar impact tests were carried out at room temperatures on a PSd 300 J impact machine (WPM) using V-notch-specimen (DIN 50 115).

#### 4.4.5 Torsion test

Information about the work-hardening behaviour of a material can be obtained with hardness measurements. However, the hardness increase depends on several parameters like the type and velocity of its working. Compared to the upsetting or tensile test, the torsion test offers several advantages. It allows the simultaneous determination of both yield stress and plasticity (Spittel et al., 1994). Its disadvantages are the uneven distribution of stresses, deformation-induced strain, and yield rate. The shear deformation has to be converted into a reference deformation for which there is more than one plasticity theory (Spittel et al., 1994).

A specimen is twisted with constant speed in a torsion plastometer and the torsion angle and torsion moment are measured. The reference stress  $\sigma_v$  after Mises is calculated from the torsion moment  $M_D$  with the shear stress  $\tau$  and hardening exponent  $P$ :

$$\sigma_v = \sqrt{3}\tau \quad (4.8)$$

$$\tau = \frac{(3+P)M_D}{2 \cdot \pi \cdot R^3} \quad (4.9)$$

The reference amount of deformation according to Nadei and Mises  $\phi_v$  is calculated with the number of twists  $n$ , the diameter of the specimen  $D$ , and the length of the specimen  $L$ :

$$\gamma^* = \frac{3D \cdot \pi \cdot n}{4L} \quad (4.10)$$

$$\gamma_N = 2 \ln \left( \frac{\gamma^*}{2} + \sqrt{\frac{\gamma^{*2}}{4} + 1} \right) = 2 \operatorname{arsinh} \frac{\gamma^*}{2} \quad (4.11)$$

$$\phi_v = \frac{\gamma_N}{\sqrt{3}} \quad (4.12)$$



---

From the  $\phi_v$ - $\sigma_v$ -diagram (flow curve) the maximum degree of deformation  $\phi_{v,max}$  was determined. The hardening exponent  $P$  is the inclination of the straight line which results, if the reference stress and the reference amount of deformation are plotted on a double logarithmic diagram.

The torsion test was carried out at room temperatures with the torsion plastometer I (Institut für Metallformung). The nominal moment was 23.5 Nm, the scanning frequency for the torsion moment 100 Hz.



## Chapter 5

# X-ray fluorescence analyses of Early Bronze Age ingot torques

Compositional investigations of artefacts have a long tradition. It was expected that metal analyses might assist the search for an artefact's origin and the provenance of the raw material (Krause and Pernicka, 1996). These hopes were not always fulfilled. The first substantial analyses with the aim of provenancing artefacts and find the related ores were made by Otto and Witter (1952); Neuninger and Pittioni (1962); Neuninger et al. (1960, 1969). To date, the most comprehensive investigations are those of Junghans et al. (1960, 1968a), which set the focus on the beginnings and the spread of metallurgy and materials. Based on this huge analytical database, Butler (1978), Menke (1982), Eckel (1992), and Krause and Pernicka (1996, 1998a) suggested new classifications and interpretations of the data, including the provenance of the copper types.

In the course of this project, new hoard finds from the Upper Bavarian foothills of the Alps (Fig. A.1, p. 190, see also Möslein (1999)) were investigated. The drill shavings of the artefacts were taken by S. Möslein, the energy dispersive X-ray fluorescence analysis was carried out by the author at the Institut für Archäometrie. In this work only the analyses of ingot torques are published.

It was investigated, whether there is a grouping of the analyses and how the data are related to the published ones. Therefor it was tried to allocate the new analyses to existing material groups. Furthermore, it was examined if there were any rules and typological features for the use of a specific metal or alloy and its distribution within individual hoards.

## 5.1 Andechs-Erling, Kr. Starnberg

The two hoards from Andechs with nine and five ingot torques, respectively, were found in spring 1997. The first one was discovered in a few centimetres depth and probably not in its original place (Möslein, 1999). It was reported that in a distance of approximately 60 cm, there were two or three and six or seven rings. About 18 m from this deposit a bundle of five ingot torques was found. Together with these rings a piece of charcoal was found (Möslein, 1999).

### X-ray fluorescence analyses

The XRF-analyses (Fig. 5.1, p. 49 and Table A.1, p. 191) show that the Andechs ingots have a quite narrow arsenic content ranging from 1.7 to 2.9 % and an antimony content between 1.0 and 1.9 %. Only one ring contains less arsenic (0.8 %), but has a higher antimony content of 2.2 %. The silver contents are almost constant at 0.8 to 1.2 %. The alloy contains up to 0.2 % bismuth and up to 0.05 % nickel. Iron has not been found in the samples. The total amount of impurities ranges from 3.7 to 5.3 %.

According to the grouping by Otto and Witter (1952) the material of the Andechs ingot torques can be considered as fahlore metal with silver. In the Stuttgart classification the analyses can be allocated to the group of fahlore metals without nickel. Most of the samples can be regarded as material class C2 according to Junghans et al. (1968a). Three samples were allocated to material class C2D which is characterised by higher nickel contents, one bismuth rich sample belongs to C2C. On average, the copper contains less antimony than arsenic, the average ratio As:Sb:Ag is about 2:1.3:1, which does not exactly agree with the so-called 'classical *Ösenring* metal'. Butler (1978) defined this material by an As:Sb:Ag ratio of 2:2:1. Between the two hoards there are no obvious material differences, so that the ingot torques might be from the same workshop/origin.

## 5.2 Piding, Kr. Berchtesgadener Land

Four ingot torques were found at Piding around 1960. Close to this deposit in 1997 a flanged axe was found. Whether it belongs to the first discovery is not certain. In the same year, at this place 60 ingot torques were found and recovered *en bloc* (Möslein, 1999).

These ingot torques were stored within an oval pit of about 40 to 35 cm

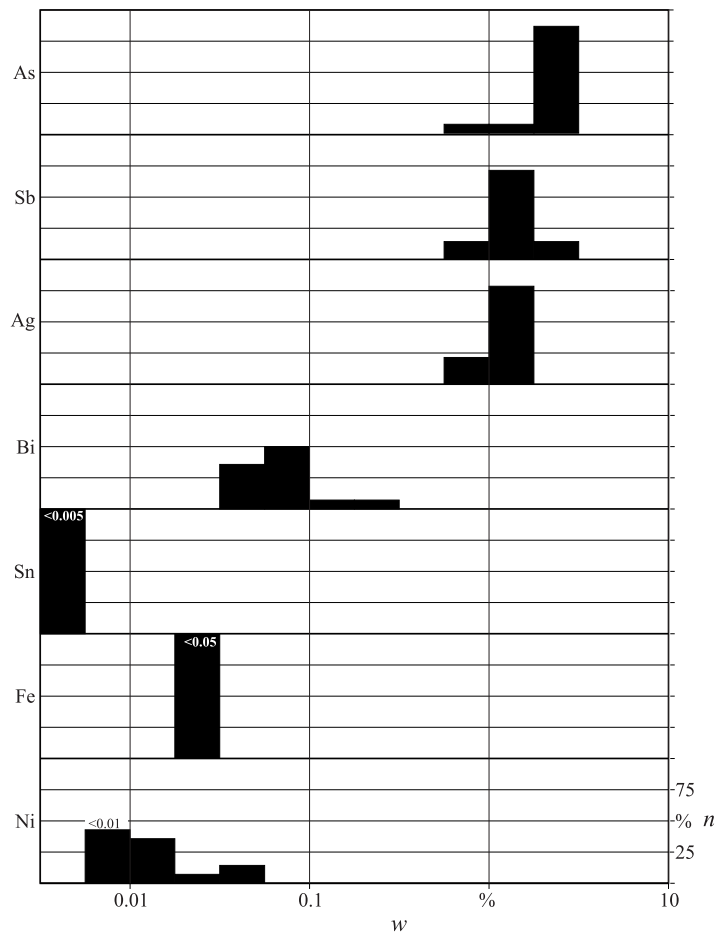


**Figure 5.1:** XRF-analyses of the Andechs ingot torques. Given are the mass fractions of the elements  $w$  on a logarithmic scale and the fraction of analyses in each class  $n$  as a percentage of the total number of 14 ingot torques.

(Möslein, 1998). The hoard contained eight bundles of five ingot torques, one of four, and one of six ingots. Perhaps originally the upper layer of ten ingots also consisted of bundles of five. One small fragment was wrapped in bast and attached to one bundle (Möslein, 1998). The bast binding at the ends of the bundles was partly preserved.

Two types of reworked ingot torques could be distinguished within the bundles: 23 ingot torques have a forging seam, the remaining rings have faceted to rounded cross-sections (priv. comm. S. Möslein).

In all bundles, except no. 10, the two ingot types were mixed (Table A.7, p. 199ff.). It is important to note, that in most cases, two of five ingots within a bundle have a forging seam. In the large bundle comprising ten ingot torques, four rings have forging seams. Whether this implies intentional mixing or coincidence is not known.

### **X-ray fluorescence analyses**

Two compositional groups were identified within the hoard from Piding (Fig. 5.2, p. 51 and Table A.2, p. 192ff.). Thirty-two ingots consist of low-impurity copper. The remaining 28 have the characteristic composition of fahlore metals.

The low-impurity copper (Fig. 5.2, p. 51) contains less than 0.15 % arsenic and 0.08 % antimony. A few ingot torques show minor tin amounts up to 0.35 %. For most ingots of this compositional group, the nickel contents range between 0.02 and 0.09 %.

According to Otto and Witter (1952), the above-mentioned material can be considered as 'pure copper'. Butler (1978) defined such a material as low-impurity copper. The classification after the Stuttgart system shows, that the analyses in this group can be further divided. Fourteen ingots were allocated to pure copper types E00, E00FC, FC, and C1A. Eighteen ingot torques belong to the material groups FA and E01A, i.e. they can be considered as arsenical copper (Junghans et al., 1968a; Pernicka, 1990). In Piding this copper type is characterised by very low arsenic average of 0.06 % and nickel average of 0.05 %. The average of the iron content is about 0.14 %. Krause and Pernicka (1998a) considered this material as East Alpine copper, because the copper ores from Mitterberg are associated with arsenic and nickel minerals (priv. comm. E. Pernicka). However, a definite provenance association is not implied by this designation.

The fahlore metal from Piding (Fig. 5.2, p. 51) is characterised by 1.4 to 3 % arsenic, 0.8 to 2 % antimony and 0.4 to 1.3 % silver. Between 0.07 and 0.18 % bismuth were found. The total amount of alloying elements ranges between 3.5 and 5.4 %.

Like the ingot torques of Andechs, those from Piding are made of silver-containing fahlore metal according to Otto and Witter (1952). In the Stuttgart scheme most of the analyses could be allocated to the group of fahlore metals without nickel. The majority (23 ingots) consists of C2, three ingots were made of bismuth-rich C2C, two of nickel-containing C2D. One sample with a low silver content was identified as C6A, another sample as C5, i.e. fahlore metal with nickel. Similar to the Andechs ingot torques, the rings from Piding contain more

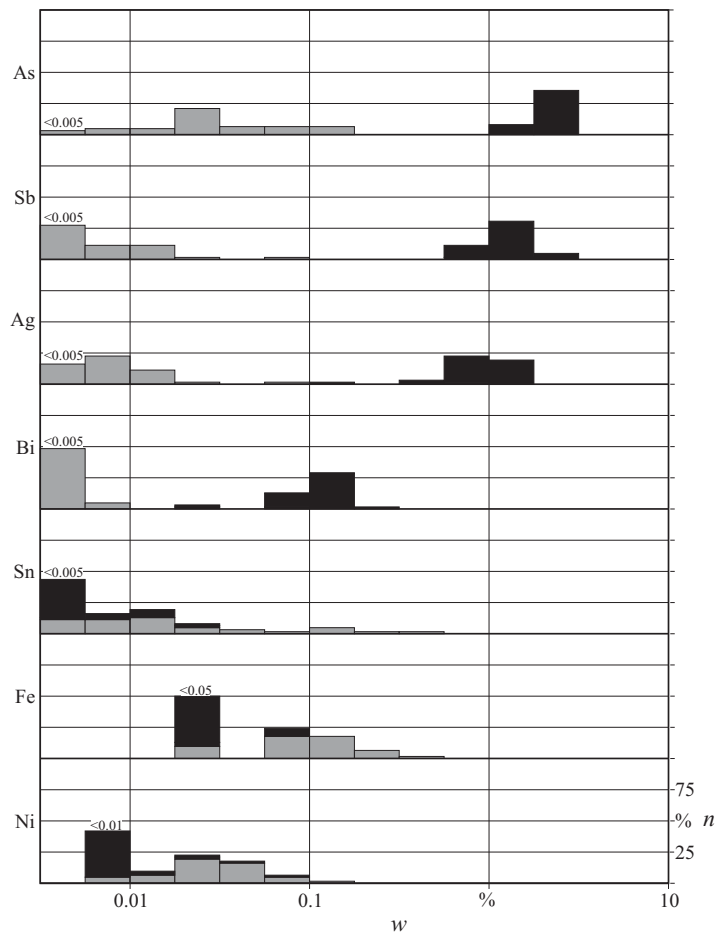


**Figure 5.2:** XRF-analyses of the Piding ingot torques. Given are the mass fractions of the elements  $w$  on a logarithmic scale and the fraction of analyses in each class  $n$  as percentage of the total number of 60 ingot torques. The grey bars represent the low-impurity copper, the black bars the ingot torque metal.

arsenic that antimony. The average ratio As:Sb:Ag of 2.5:1.5:1 does not exactly correspond to the ‘classical *Ösenring* metal’ (Butler, 1978). However, if one considers arsenic and antimony together, the ratio of (As+Sb):Ag would be 4:1, fitting the ingot torque metal.

Even if the analyses were allocated to the same groups, the ingot torque metal used in Piding slightly differs from that in Andechs. On average the silver contents are lower in the Piding ingots while bismuth amounts are higher.

### **Correlation between typology and material**

As mentioned above, 23 ingot torques have a forging seam, with additional four that may have one. Twenty-two of these ingots consist of ingot torque metal, five are made of low-impurity copper. Of the 33 ingot torques without a forging seam only six consist of ingot torque metal, the others are made of low-impurity copper (Table A.7, p. 199ff.). It seems, that the forging seam is characteristic for rings made of ingot torque metal.

If one presumes no coincidence but intention, 11 rings (18 %) were of different material than expected from their appearance. This means, that the correlation between ingot torques with a forging seam and ingot torque metal on the one side and reworked rings and copper on the other side is about 82 %.

## **5.3 Sicharting, Kr. Traunstein**

In the early 1980s, two neckrings were found at Sicharting, in the Taching am See village (Möslein, 1999).

### **X-ray fluorescence analyses**

One neckring contains 2 % arsenic, 1.6 % antimony, and 1.2 % silver. The other one consists of copper with 1.3 % arsenic, 2 % antimony, and 0.9 % silver. Both contain only minor bismuth (0.04 %), the iron and nickel values were below the detection limits (Fig. 5.3, p. 53 and Table A.1, p. 191).

The material from Sicharting is a silver-containing fahlore metal according to Otto and Witter (1952), which can be considered as copper type C2 in the classification scheme by Junghans et al. (1968a). The As:Sb:Ag ratios of 1.7:1.4:1 and 1.4:2.2:1 do not agree well with the composition of the ‘classical *Ösenring* metal’ as described by Butler (1978). The composition of the material is similar to that of the Andechs ingots.

## **5.4 Staudach-Egerndach, Kr. Traunstein**

Four ingot torques of the Staudach-Egerndach hoard were recovered in December 1992. In 1993, the find was completely excavated and 17 additional ingot torques and three neckrings recovered *in situ*. A bundle of five ingot torques was found on the bottom layer, for the other rings such a grouping can only be presumed



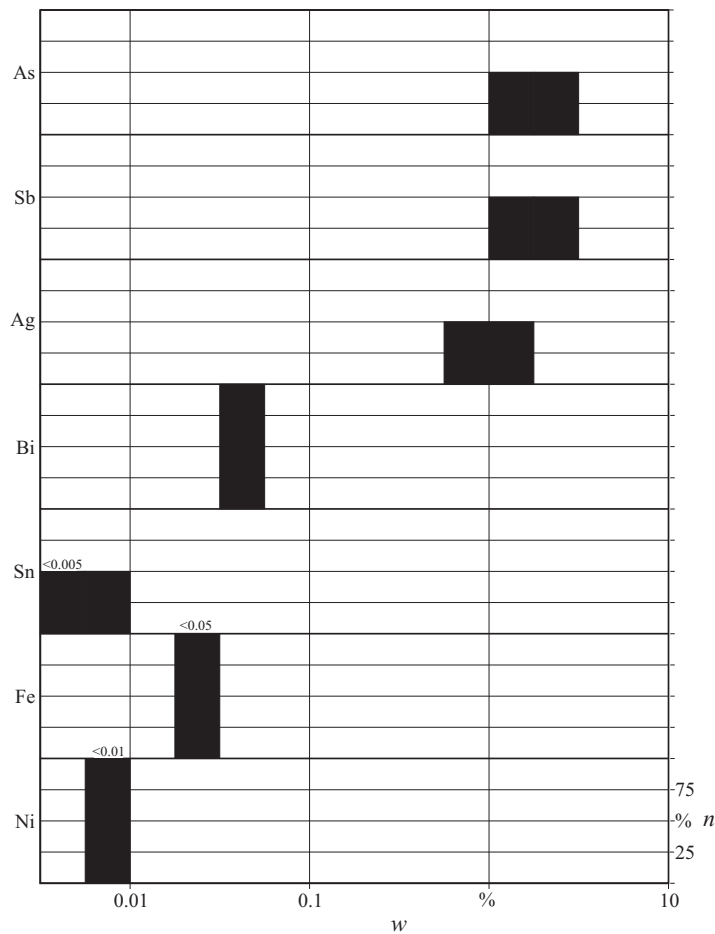


**Figure 5.3:** XRF-analyses of the Sicharting neckrings. Given are the mass fractions of the elements  $w$  on a logarithmic scale and the fraction of analyses in each class  $n$  as a percentage of the total number. Since there are only two ingot torques, this diagram was drawn only for visualising purposes.

(Möslein, 1999). The deposit was closed on three sides with larger stones, the fourth side was disturbed by a tree root.

### X-ray fluorescence analyses

The ingot torques from Staudach have the characteristic composition of fahlore metals, containing between 1.4 and 3 % arsenic, between 0.8 and 2.2% antimony and 0.3 to 1.3 % silver (Fig. 5.4, p. 54 and Table A.3, p. 195). Bismuth was found

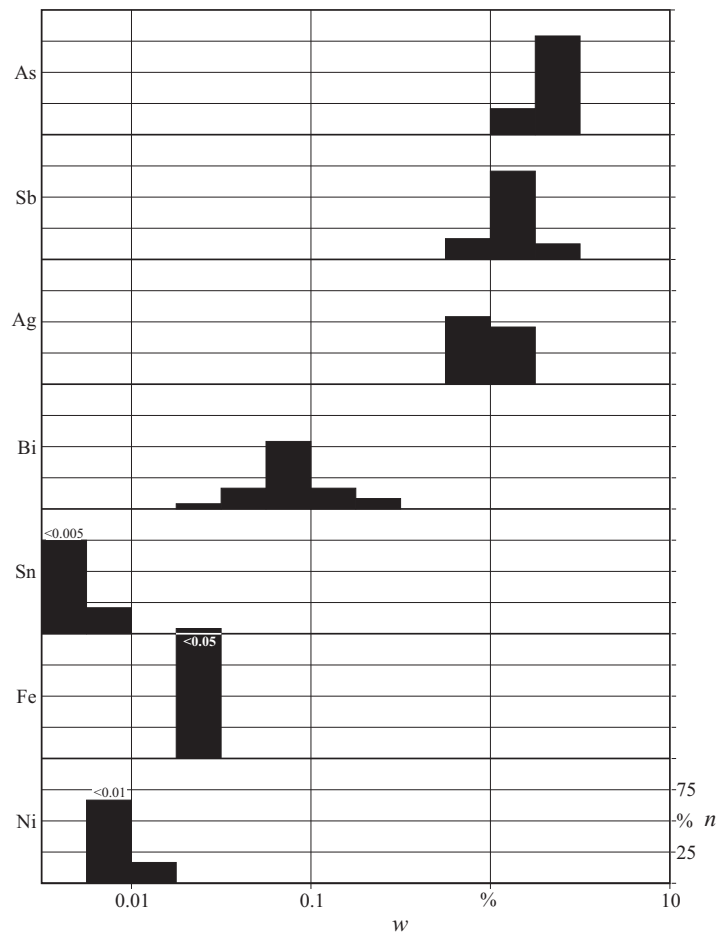


**Figure 5.4:** XRF-analyses of the Staudach ingot torques. Given are the mass fraction of the elements  $w$  on a logarithmic scale and the fraction of analyses in each class  $n$  as a percentage of the total number of 20 ingot torques.

in amounts of up to 0.2 %. Nickel and iron were mostly below the detection limit.

As the ingots from Andechs and Piding, the material of the Staudach ingot torques can be considered as silver containing fahlore metal (Otto and Witter, 1952). It belongs to the Stuttgart material class of fahlore metal without nickel, including C2, C2C (3 ingots), and C2D (4 ingots). The average ratio As:Sb:Ag is about 2:1.4:1, like that of the Andechs finds. Furthermore the impurity patterns of both hoards are very similar.

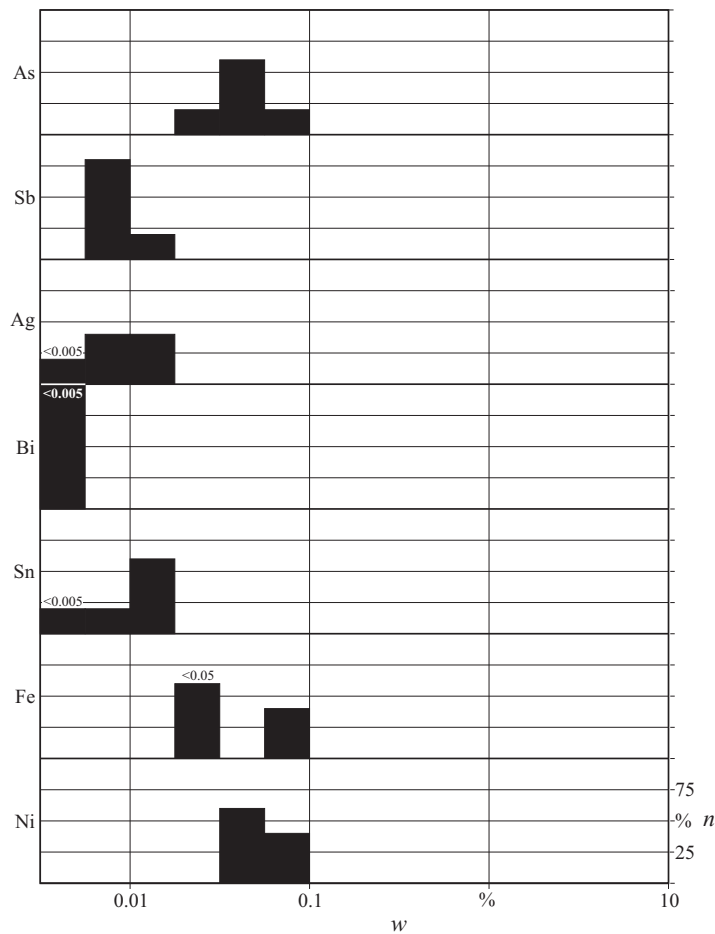


**Figure 5.5:** XRF-analyses of the Unterwössen ingot torques. Given are the mass fractions of the elements  $w$  in a logarithmic scale and the amount of analyses in each class  $n$  as a percentage from the total number of the 5 ingot torques.

## 5.5 Unterwössen, Kr. Traunstein

In 1999, five ingot torques, piled above each other were found at Unterwössen (Möslein, 1999).

### X-ray fluorescence analyses

The arsenic content of the ingot torques from Unterwössen is below 0.08 %, that of antimony below 0.01 % (Fig. 5.5, p. 55 and Table A.1, p. 191). The material

contains between 0.04 and 0.06 % nickel. The maximum content of impurities is 0.3 %.

The composition of these ingot torques is characteristic for the ‘pure copper’ according to Otto and Witter (1952). Butler (1978) considered such a material as a low-impurity copper characteristic for the Bavarian hoards. In the Stuttgart classification the analyses could be allocated to arsenical copper type FA (Jung-hans et al., 1968a), a material which is considered as East Alpine copper (Krause and Pernicka, 1998a). As the copper from Piding it is characterised by an average of 0.05 % arsenic and 0.05 % nickel. In contrast to Piding, the samples from Unterwössen contained less iron.

## 5.6 Valley, Kr. Miesbach

From 1986 until 1990, 17 ingot torques and fragments were found in a ploughed field. In 1990, the remaining rings were recovered *in situ*. The hoard consists of 66 ingot torques and 4 fragments. The rings were stored in a tiny space in bundles of five (Winghart, 1990; Möslein, 1999).

Within the hoard two types of rings could be distinguished: rough cast ingot torques and reworked ingot torques with forging seam (Fig. 5.6, p. 57). In contrast to the Piding hoard, the two types were clearly separated in different bundles (see also Table A.8, p. 202ff.) (priv. comm. S. Möslein). Seven bundles contained only ingot torques with forging seams, three bundles only rough ingots. One bundle consisted of four ingots with forging seam and one rough cast ingot.

### X-ray fluorescence analyses

Similar to the Piding hoard, the analyses of the Valley ingot torques can be divided into two material groups, low-impurity copper and fahlore metal (Fig. 5.7, p. 58 and Table A.4, p. 196f.).

Sixteen ingot torques consist of low-impurity copper, containing up to 0.3 % arsenic, between 0.1 and 0.4 % nickel, and up to 0.2 % iron. The total amount of impurities reaches 0.7 %.

After Otto and Witter (1952) the samples can be considered as ‘pure copper’. Due to the high nickel content it can not be regarded as a low-impurity copper or any other group according to Butler (1978). In the Stuttgart classification this material would be regarded as copper type FA, i.e. arsenical copper from East Alpine provenance (Junghans et al., 1968a; Pernicka, 1990). But the copper type

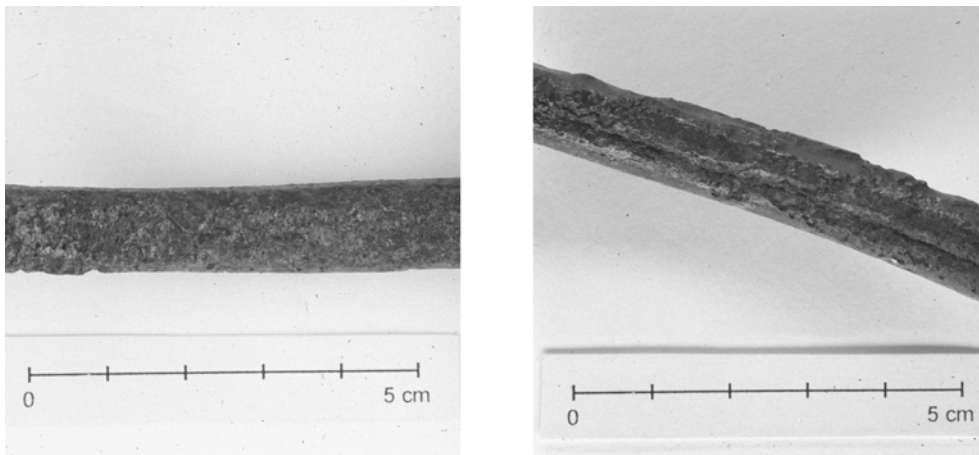


**Figure 5.6:** Typology of the Valley ingot torques. Left: detail of a rough cast ingot torque (Val3). Right: detail of a reworked ingot torque with forging seam (Val5). (Photo: P. Müller)

FA from Valley is very different from those found in Piding and Unterwössen since it contains on average 0.1 % arsenic and 0.2 % nickel.

The remaining samples show the characteristics of fahlore metals. They contain between 1.6 and 2.4 % arsenic, between 1 and 1.8 % antimony, and 0.5 to 1.2 % silver. The bismuth contents are between 0.02 and 0.08 %. The nickel values are below 0.06 %, iron was below the detection limit. The total amount of alloying elements ranges between 3.7 and 4.9 %.

According to Otto and Witter (1952) this metal is a silver-containing fahlore metal. After Junghans et al. (1968a) two types of fahlore metal without nickel were found. Thirteen samples consist of C2, 19 of the nickel-containing C2D. Three samples were allocated to fahlore metals with nickel G and C5. The metal does not correlate well with the ‘classical *Ösenring* metal’ of Butler (1978), since its As:Sb:Ag ratio is about 2.7:1.8:1. It rather corresponds to the nickel-containing ‘modified *Ösenring* metal’ by Liversage and Liversage (1991). Compared to the ingot torques from Andechs, Piding, and Staudach the Valley finds contain more nickel but less bismuth.

### Correlation between typology and material

The very clear differentiation of the Valley ingot torques by typological features is reflected in the analyses (Table A.8, p. 202ff.). The ingot torques with forg-

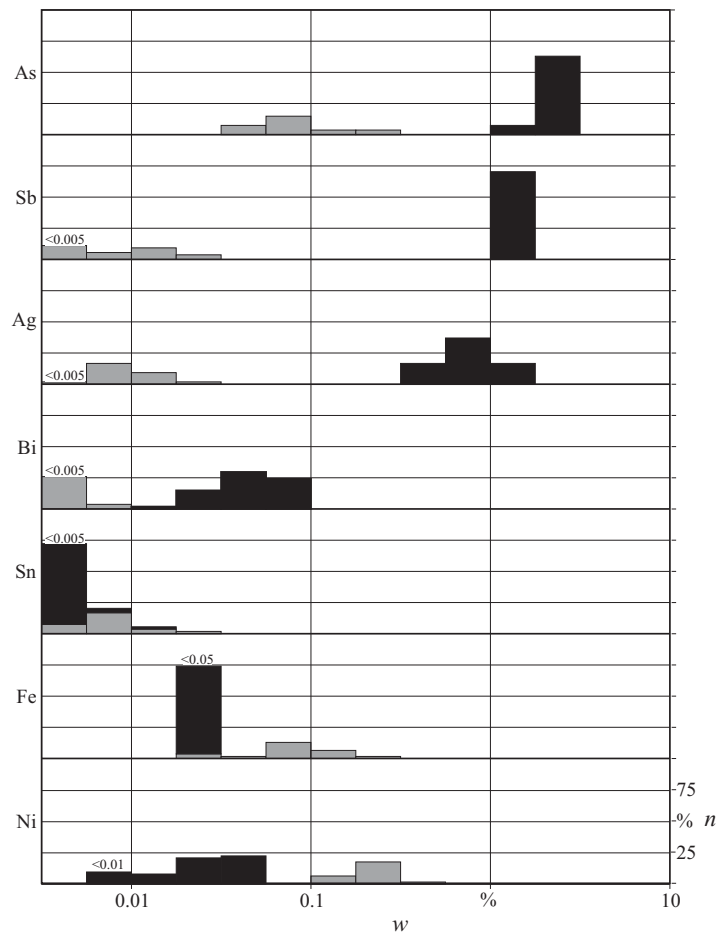


**Figure 5.7:** XRF-analyses of the Valley ingot torques. Given are the mass fractions of the elements  $w$  on a logarithmic scale, the fraction of analyses in each class  $n$  is given as a percentage from the total number of 66 ingot torques. The grey bars represent the low-impurity copper, the black bars the ingot torque metal.

ing seam consist of ingot torque metal, the rough cast ingots were made of low-impurity copper.

In contrast to the Piding hoard, the correlation between typology and analysis in the Valley hoard is 100 %. If the separation was intentional, all ingots were of the material expected from their appearance.

## 5.7 Summary

The analyses of the new hoards confirm the existence of two main material groups used for ingot torques: more or less pure copper and fahlore metal.

The copper can be further divided into pure copper (E00, E00FC, FC, C1A) as it was found in Piding and arsenical copper (E01A, FA) which was found in Piding, Unterwössen and Valley. Especially the Stuttgart copper type FA shows variations. Whereas the ingot torques from Piding and Unterwössen contain only 0.05 % nickel, the ingots from Valley have about 0.2 % nickel (Table A.5, p. 198). These differences probably imply different ore sources. The higher iron content of 0.14 % in the copper from Piding may be an indicator for more reducing conditions during smelting.

As the copper, the composition of the fahlore metal varies between the hoard finds. The Piding ingot torque metal is characterised by higher amounts of bismuth compared to Andechs, Sicharting and Staudach (Table A.6, p. 198). The ingots from Valley contain more nickel but less bismuth than those of the other finds. The differences in the composition may be the result of different primary ores or different smelting technologies.

Two of the investigated hoards, Piding and Valley, contained both types of material. For the first time, a correlation was found between the typology of the ingot torques and their metal composition. In both hoards a part of the ingot torques had a forging seam. These ingots were made of the ingot torque metal (Table A.7, p. 199ff. and Table A.8, p. 202f.). The rings without forging seams were made of low-impurity copper. For the Piding hoard this correlation was 82 %, for Valley 100 %. The ingot torques in both hoards are different in typology and material, so that a common production site is unlikely.

Some of the hoards earlier found, like Bernhaupten and Gammersham, also contain different metal groups. But in contrast to Piding and Valley, the correlation between typological differences and composition within the hoards is not so clear<sup>1</sup>. In the Mauthausen ingot hoard Menke (1982) found typological differences which he interpreted as different manufacturing stages. Whether there are also compositional differences is uncertain, since only six of the six hundred ingot torques were analysed (Menke, 1982).

---

<sup>1</sup>Unfortunately it was rarely possible to relate the analyses to individual artefacts. On the one hand the majority of finds were discovered at the beginning of the 20th century and in most cases the whole find got only one inventory number. On the other hand with the documentation of the Stuttgart analyses (rough sketches, no information about sample location) a sure correlation between artefact and analysis was not possible.

At present it cannot be determined whether the correlation between typology and composition was intentional or by coincidence. The careful separation of different ingot torques in different bundles on the one hand (Valley) and the mixing on the other hand (Piding) suggests that the ancient metal-worker or tradesman noticed the different nature of these ingot torques.

The next chapter summarises the metallographical studies of ingot torques. It will be investigated, whether the different materials have been worked in the same way or if different technologies were applied depending on material or provenance.



## **Chapter 6**

# **Metallographic investigation of Early Bronze Age ingot torques**

In the previous chapter it was shown that mainly two material types were used for ingot torques: low-impurity copper and a characteristic copper alloy, the ingot torque metal. In some hoard finds, ingot torques consisting of different materials appear to have been deliberately separated. These observations raise several questions: Are there any technological differences depending on the material? Was it possible to distinguish between the different material types? If so, during which stage of the production process could the material have been tested and separated?

In order to answer these questions, ingot torques and fragments from different origin, typology and composition were sampled for metallographic investigation (Fig. A.1, p. 190 and Table B.1, p. 206). Usually, two ingot torques or fragments, chosen for their typological characteristics, were investigated.

### **6.1 Aschering, Kr. Starnberg**

The ingot hoard of Aschering was found in summer 1911 near the reservoir of Grubmoos. It was located directly beneath the humus layer. In 1921 the owner of the find, Dr. Brubacher, donated 70 ingot torques and 32 fragments with a total weight of 11.2 kg to the Prähistorische Staatssammlung München. The documentation of the find noted an alignment of the ingot torques over 1.5 m, with the open side downwards (inventory, Prähistorische Staatssammlung München). It has been suggested that the torques had been originally deposited threaded on a string or rod (Menke, 1982; Stein, 1976a).

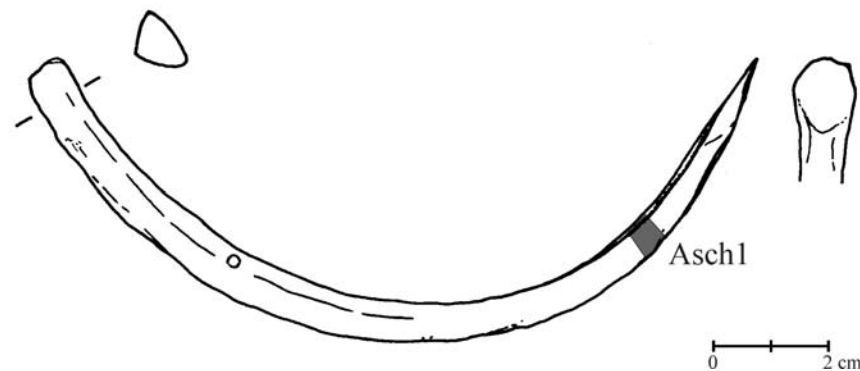


**Figure 6.1:** Ingot torque fragment Asch1 with sample location. The grey area represents the surface of the metallographic section.

Stein (1976b) characterised the ingot torques and fragments as roughly re-worked with poorly hammered and bent endings. Most items had dented, grooved or partly concave cross-sections (Stein, 1976b). According to the Stuttgart analyses, the majority of the Aschering ingot torques consists of ingot torque metal, only three rings of copper (SMAP database, 1999).

### 6.1.1 Fragment Asch1

Fragment Asch1 (Fig. 6.1, p. 62) represents half of an ingot torque with a triangular shape in cross-section. The flattened end is somewhat wider than the body of the ring and not bent. The broken end could not be investigated further, since the fracture was varnished. The fragment is covered with a blackish-green patina. One sample was taken close to the flattened end.

The X-ray fluorescence analysis showed that the sample Asch1 consists of copper with 1.9 % arsenic, 1.25 % antimony, 1.7 % silver and 0.1 % bismuth (Table B.2, p. 207). In the Stuttgart classification (Junghans et al., 1968b) this material would be C2, i.e. the fahlore metal which is characteristic for ingot torques.

### Metallography

The metallographic section (Figs. 6.2, p. 63 and B.3, p. 212) shows a two-phase microstructure with a copper solid solution and a few domains of a pale blue phase at the triple points. In polarised light this second phase appears dark grey and strongly anisotropic.

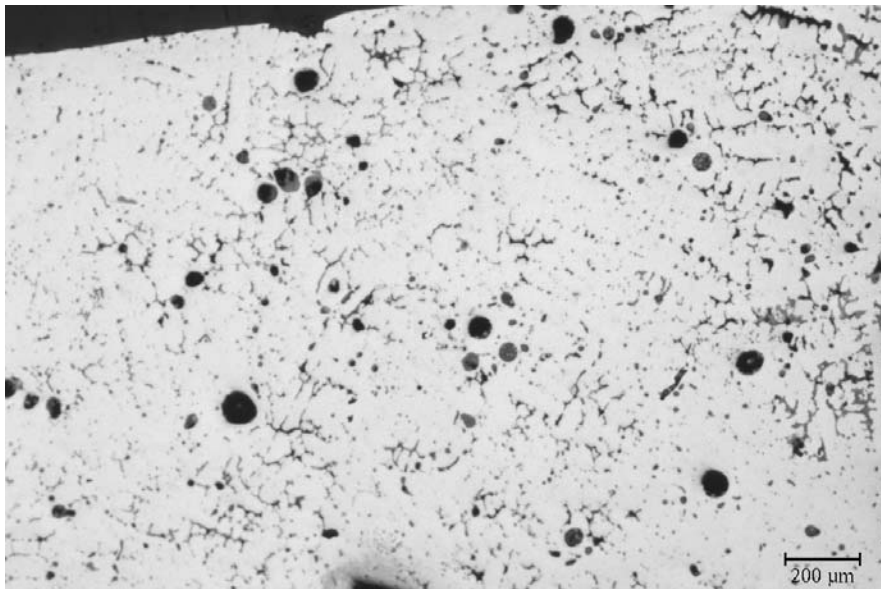


**Figure 6.2:** Asch1, metallographic section. Visible is a two-phase microstructure with inclusions of copper arsenate and copper antimonate.

Along the grain boundaries and triple points a network of bluish grey inclusions was found, marking the casting structure. In polarised light these inclusions appear grey. The second type of inclusions is globular to elongated, grey, with sizes ranging between 10 and 50  $\mu\text{m}$ . These inclusions are red to yellow in polarised light. Globular two-phase inclusions with about 50 to 100  $\mu\text{m}$  diameter are regularly distributed in the sample. They appear grey with an internal bluish grey globular to angular structure (Fig. B.3, p. 212). In polarised light both parts of the two-phase inclusions show the distinctly red colour of copper oxide. Copper oxide was also found within some pores.

The sample etched with ammonia/hydrogen peroxide (Fig. 6.3, p. 64) shows a dendritic, i.e. cast structure. The dendrites are not deformed and have no preferred orientation. The secondary dendrite arm spacings range from 20 to 50  $\mu\text{m}$ . The same metallographic section etched with potassium dichromate solution (Fig. 6.4, p. 64) displays a partly recrystallised structure with annealing twins. The grain sizes are between 20 and 100  $\mu\text{m}$ .

In the internal part of sample Asch1 a low load hardness of 78 HV0.2 was determined which increases to 81 HV0.2 towards the surface of the sample (Table B.3, p. 209).

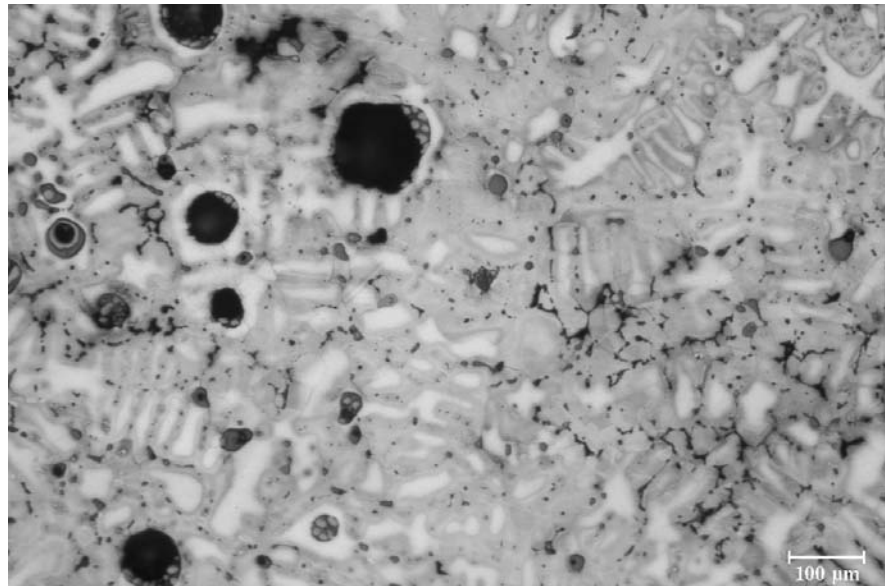


**Figure 6.3:** Asch1, metallographic section etched with  $\text{NH}_3/\text{H}_2\text{O}_2$ . The sample shows a dendritic cast structure.

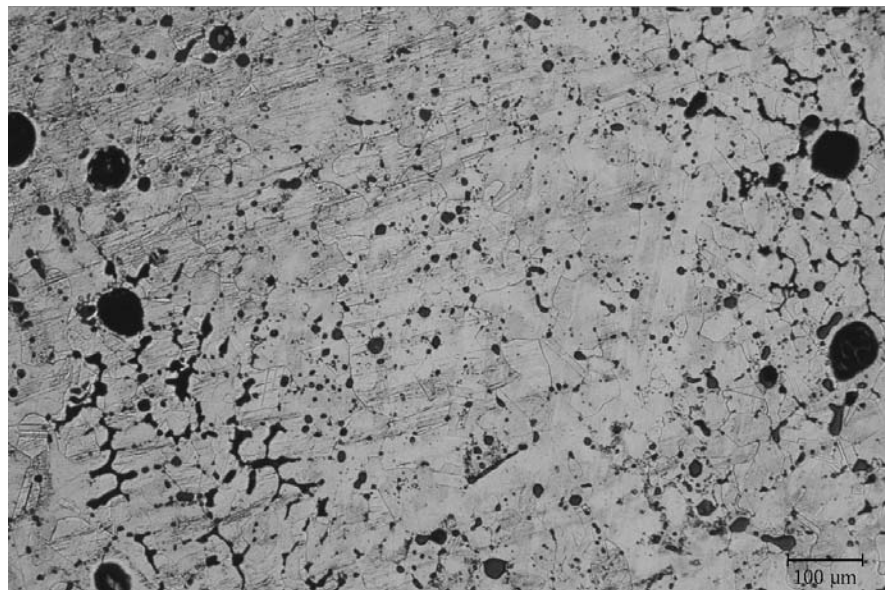


**Figure 6.4:** Asch1, metallographic section etched with  $\text{K}_2\text{Cr}_2\text{O}_7$  solution. Recrystallised grains with annealing twins are visible.

### Microanalysis

By electron microprobe analysis the grey, globular inclusions were identified as mixed oxides of copper, arsenic and antimony (Table B.4, p. 212). Ruhrmann (1925) interpreted similar inclusions in copper-arsenic alloys as copper arsenate  $\text{Cu}_2\text{O}\cdot\text{As}_2\text{O}_5$ . According to Ruhrmann (1925) and Keesmann and Moreno Onorato (1999) the grey inclusions in Asch1 can be considered as a mixture of copper arsenate and copper antimonate. The bluish grey inclusions were found to be mainly copper oxide  $\text{Cu}_2\text{O}$ .

In the backscattered electron image of the microprobe some tiny areas of the sample appeared to be very bright. In optical microscopy these parts showed a light bluish colour. In EPMA they were found to contain high amounts of antimony, silver, and bismuth, besides copper.

The matrix consisted of a copper solid solution which differs from the bulk composition determined with EDXRF (cf. Tables B.4, p. 212 and B.2, p. 207). Only about 24 % of the arsenic bulk content, 14 % of the antimony, 34 % of the silver and 68 % of the bismuth were found within the matrix while the majority of alloying elements occurs in the inclusions.

### 6.1.2 Fragment Asch2

The second fragment from Aschering investigated Asch2 (Fig. 6.5, p. 66) appears more like a part of a rib shaped ingot, since the end is not reworked. The blackish green patinated fragment has a triangular cross-section. Similar to fragment Asch1, the fracture is varnished, so that an investigation was precluded. The sample was taken from the region close to the end.

The material of sample Asch2 could be considered as fahlore metal C2 (ingot torque metal) containing about 2.7 % arsenic, 1.3 % antimony, 0.9 % silver and 0.1 % bismuth.

### Metallography

The metallographic section (Figs. 6.6, p. 67 and B.4, p. 213) shows a two-phase microstructure similar to Asch1. Compared to Asch1 there is a larger amount of the pale blue phase.

In addition to this pale blue phase two types of inclusions were found. The first are globular to elongated grey inclusions ranging in size between 5 and 50  $\mu\text{m}$ . In polarised light they appeared red to yellow. The second type seems to consist of

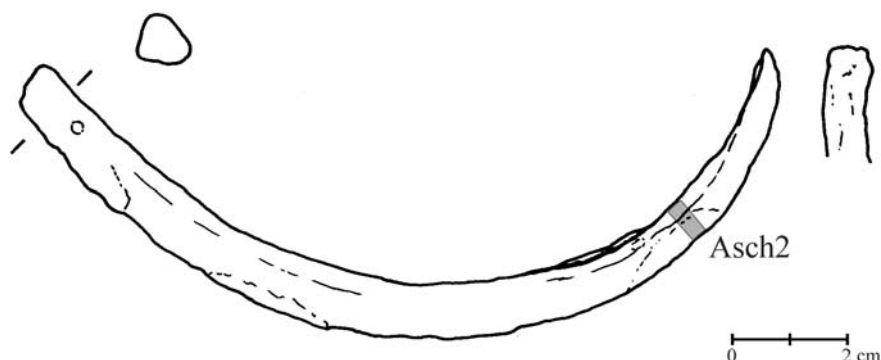


**Figure 6.5:** Ingot torque fragment Asch2 with sample location on the reverse side of the fragment

two phases. In the grey matrix of these inclusions a bluish grey, globular internal structure was found. The inclusions have sizes ranging between 50 and 100  $\mu\text{m}$ . Partly oxidised pores with sizes of up to 100  $\mu\text{m}$  were found in the core of the ingot.

The sample etched with ammonia/hydrogen peroxide shows a cast structure with a strong microsegregation, similar to Asch1. A deformation or preference direction of the dendrites was not recorded. The secondary dendrite arm spacing ranges in size between 20 and 50  $\mu\text{m}$ . Etching with potassium dichromate solution revealed a partially recrystallised structure.

The low load hardness in the centre of sample Asch2 increases from 75 HV0.2 to 109 HV0.2 at the surface (Table B.3, p. 209). The total increase in hardness is larger than in sample Asch1.

### Microanalysis

With EPMA the pale blue phase was identified as a ternary phase of copper, arsenic and antimony (Table B.5, p. 213). The composition may be described by the formula  $\text{Cu}_3(\text{As,Sb})$ , since the amount of arsenic and antimony is not constant.

The globular grey inclusions were found to be oxides of copper, arsenic and antimony, i.e. copper arsenate and antimonate.

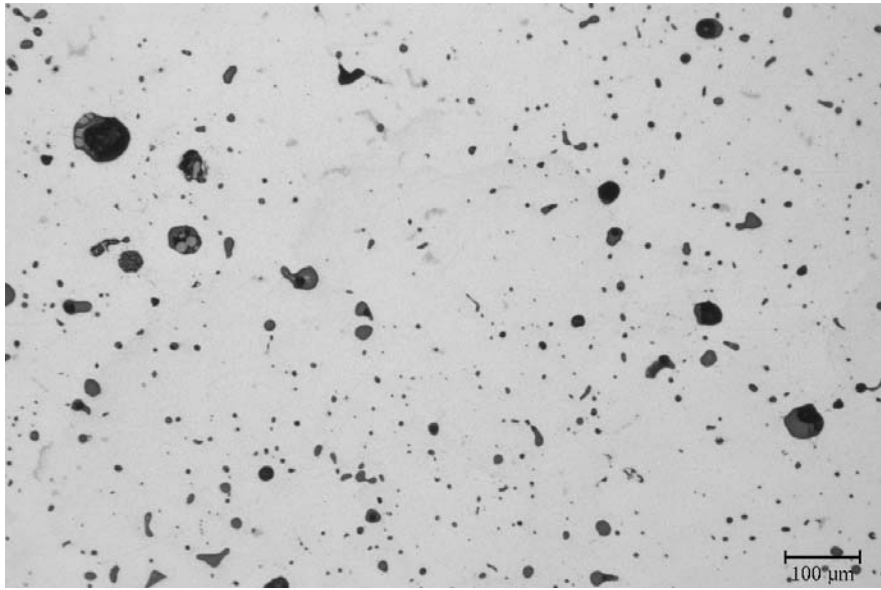


**Figure 6.6:** Asch2, metallographic section. Shown is a two-phase microstructure similar to sample Asch1. The inclusions are copper arsenate and copper antimonate.

## 6.2 Bernhaupten, Kr. Traunstein

The Bernhaupten hoard was discovered in 1883 during repair works on the railway track close to the Bergen station. The 108 rough faceted ingot torques and fragments were found in bundles of 5 in 75 cm depth (inventory, Prähistorische Staatssammlung München). Ninety-one preserved ingot torques are kept in the Prähistorische Staatssammlung München and 7 in the Traunstein museum.

The Bernhaupten ingot torques were described by Stein (1976b) as roughly faceted. Of the 90 ingot torques investigated, 46 ingot torques have a more or less visible forging seam, while 44 ingots lack such a seam (Stein, 1976a,b). The Stuttgart database shows that 49 analysed ingot torques from Bernhaupten were made of copper, 14 of ingot torque metal and 21 belong to the transitional group. Four analyses could not be allocated to any group (SMAP database, 1999). Unfortunately, it was impossible to relate the Stuttgart analyses to the individual ingot torques. Any correlations between typology and composition can therefore only be presumed.

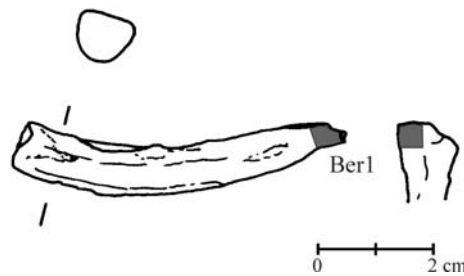


**Figure 6.7:** Ingot torque fragment Ber1 with sample location

### 6.2.1 Fragment Ber1

The fragment Ber1 (Fig. 6.7, p. 68) is a 6 cm long end-piece of a green patinated ingot torque. Its cross-section is D-shaped and slightly faceted. One end is somewhat wider than the body of the fragment, flattened and slightly bent outwards. The other end is a bending mixed fracture with pores in the fracture area (Fig. B.1, p. 210). The sample was cut from the flattened end.

The fragment Ber1 consists of an impure copper with 0.1 % arsenic, 0.03 % antimony and 0.07 % iron (Table B.2, p. 207). In the Stuttgart scheme (Junghans et al., 1968b) this metal can be regarded as highly diluted fahlore metal type G.

#### Metallography

The polished metallographic section (Fig. 6.8, p. 69) shows a single phase microstructure with light blue, globular to elongated inclusions ranging in size between 10 and 20  $\mu\text{m}$ . In polarised light these inclusions appear grey and, hence, they were considered as copper sulfide.

The metallographic section etched with ammonia/hydrogen peroxide (Fig. 6.9, p. 69) shows a recrystallisation structure with annealing twins. The equiaxed grains have diameters ranging between 50 and 100  $\mu\text{m}$ . Traces of a cast structure, e.g. microsegregations, are lacking.

The low load hardness is 55 HV0.2 in the centre of sample Ber1, but increasing towards the surface to 77 HV0.2 (Table B.3, p. 209).

### 6.2.2 Fragment Ber3

Fragment Ber3 (Fig. 6.10, p. 70) represents a third of an ingot torque with a rounded cross-section and an outside forging seam. The flattened end is hook-



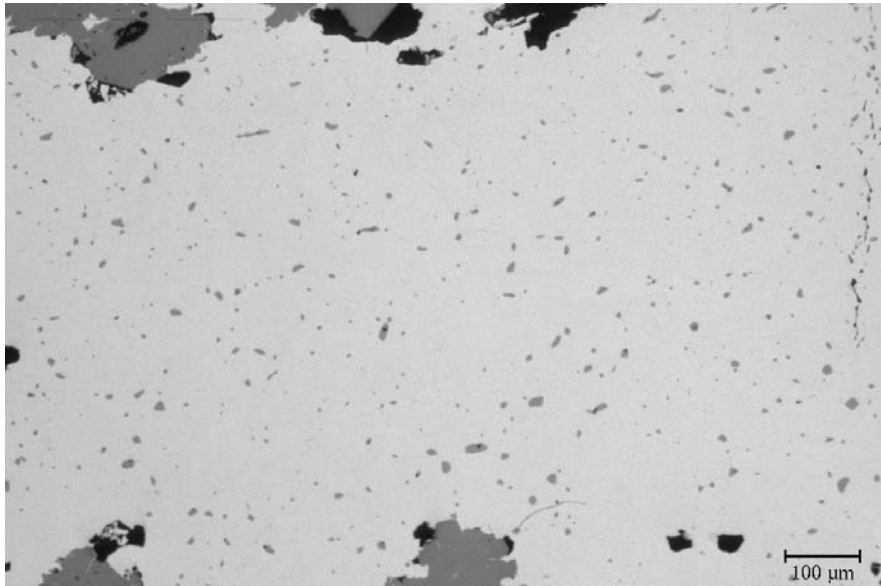


**Figure 6.8:** Ber1, metallographic section. The sample has a single phase microstructure with copper sulfide inclusions

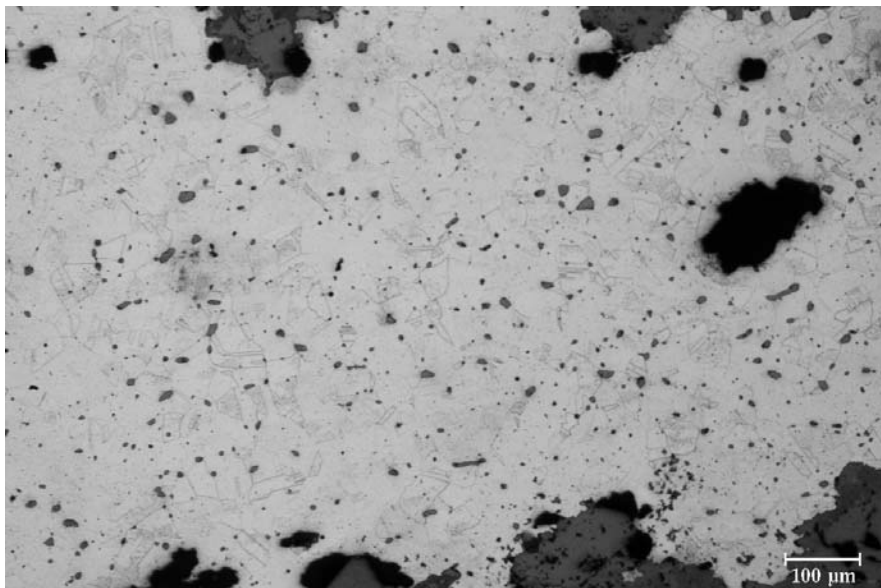


**Figure 6.9:** Ber1, metallographic section etched with  $\text{NH}_3/\text{H}_2\text{O}_2$ . A recrystallisation structure with annealing twins is visible.

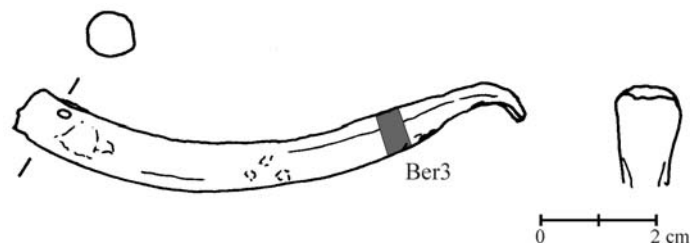


**Figure 6.10:** Ingot torque fragment Ber3 with sampling location

shaped. The other end shows a brittle fracture consisting of two parts: a dark prehistoric or historic crack and a copper-coloured (i.e. modern) residual fracture (Fig. B.1, p. 210). The fragment is covered with a green patina. The sample was taken from the fragment near the flattened end.

With 2.5 % arsenic, 1.9 % antimony, 1 % silver, and 0.24 % bismuth the material of sample Ber3 can be considered as ingot torque metal (Table B.2, p. 207). Due to its high bismuth content it is allocated to material class C2C according to Junghans et al. (1968b).

### **Metallography**

The metallographic section of Ber3 (Fig. 6.11, p. 71) shows a single phase microstructure. Grey, globular to elongated inclusions with sizes ranging between 5 and 100  $\mu\text{m}$  were recorded. In dark-field illumination and polarised light they appear red and yellow, which is the characteristic colour of impure copper oxide. On the sample surface traces of intercrystalline corrosion were observed.

The etched sample (Fig. 6.12, p. 71) shows a strongly cored structure. In polarised light a recrystallisation structure with grain sizes between 50 and 100  $\mu\text{m}$  is apparent. In a few grains slip traces were also found.

The low load hardness of the alloyed material Ber3 is lower than that of comparable material from Aschering. It increases from 66 HV0.2 in its centre to 72 HV0.2 near the surface (Table B.3, p. 209).

## **6.3 Gammersham, Kr. Wasserburg am Inn**

In 1908 a hoard of ingot torques was found while ploughing the 'Schelmenwiese' in Gammersham. The ingots were distributed in 10 cm depth over an area of about one square meter (inventory, Prähistorische Staatssammlung München). In

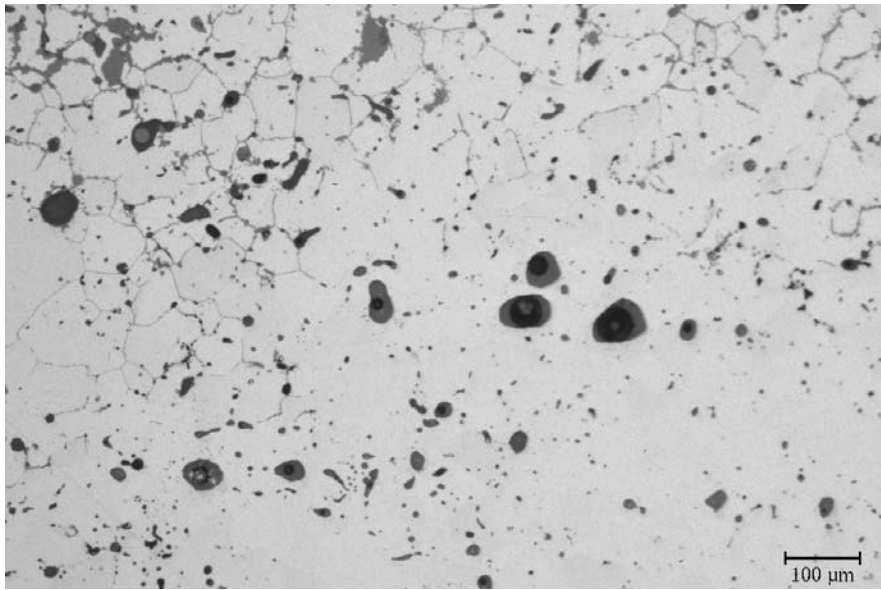


**Figure 6.11:** Ber3, metallographic section. The sample shows a single phase microstructure rich in inclusions.

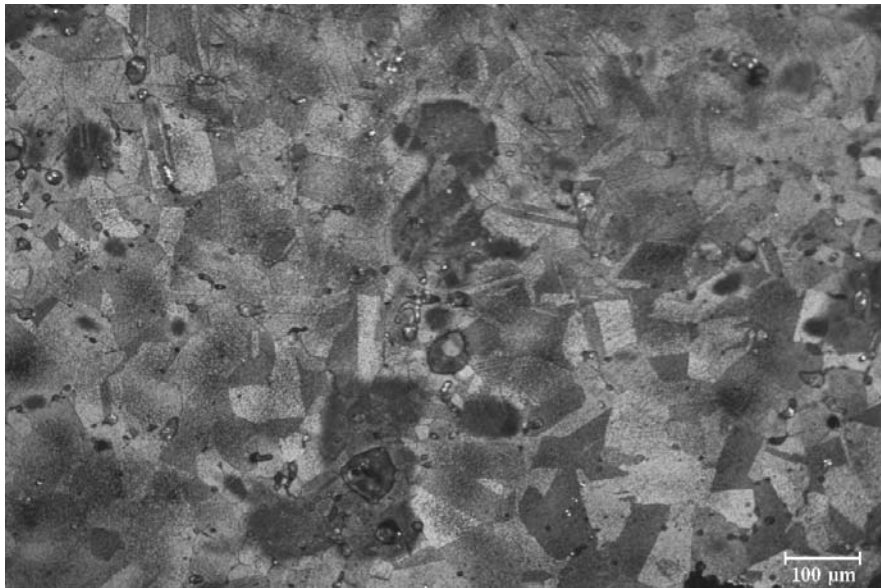


**Figure 6.12:** Ber3, metallographic section etched with  $(\text{NH}_4)_2\text{S}_2\text{O}_8$  solution and shown in polarised light. The sample shows a recrystallised structure overlapping with residual coring.

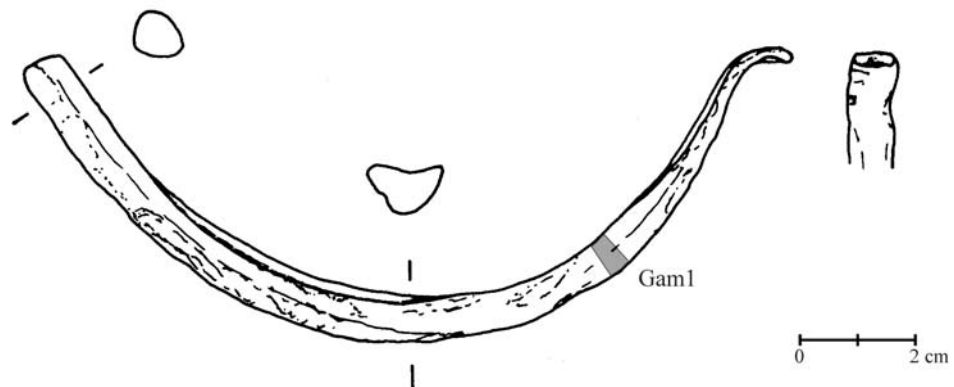


**Figure 6.13:** Ingot torque fragment Gam1 with sample location on the reverse side of the ingot.

1910 the Prähistorische Staatssammlung München bought 62 ingot torques from this hoard. At present the museum owns 117 ingot torques from Gammersham, at least 7 remain with private collectors.

According to Stein (1976b) the Gammersham ingot torques have D-shaped or triangular cross-sections, the ends are only slightly bent. 56 ingot torques have a dented or a partly concave shape in cross-section, 18 have a groove. At least 39 ingots showed none of these features (Stein, 1976b). The ingot torques in the Gammersham hoard consist of two material types. Sixty one ingot torques consist of copper, while 55 were made from ingot torque metal (SMAP database, 1999). Three analyses could not be allocated to any group.

### 6.3.1 Fragment Gam1

Fragment Gam1 (Fig. 6.13, p. 72) represents the half of a blackish-green patinated ingot torque. It has a triangular cross-section with a slightly faceted surface and in some parts a central dent. One end is flattened and bent outwards to hook-shape. The broken end is slightly notched and has a mixed fracture (Fig. B.1, p. 210). The sample was taken close to the hook-shaped end.

The sample Gam 1 consists of copper with 2.9 % arsenic, 1.8 % antimony, 1.2 % silver, 0.2 % bismuth, and 0.05 % nickel (Table B.2, p. 207). Hence, the metal can be considered as fahlore metal type C2D.

### **Metallography**

The metallographic section (Figs. 6.14, p. 74 and B.5, p. 214) shows a two-phase microstructure similar to that of the Aschering samples. The second, pale blue, phase is mainly found at the grain boundaries.

The initial grains of the cast structure are marked by grey, globular inclusions with sizes ranging between 5 and 10  $\mu\text{m}$ . Larger grey, globular inclusions of 50 to 100  $\mu\text{m}$  are regularly distributed in the metallographic section. These inclusions have red to orange colours in polarised light. By contrast, some unevenly shaped inclusions appear dark grey in polarised light. Another type of inclusion consists of two phases, grey with bluish grey, sometimes dendritic, internal structures. These inclusions have diameters of about 100  $\mu\text{m}$  and are red coloured in polarised light. In the centre of the sample, pores with oxidised inner surfaces were found.

The sample etched with ammonia persulfate solution (Fig. 6.15, p. 74) shows a dendritic cast structure with secondary dendrite arm spacings ranging between 50 and 100  $\mu\text{m}$ . There was no preferential direction of the dendrites visible.

Compared to the other investigated samples Gam1 has the highest low load hardness of 96 HV0.2 in the core (Table B.3, p. 209). The surface hardness is about 131 HV0.2. By contrast, the hardness of sample Asch2, which has a similar bulk composition, was about 20 HV0.2 lower.

### **Microanalysis**

EPMA has shown that the pale blue phase consists of copper, arsenic, antimony, silver, and small amounts of bismuth (Table B.6, p. 214). It can be considered as a kind of an impure ternary phase  $\text{Cu}_3(\text{As,Sb})$ .

The grey inclusions are oxides with varying contents of copper, arsenic, antimony, and silver. They are similar to the inclusions found in the Aschering samples, which were described as copper arsenate and copper antimonate.

As in sample Asch1, in sample Gam1 light bluish inclusions were found along some grain boundaries. The composition is similar to those in Asch1: copper with high amounts of antimony, silver, and bismuth (cf. Tables B.4, p. 212 and B.6, p. 214).

Matrix analyses show an arsenic and silver rich copper solid solution. In contrast to the other investigated samples, in sample Gam1 about 76 % of the bulk amount of arsenic is dissolved in the matrix. Antimony and bismuth are enriched in the inclusions and only 32 % of the antimony and 15 % of the total bismuth contents were found in the matrix.

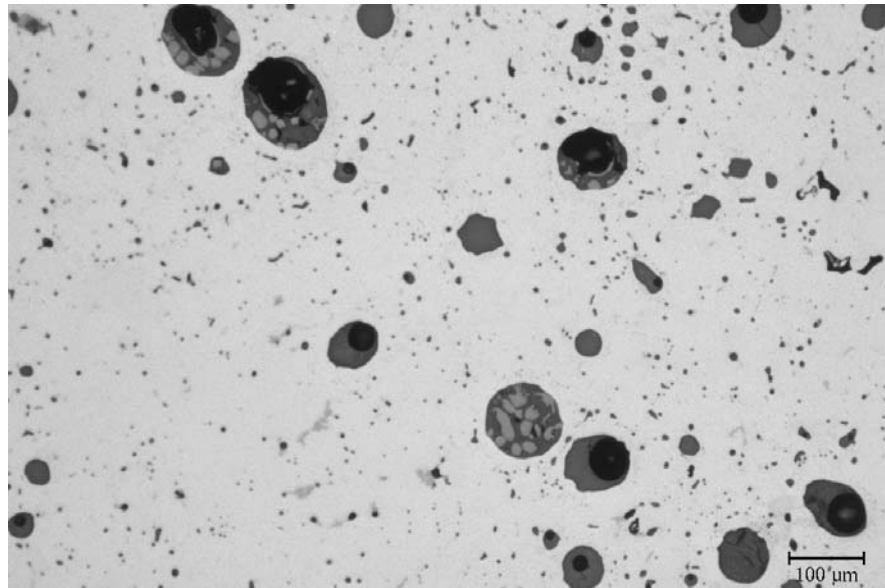


**Figure 6.14:** Gam1, metallographic section. The sample has a two-phase microstructure with inclusions of copper arsenate and copper antimonate.

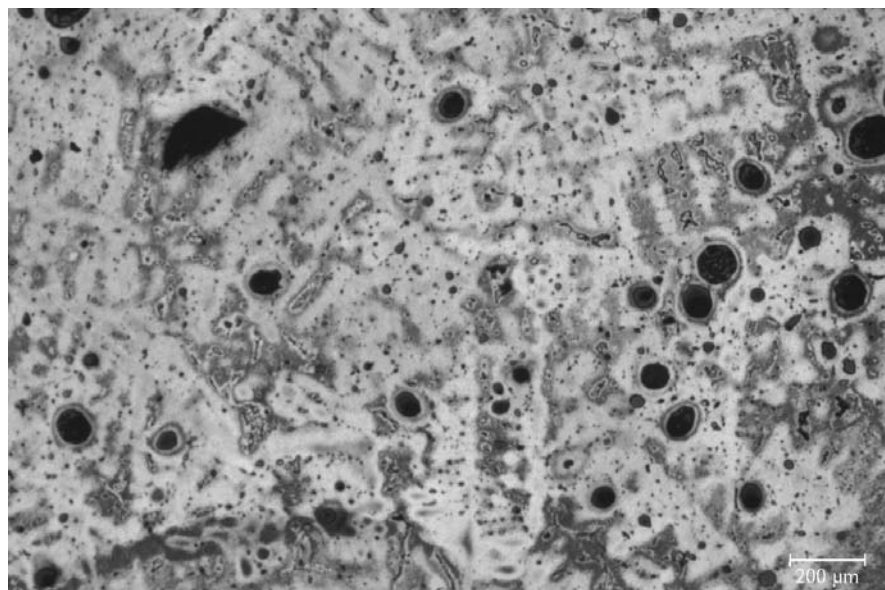


**Figure 6.15:** Gam1, metallographic section etched with  $(\text{NH}_4)_2\text{S}_2\text{O}_8$  solution. A dendritic cast structure is visible.

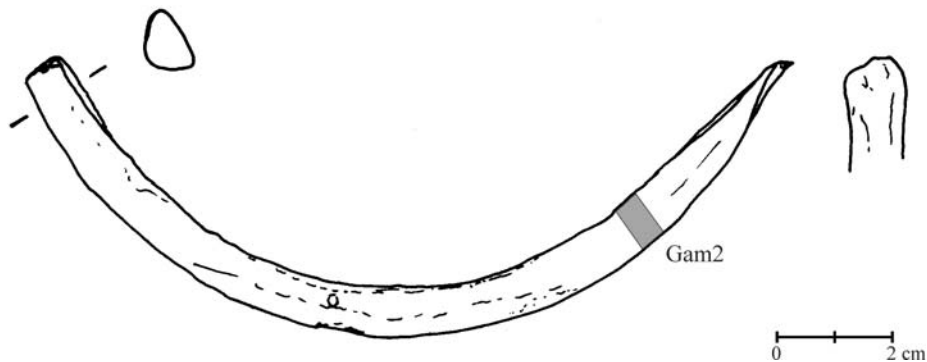


**Figure 6.16:** Ingot torque fragment Gam2 with sample location on the reverse side of the fragment.

### 6.3.2 Fragment Gam2

The fragment Gam2 (Fig. 6.16, p. 75) represents, similar to Gam1, one half of an ingot torque with a triangular cross-section. One end is flattened, but not bent. The other end shows a patinated crack and a small copper-coloured residual fracture (Fig. B.1, p. 210). In contrast to Gam 1, the fragment Gam2 is coated with a brownish-green patina. The investigated sample was taken close to the the flattened end.

The XRF-analysis shows that sample Gam2 was made from fahlore metal type C2C which can be regarded as ingot torque metal. Compared with Gam1 it has a lower arsenic content of 2.5 % and 1.6 % antimony and a higher silver content of 1.6 % (Table B.2, p. 207). The nickel content of 0.02 % is much lower than for sample Gam1.

#### Metallography

The metallographic section (Fig. 6.17, p. 76) shows a two-phase microstructure with a copper solid solution and small amounts of a pale blue phase at the grain boundaries.

The cast structure is marked by grey, globular inclusions with sizes ranging between 5 and 10  $\mu\text{m}$ . Larger, grey, globular inclusions of 50 to 100  $\mu\text{m}$  are regularly distributed. Both inclusion types appear in polarised light in red to yellow colours. Some grey, elongated inclusions appear dark grey in polarised light.

Etched with ammonia/hydrogen peroxide the sample shows an overlap of dendritic and recrystallisation structures. The secondary dendrite arm spacing ranges

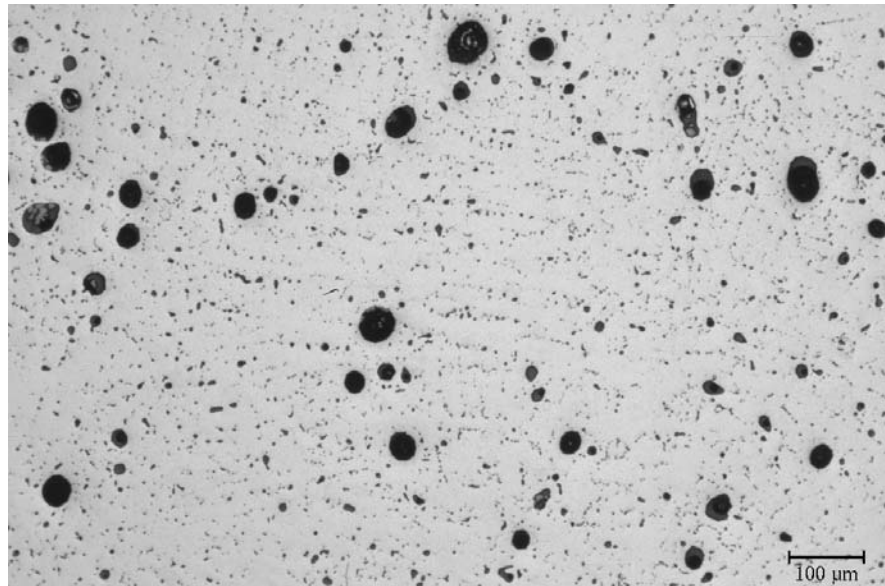


**Figure 6.17:** Gam2, metallographic section. The sample has an inclusion rich, two-phase microstructure.

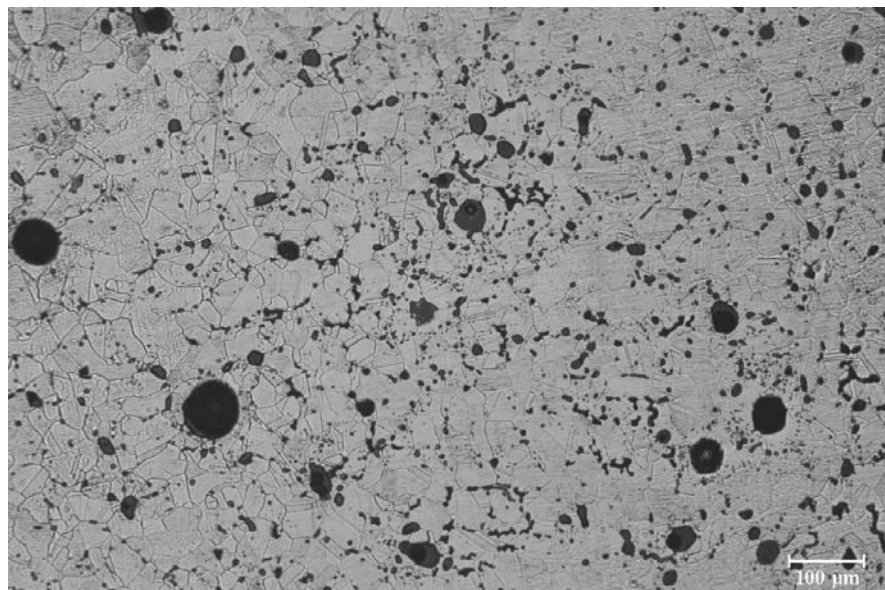


**Figure 6.18:** Gam2, metallographic section etched with  $K_2Cr_2O_7$  solution. A recrystallisation structure is visible.



between 20 and 50  $\mu\text{m}$  in size, the size of the recrystallised grains between 50 and 100  $\mu\text{m}$ . In the metallographic section etched with potassium dichromate solution (Fig. 6.18, p. 76) a recrystallised structure is apparent. In some grains slip traces were found.

Compared to sample Gam1, Gam2 has a much lower core hardness of about 64 HV0.2 which increases towards the surface up to 79 HV0.2 (Table B.3, p. 209).

## 6.4 Hechendorf am Pilsensee, Kr. Starnberg

In 1939 about 20 ingot torques were found in about 1.8 m depth in the cellar of the house Seestrasse 94 in Hechendorf (inventory, Prähistorische Staatssammlung München). The site is at the western shore of the Pilsensee, about 85 m from the present shore line, in a boggy terrain. The rings were found standing in a circle, like a basket (Stein, 1976a). According to Menke (1982), a relocation of the hoard can not be excluded. Eight ingot torques and three fragments are in the Prähistorische Staatssammlung München, some are in the Starnberg museum and with private collectors (Menke, 1982).

According to Stein (1976b), most of the ingots and fragments have slightly faceted cross-sections. She further noted, that six ingots and fragments display the remains of a groove (Stein, 1976b). The Stuttgart analyses imply that two types of material were used for the Hechendorf ingot torques. Six ingots and fragments consist of ingot torque metal, the other ingots of copper which contains nickel (SMAP database, 1999).

### 6.4.1 Fragment Hech1

Fragment Hech1 (Fig. 6.19, p. 78) has an oval, slightly faceted shape in cross-section. One end is flattened and slightly bent outwards. The other end shows a (recent?) fissured and very porous fracture (Fig. B.2, p. 211). The green to brown patina seems to be partly removed. One sample was taken from the central part of the fragment Hech1.

The sample Hech1 consists of impure copper with 0.04 % arsenic and 0.02 % nickel (Table B.2, p. 207). Although the amount of impurities is low, the material would be regarded as arsenical copper type FA according to Junghans et al. (1968b).

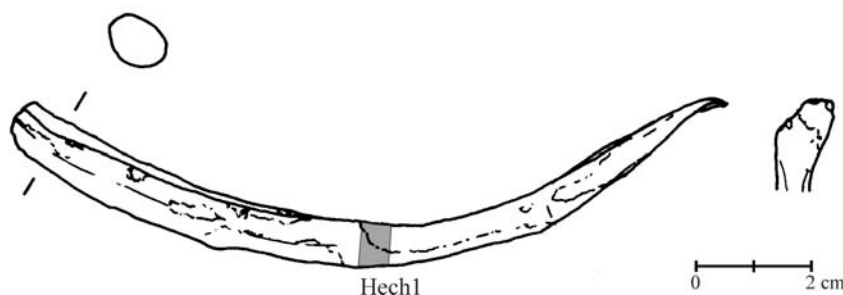


**Figure 6.19:** Ingot torque fragment Hech1 with sample location on the reverse side of the fragment

### **Metallography**

The metallographic section (Figs. 6.20, p. 79 and B.6, p. 215) shows a single phase microstructure similar to sample Ber3. The regularly distributed light blue inclusions have sizes of about  $10\ \mu\text{m}$ . Their appearance varies from globular, oval to unevenly shaped. In polarised light these inclusions appear grey.

The sample etched with ammonia/hydrogen peroxide (Fig. 6.21, p. 79) displays a recrystallisation structure. In the centre of the sample grain sizes of up to  $300\ \mu\text{m}$  were measured.

The sample from fragment Hech1 has quite a low core hardness of 51 HV0.2, which increases towards the surface to 64 HV0.2 (Table B.3, p. 209).

### **Microanalysis**

Using EPMA facilities the light blue inclusions were defined as copper sulfide  $\text{Cu}_2\text{S}$  (Table B.7, p. 215).

## **6.4.2 Fragment Hech2**

The second fragment investigated, Hech2 (Fig. 6.22, p. 80), is a third of an ingot torque. It has a triangular shape in cross-section with a forging seam. The flattened end is not bent. The broken end shows a mixed bending fracture with small amounts of deformation (Fig. B.2, p. 211). The patina of the fragment is green to brown. A sample was taken close to the flattened end.

Like the other sample from Hechendorf, Hech2 consists of impure copper with about 0.04 % arsenic, 0.03 % antimony, 0.08 % nickel, and 0.07 % iron (Table B.2, p.207).

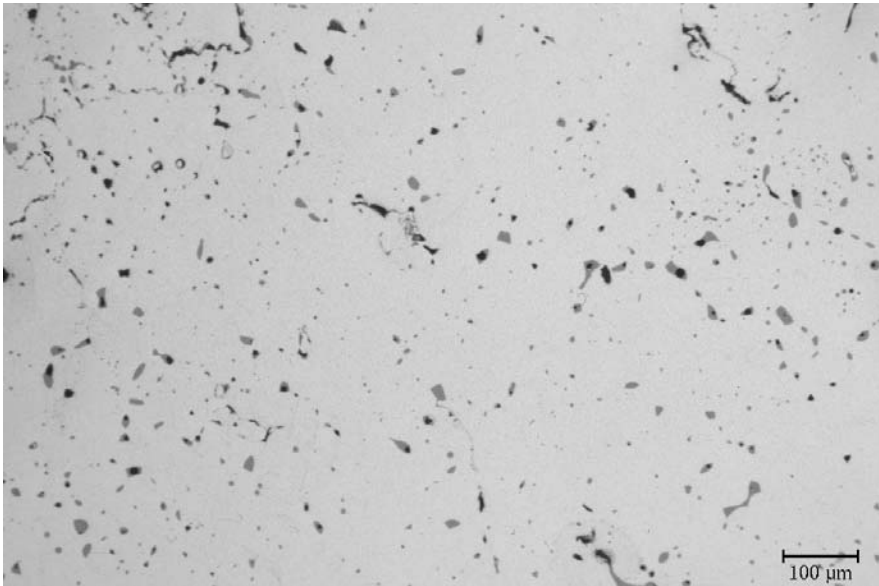


**Figure 6.20:** Hech1, metallographic section. The sample had a single phase microstructure similar to sample Ber1.

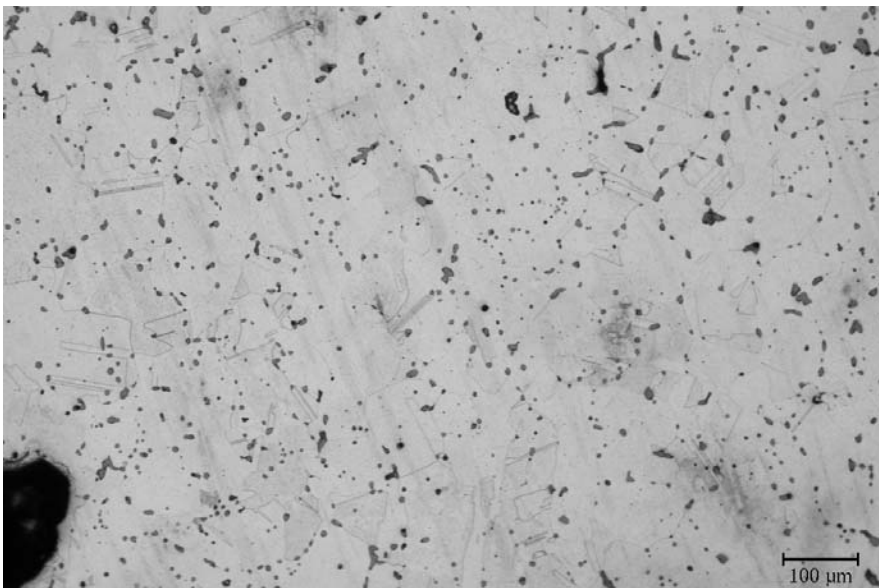


**Figure 6.21:** Hech1, metallographic section etched with  $\text{NH}_3/\text{H}_2\text{O}_2$ . Recrystallised grains are visible.

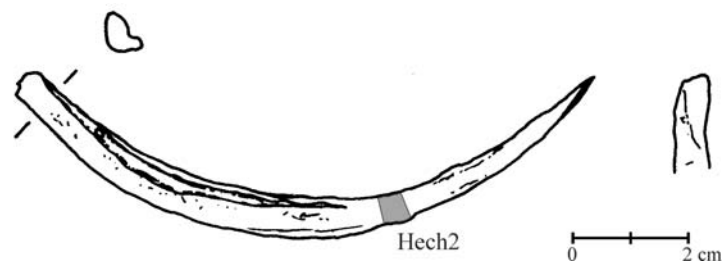


**Figure 6.22:** Ingot torque fragment Hech2 with sample location on the reverse side of the fragment

### Metallography

The metallographic section of Hech2 shows a structure entirely different from Hech1. The small light blue inclusions form an eutectic structure. In polarised light the inclusions appear grey, and are interpreted as copper sulfide.

The sample etched with ammonia/hydrogen peroxide (Fig. 6.23, p. 81) shows recrystallised grains with annealing twins. The grain sizes range between 50 and 100  $\mu\text{m}$ .

The core hardness of sample Hech2 was 84 HV0.2, i.e. even higher than the hardness of most samples made of ingot torque metal. A hardness of 91 HV0.2 was measured close to the surface (Table B.3, p. 209).

## 6.5 Hohenlinden-Mühlhausen, Kr. Ebersberg

The jewellery hoard of Hohenlinden-Mühlhausen was allegedly found in 1854 in a forest while digging a ditch. Since the findings have a bog patina, it was suggested that the original place was rather in the damp lowlands east of Altmühlhausen and north of Hohenlinden (Menke, 1982). The Prähistorische Staatssammlung München owns three arm spirals, one spiral fragment and three neckrings.

Stein (1976b) described the neckrings as rounded and slightly faceted. The Stuttgart analyses show that the artefacts from Hohenlinden-Mühlhausen consist of copper with 0.5 to 3.5 % arsenic, 0.5 to 3 % antimony and, 0.4 to 1.5 % silver (SMAP database, 1999). There are no significant differences in the composition between the spirals and the neckrings.

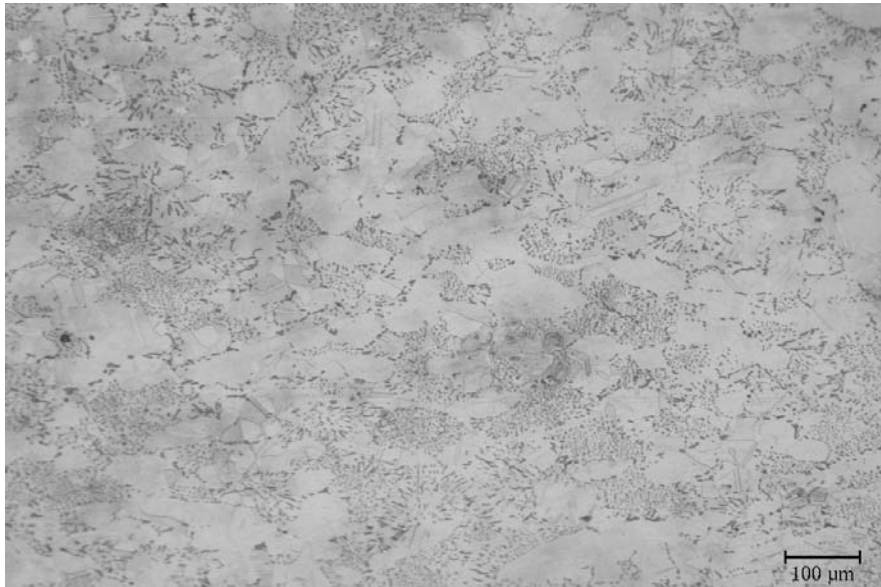


**Figure 6.23:** Hech2, metallographic section etched with  $\text{NH}_3/\text{H}_2\text{O}_2$ . The sample reveals a copper-copper sulfide eutectic and shows a recrystallisation structure.

### 6.5.1 Fragment Hoh1

The investigated fragment Hoh1 (Fig. 6.24, p. 82) represents the half of a neckring with a round cross-section. One end is flattened and curled into a loop. The fracture is partly patinated and copper-coloured. It shows a low deformation bending fracture with little amounts of torsion (Fig. B.2, p. 211). The brown patina of the fragment is partly broken off. The sample was taken close to the curled end.

The XRF-analyses revealed that the neckring fragment Hoh1 consists of nickel-containing ingot torque metal with 2.1 % arsenic, 1.6 % antimony, 1.3 % silver, 0.1 % bismuth, and 0.03 % nickel (Table B.2, p. 207). Even if the sample Hoh1 belongs to the Stuttgart material class C2D, its composition is comparable to that of the Aschering ingot torques.

#### Metallography

The metallographic section (Fig. 6.25, p. 83) shows a single phase inclusion-rich microstructure. Grey, globular inclusions with sizes smaller than  $10 \mu\text{m}$  are distributed along the grain boundaries. Another kind of grey inclusions with sizes ranging between  $50$  and  $100 \mu\text{m}$  occurs unevenly shaped in the core of the ring

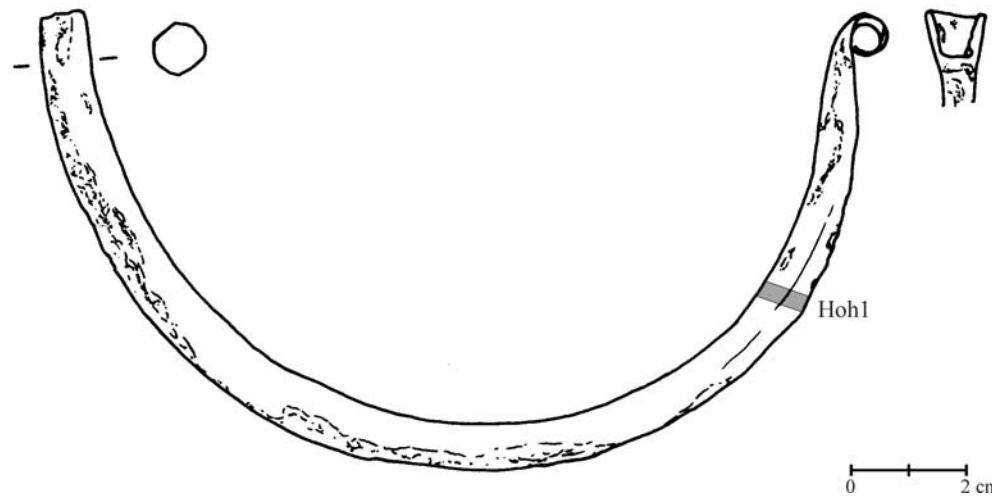


**Figure 6.24:** Neckring fragment Hohl1 with sample location on the reverse side of the fragment.

and elongated close to its surface. In polarised light both types have red to orange colours.

In the metallographic section etched with ammonia/hydrogen peroxide an overlapping of residual coring and recrystallisation structure was noted. The recrystallised grains have sizes ranging between 50 and 200  $\mu\text{m}$ . The sample etched with potassium dichromate solution (Fig. 6.26, p. 83) shows a recrystallisation structure.

The low load hardness values of sample Hohl1 are comparable to the values for the other ingot torque metal artefacts. In the core of the sample a hardness of 73 HV0.2 was determined. Towards the sample surface it increased to 112 HV0.2 (Table B.3, p. 209).

### Microanalysis

EPMA revealed that the inclusions are copper oxides with small amounts of arsenic, antimony, and silver (Table B.8, p. 216). They can be considered as copper oxide mixed with some copper arsenate and antimonate.

Analyses of the matrix show that about 96 % of the total arsenic content is dissolved in the matrix (cf. Tables B.2, p. 207 and B.8, p. 216). A large part of antimony is bound to inclusions, only 46 % occur in the matrix. Bismuth is almost completely bound to inclusions.

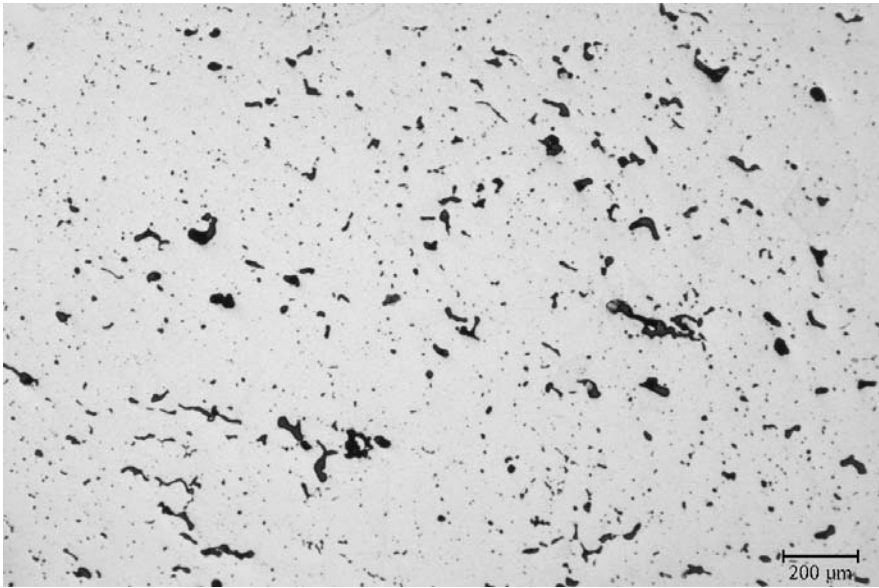


**Figure 6.25:** Hoh1, metallographic section. The sample has a single phase microstructure with inclusions of copper oxide, copper arsenate and antimonate.

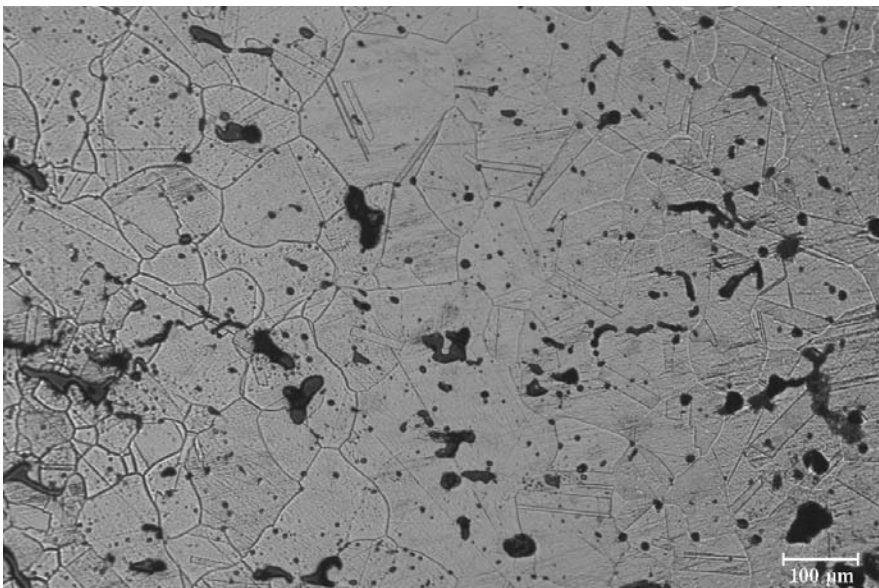


**Figure 6.26:** Hoh1, metallographic section etched with  $K_2Cr_2O_7$  solution. The sample shows a recrystallisation structure.

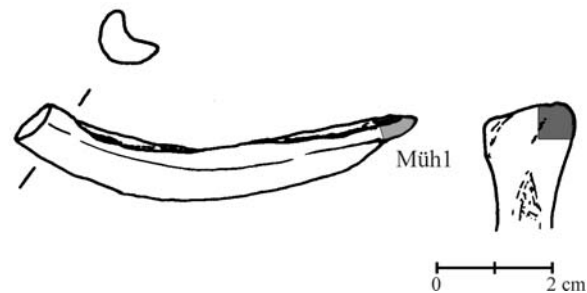


**Figure 6.27:** Ingot torque fragment Müh1 with sample location

## 6.6 Mühldorf am Inn, Kr. Mühldorf

In 1890 the Prähistorische Staatssammlung München bought one ingot torque and one fragment which allegedly came from Mühldorf am Inn. The circumstances of the find and the exact location are unknown (Menke, 1982).

### 6.6.1 Fragment Müh1

The investigated fragment Müh1 (Fig. 6.27, p. 84) represents a 7 cm long part of a rough cast ingot. It has a D-shaped to concave cross-section with a casting groove. One end was wider than the body of the ingot torque and a little flattened. The mixed bending fracture on the other end of the fragment is stepped and brown patinated (Fig. B.2, p. 211). The metal was covered with a pale greenish patina. The sample was taken from the flattened end.

The sample Müh1 consists of the characteristic ingot torque metal with about 2.4 % arsenic, 1.6 % antimony, 1.1 % silver, and 0.2 % bismuth (table B.2, p. 207). The iron value of 0.14 % and the nickel value of 0.04 % are comparably high, so that the material was allocated to material class C2D.

### Metallography

The metallographic section (Fig. 6.28, p. 85) shows a single phase microstructure. Grey, globular inclusions with sizes ranging between 5 and 10  $\mu\text{m}$  were found at the grain boundaries. Furthermore, larger grey, unevenly shaped inclusions about 50  $\mu\text{m}$  were found. In dark-field illumination and polarised light both appear red to white in colour. Pores with oxidised inner surfaces are evenly distributed in the metallographic section.



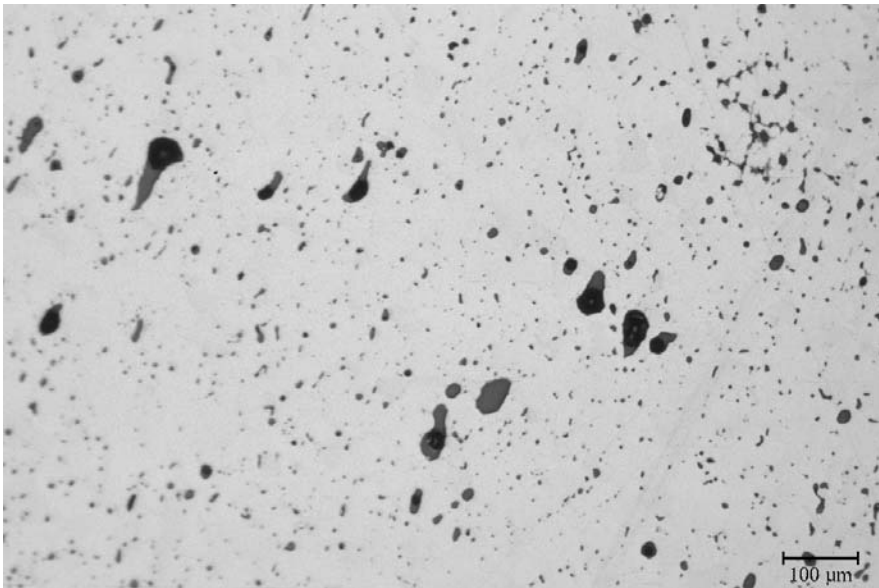


**Figure 6.28:** Mühl1, metallographic section. The sample has a single-phase, inclusion rich microstructure.

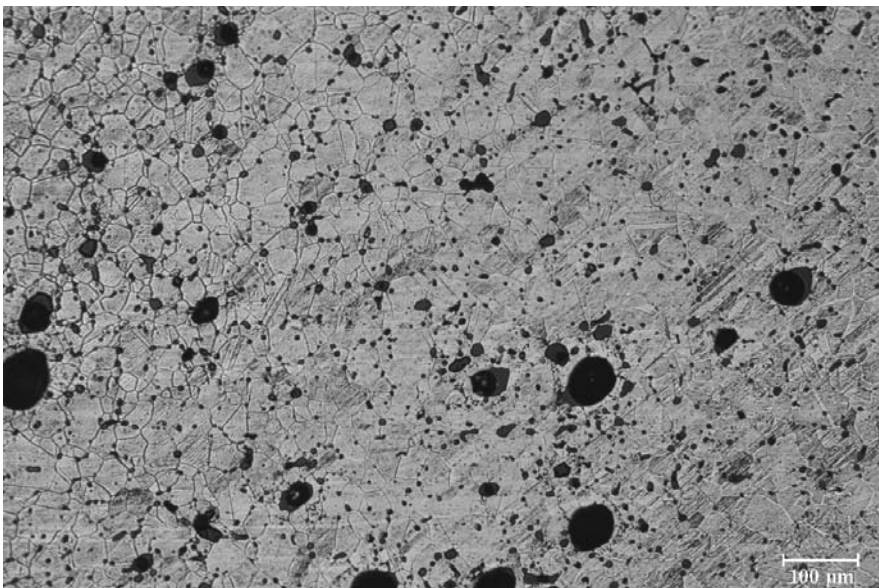


**Figure 6.29:** Mühl1, metallographic section etched with  $K_2Cr_2O_7$  solution. Shown is the recrystallisation structure.

Etching with ammonia/hydrogen peroxide shows an overlapping of cast and recrystallisation structure. The grain size is between 50 and 100  $\mu\text{m}$ . The sample etched with potassium dichromate solution (Fig. 6.29, p. 85) solution shows a recrystallisation structure with annealing twins. In some grains slip traces are visible.

The low load hardness values of sample Müh1 are relatively low with 60 HV0.2 in the centre and 64 HV0.2 close to the surface (Table B.3, p. 209).

## 6.7 Pfedelbach-Untersteinbach, Hohenlohekreis

In 1996 a hoard with 19 ingot torques was found in the southern part of the Hohenloher plateau near Pfedelbach. As Krause (1996) mentioned, the site is hardly accessible, located high on a steep cliff towering over a deep valley of the Waldenburg mountains. A group of two torques and another of three were found *in situ* 60 cm deep beneath a stone (Krause, 1996).

The ingot torques from Pfedelbach are neckring-size and round, with ends hammered and formed to a loop (Junk et al., 2001). Thirteen rings have a forging seam. Previous studies show that the ingot torques from Pfedelbach consist of ingot torque metal, containing about 1.5 to 3.2 % arsenic, 0.9 to 2.1 % antimony, 0.7 to 1.5 % silver, and less than 0.06 % nickel. Six ingots are quite iron-rich, with 0.12 to 0.27 % iron.

### 6.7.1 Ingot torque Pfe10

The ingot torque no. 10 (Fig. 6.30, p. 87) has a rounded, slightly faceted cross-section with a forging seam on the inner side (Fig. 6.31, p. 87). The flattened ends are broken. The surface is covered with a blackish green, smooth patina. A sample was taken by R. Krause from the central part of the ingot torque.

The sample from Pfe10 consists of ingot torque metal C2C with about 2.0 % arsenic, 1.2 % antimony, 1.0 % silver, and 0.2 % bismuth (Table B.2, p. 207).

### Metallography

The metallographic section (Figs. 6.32, p. 88 and B.8, p. 217) shows a two-phase microstructure. At some triple points a pale blue phase was found. In polarised light it appeared grey and strongly anisotropic. This appearance indicates a ternary phase, similar to the one in the samples from Aschering and Gammersham.

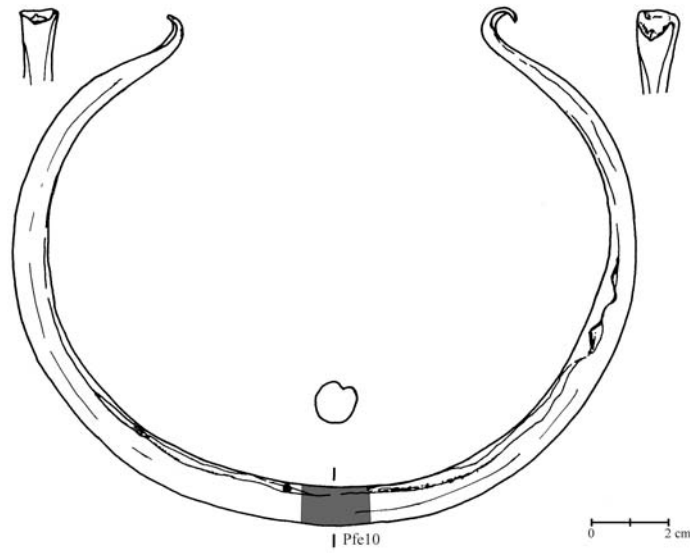


**Figure 6.30:** Ingot torque Pfe10 with sample location.

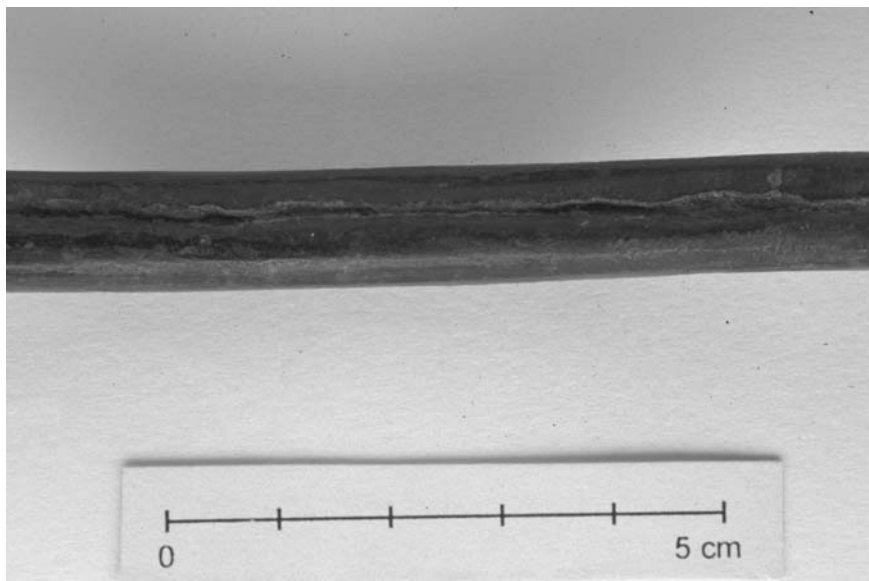


**Figure 6.31:** Ingot torque Pfe10. The detail shows the forging seam. (Photo P. Müller)

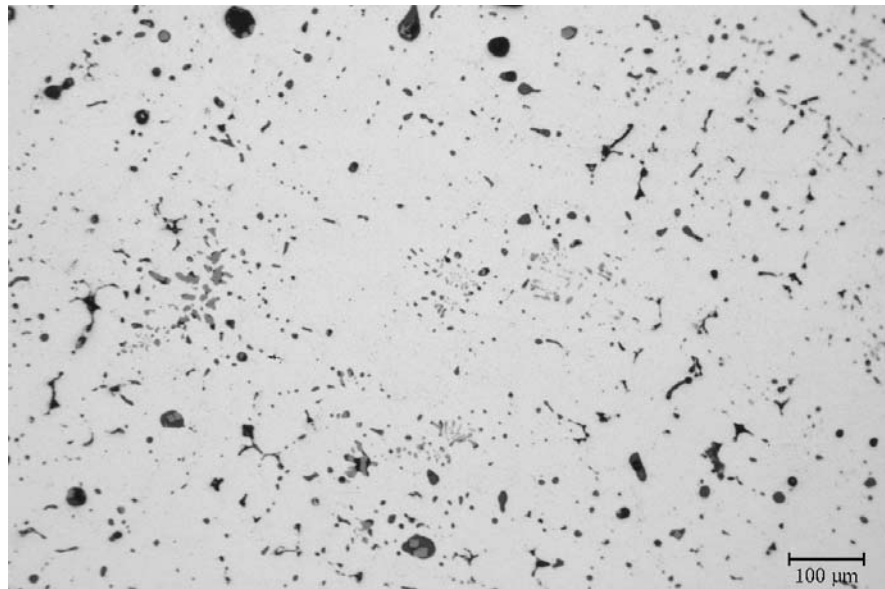


**Figure 6.32:** Pfe10, metallographic section. The sample has a two-phase microstructure with inclusions of copper oxides, copper arsenate and antimonate.

Light blue, globular inclusions with sizes ranging from 3 to 10  $\mu\text{m}$  mark the grain boundaries of the initial cast structure. Larger grey inclusions with sizes of up to 50  $\mu\text{m}$  are distributed uniformly over the sample. These inclusions are globular in the centre of the sample and elongated near its surface. Both, bluish grey and grey inclusions appear in red to yellow colour in dark-field illumination and polarised light. Similar to the samples from Aschering and Gammersham, the metallographic section of Pfe10 shows two-phase inclusions with a grey matrix and bluish grey square-cut inner structures. In contrast to the other samples, some of the two-phase inclusions in Pfe 10 are dendritic. The area near the forging seam is porous. Some of the pores show oxidised internal surfaces.

The sample etched with ammonia/hydrogen peroxide (Fig. 6.33, p. 89) shows a dendritic cast structure overlapping with a recrystallisation structure. The secondary dendrite arm spacing ranges in size between 20 and 50  $\mu\text{m}$ . A preference direction or deformation of the dendrites was not observed. In the sample etched with potassium dichromate solution (Fig. 6.34, p. 89) the recrystallisation structure is more pronounced. The equiaxed grains have sizes between 50 and 100  $\mu\text{m}$ .

The sample Pfe10 has a quite low core hardness, which increases towards the surface from 63 HV0.2 to 73 HV0.2 (Table B.3, p. 209). The low load hard-

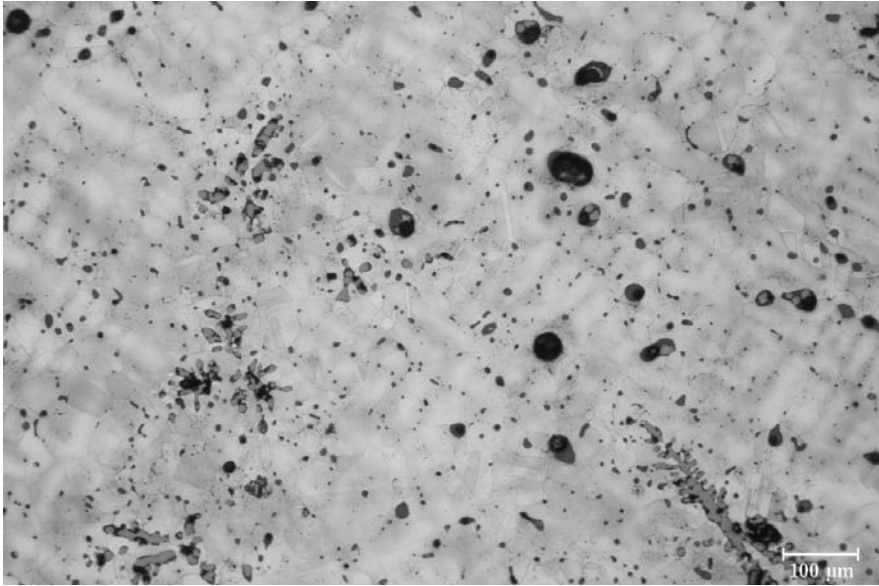


**Figure 6.33:** Pfe10, metallographic section etched with  $\text{NH}_3/\text{H}_2\text{O}_2$ . The sample shows a dendritic cast structure overlapping with a recrystallisation structure

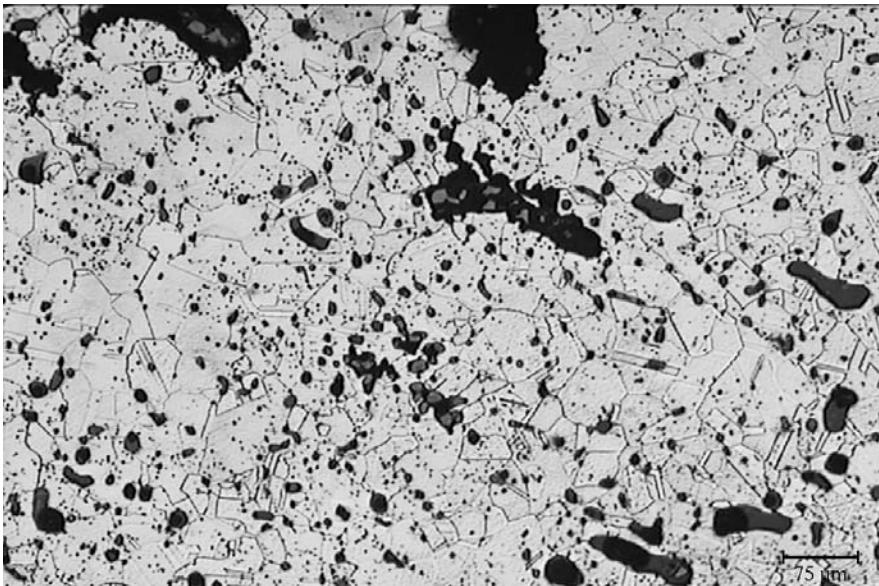


**Figure 6.34:** Pfe10, metallographic section etched with three acid mixture and  $\text{K}_2\text{Cr}_2\text{O}_7$  solution. The recrystallisation structure is distinct.

ness measured over the sample cross-section (Fig. B.13, 221) shows not only the hardness differences between centre and surface of the sample, but also within the same region of the metallographic section. These differences result from the two-phase structure of sample Pfe10.

### **Microanalysis**

Electron microprobe analysis of grey, globular inclusions and of the grey part of the two-phase inclusions revealed that they are oxides with varying amounts of copper, arsenic and, antimony (Table B.9, p. 217). They can be considered as copper arsenate and copper antimonate. The bluish grey internal structures in the two-phase inclusions show much higher copper values, whereas only comparably small amounts of arsenic and antimony were found. They can be considered as impure copper(I)-oxide. The SEM back scatter electron image of a two phase inclusion (Fig. B.9, p. 218) and an EPMA line scan (Fig. B.10, p. 218) further reveal the compositional differences within the inclusion.

About 64 % of the arsenic and 20 % of the total antimony content are dissolved in the copper. The EPMA line scan (Fig. B.11, p. 219) shows that the arsenic and antimony contents of the matrix are nearly constant over the sample cross-section. The alloying elements are strongly enriched in the inclusions.

### **6.7.2 Ingot torque Pfe14**

The ingot torque Pfe14 (Fig. 6.35, p. 91) is very similar to Pfe10. It has a rounded, slightly faceted cross-section. The flattened ends are broken. The ring is covered with a blackish green, smooth patina. Sample Pfe14 was taken by R. Krause from central part the ingot torque.

The composition of sample Pfe14 is similar to Pfe10, with a slightly higher silver contents of 1.2 % and a lower bismuth content of 0.1 % (Table B.2, p. 207). This material can be regarded as fahlore metal type C2.

### **Metallography**

The metallographic section (Fig. 6.36, p. 92) shows a single phase microstructure with regularly distributed inclusions.

Light blue to bluish grey globular inclusions with sizes between 3 and 20  $\mu\text{m}$  are found along the grain boundaries marking the initial cast structure. Partly elongated, grey inclusions of about 50  $\mu\text{m}$  are distributed in the whole sample. In

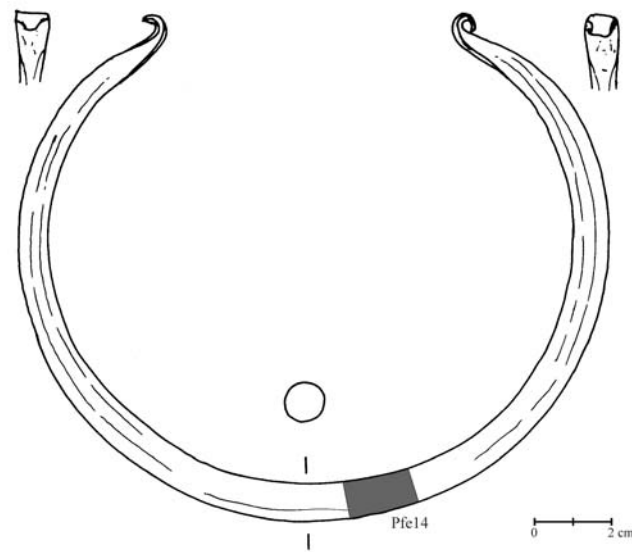


**Figure 6.35:** Ingot torque Pfe14 with sample location.

dark-field illumination and polarised light both inclusion types have red to yellow colours. As in sample Pfe10, two-phase inclusions were found. In bright field illumination they appear grey with a bluish grey square-cut internal structure, in dark-field illumination in red colours.

The metallographic section etched ammonia/hydrogen peroxide shows an overlapping of remnant coring and recrystallisation structure similar to sample Pfe10. The secondary dendrite arm spacing ranges between 20 and 50  $\mu\text{m}$ . In the sample etched with potassium dichromate solution (Fig. 6.37, p. 92) recrystallised grains with sizes ranging between 50 and 100  $\mu\text{m}$  are visible. A preference direction of the dendrites or the annealing twins could not be observed.

The hardness increase is somewhat higher for Pfe14 compared to Pfe10; it is about 60 HV0.2 in the centre and up to 80 HV0.2 near the surface (Table B.3, p. 209). The low load hardness measured over the sample cross-section (Fig. B.14, p. 221) shows the contrast between both the centre and surface of the sample.

### Microanalysis

Electron microprobe analyses of grey, globular to elongated inclusions revealed that they are copper arsenate and antimonate similar to those in sample Pfe10 (Table B.10, p. 220).

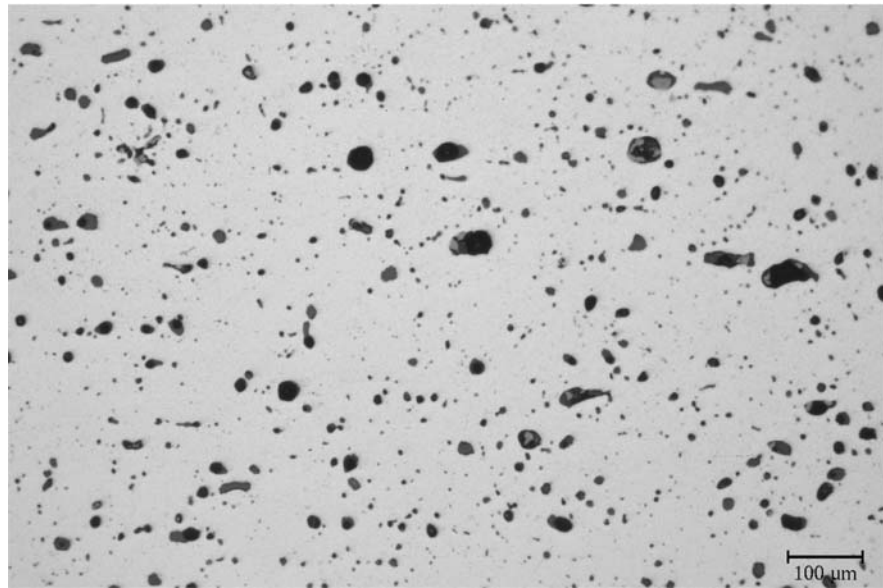


**Figure 6.36:** Pfe14, metallographic section. The sample has a single-phase microstructure with inclusions of copper arsenate and copper antimonate.

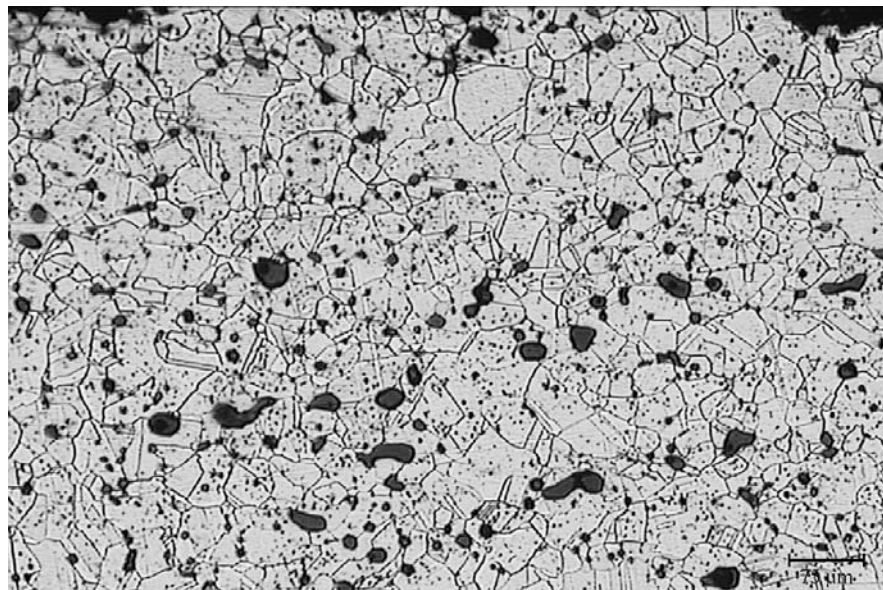


**Figure 6.37:** Pfe14, metallographic section etched with three acid mixture and  $K_2Cr_2O_7$  solution. Visible is the recrystallisation structure.



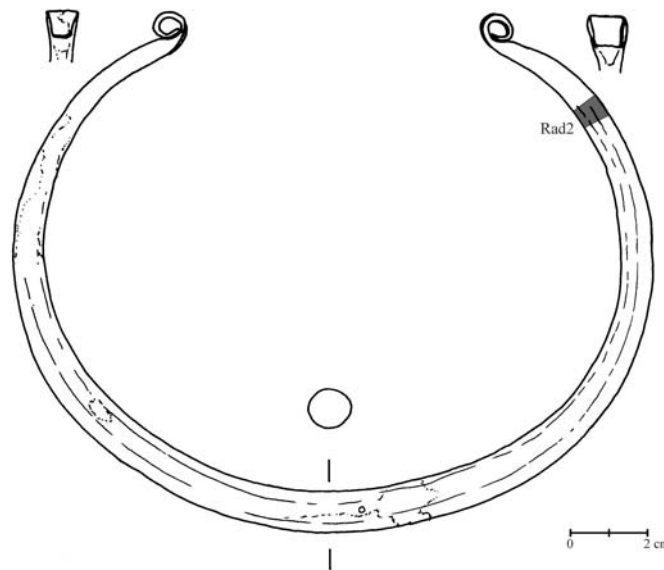


**Figure 6.38:** Ingot torque Rad2 with sample location.

## 6.8 Radostice, okr. Litomeřice

The Radostice hoard of ingot torques was found in 1933 in a quarry at the footwall of the Ovcim mountain. At least 191 ingot torques and 6 spiral arm-rings were deposited in about 85 cm depth beneath two flat stones (Bartelheim, 1998). The largest part of the find is preserved in the Litomeřice museum, some pieces are stored in České Budejovice and in the National Museum of Prague.

According to the Stuttgart analyses, the ingot torques from Radostice are made of ingot torque metal. The arsenic content ranges from 0.4 to 2.4 %, antimony from 0.8 to 2.3 %, and silver from 0.4 to 1.5 % (SMAP database, 1999).

### 6.8.1 Ingot torque Rad2

The ingot torque Rad2 (Fig. 6.38, p. 93) has a rounded, slightly faceted cross-section. The ends are flattened and curled into loops. The smooth patina is blackish green. A sample was taken from the region close to the loop.

The sample Rad2 consists of ingot torque metal C2 with 2.1 % arsenic, 1.9 % antimony, 1.1 % silver, and 0.3 % bismuth.

### **Metallography**

The metallographic section of sample Rad2 (Fig. 6.39, p. 95) shows a single phase microstructure. Light blue to bluish grey, globular inclusions with sizes between 5 and 10  $\mu\text{m}$  mainly occur along the grain boundaries. Larger grey inclusions with sizes of up to 100  $\mu\text{m}$  are elongated in the longitudinal direction of the ring. Several two-phase inclusions similar to those in the Aschering samples were found. In polarised light all of these inclusions have red to yellow colours.

The sample etched with ammonium persulfate solution shows a dendritic cast structure. Etching the metallographic section with potassium dichromate solution revealed the recrystallised structure with annealing twins (Fig. 6.40, p. 95). The grain sizes range between 50 and 200  $\mu\text{m}$ .

The low load core hardness of sample Rad2 is 82 HV0.2 and increases to 88 HV0.2 towards its surface (Table B.3, p. 209).

### **6.8.2 Ingot torque Rad4**

The ingot torque Rad4 (Fig. 6.41, p. 96) is very similar to Rad2. It has a rounded, slightly faceted cross-section, the flattened ends are curled into loops. The patina is blackish green. Similar to ingot torque Rad2, the sample was taken from close to the loop.

Sample Rad4 has a similar composition to Rad2. The copper contains 2.2 % arsenic, 1.3 % antimony, and 0.2 % bismuth (Table B.2, p. 207). Due to the higher nickel content of 0.03 % the material was allocated to the Stuttgart material group C2D.

### **Metallography**

The metallographic section (Fig. 6.42, p. 97) shows a single phase microstructure similar to sample Rad2. Very small light blue to bluish grey, globular inclusions were found along the grain boundaries. Grey inclusions with sizes up to 100  $\mu\text{m}$  are elongated and oriented in the direction of the ring. Some of the grey inclusions show an internal bluish grey structure. In polarised light the inclusions have red to yellow colours.

The sample etched potassium dichromate solution shows a recrystallised structure with annealing twins (Fig. 6.43, p. 97). The grain sizes are between 50 and 200  $\mu\text{m}$ .

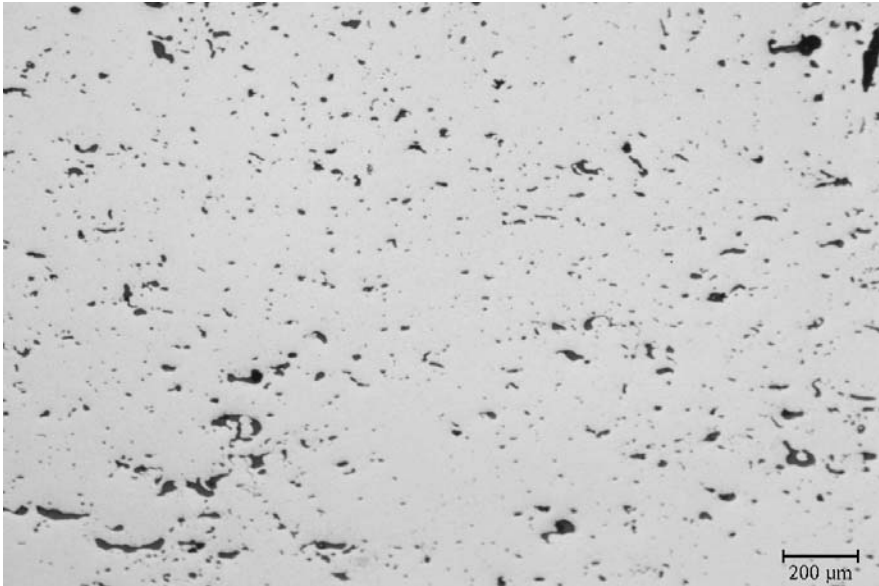


**Figure 6.39:** Rad2, metallographic section. The sample has a single phase, inclusion rich microstructure.

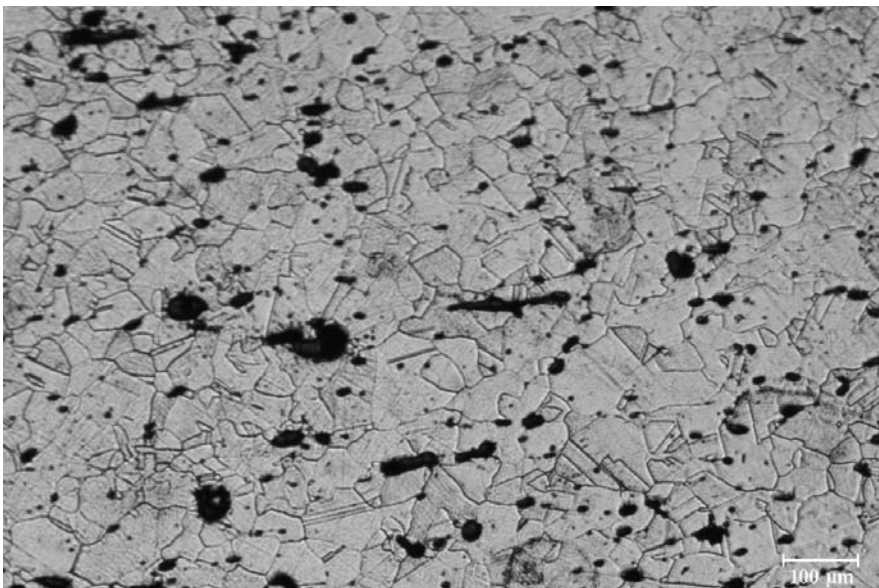


**Figure 6.40:** Rad2, metallographic section etched with  $K_2Cr_2O_7$  solution. A recrystallization structure with annealing twins is visible.

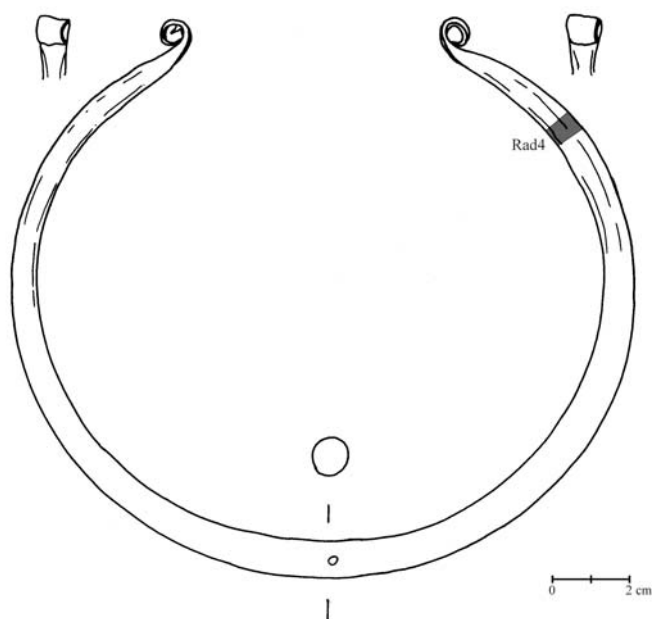


**Figure 6.41:** Ingot torque Rad4 with sample location.

The low load hardness in the centre of sample rad 4 is about 70 HV0.2, which is lower than that of sample Rad2 (Table B.3, p. 209). The surface hardness of 84 HV0.2 is similar to that of Rad2.

### Microanalysis

Electron microprobe analyses of grey inclusions revealed oxides of copper, antimony and some arsenic (Table B.11, p. 222). They can be considered mainly as copper antimonate with minor copper arsenate.

Matrix analyses imply that about 70 % of the total arsenic content and all of the silver occur dissolved in the matrix (cf. Tables B.2, p. 207 and B.11, p. 222). Antimony and bismuth are mainly bound in the inclusions. Only 18 % of the antimony and 14 % of the bismuth occur in the copper solid solution. EDX analyses with the scanning electron microscope confirmed these observations. The elemental distribution (Fig. B.17, p. 223) shows an enrichment of arsenic, antimony, and bismuth in oxidic inclusions.

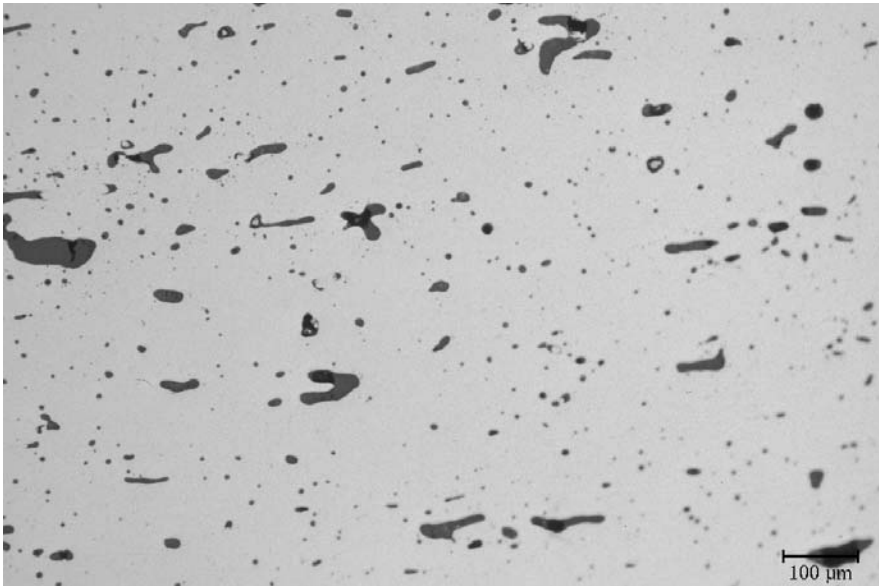


**Figure 6.42:** Rad4, metallographic section. The sample has a single phase microstructure similar to sample Rad2.

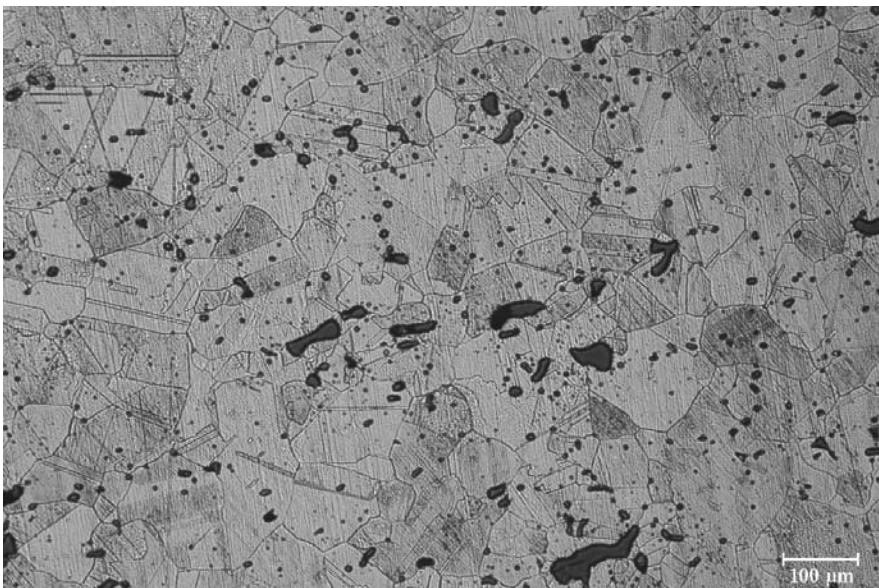


**Figure 6.43:** Rad4, metallographic section  $K_2Cr_2O_7$  solution. Shown is a recrystallised structure with annealing twins.

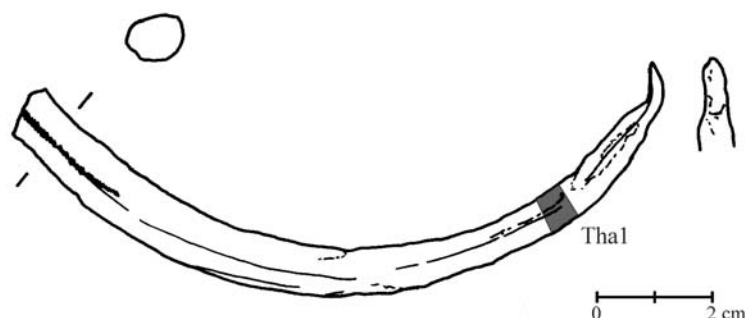


**Figure 6.44:** Ingot torque fragment Tha1 and sample location.

## 6.9 Thailing, Kr. Ebersberg

In 1953 three ingot torques were found while ploughing the ‘Große Wiese’ (‘big meadow’) in Thailing. A reinvestigation resulted in the discovering of seven further ingots (inventory, Prähistorische Staatssammlung München). The Prähistorische Staatssammlung obtained these seven rings, and one and a half ingot torques from the first find.

Stein (1976b) described the ingots as poorly preserved and reworked with faceted cross-section. The ends are mostly pointed and bent (Stein, 1976b). The Stuttgart analyses suggest that the Thailing ingot torques and fragments are made of ingot torque metal (SMAP database, 1999).

### 6.9.1 Fragment Tha1

The investigated fragment Tha1 (Fig. 6.44, p. 98) represents about one third of an ingot torque. It has a slightly oval shape in cross-section. The flattened end is hook-shaped and bent inwards. An investigation of the fracture was precluded because it was filed flat. The fragment was covered with a brownish-green patina. A sample was taken from the area close to the hook-shaped end.

The fragment Tha1 consists of an ingot torque metal with 1.8 % arsenic, 1.5 % antimony, and 1.3 % silver (Table B.2, p. 207). This composition is comparable to those of the Pfedelbach ingot torques. However, in contrast to that material, the sample contains 0.3 % bismuth, i.e. a fahlore metal C2C.

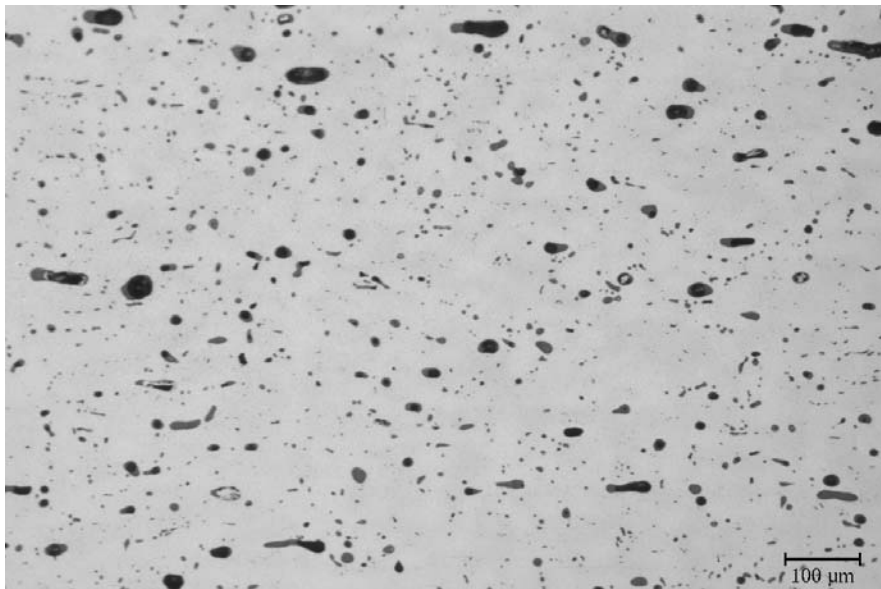


**Figure 6.45:** Tha1, metallographic section. The sample has a single phase, inclusion rich microstructure.

### **Metallography**

The metallographic section (Fig. 6.45, p. 99) shows a single phase microstructure. The inclusions are similar to those in samples Hoh1 and Müh1. Grey, globular inclusions of about  $10\ \mu\text{m}$  are distributed mainly along the grain boundaries. Bluish grey to grey inclusions with sizes ranging between  $50$  and  $100\ \mu\text{m}$  are elongated in the longitudinal direction of the sample. In polarised light the inclusions have red to orange colours.

The sample etched with ammonia persulphate solution (Fig. 6.46, p. 100) shows a dendritic cast structure. The same metallographic section etched with potassium dichromate solution (Fig. 6.47, p. 100) revealed a recrystallised structure with annealing twins. The grain sizes range between  $50$  and  $100\ \mu\text{m}$ . A preference direction of the annealing twins and the dendrites could not be defined.

The core low load hardness of the ingot torque is about  $66\ \text{HV}0.2$ , thus comparable to the values of the Pfedelbach samples (Table B.3, p. 209). Towards the surface the hardness increases to  $90\ \text{HV}0.2$ .

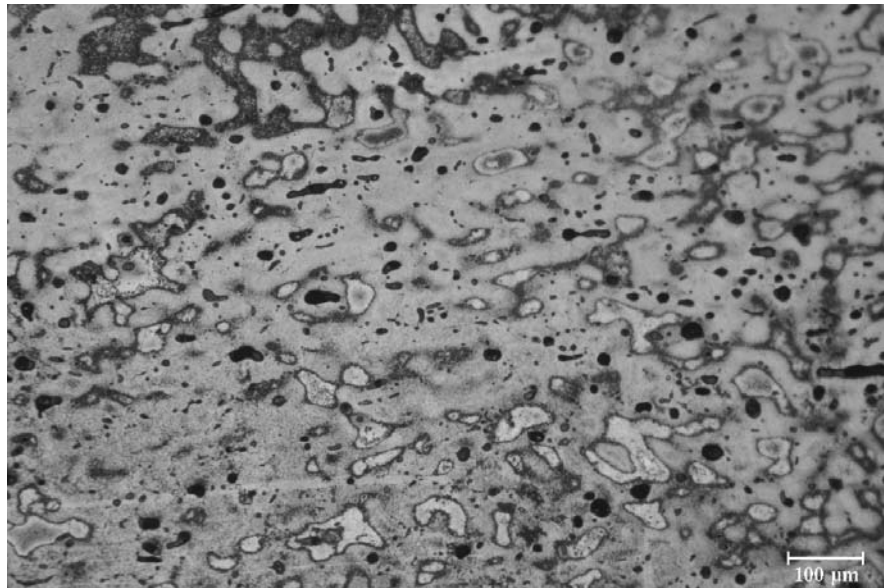


**Figure 6.46:** Tha1, metallographic section etched with  $(\text{NH}_4)_2\text{S}_2\text{O}_8$  solution. The sample shows a dendritic cast structure.

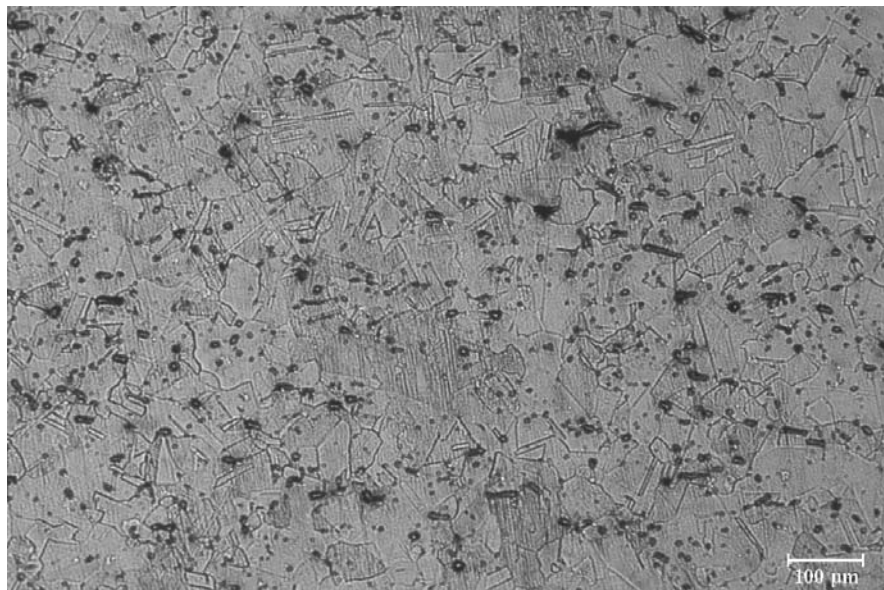


**Figure 6.47:** Tha1, metallographic section etched with  $\text{K}_2\text{Cr}_2\text{O}_7$  solution. Shown are recrystallised grains with annealing twins.



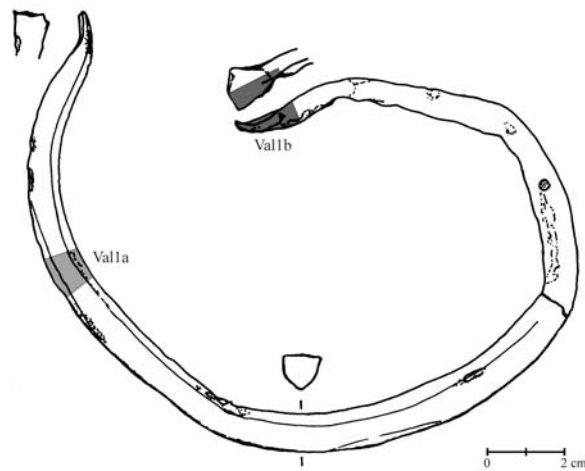


**Figure 6.48:** Ingot torque Val1 with sample locations Val1a at the reverse side of the ingot and Val1b at the flattened end.

## 6.10 Valley, Kr. Miesbach

The ingot hoard from Valley has already been described in chapter 5.6, p. 56.

### 6.10.1 Ingot torque Val1

The ingot torque Val1 (Fig. 6.48, p. 101) was deformed and broken, and the two pieces were later joined together. The ring has a triangular, little faceted cross-section with a casting groove on the inside. The ends are flattened and slightly bent outwards. The blue to green patina is partly broken off. Two samples were taken from the ring: Val1a from the outer third of one fragment and Val1b from the flattened end of the other one.

Sample Val1a consists of impure copper with about 0.05 % arsenic. Sample Val1b has a slightly higher arsenic content of 0.08 %. Remarkable are the high nickel values of 0.2 % in Val1a and 0.17 % in Val1b (Table B, p. 208). According to the Stuttgart classification (Junghans et al., 1968b) the ingot torque is made of arsenical copper type FA.

### Metallography

**Val1a** The metallographic section of sample Val1a (Fig. 6.49, p. 102) shows a single phase microstructure. Very small bluish grey to light blue inclusions are

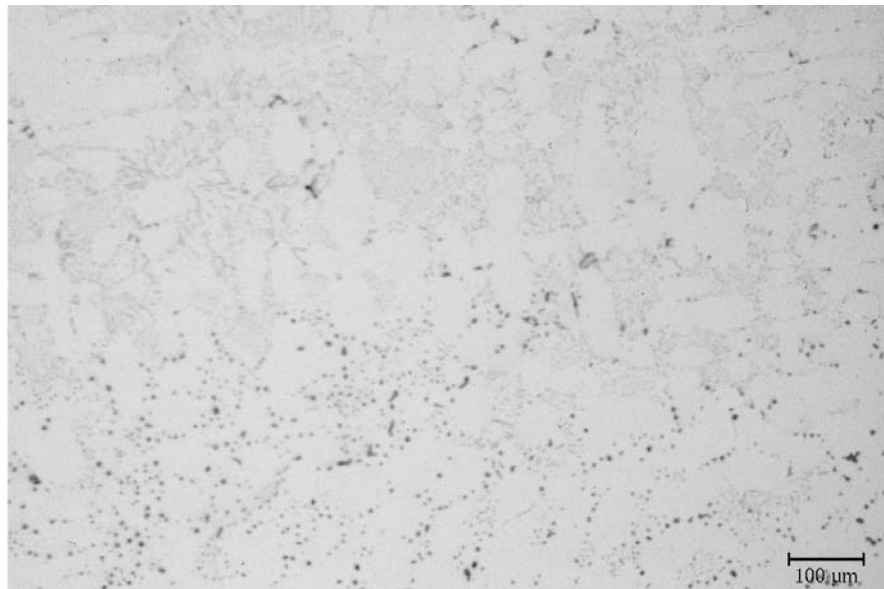


**Figure 6.49:** Vall1a, metallographic section. The sample has a single phase, inclusion-rich microstructure.

distributed along the grain boundaries and triple points. They form an eutectic structure and mark the initial cast structure. In polarised light these inclusions are red, which is characteristic for copper oxides. Light blue inclusions in sizes of about  $10\ \mu\text{m}$  were found mainly close to the surface. In polarised light they have a grey colour.

The sample etched with ammonia/hydrogen peroxide (Fig. 6.50, 103) shows a recrystallised microstructure with annealing twins. The grains have sizes ranging between  $20$  and  $100\ \mu\text{m}$ . The grain areas were contrasted with ammonium persulfate solution (Fig. 6.51, 103). The areas with the same lattice orientation (casting domains) have sizes of up to  $1.5\ \text{mm}$ . A dendritic cast structure with a secondary dendrite arm spacing of  $20$  to  $50\ \mu\text{m}$  could be recognised.

Sample Vall1a has a quite low core hardness of  $64\ \text{HV}0.2$ , which increases towards the surface to  $74\ \text{HV}0.2$  (Table B.3, p.209).

**Val1b** The metallographic section (Figs. 6.52, p. 105 and B.18, p. 224) of the flattened end shows a similar single phase microstructure like that of sample Vall1a. Close to the surface the eutectic structure of copper oxide and the light blue inclusions are elongated parallel to the surface. In the centre of the sample

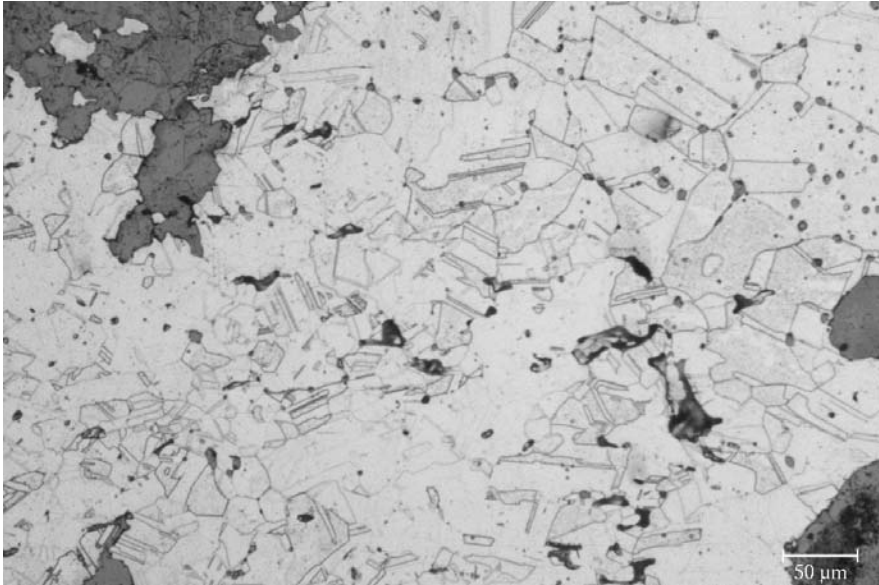


**Figure 6.50:** Vall1a, metallographic section etched with  $\text{NH}_3/\text{H}_2\text{O}_2$ . The sample shows a recrystallised structure with annealing twins.

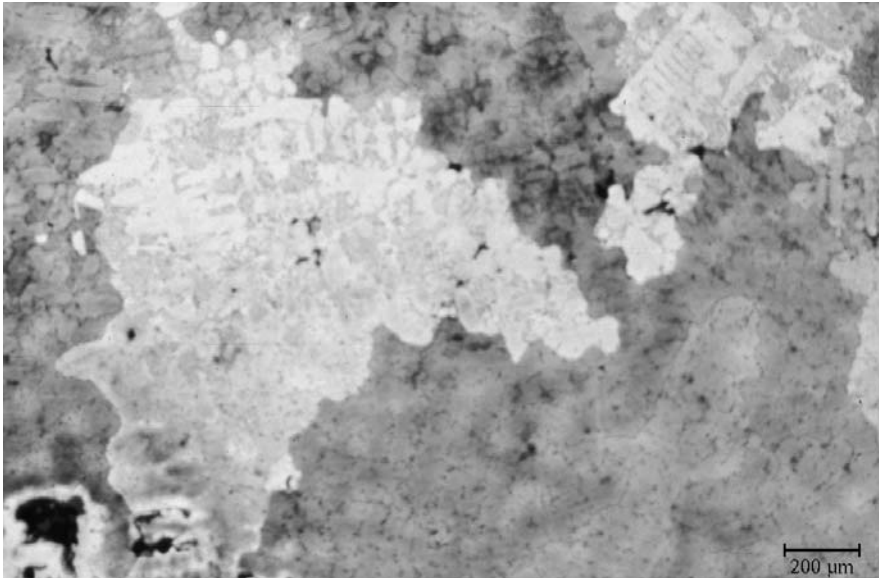


**Figure 6.51:** Vall1a, metallographic section etched with three acid mixture and  $(\text{NH}_4)_2\text{S}_2\text{O}_8$  solution. Shown are areas of same lattice orientation and a dendritic cast structure.

a region with bigger light blue inclusions and large specks of corrosion products are found.

In the sample etched with ammonia/hydrogen peroxide a dendritic cast structure is visible. The metallographic section etched with ammonium persulfate solution (Fig. 6.53, 105) reveals a recrystallised structure with annealing twins. The grain sizes range between 50 and 100  $\mu\text{m}$  in size.

The low load hardness HV0.2 of the sample Val1b is similar to that of samples Hech1 and Hech2. The core hardness is 58 HV0.2, which is relatively low. Towards the surface the hardness increases only to 61.5 HV0.2 (Table B.3, p.209).

### Microanalysis

With electron microprobe analyses the light blue inclusions in sample Val1b were identified as copper sulfide  $\text{Cu}_2\text{S}$  with small amounts of oxygen (Table B.12, p. 224). The large islands of corrosion products consist of copper oxide.

### 6.10.2 Fragment Val2

The fragment Val2 (Fig. 6.54, 106) represents one half of an ingot torque. It has a rounded, little faceted cross-section with a forging seam. The flattened end is rolled into a loop. The broken end shows a low deformation bending fracture. The blue-green patina is partly broken off. Three samples were taken from this fragment. Sample Val2a was taken from the fracture side, Val2b from the last third of the ring and sample Val2c from the loop.

Fragment Val2 shows the characteristic composition of ingot torque metal C2. It contains between 1.8 and 2.0 % arsenic, 1.4 to 1.6 % antimony, between 0.9 and 1.4 % silver, and between 0.08 and 0.1 % bismuth (Table B, p. 208). By contrast, the sample from the loop, Val2c, contained about 0.2 % iron.

### Metallography

**Val2a** The metallographic section of the broken end (Fig. 6.55, p. 107) has a single phase microstructure and shows some interdendritic shrinkage. Bluish grey, globular inclusions with sizes smaller than 5  $\mu\text{m}$  mark the grain boundaries. The larger grey inclusions with sizes between 10 and 50  $\mu\text{m}$  are globular in the centre of the sample and elongated close to its surface. In polarised light both inclusion types are red to yellow. Similar to the Aschering or Pfedelbach samples, two-phase inclusions occur. These up to 50  $\mu\text{m}$  large inclusions are globular to



**Figure 6.52:** Val1b, metallographic section. The sample has a single phase microstructure with inclusions deformed parallel to the surface and corrosion products at the surface and in the centre of the sample.



**Figure 6.53:** Val1b, metallographic section etched with  $(\text{NH}_4)_2\text{S}_2\text{O}_8$  solution. The sample shows a recrystallised structure with annealing twins.

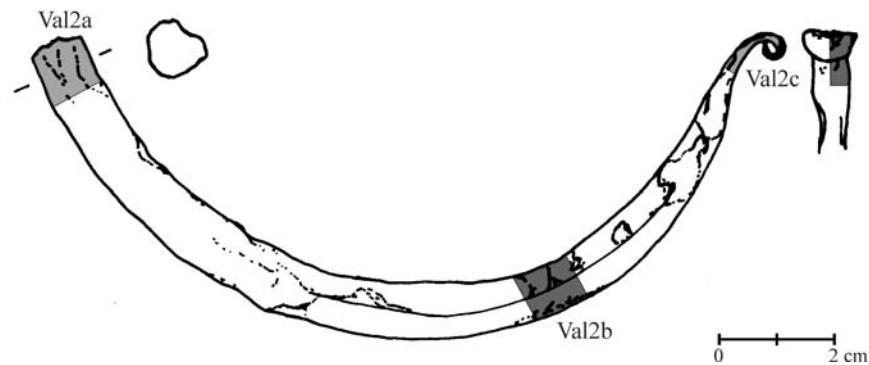


**Figure 6.54:** Ingot torque fragment Val2 with sample locations. The samples Val2a and Val2c were taken from the reverse side, and Val2b from the front side of the fragment.

elongated in shape. Within a grey matrix bluish grey to light blue, in some cases dendritic, inner structures were found. In polarised light these two-phase inclusions show the characteristic red colour of copper oxide.

The sample etched with ammonia/hydrogen peroxide (Fig. 6.56, p. 107) shows a dendritic cast structure.

The low load hardness values of sample Val2a are comparable to those from Pfedelbach. The sample has a core hardness of about 73 HV0.2 and a surface hardness of 80 HV0.2 (Table B.3, p.209).

**Val2b** Sample Val2b (Figs. 6.57, p. 108 and B.19, p. 225) shows the same single phase microstructure than sample Val2a. Small bluish grey to grey, globular inclusions occur along the grain boundaries. Larger grey inclusions which appear in red to yellow colour in polarised light are regularly distributed in the matrix. Compared to sample Val2a, the two-phase inclusions are elongated. In the centre of the sample many pores with diameters of up to 100  $\mu\text{m}$  occur. Some of these pores have oxidised internal surfaces.

Etching with ammonium persulfate solution highlighted the residual cast structure (Fig. 6.58, p. 108). A preference direction of the dendrites could not be observed.

Compared to sample Val2a, Val2b has a lower hardness of about 60 HV0.2 in the centre and 70 HV0.2 at the surface (Table B.3, p.209).

**Val2c** The metallographic section Val2c from the loop (Fig. 6.59, p. 109) has a single phase microstructure. Most of the grey and two-phase inclusions are

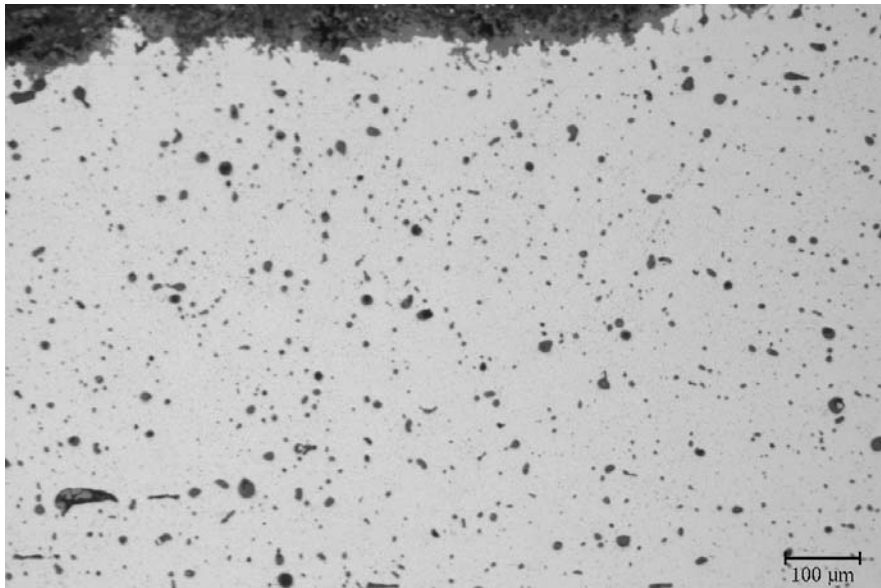


**Figure 6.55:** Val2a, metallographic section. The sample has a single phase, inclusion-rich microstructure.

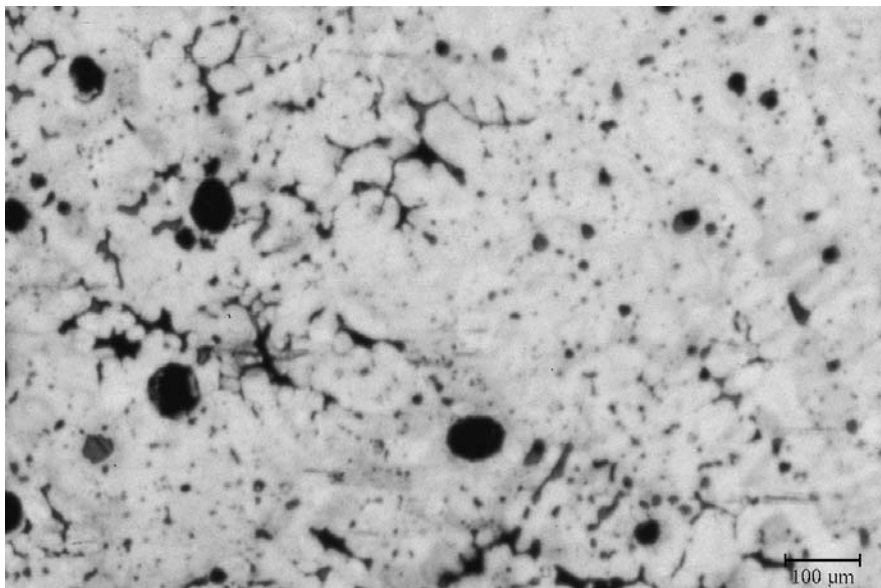


**Figure 6.56:** Val2a, metallographic section etched with  $\text{NH}_3/\text{H}_2\text{O}_2$ . Shown is a dendritic cast structure and some interdendritic shrinkage.

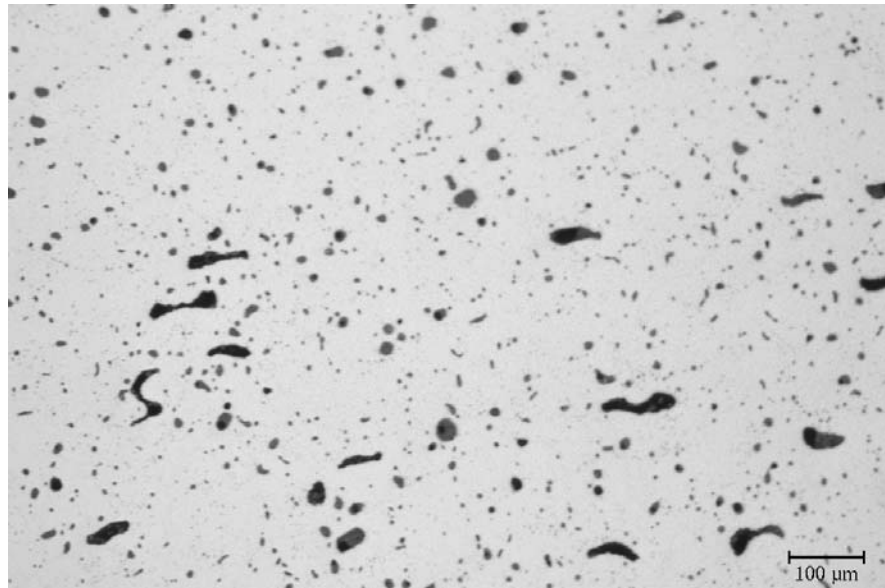


**Figure 6.57:** Val2b, metallographic section. The sample has a single phase, inclusion-rich microstructure similar to sample Val2a.

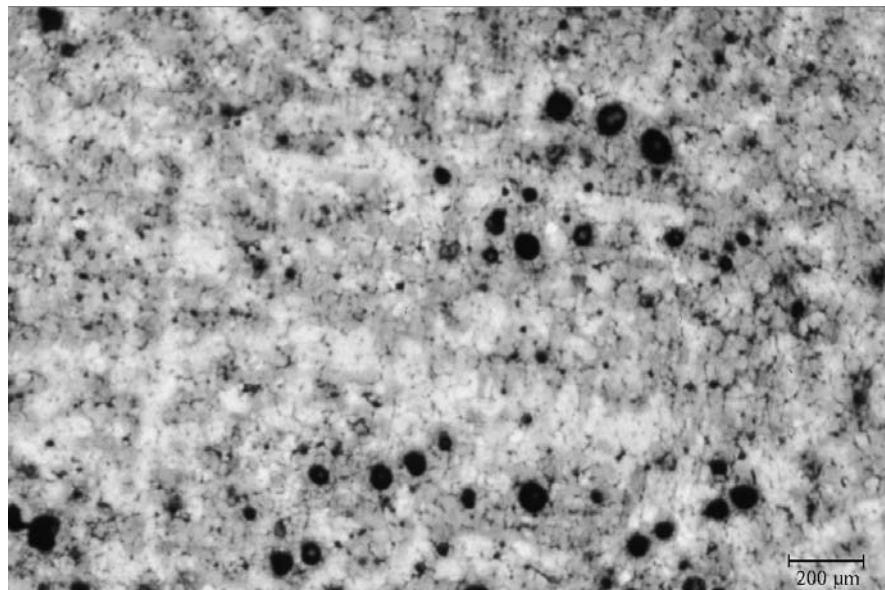


**Figure 6.58:** Val2b, metallographic section etched with  $(\text{NH}_4)_2\text{S}_2\text{O}_8$  solution. A dendritic cast structure is visible.





**Figure 6.59:** Val2c, metallographic section. The sample has a single phase microstructure with inclusions deformed parallel to the sample surface.

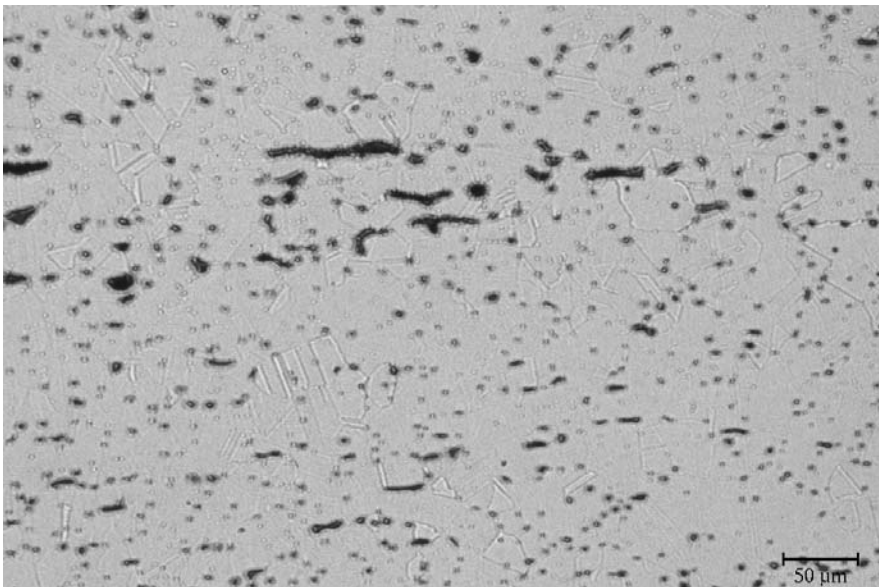


**Figure 6.60:** Val2c, metallographic section. With closed aperture diaphragm the recrystallisation structure is visible.

elongated parallel to the sample surface. The very small bluish grey inclusions remained globular. They mark the grain boundaries of the deformed microstructure. Since the sample was slightly etched during polishing, some recrystallised grains are visible even within the unetched metallographic section (Fig. 6.60, p. 109).

The sample etched with ammonia/hydrogen peroxide shows a heavily deformed dendritic cast structure.

The core hardness of the sample from the loop is 74 HV0.2 (Table B.3, p.209). Towards the surface it increases to 90 HV0.2.

### Microanalysis

In sample Val2b some of the inclusions were analysed by electron microprobe facilities. The grey globular inclusions are oxides with variable copper, arsenic, and antimony contents comparable to those of the Aschering samples (Table B.13, p. 225). They can be considered as copper arsenate and copper antimonate.

### 6.10.3 Fragment Val3

Val3 (Fig. 6.61, p. 111) represents a deformed fragment of an ingot torque. It has a rounded, slightly faceted cross-section with a casting groove. The flattened end is partly bent into a loop. This fragment has a low deformation mixed bending fracture similar to Val2. Additionally there is a crack in the middle of the fragment. The blue to green patina is partly broken off and the metal surface appears to be porous. The samples were taken in the same order than those from Val2. Sample Val3a was taken from the fracture side, Val3b near the crack and Val3c was taken from the bent end.

XRF-analyses of the samples show, that they consist of impure copper with 0.05 to 0.07 % arsenic (Table B, p. 208). The material contains between 0.2 and 0.4 % iron and about 0.2 % nickel and can be regarded as arsenical copper type FA.

### Metallography

**Val3a** The metallographic section from the broken end of Val3 (Fig. 6.62, p. 112) shows a single phase structure similar to Val1. Bluish grey to light blue, globular inclusions with sizes below 5  $\mu\text{m}$  were found in an eutectic structure in the centre of the sample. Larger light blue, globular inclusions occur along the grain boundaries marking the initial cast structure. In polarised light these inclusions

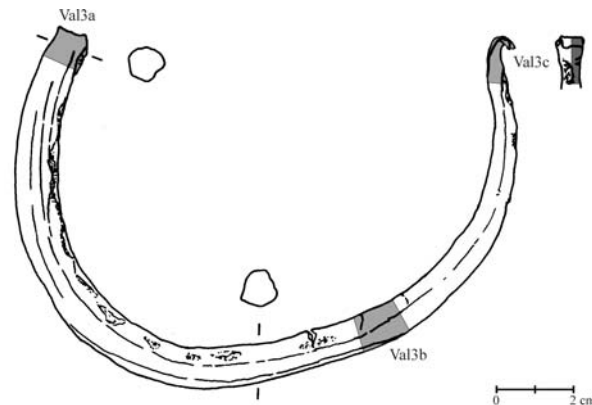


**Figure 6.61:** Ingot torque fragment Val3 with sample locations at the reverse side of the fragment.

are grey. In the region of the casting groove the inclusions close to the surface are elongated.

The metallographic section etched with ammonia/hydrogen peroxide shows a recrystallised structure overlapping with a cast structure. The grain sizes range between 0.1 and 1 mm. The sample etched with ammonium persulfate solution (Fig. 6.63, p. 112) has recrystallised grains with annealing twins. In the area of the casting groove stretched grains were found.

The low load hardness values are similar to Val1. Sample Val3a has a core hardness of 55 HV0.2 which increases towards the surface to 68 HV0.2 (Table B.3, p.209).

**Val3b** The metallographic section Val3b (Figs. 6.64, p. 113 and B.20, p. 226) has a similar structure as sample Val3a. In a single phase matrix light blue, globular inclusions of less than 10  $\mu\text{m}$  occur along the grain boundaries. In polarised light these inclusions are grey.

The etched metallographic section (Fig. 6.65, p. 113) shows a recrystallisation structure. The equiaxed grains with annealing twins have sizes between 50 and 100  $\mu\text{m}$ .

Sample Val3b has a similar core hardness as sample Val3a, 55 HV0.2 (Table B.3, p.209). The hardness increase towards the surface was less pronounced and the final hardness was 61 HV0.2.

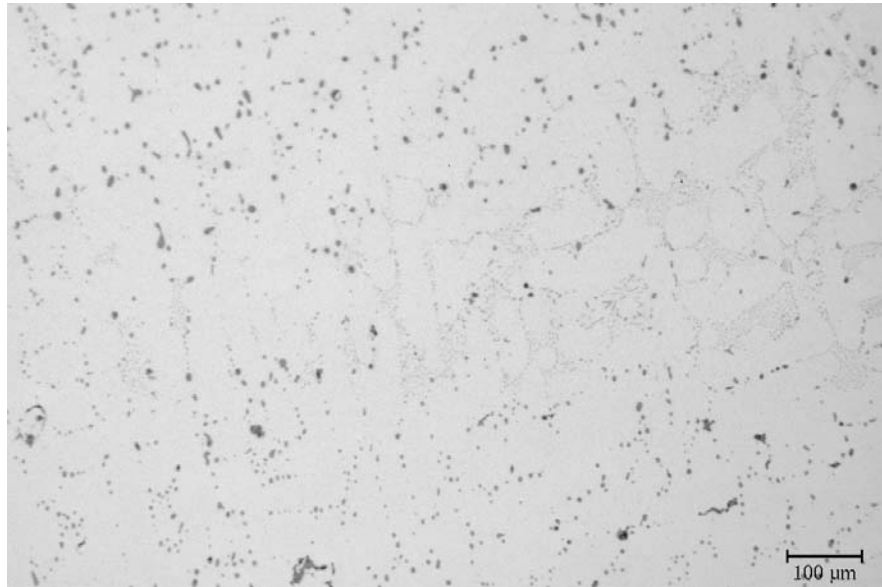


**Figure 6.62:** Val3a, metallographic section. The sample shows a single phase structure similar to Val1.

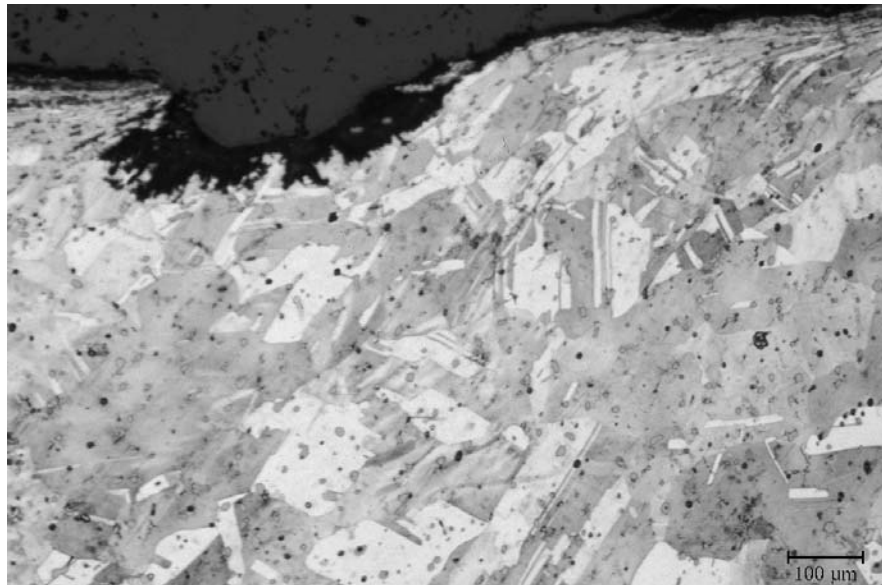


**Figure 6.63:** Val3a, metallographic section etched with three acid mixture and  $(\text{NH}_4)_2\text{S}_2\text{O}_8$  solution. The sample shows a recrystallised structure overlapping with a cast structure.

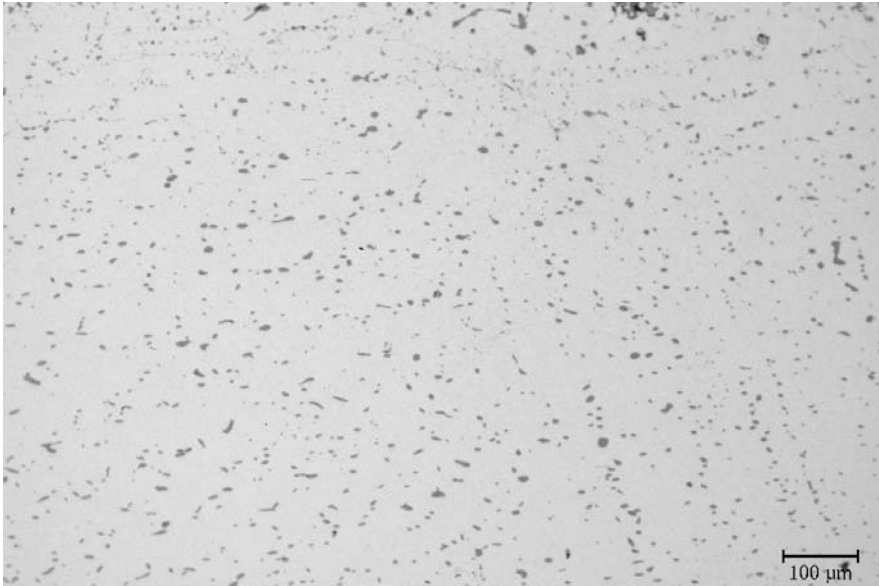


**Figure 6.64:** Val3b, metallographic section. The sample shows a single phase microstructure similar to Val3a.

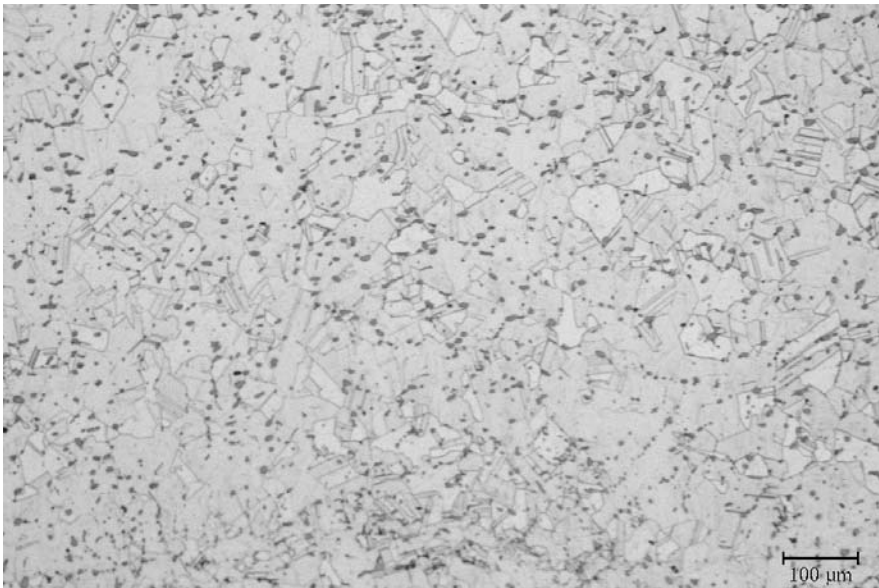


**Figure 6.65:** Val3b, metallographic section etched with  $\text{NH}_3/\text{H}_2\text{O}_2$ . Shown is a recrystallisation structure with annealing twins.



**Figure 6.66:** Val3c, metallographic section. The sample shows a single phase microstructure with deformed inclusions.

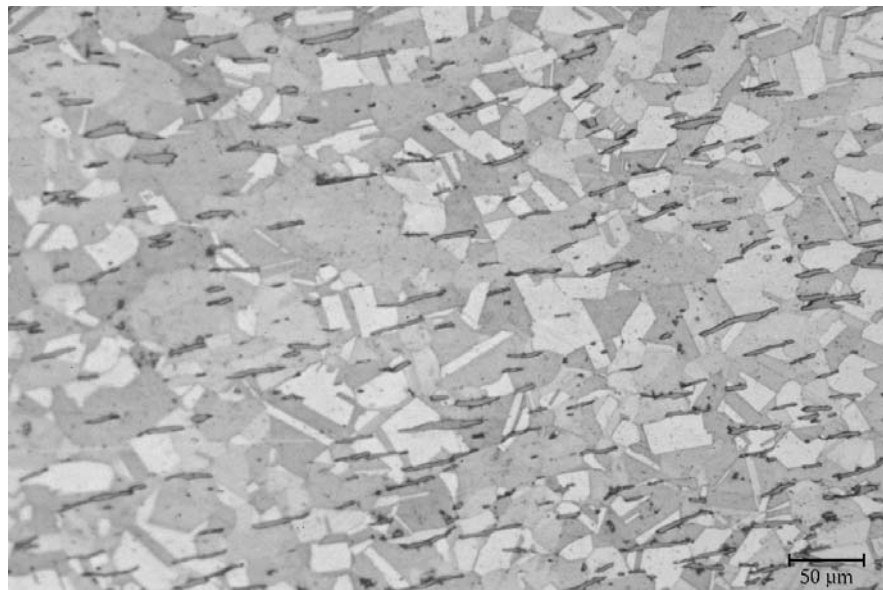


**Figure 6.67:** Val3c, metallographic section etched with three acid mixture and  $(\text{NH}_4)_2\text{S}_2\text{O}_8$  solution. The etching reveals the recrystallisation structure.

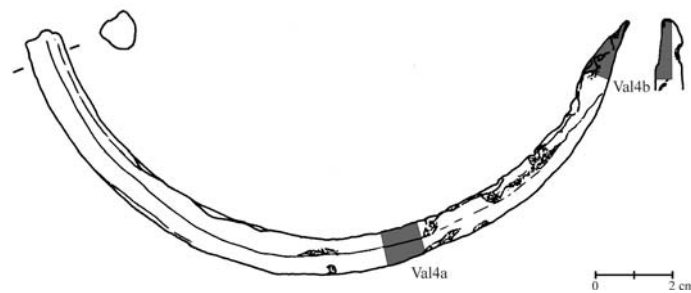


**Figure 6.68:** Ingot torque fragment Val4 with sample locations.

**Val3c** Similar to the other samples from ingot torque fragment Val3, the metallographic section from the loop (Fig. 6.66, p. 114) displayed a single phase microstructure. The light blue inclusions in Val3c are elongated in the direction of deformation with a length-to-width ratio of about ten.

The metallographic section etched with ammonium persulphate solution (Fig. 6.67, p. 114) shows a recrystallised structure with grain sizes ranging between 10  $\mu\text{m}$  close to the edge and 50  $\mu\text{m}$  in the centre of the sample.

Sample Val3c has a core hardness of 57 HV0.2 (Table B.3, p.209). The surface hardness of 69 HV0.2 is comparable with that of sample Val3a.

### Microanalysis

The inclusions in sample Val3b were analysed with the electron microprobe (Table B.14, p. 226). They consist of copper sulfide  $\text{Cu}_2\text{S}$ , similar to the inclusions found in Val1.

### 6.10.4 Fragment Val4

The fragment Val4 (Fig. 6.68, p. 115) represents one half of an ingot torque with a triangular, faceted cross-section and a casting groove. The worked end is slightly flattened but not bent. The broken end shows a corroded bending fracture with a crack. The blue to green patina of the fragment is partly flaked off. Sample Val4a was taken from the middle of the fragment and Val4b from the flattened end.

XRF analyses show that these samples have similar compositions to those from Val3. The arsenic content is about 0.06 %, and about 0.06 to 0.08% iron and 0.18 to 0.2 % nickel were found (Table B, p. 208). As ingot torque Val3, the fragment Val4 consists of arsenical copper type FA.

### **Metallography**

**Val4a** The metallographic section (Figs. 6.69, p. 117 and B.21, p. 227) shows a single phase microstructure similar to Val1 and Val3. Bluish grey to light blue, globular inclusions smaller than 5  $\mu\text{m}$  were found along grain boundaries and at triple points. They form an eutectic structure and mark the cast structure. In polarised light these inclusions are red. Light blue, globular to elongated inclusions with sizes of about 10  $\mu\text{m}$  were also distributed along the grain boundaries. These inclusions are grey in polarised light.

The sample etched with ammonia/hydrogen peroxide (Fig. 6.70, p. 117) shows a recrystallised structure with annealing twins. The grain sizes range between 50  $\mu\text{m}$  near the edge and 500  $\mu\text{m}$  in the centre of the sample. The metallographic section etched with ammonium persulfate solution shows parts of the dendritic cast structure overlapping with recrystallised grains.

The low load hardness of sample Val4a is similar to those of samples Val1 and Val3. Val4a has a core hardness of 60 HV0.2 and a surface hardness of 68 HV0.2 (Table B.3, p.209).

**Val4b** The metallographic section from the flattened end of the fragment Val4 (Fig. 6.71, p. 118) shows a single phase microstructure. The inclusion types are similar to those in sample Val4a. Bluish grey to light blue, globular inclusions of less than 5  $\mu\text{m}$  occur along the grain boundaries and triple points. The eutectic structure was stretched in the direction of deformation. The light blue inclusions are elongated, too.

The sample etched with ammonium persulfate solution (Fig. 6.72, p. 118) shows a recrystallised structure with annealing twins. The grain sizes vary between 10  $\mu\text{m}$  at the edge and 100  $\mu\text{m}$  in the centre of the metallographic section.

Sample Val4b has low load hardness values of about 56 HV0.2 in the centre and 61 HV0.2 close to the surface (Table B.3, p.209).

### **Microanalysis**

A microanalysis of a globular light blue inclusion revealed that it is copper sulfide similar to that in the samples Val1b and Val3b (Table B.15, p.227).



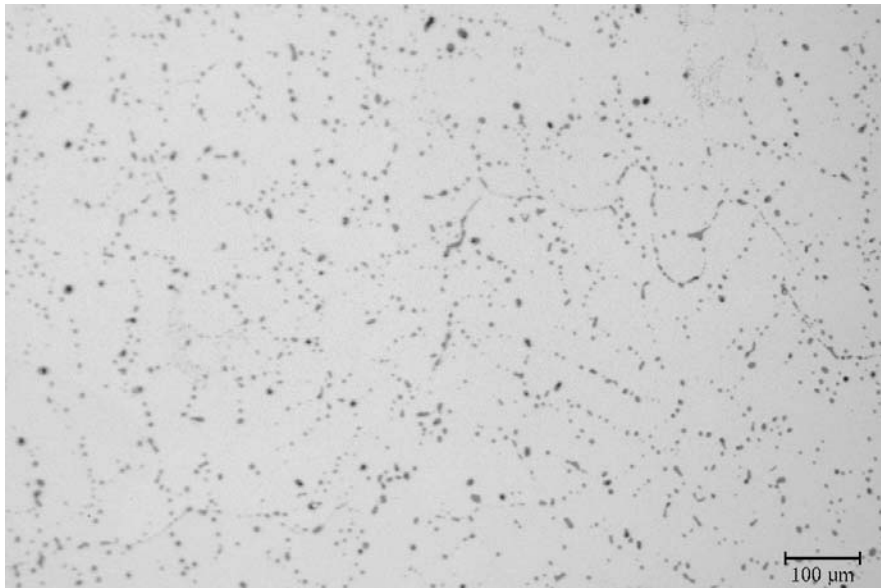


**Figure 6.69:** Val4a, metallographic section. The sample shows a single phase microstructure similar to Val1 and Val3.



**Figure 6.70:** Val4a, metallographic section etched with  $\text{NH}_3/\text{H}_2\text{O}_2$ . Visible is a recrystallised structure with annealing twins.



**Figure 6.71:** Val4b, metallographic section. The sample shows a single phase, inclusion rich microstructure similar to Val4a.

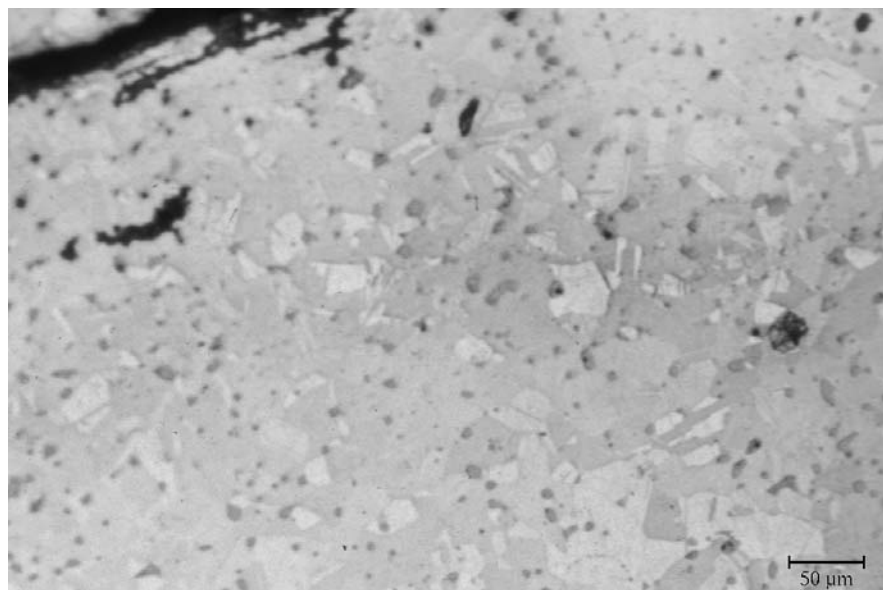


**Figure 6.72:** Val4b, metallographic section etched with  $(\text{NH}_4)_2\text{S}_2\text{O}_8$  solution. The sample shows a recrystallised structure with annealing twins.

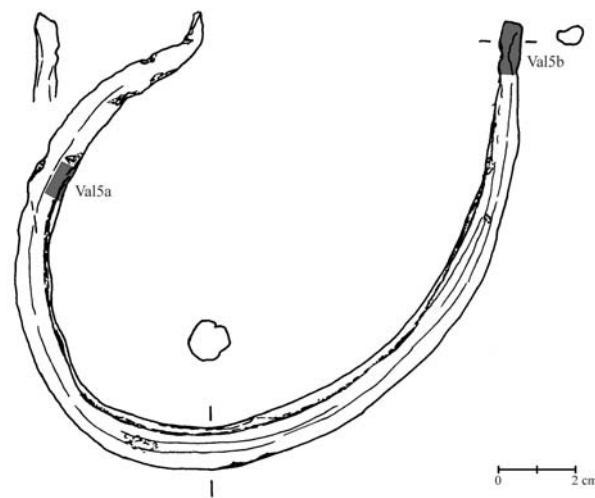


**Figure 6.73:** Ingot torque Val5 with sample locations.

### 6.10.5 Ingot torque Val5

The ingot torque Val5 (Fig. 6.73, 119) is heavily deformed with a rounded and slightly faceted cross-section and an inside forging seam. One end is flattened and bent outwards. The other end is broken. As at the other rings only parts of the blue to green patina remained. One sample, Val5a was taken from one third of the ingot, including the forging seam. The second sample, Val5b, was taken from the fracture.

The ingot torque Val5 consists of ingot torque metal with 1.9 to 2 % arsenic, 1.3 to 1.5 % antimony, 1 % silver, and 0.1 % bismuth (Table B, p. 208). Due to the nickel content of 0.02 % sample Val5a was allocated to the Stuttgart material class C2D, while sample Val5b can be regarded as fahlore metal C2.

#### **Metallography**

**Val5a** The metallographic section of sample Val5a (Fig. 6.74, p. 120) shows an inclusion-rich single phase microstructure similar to Val2a. Bluish grey, globular inclusions smaller than 5  $\mu\text{m}$  mark the initial cast structure. In polarised light these inclusions are red to yellow. Grey, globular to elongated inclusions with sizes between 10 and 50  $\mu\text{m}$  are distributed throughout the sample. In polarised light they are red to yellow, similar to the very small inclusions. Similar as in sample Val2a, some two-phase, globular to elongated inclusions with sizes of up

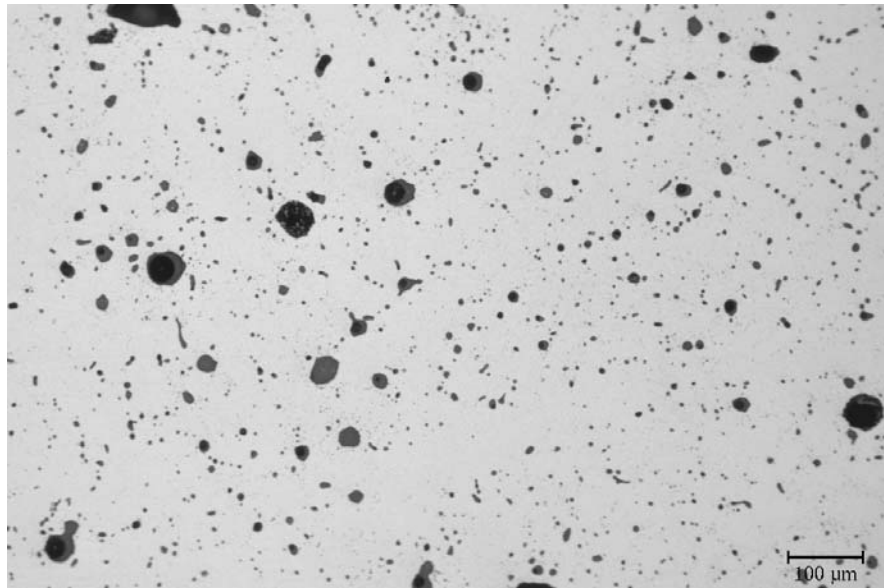


**Figure 6.74:** Val5a, metallographic section. The sample shows a single phase, inclusion-rich microstructure similar to Val2a.

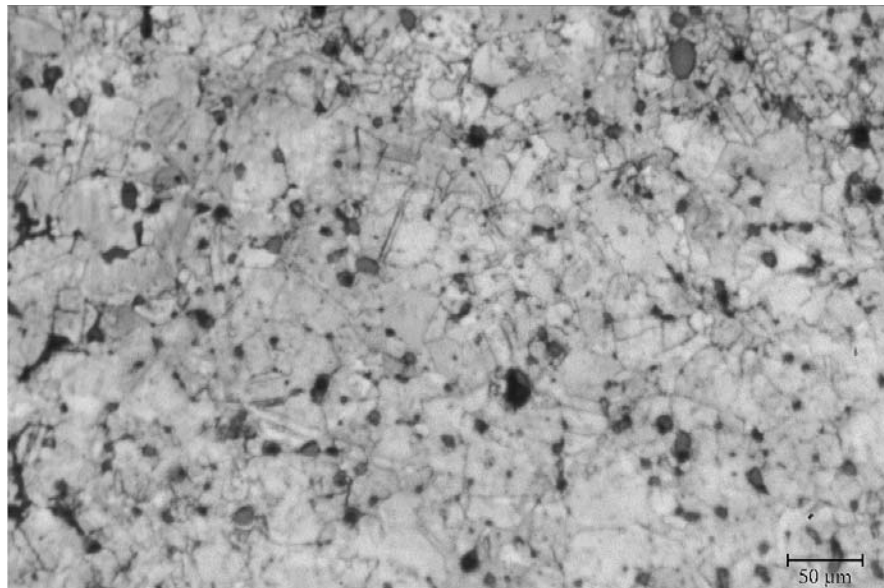


**Figure 6.75:** Val5a, metallographic section etched with NH<sub>3</sub>/H<sub>2</sub>O<sub>2</sub>. The etching reveals a recrystallisation structure overlapping with the initial dendritic cast structure.

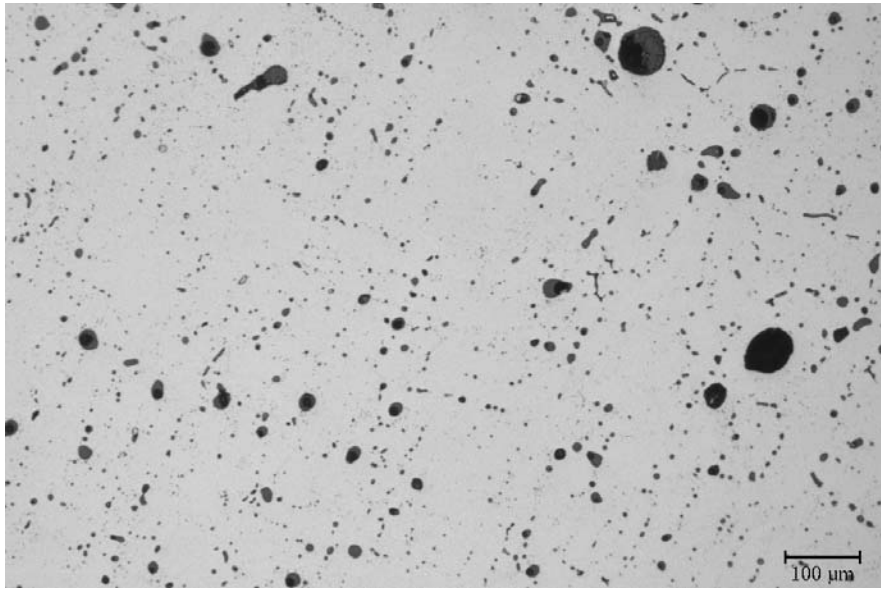


**Figure 6.76:** Val5b, metallographic section. The sample shows a single phase, inclusion-rich microstructure similar to sample Val5a

to 50  $\mu\text{m}$  were found. Bluish grey dendritic structures are set within a grey matrix. In polarised light these inclusions have a red colour.

The sample etched with ammonia/hydrogen peroxide (Fig. 6.75, p. 120) displays a recrystallisation structure with grain sizes of up to 50  $\mu\text{m}$ . Remnants of the original dendritic cast structure are still preserved.

Sample Val5a had a core hardness of about 68 HV0.2 which increased towards the surface up to 78 HV0.2 (Table B.3, p.209).

**Val5b** The sample from the broken end (Figs. 6.76, p. 121 and B.22, p. 228) shows a single phase microstructure similar to sample Val5a. The same inclusion types occur. The initial cast structure is marked by bluish grey, globular inclusions with sizes below 5  $\mu\text{m}$ . Larger grey inclusions are found mainly along grain boundaries. In polarised light both types have red to yellow colours. Two-phase inclusions of about 50  $\mu\text{m}$  are evenly distributed throughout the sample cross-section.

The metallographic section etched with ammonia/hydrogen peroxide has a recrystallised structure overlapping with the initial cast structure.

For sample Val5b from the broken end higher hardness values than those of

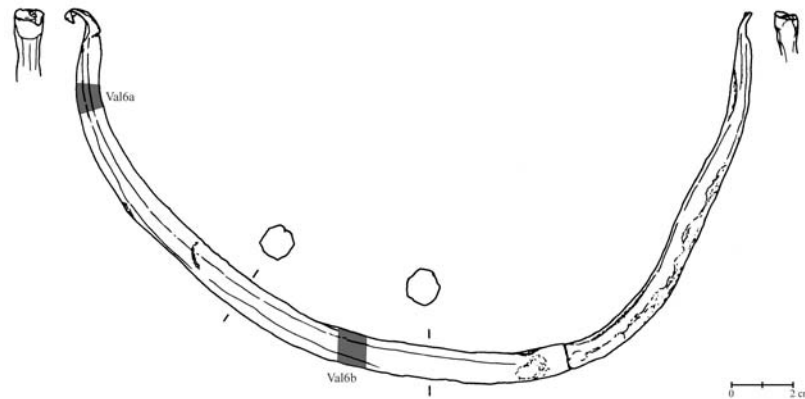


**Figure 6.77:** Ingot torque Val6 with sample locations.

sample Val5a were determined. The low load hardness increases from 71 HV0.2 in the centre of the sample to 89 HV0.2 at the surface (Table B.3, p.209).

### Microanalysis

Electron microprobe analyses show, that the small bluish grey to grey inclusions are oxides with variable amounts of copper, arsenic, and antimony (Table B.16, p. 228). The larger grey inclusions have similar compositions. These inclusions can be considered as copper arsenate and copper antimonate. The bluish grey part of the two-phase inclusions represents impure copper oxide.

### 6.10.6 Ingot torque Val6

The ingot torque Val6 is heavily deformed and broken, its two parts were joined together. The cross-section is rounded with a inside forging seem, the flattened ends are bent outwards. As reported from the other ingots from Valley, the patina is partly flaked off. The samples were taken from one part of the ingot torque. Sample Val6a was taken close to the end and sample Val6b from the middle of the ingot (Fig. 6.77, 122).

The ingot torque Val6 is made of ingot torque metal with 1.4 to 1.6 % arsenic, 1.2 to 1.3 % antimony, 0.4 to 0.5 % silver, and 0.02 to 0.03 % bismuth (Table B, p. 208). These samples consist of fahlore metal C2C after the classification scheme of Junghans et al. (1968b).

## Metallography

**Val6a** The sample Val6a shows a single phase microstructure similar to Val2b (Figs. 6.78, p. 124 and B.23, p. 229). Bluish grey, globular inclusions with sizes below 5  $\mu\text{m}$  are found along the grain boundaries. In some cases, they form small eutectic domains within the matrix. Grey, globular to elongated inclusions with sizes ranging between 10 and 50  $\mu\text{m}$  are also distributed along the grain boundaries. In polarised light both inclusion types are red to yellow. The two-phase inclusions have a similar structure than those in the Aschering and Gammersham samples. Within the grey inclusions bluish grey to light blue globular and angular internal structures were found. These two-phase inclusions have sizes of about 50  $\mu\text{m}$ . In polarised light they appeared in red colour. In the centre of the sample pores with diameters of up to 100  $\mu\text{m}$  and sometimes oxidised internal surfaces occur. With closed aperture diaphragm the recrystallisation structure is visible (Fig. 6.79, p. 124).

The metallographic section etched with ammonia/hydrogen peroxide shows a dendritic cast structure overlapping with a recrystallised structure. A preferred direction of the dendrites has not been observed. The sizes of the recrystallised grains are below 50  $\mu\text{m}$ .

By contrast to the other highly alloyed ingots, the low load hardness of the sample Val6a is relatively low. From the centre towards its surface values of 58 to 78 HV0.2 were measured (Table B.3, p. 209).

**Val6b** The metallographic section (Fig. 6.80, p. 125) shows a single phase microstructure similar to sample Val6a. Very small, bluish grey, globular inclusions mark the grain boundaries and triple points. Furthermore grey, globular inclusions with sizes ranging between 10 and 50  $\mu\text{m}$  are found. Both inclusion types are red to yellow in polarised light. The third inclusion type consists of two phases, a grey matrix with bluish grey internal structures. In polarised light these inclusions are red. In the centre of the sample interdendritic shrinkage and pores occur.

The sample etched with ammonia/hydrogen peroxide (Fig. 6.81, p. 125) shows the initial cast structure overlapping with a recrystallisation structure and annealing twins. The recrystallised grains have sizes ranging between 20 to 50  $\mu\text{m}$ .

The low load hardness values for sample Val6b are higher than for Val6a: 63 HV0.2 in the centre, and 84 HV0.2 close to the sample surface (Table B.3, p. 209). The hardness increase of 20 HV0.2 is comparable to that of Val6a.

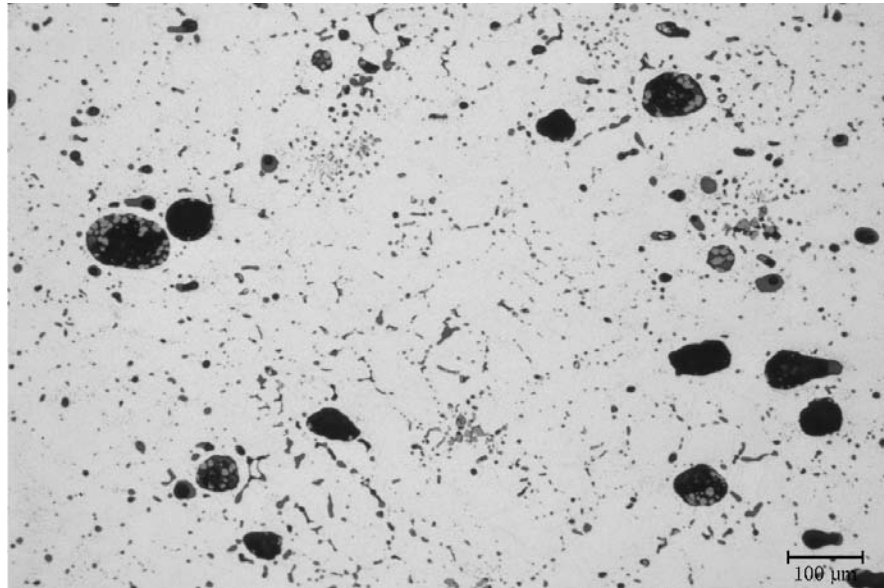


**Figure 6.78:** Val6a, metallographic section. The sample shows a single phase, inclusion-rich microstructure similar to Val2b.

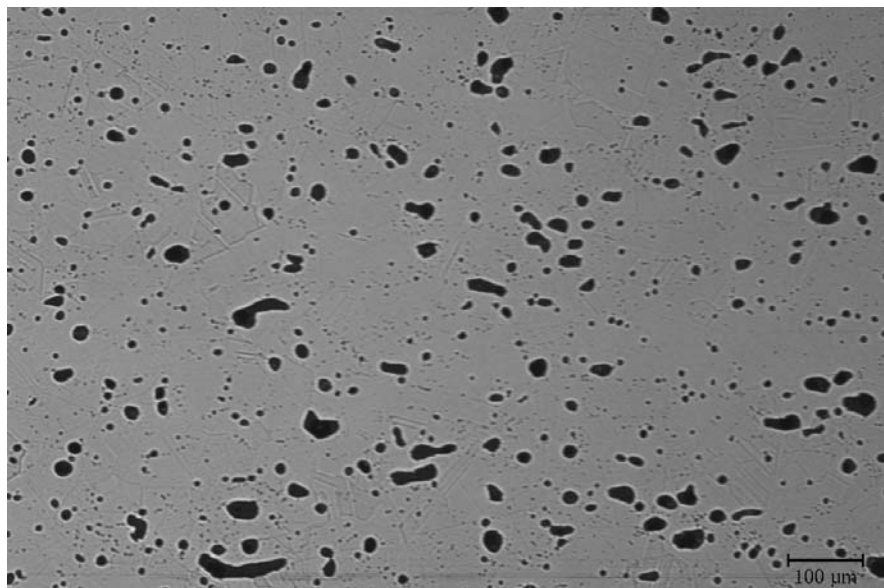


**Figure 6.79:** Val6a, metallographic section. With closed aperture diaphragm the recrystallisation structure is visible.



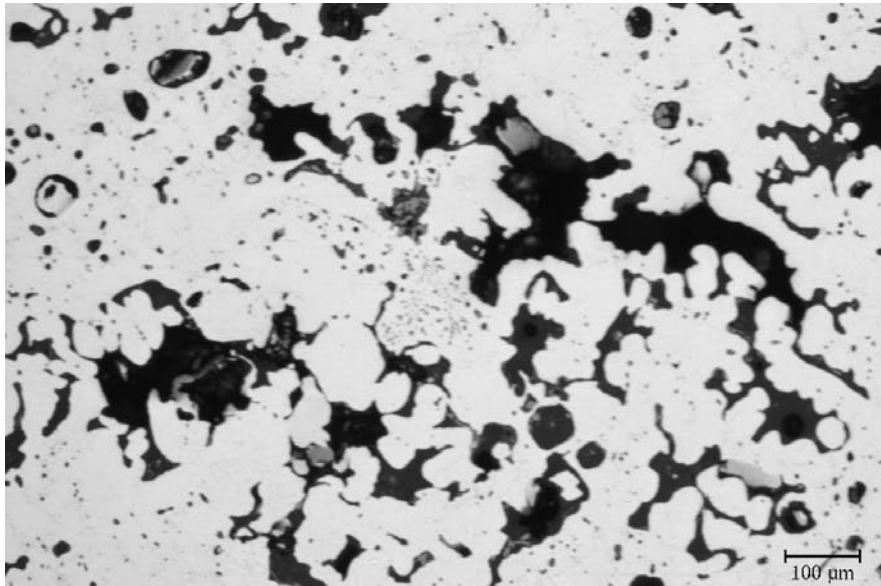


**Figure 6.80:** Val6b, metallographic section. The sample shows single phase, inclusion-rich microstructure and interdendritic shrinkage

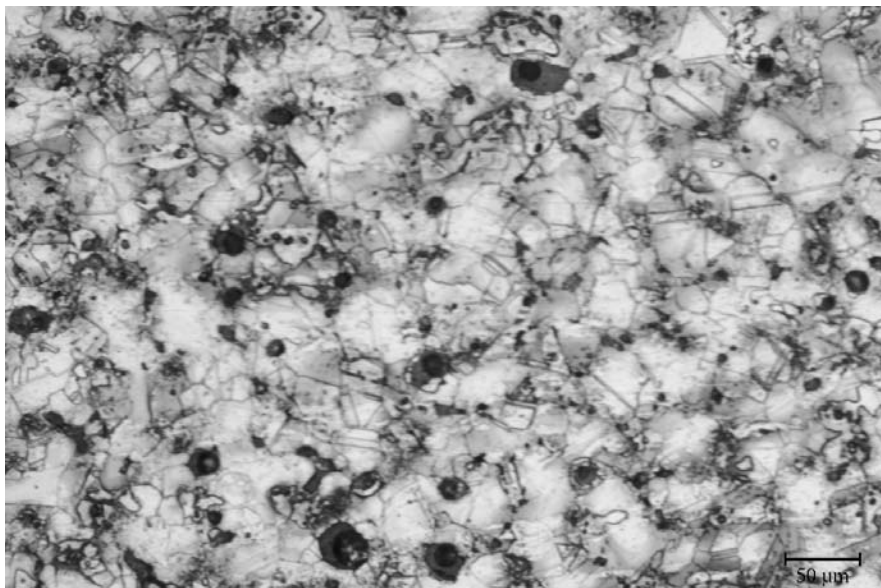


**Figure 6.81:** Val6b, metallographic section etched with  $\text{NH}_3/\text{H}_2\text{O}_2$ . Visible is an overlapping of initial cast structure with recrystallisation structure.

### Microanalysis

Electron microprobe analyses reveal, that the grey inclusions are oxides with varying amounts of copper, arsenic and antimony (Table B.17, p. 229). Hence, they can be considered as copper arsenate and copper antimonate. Based on matrix analysis about 70 % of the total arsenic, 16 % of the antimony, and 66 % of the silver contents are dissolved in the copper solid solution (cf. Tables B.2, p. 207 and B.17, p. 229). A major part of antimony and bismuth is bound to the inclusions.

## 6.11 Summary

The investigated ingot torques can be divided into two groups: rings and fragments made of low-impurity copper and items made of ingot torque metal.

The first group comprises one sample from Bernhaupten (Ber1), both fragments from Hechendorf and three samples from Valley (Val1, Val3, and Val4). All investigated ingot torques made of low-impurity copper have inclusions of copper sulfide  $\text{Cu}_2\text{S}$ . The samples Val1 and Val4 further contain eutectic structures of copper oxide. The etched metallographic sections have recrystallised structure with grain sizes ranging between 50 and 100  $\mu\text{m}$ .

The ingot torques and fragments made of the ingot torque metal came from Aschering, Bernhaupten (Ber3), Gammersham, Hohenlinden-Mühlhausen, Mühlendorf, Pfedelbach, and Valley (Val2, Val5 and Val6). In all cases, the samples contain oxide inclusions which can be considered as copper arsenate and copper antimonate. Several samples (Asch1, Asch2, Gam1, Gam2, Pfe10, Pfe14, Rad2, Rad4, Val2, Val5 and Val6) have two-phase inclusions consisting of copper arsenate and copper antimonate with internal structures of copper oxide. The samples of the ingot torques from Aschering (Asch1 and Asch2), Gammersham (Gam1 and Gam2) and Pfedelbach (Pfe10) have a two-phase microstructure. In the metallographic sections a pale blue phase was dispersed along the grain boundaries of the copper solid solution. Electron probe microanalysis revealed that this phase is  $\text{Cu}_3(\text{As,Sb})$ , in some cases containing silver. The etched metallographic sections show an overlap of remnant coring and recrystallisation structure with annealing twins. A few samples contain grains with slip traces (Ber3, Gam2, Müh1).

Comparisons of bulk and matrix analyses imply that the main alloying elements arsenic and antimony are depleted in the matrix (Fig. 6.82, p. 127). For an-

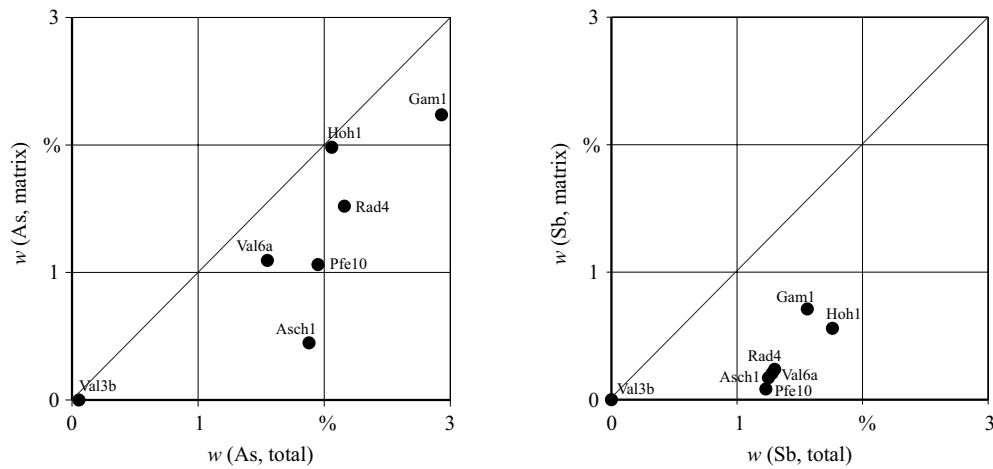


**Figure 6.82:** Comparison of the arsenic and antimony contents of the matrix of selected samples with their bulk analysis. The bulk analyses were performed using EDXRF, the matrix analyses by utilising EPMA. The diagonal line in the diagram marks the 100 % solubility limit of the elements in the matrix.

timony this effect is more pronounced than for arsenic. Silver is usually dissolved in the copper matrix, whereas bismuth occurs in the inclusions. The fraction of arsenic, antimony, and silver dissolved in the copper matrix varies between 25 % (sample Asch1) and 84 % (sample Hoh1). Since the mechanical properties of a material depend mainly on the matrix, samples with similar bulk compositions may show a very different mechanical and working behaviour.

The copper samples have low load hardness values ranging between 51 and 84 HV0.2 in the centre and between 61 and 91 HV0.2 close to the surface. The highest values are derived from sample Hech2, which shows a distinct copper-copper sulfide eutectic. The low load hardness values of the samples of ingot torque metal are between 59 and 96 HV0.2 in the centre and between 64 and 131 HV0.2 close to the surface. The hardness seems to show less variations, than expected from the different composition of the ingot torques.



# Chapter 7

## Reference material and material testing

As shown in the previous chapter, it seems that the ingot torques were produced by a standardised technology, independent of the material. This begs the questions, whether the Bronze Age metalworker did not adapt different technologies for different materials or if he was able to distinguish between different alloys. The latter was certainly possible considering that the mechanical and technological properties change significantly with the composition of the metal.

In order to investigate the dependence of the mechanical and technological properties on the composition, reference materials similar to that of the ingot torques were prepared (Fig. 7.1, p. 130). In contrast to the ingot torque metal, the reference material was only alloyed with arsenic, antimony and bismuth. Other elements occurring in fahlore metals, such as silver, iron and nickel, were ignored.

### 7.1 Preparation of reference materials

In order to produce sufficient material for mechanical testing, charges of 8 kg for each reference material were cast in the shape of rods with 2 cm diameter and about 20 cm length.

The first reference material (Cu, Cu As<sub>0.5</sub> Sb<sub>0.5</sub> Bi<sub>0.1</sub>, Cu As<sub>2</sub> Sb<sub>2</sub> Bi<sub>0.1</sub>; see also Table C.1, page 234) was bottom-cast in sand moulds with central riser and baseplate. Prior to casting the sand moulds were dried and pre-heated up to 180°C in order to drive out any residual water inside the moulds which is one reason for porous castings. Although the sand of the moulds was bound with synthetic

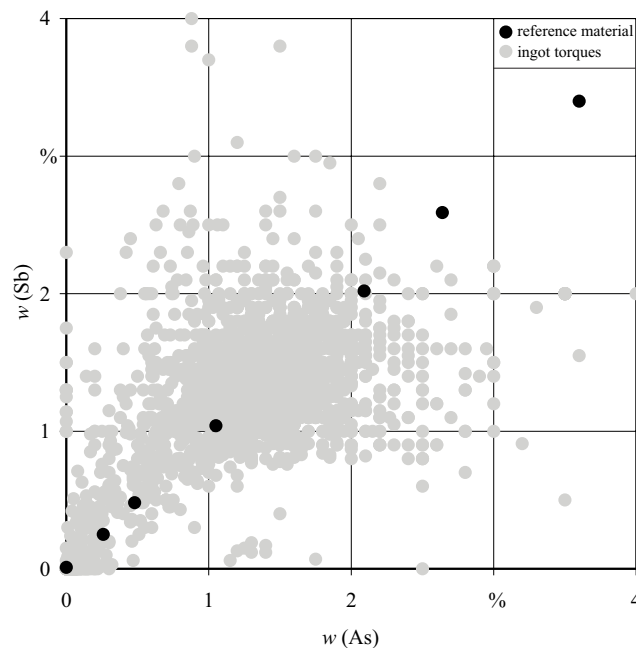


**Figure 7.1:** Composition of reference alloys (black dots) compared with the composition of ingot torques (grey dots). The composition of the reference materials is taken from Table 7.1, p. 132, the compositions of ingot torques are taken from the SMAP database (1999) (cf. Fig. 2.3, p. 14).

resin to increase their mechanical stability they had to be embedded in sand. The electrolytic copper was melted in a clay-graphite-crucible in an induction furnace whereby deoxidation was achieved by inserting a graphite rod for about 1 hour. Arsenic, antimony and bismuth were added as pure metals to the melted copper. In order to avoid evaporation, the melt was covered with glass and the alloying elements, wrapped in copper foil, were pushed with a bell under the surface of the melt. The steel bell was covered with  $\text{Al}_2\text{O}_3$  in order to prevent contamination of the copper melt.

In the second casting series the Cu As4 Sb4 Bi0.1 reference material was prepared similar to the previous alloys from the pure metals. In contrast to the first charges, the electrolytic copper was remelted and degassed in a vacuum furnace. This copper was subsequently melted in a clay-graphite-crucible in an induction furnace with deoxidation below a charcoal layer for about 1 hour. Since the binder in the moulding sand decomposed during casting, the first casts were very porous and could not be used for material testing. Therefore, the technology was changed

to direct (top) casting in graphite moulds (Table C.1, page 234). The other reference alloys (Cu As<sub>0.25</sub> Sb<sub>0.25</sub> Bi<sub>0.1</sub>, Cu As<sub>1</sub> Sb<sub>1</sub> Bi<sub>0.1</sub>, and Cu As<sub>3</sub> Sb<sub>3</sub> Bi<sub>0.1</sub>, see Tab. C.1, page 234) were cast a massive graphite mould and in graphite tubes embedded in sand. For these alloys the remaining (scrap) metal from the previous castings, i.e. the base plate, the riser and material with shrinkage and pores, was used as a pre-alloy.

After cooling, the cast was removed from the mould and cleaned. In the case of the sand castings the rods were cut from the base plate. The soundness of the material was controlled by X-radiography of the rods. If the cast was not acceptable, i.e. there was not enough material free of pores and shrinkage, the alloy was remelted and cast again. For example, the pure copper had to be remelted and deoxidised several times in order to obtain a satisfactory sound cast (Table C.1, p. 234). With increasing amounts of arsenic and antimony the castability improved.

## **7.2 Metallographic investigation and analysis of the cast material**

### **7.2.1 X-ray fluorescence analysis**

The final composition of the cast alloys was determined on flat samples by energy dispersive X-ray fluorescence analysis (Table 7.1, p. 132).

The sand cast alloys, which were prepared from pure metallic stock, show a good correspondence between the composition calculated from added metals and the one obtained. The material with the highest amount of alloying elements Cu As<sub>4</sub> Sb<sub>4</sub> Bi<sub>0.1</sub> shows a significant evaporation loss of arsenic and antimony. This alloy was remelted and cast five times, since the binder in the moulding sand decomposed and caused a very porous cast. The composition of the reference alloy Cu As<sub>3</sub> Sb<sub>3</sub> Bi<sub>0.1</sub> also differs from the calculated one. Since Cu As<sub>4</sub> Sb<sub>4</sub> Bi<sub>0.1</sub> was used as a pre-alloy for this material the loss of alloying elements could not be compensated completely.

**Table 7.1:** EDXRF-analyses of the reference material. Given are the mass fractions  $w$  of arsenic, antimony and bismuth. The names of the alloys are based on the calculated composition.

reference material	$w(\text{As})$ [%]	$w(\text{Sb})$ [%]	$w(\text{Bi})$ [%]
Cu	< 0.005	0.01	< 0.005
Cu As0.25 Sb0.25 Bi0.1	0.26	0.25	0.10
Cu As0.5 Sb0.5 Bi0.1	0.48	0.48	0.09
Cu As1 Sb1 Bi0.1	1.05	1.04	0.11
Cu As2 Sb2 Bi0.1	2.09	2.02	0.12
Cu As3 Sb3 Bi0.1	2.64	2.59	0.09
Cu As4 Sb4 Bi0.1	3.60	3.40	0.09

## 7.2.2 Copper

### Metallography

The metallographic section of the pure copper (Figs. 7.2, p. 133 and C.1, p. 235) shows very few, finely distributed bluish grey inclusions with sizes between 5 and 10  $\mu\text{m}$  in the copper matrix. These inclusions are red in polarised light. In the centre of the rod a small string of a copper-copper oxide eutectic is visible.

### Microanalysis

Electron microprobe analyses of selected inclusions have shown that the bluish grey inclusions consist mainly of copper oxides  $\text{CuO}$  and  $\text{Cu}_2\text{O}$  (Table C.2, p. 235). Furthermore, about 1 % sulfur was found in the inclusions.

## 7.2.3 Cu As0.25 Sb0.25 Bi0.1

### Metallography

The metallographic section of the reference alloy Cu As0.25 Sb0.25 Bi0.1 (Figs. 7.3, p. 134 and C.2, p. 236) shows a single-phase microstructure. Bluish grey to grey inclusions of about 5  $\mu\text{m}$  are distributed along the grain boundaries. In polarised light these inclusions appear red to yellow. In the centre of the sample



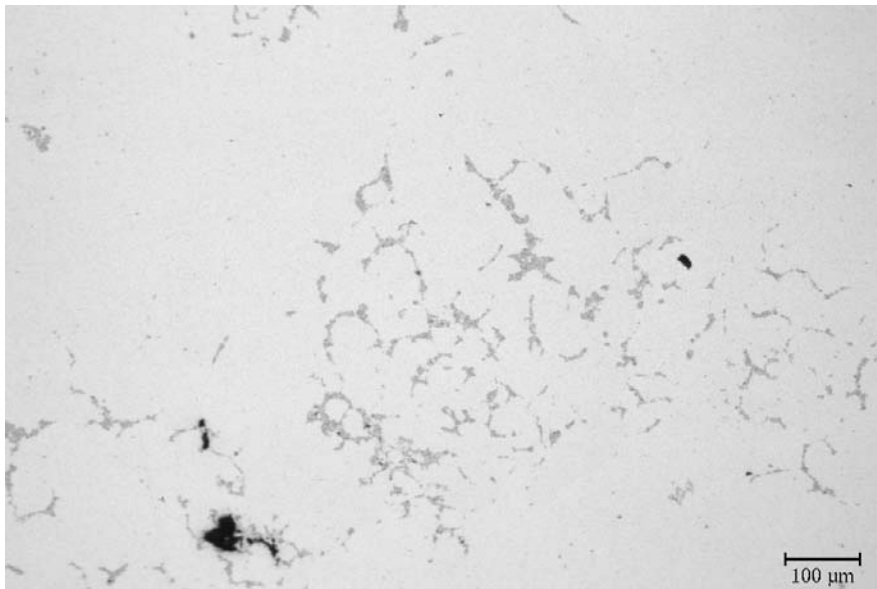


**Figure 7.2:** Cu, metallographic section. Shown is a single-phase microstructure with copper-copper oxide eutectic inclusions in the centre of the sample.

the inclusions have sizes of up to 20  $\mu\text{m}$ . Some of them appear two-phased, grey with light blue internal structures (Fig. 7.4, p. 134).

The metallographic section etched with ammonia/hydrogen peroxide shows in polarised light about 1 mm big areas with the same orientation in microstructure. Close to the surface these grains are columnar, towards the centre they become more equiaxed.

### Microanalysis

Electron microprobe analysis revealed that the grey inclusions are oxides (Table C.3, p. 236). Apart from copper, they contain arsenic and antimony so that, based on the analyses, a mixture of  $\text{CuO}$ ,  $\text{Cu}_2\text{O}$ ,  $\text{As}_2\text{O}_5$  and  $\text{Sb}_2\text{O}_5$  can be assumed. Bismuth is concentrated in the inclusions.

As Ruhrmann (1925) and Hanson and Marryat (1927) noticed, with increasing arsenic content  $\text{Cu}_2\text{O}$  is replaced by a copper arsenate  $\text{Cu}_2\text{O}\cdot\text{As}_2\text{O}_5$ . Ruhrmann (1925) further stated that in copper containing less than 0.31 % arsenic and less than the eutectic amount of oxygen only  $\text{Cu}_2\text{O}$  is formed. Taking into account that the reference alloy contains in sum 0.5 % arsenic and antimony, a kind of copper arsenate/antimonate can be assumed.



**Figure 7.3:** Cu As<sub>0.25</sub> Sb<sub>0.25</sub> Bi<sub>0.1</sub>, metallographic section. Visible is a single-phase microstructure with inclusions along the grain boundaries.

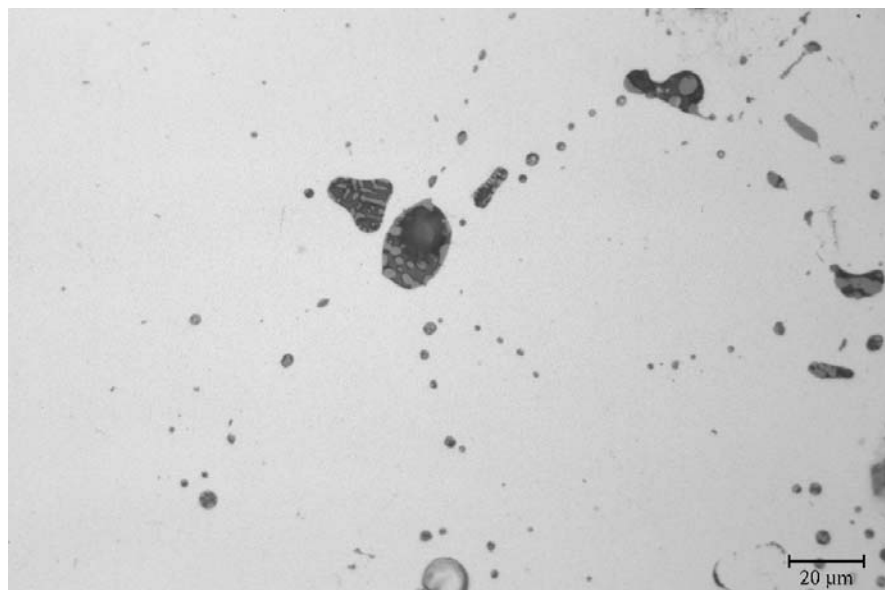


**Figure 7.4:** Cu As<sub>0.25</sub> Sb<sub>0.25</sub> Bi<sub>0.1</sub>, metallographic section. Shown are two-phase inclusions in the centre of the sample.

The EPMA line scan over the sample cross-section (Fig. C.3, p. 237) shows much lower arsenic and antimony values than the bulk analysis by EDXRF. About 23 % of the arsenic and only about 12 % of the antimony are dissolved in the copper.

#### **7.2.4 Cu As<sub>0.5</sub> Sb<sub>0.5</sub> Bi<sub>0.1</sub>**

##### **Metallography**

The metallographic section of the Cu As<sub>0.5</sub> Sb<sub>0.5</sub> Bi<sub>0.1</sub> alloy (Figs. 7.5, p. 136 and C.4, p. 238) shows a single phase microstructure. In the cross-section of the sample a considerable amount of microporosity was found. Two inclusion types were found. The first type are grey, globular to unevenly shaped inclusions of about 20  $\mu\text{m}$  which appear red to yellow in polarised light. The second inclusion type appears bluish-grey in bright field illumination and grey in polarised light.

The metallographic section etched with ammonia/hydrogen peroxide (Fig. 7.6, p. 136) shows in polarised light a coarse dendritic microstructure with a secondary dendrite arm spacing of about 50  $\mu\text{m}$ . Furthermore, areas of about 1 mm with the same microstructural orientation are visible.

##### **Microanalysis**

Electron microprobe analyses have shown that the inclusions are mainly copper oxides with small amounts of arsenic and antimony (see Table C.4, p. 238). Since the inclusions were rather small, not only the inclusions but also parts of the matrix were analysed by EPMA. Therefore, the composition of the inclusions could not be calculated. The bluish-grey inclusions contained up to 2 % sulfur. Similar observations were made with the copper specimen. Since only the inclusions in the sand cast material contained small amounts of sulfur, it is presumed that it originates from the organic binder of the moulding sand.

The EPMA line scan over the sample cross section (Fig. C.5, p. 239) revealed that about 40 % of the arsenic, 70 % of the antimony and 13 % of the bismuth are dissolved in the copper matrix.

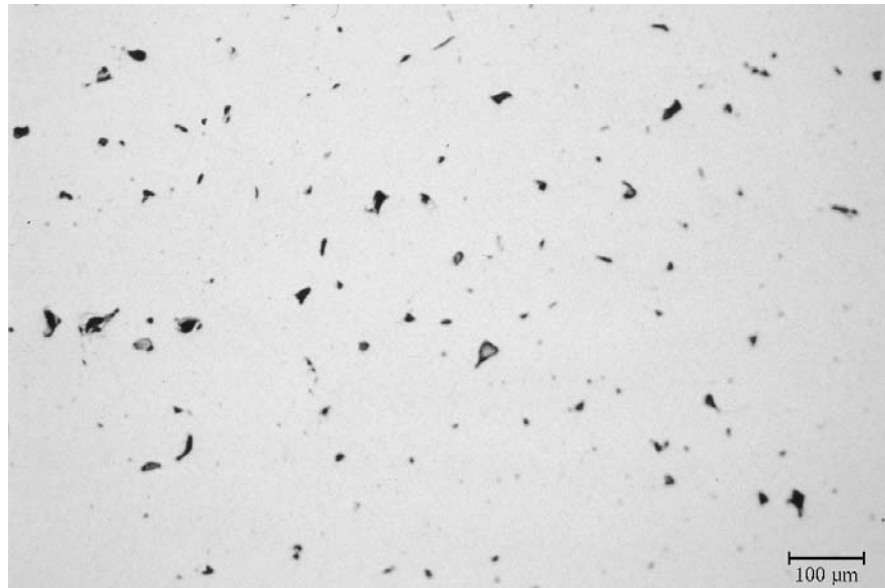


**Figure 7.5:** Cu As<sub>0.5</sub> Sb<sub>0.5</sub> Bi<sub>0.1</sub>, metallographic section. Visible is a single-phase microstructure with regularly distributed inclusions.

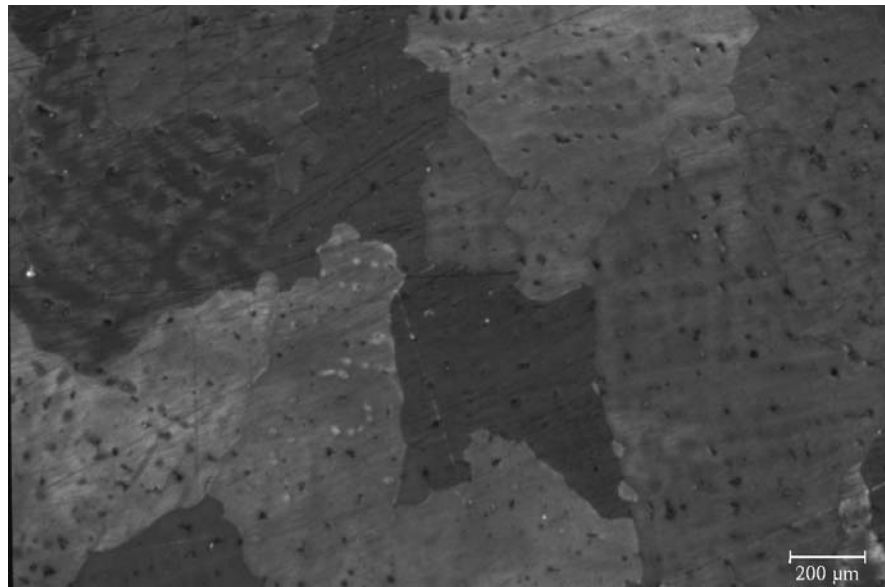


**Figure 7.6:** Cu As<sub>0.5</sub> Sb<sub>0.5</sub> Bi<sub>0.1</sub>, metallographic section etched with NH<sub>3</sub>/H<sub>2</sub>O<sub>2</sub>. In polarised light the sample shows a dendritic microstructure and areas with the same microstructural orientation.

### 7.2.5 Cu As1 Sb1 Bi0.1

#### Metallography

The metallographic section of the reference alloy Cu As1 Sb1 Bi0.1 (Figs. 7.7, p. 138 and C.6, p. 240) has a two-phase microstructure. Small pale blue islands of a second phase were found in the centre of the sample. Grey, globular inclusions with sizes of up to 50  $\mu\text{m}$  are regularly distributed over the sample cross-section. Towards the centre of the cast rod some bigger inclusions occur. In polarised light both inclusion types appear red to yellow.

The metallographic section etched with ammonia/hydrogen peroxide (Fig. 7.8, p. 138) shows a dendritic structure with secondary dendrite arm spacings of about 20  $\mu\text{m}$ . In polarised light areas with the same microstructural orientation are visible. These areas are smaller than those in the Cu As0.5 Sb0.5 Bi0.1 reference alloy.

#### Microanalysis

Electron microprobe analyses (Table C.5, p.240) have shown that the grey inclusions consist of oxides of copper, arsenic, and antimony. Similar to the reference alloy Cu As0.25 Sb0.25 Bi0.1, a mixture of copper arsenate and copper antimonate can be assumed.

The matrix contents of the alloying elements determined in the EPMA line scan is much lower than the results from the bulk XRF analysis (Fig. C.7, p. 241). About 50 % of the total arsenic amount and 23 % of the antimony were found in the matrix. Bismuth is bound to the inclusions.

### 7.2.6 Cu As2 Sb2 Bi0.1

#### Metallography

In the metallographic section of the reference alloy with 2 % arsenic and antimony (Figs. 7.9, p. 139 and C.8, p. 242) a two-phase microstructure is visible. The second, pale blue phase is much more pronounced than in sample Cu As1 Sb1 Bi0.1. A few grey, globular to unevenly shaped inclusions smaller than 10  $\mu\text{m}$  were found. In polarised light they appear grey. In the centre of the sample there is some interdendritic shrinkage.

The sample etched with ammonia/hydrogen peroxide (Fig. 7.10, p. 139) shows more clearly the cast structure with coarse dendrites. The secondary dendrite

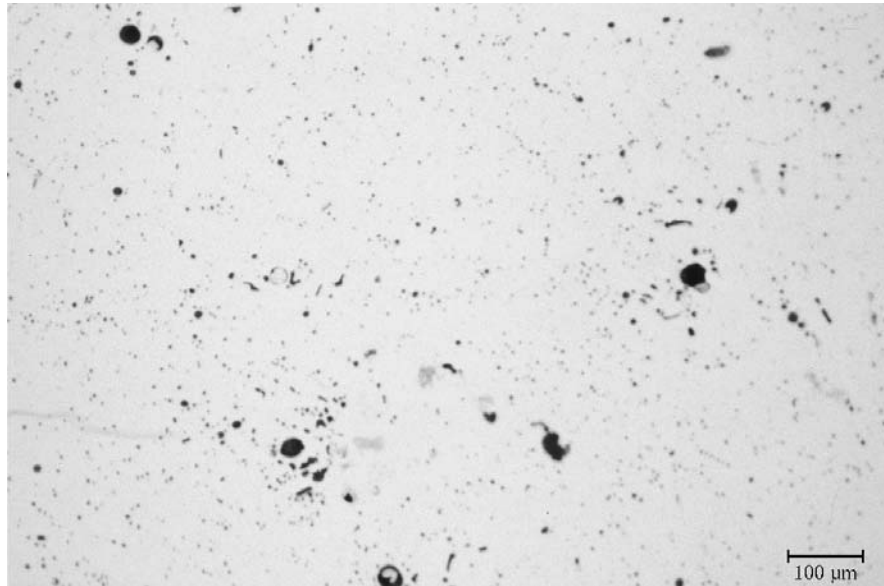


**Figure 7.7:** Cu As1 Sb1 Bi0.1, metallographic section. Shown is a two-phase microstructure with regularly distributed inclusions.

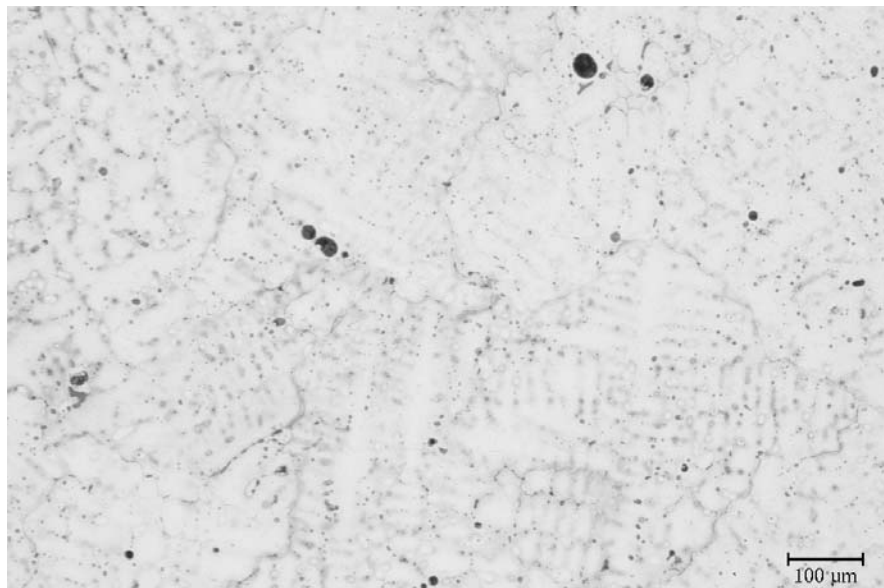


**Figure 7.8:** Cu As1 Sb1 Bi0.1, metallographic section etched with  $\text{NH}_3/\text{H}_2\text{O}_2$ . The sample shows a dendritic microstructure.

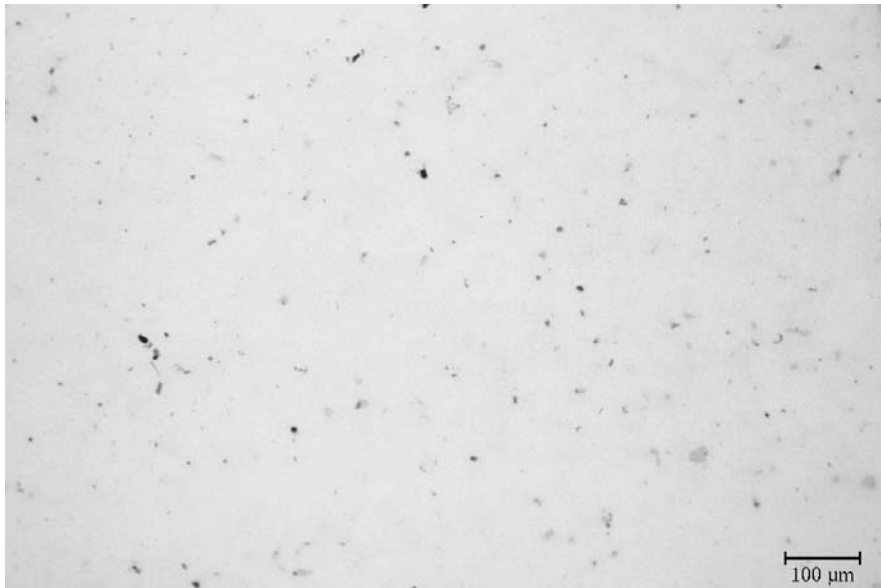


**Figure 7.9:** Cu As<sub>2</sub> Sb<sub>2</sub> Bi<sub>0.1</sub>, metallographic section. Visible is a two-phase microstructure with few inclusions.

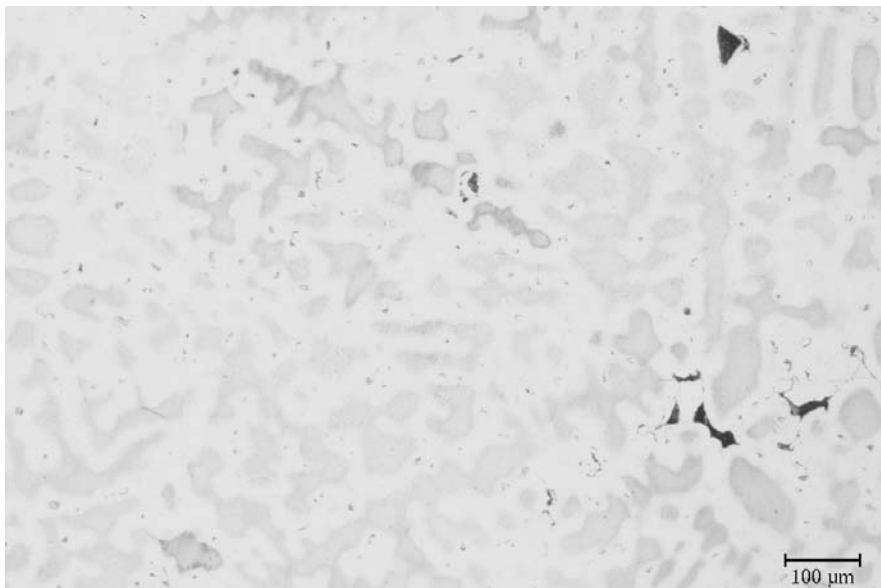


**Figure 7.10:** Cu As<sub>2</sub> Sb<sub>2</sub> Bi<sub>0.1</sub>, metallographic section etched with NH<sub>3</sub>/H<sub>2</sub>O<sub>2</sub>. The sample shows a dendritic microstructure.

arm spacings are about  $50\ \mu\text{m}$ , which is similar to that of the other sand-cast material. The second phase was found in the interdendritic space. In polarised light areas with the same microstructural orientation are visible. These areas have sizes ranging between 0.5 and 1 mm, i.e. they are smaller than those of the lower alloyed sand cast material.

### Microanalysis

Electron microprobe analyses show that the pale blue phase contains copper, antimony and small amounts of arsenic (Table C.6, p. 242). This phase can be considered as impure  $\delta$ -phase  $\text{Cu}_9\text{Sb}_2$  with some arsenic. But it could also be a real ternary intermetallic phase  $\text{Cu}_3(\text{As},\text{Sb})$ , as described by several authors (Tedenac, 1994; Hein and Bombach, 1980; Northover, 1998). The grey inclusions consist of copper oxide with up to 2 % sulfur. A similar composition was observed in the samples of copper and the reference alloy Cu As0.5 Sb0.5 Bi0.1, i.e. in the sand cast material.

Similar to the other samples, the matrix contents of the alloying elements in the Cu As2 Sb2 Bi0.1 reference alloy is much lower than the results from the bulk XRF analysis would suggest (Fig. C.9, p. 243). The EPMA line scan over the sample cross section revealed that about 37 % of the arsenic, 64 % of the antimony and 17 % of the bismuth are dissolved in the copper solid solution and the ternary phase.

## 7.2.7 Cu As3 Sb3 Bi0.1

### Metallography

The metallographic section of the reference alloy Cu As3 Sb3 Bi0.1 (Figs. 7.11, p. 142 and C.10, p. 244) shows a two-phase microstructure with a copper matrix and a second, pale blue phase. Some grey, globular inclusions with diameters of about  $5\ \mu\text{m}$  were found. In polarised light these particles appear orange to yellow in colour.

In the etched metallographic section (Fig. 7.12, p. 142) a fine dendritic microstructure with the second phase in the interdendritic space is visible. The secondary dendrite arm spacings are about  $20\ \mu\text{m}$ . Areas with the same microstructural orientation are visible in polarised light. Compared to the other alloys their size of about 0.5 mm is rather small.



### Microanalysis

Electron microprobe analyses have shown, that the second, pale blue phase is a ternary intermetallic phase  $\text{Cu}_3(\text{As,Sb})$  (Table C.7, p. 244). The ratio of arsenic and antimony amount fractions within the phase is about 1:2. The grey inclusions consist of oxides of copper, antimony, and small amounts of arsenic, i.e. they are mainly copper antimonate.

The EPMA line scan over the sample cross-section (Fig. C.11, p. 245) shows that the alloying elements arsenic and antimony are diminished in the matrix. About 60 % of the total arsenic content, 50 % of the antimony and 6 % of the bismuth are found in the copper solid solution and the ternary phase.

### 7.2.8 Cu As<sub>4</sub> Sb<sub>4</sub> Bi<sub>0.1</sub>

#### Metallography

The metallographic section of the Cu As<sub>4</sub> Sb<sub>4</sub> Bi<sub>0.1</sub> reference alloy (Figs. 7.13, p. 143 and C.12, p. 246) has a two-phase microstructure similar to that of the Cu As<sub>3</sub> Sb<sub>3</sub> Bi<sub>0.1</sub> reference material. The islands of the second, pale blue phase are surrounded by a light blue shaded structure which becomes more clearly in polarised light. In contrast to the lower alloyed graphite cast material the sample Cu As<sub>4</sub> Sb<sub>4</sub> Bi<sub>0.1</sub> contains more inclusions. The dark grey, globular particles with sizes below 5  $\mu\text{m}$  appear red to yellow in polarised light. The large amount of inclusions, comparable to the sand cast material, results from oxygen absorption during the repeated casting. The first charges of the Cu As<sub>4</sub> Sb<sub>4</sub> Bi<sub>0.1</sub> reference alloy were cast in a sand mould, for the final and satisfactory cast a graphite mould was used.

The etched metallographic section (Fig. 7.14, p. 143) shows a very fine dendritic structure with secondary dendrite arm spacings of about 10  $\mu\text{m}$ .

#### Microanalysis

The pale blue phase was determined by EPMA as a ternary phase of copper, arsenic and antimony (Table C.8, p. 246). It can be considered as  $\text{Cu}_6\text{AsSb}$ , as described by Tedenac (1994). The dark grey inclusions are copper and antimony oxides with a low arsenic content. They can be seen as copper antimonate.

The EPMA line scan over the sample cross-section (Fig. C.13, p. 247) revealed that about 55 % of the total arsenic and antimony content and 22 % of the bismuth are dissolved in the copper solid solution and the ternary phase.

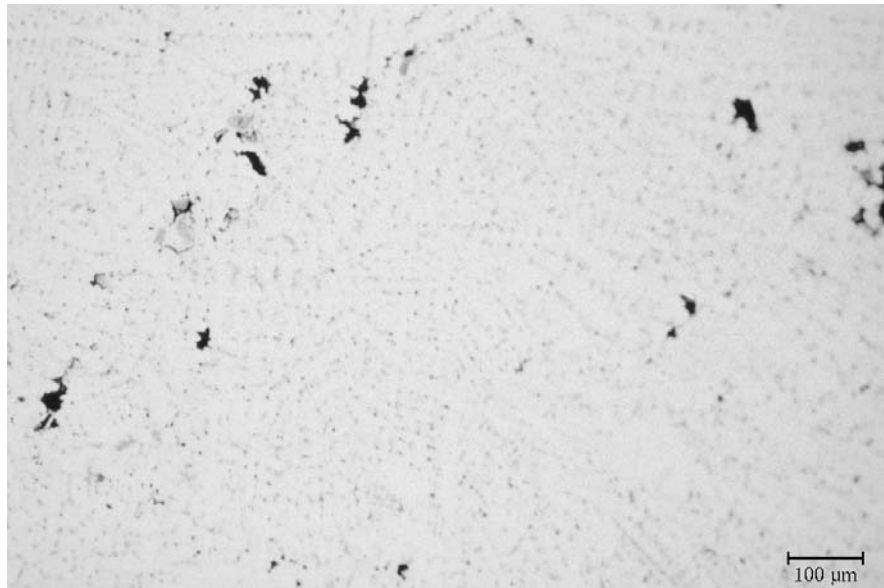


**Figure 7.11:** Cu As<sub>3</sub> Sb<sub>3</sub> Bi<sub>0.1</sub>, metallographic section. Visible is a two-phase microstructure with few inclusions.

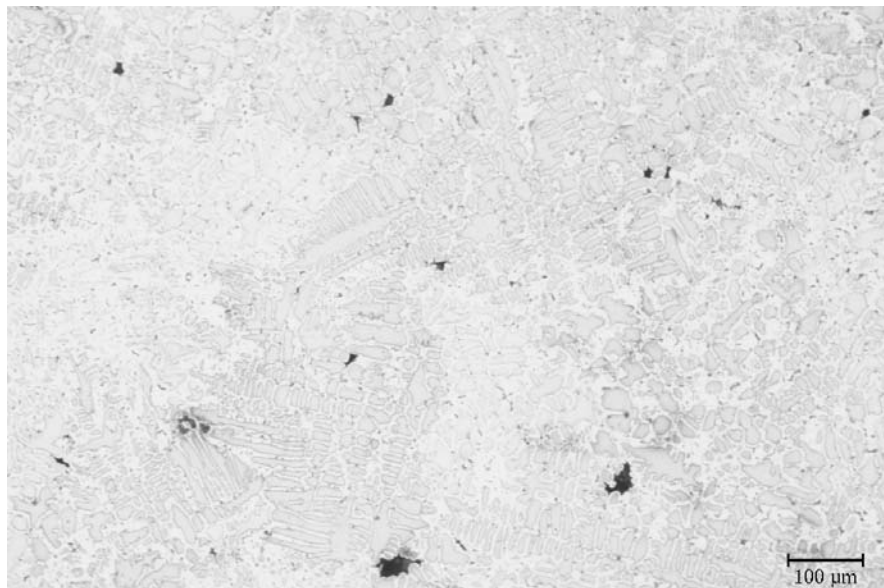


**Figure 7.12:** Cu As<sub>3</sub> Sb<sub>3</sub> Bi<sub>0.1</sub>, metallographic section etched with NH<sub>3</sub>/H<sub>2</sub>O<sub>2</sub>. The sample shows a dendritic microstructure.

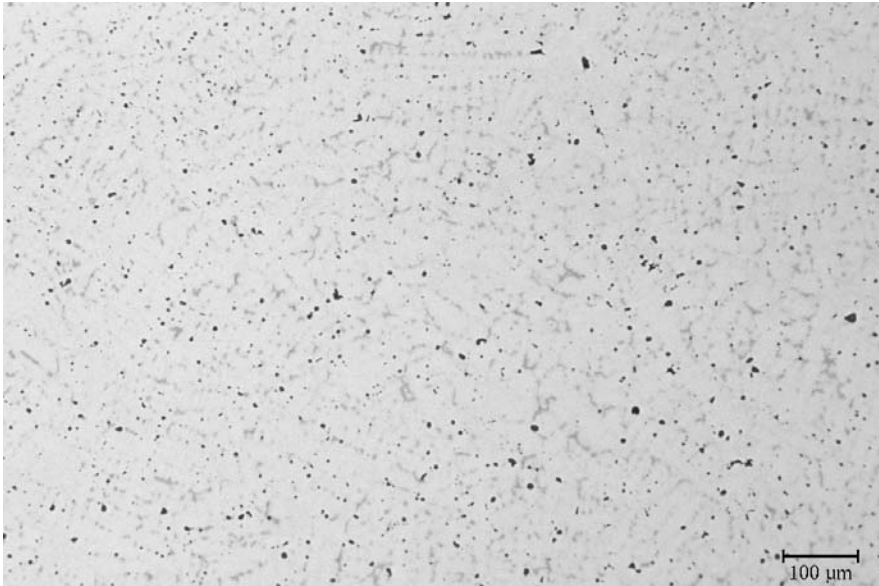


**Figure 7.13:** Cu As<sub>4</sub> Sb<sub>4</sub> Bi<sub>0.1</sub>, metallographic section. Visible is a two-phase, inclusion rich microstructure.



**Figure 7.14:** Cu As<sub>4</sub> Sb<sub>4</sub> Bi<sub>0.1</sub>, metallographic section etched with NH<sub>3</sub>/H<sub>2</sub>O<sub>2</sub>. The sample shows a dendritic microstructure.

### **7.2.9 Comparison of the reference materials with Early Bronze Age material**

The main difference between the copper reference material and the prehistoric low-impurity copper is the presence of copper sulfide inclusions in the prehistoric material. Therefore, mechanical properties of the copper reference material and the prehistoric material will not be easily comparable.

Compared to the ingot torque metal there are less oxidic inclusions in the reference alloys. The composition and size of the inclusions along the grain boundaries are comparable with those of the archaeological material. In both cases the particles consist of copper arsenate and copper antimonate. Large oxide inclusions as they are found in the Early Bronze Age material are absent in the reference material. Two-phase inclusions which are characteristic for many samples of ingot torque metal were found only in the Cu As<sub>0.25</sub> Sb<sub>0.25</sub> Bi<sub>0.1</sub> reference alloy (Fig. 7.4, p. 134). In the case of the reference material a sound cast was very important for material testing. Therefore the copper melts were deoxidised before alloying and the oxygen availability was kept as low as possible during the whole process. Hence, oxide formation was suppressed.

The formation of a second phase with copper, arsenic and antimony was observed in both the prehistoric and the reference material. In both cases this ternary intermetallic phase was formed far below the eutectic composition of the material.

The reference material shows a pronounced dendritic microstructure similar to the archaeological samples. Compared to the graphite cast reference material the sand castings have bigger secondary dendrite arm spacings due to the longer solidification time.

Electron microprobe analyses show that the amount of alloying elements in the matrix of the reference material is much lower than their total amount (Fig. 7.15, p. 145). Nevertheless, in the prehistoric material this effect is much more pronounced, particularly for antimony (cf. Fig. 6.82, p. 127).

## **7.3 Mechanical properties**

### **7.3.1 Vickers hardness test**

The low load Vickers hardness HV<sub>0.2</sub> increases with the amount of alloying elements (Fig. 7.16, p. 145 and Table C.12, p. 253f.).

Pure copper has a higher average value of hardness than the other sand cast

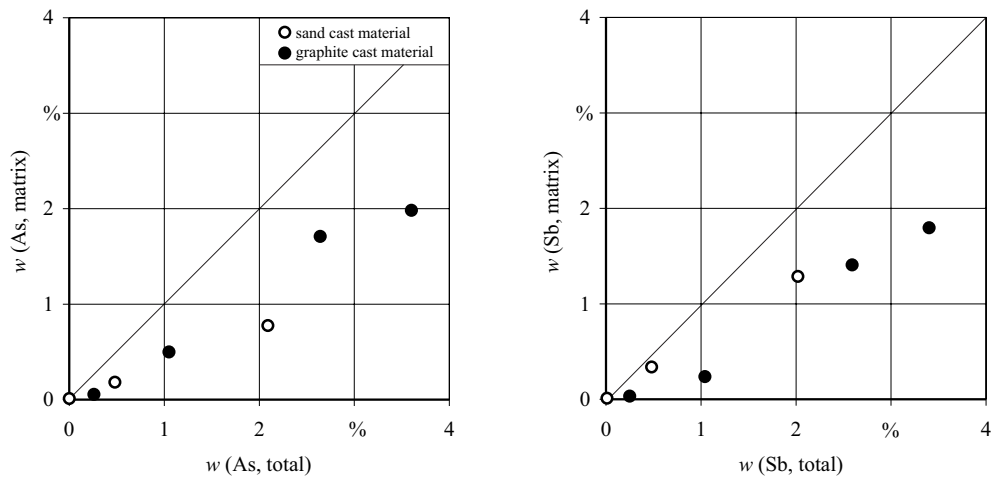


**Figure 7.15:** Comparison of the arsenic and antimony contents in the matrix of the reference material with the bulk analysis. The bulk analyses were made with EDXRF, the matrix analyses with EPMA. The diagonal line in the diagram marks the 100 % solubility limit of the alloying elements in the matrix.

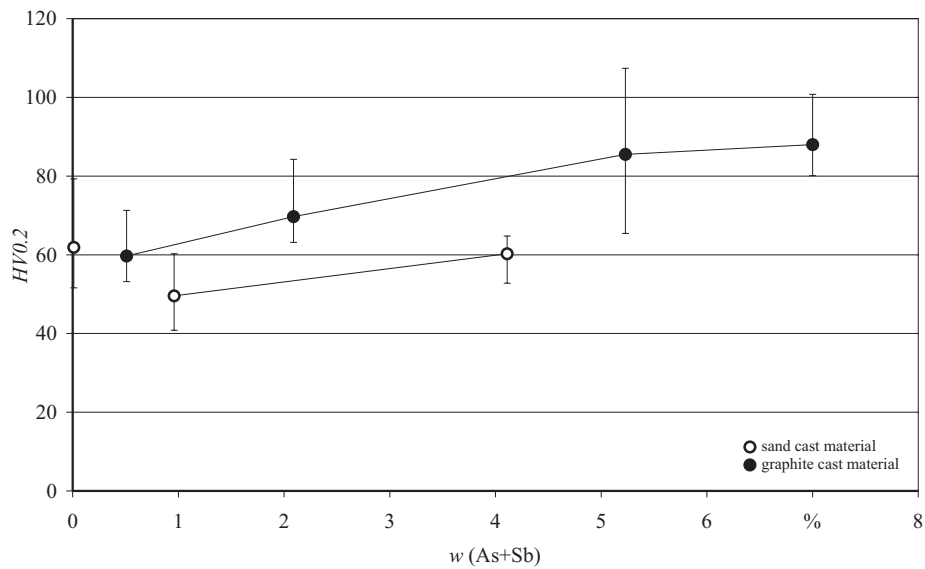


**Figure 7.16:** Vickers low load hardness  $HV_{0.2}$  of the sand cast (circles) and graphite cast (black dots) reference material. Given are the average values, the maximum and minimum values. The points are connected to show trends.

material. For the sand cast alloys the low load hardness increases from about 50 HV0.2 (Cu As0.5 Sb0.5 Bi0.1) to 60 HV0.2 (Cu As2 Sb2 Bi0.1). The graphite cast alloys have average hardness values which are 15 to 20 HV0.2 higher compared to the sand cast alloys. The low load Vickers hardness increases from 60 HV0.2 (Cu As0.25 Sb0.25 Bi0.1) to 88 HV0.2 (Cu As4 Sb4 Bi0.1).

### 7.3.2 Tensile test

With increasing alloying content the 0.2% offset yield strength  $R_{p0.2}$  increases (Fig. 7.17, p. 147 and Table C.9, p. 248). The sand cast pure copper and the specimen made of Cu As0.5 Sb0.5 Bi0.1 have a similar 0.2% offset yield strength of about 50 MPa. These values increase up to 65 MPa for the sand cast alloy Cu As2 Sb2 Bi0.1. The graphite cast material shows 0.2% offset yield strength values which are commonly about 10 MPa higher. The 0.2% offset yield strength increases from about 57 MPa for Cu As0.25 Sb0.25 Bi0.1 up to 100 MPa for the highest alloyed material Cu As4 Sb4 Bi0.1.

The tensile strength  $R_m$  shows opposite trends compared to the 0.2% offset yield strength  $R_{p0.2}$  (Fig. 7.18, p. 147 and Table C.9, p. 248). Except for the reference alloy Cu As3 Sb3 Bi0.1, the alloyed material has a lower tensile strength than pure copper. There is a distinct decrease in the tensile strength for the sand cast material from 160 MPa for pure copper to 100 MPa for Cu As2 Sb2 Bi0.1. The graphite cast alloys have higher tensile strength values compared to the sand cast material. There is a slight decrease in tensile strength from about 150 MPa for Cu As0.25 Sb0.25 Bi0.1 to about 145 MPa for Cu As4 Sb4 Bi0.1. The Cu As3 Sb3 Bi0.1 reference alloy shows a tensile strength of about 190 MPa which is higher than that of the other alloys.

The percentage elongation after fracture  $A$  decreases with increasing alloying content (Fig. 7.19, p. 148 and Table C.9, p. 248). While the pure copper specimen has an average elongation after fracture of 20 %, the sand cast alloy Cu As0.5 Sb0.5 Bi0.1 has an elongation of only 10 %. The graphite cast material shows slightly higher values of the percentage elongation after fracture. It decreases from about 15 % for Cu As0.25 Sb0.25 Bi0.1 to 3 % for Cu As4 Sb4 Bi0.1.

The percentage reduction of area after fracture  $Z$  shows a similar tendency as the elongation (Table C.9, p. 248). It decreases distinctly from 26 % for pure copper to about 9 % for Cu As0.5 Sb0.5 Bi0.1. The differences in behaviour between the sand cast and the graphite cast material are subtle. The latter shows a decrease in percentage reduction of area after fracture from about 9 % (Cu As0.25 Sb0.25 Bi0.1) to 1.8 % (Cu As4 Sb4 Bi0.1).

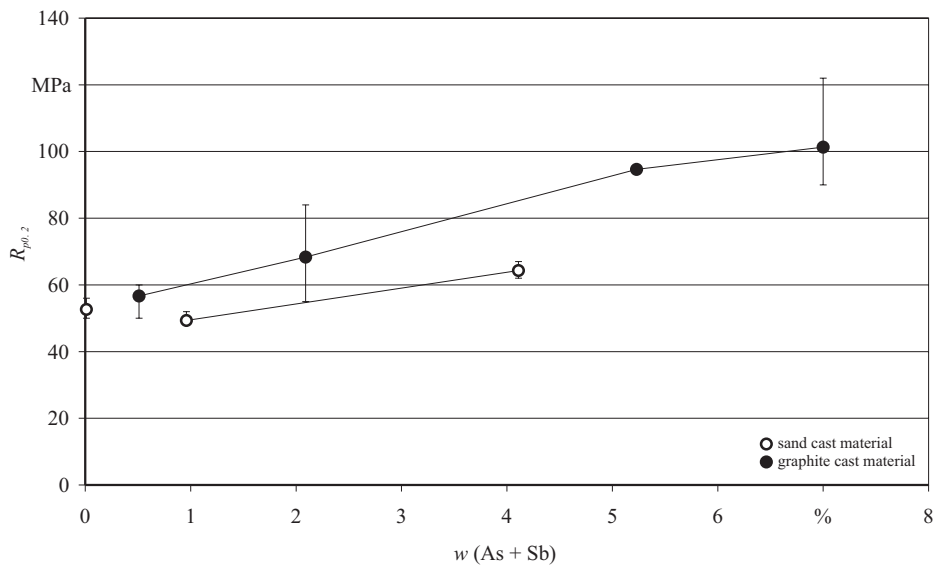


**Figure 7.17:** 0.2% offset yield strength  $R_{p0.2}$  of sand cast (circles) and graphite cast (black dots) reference material. Given are the average, maximum and minimum values. The points are connected in order to show trends.

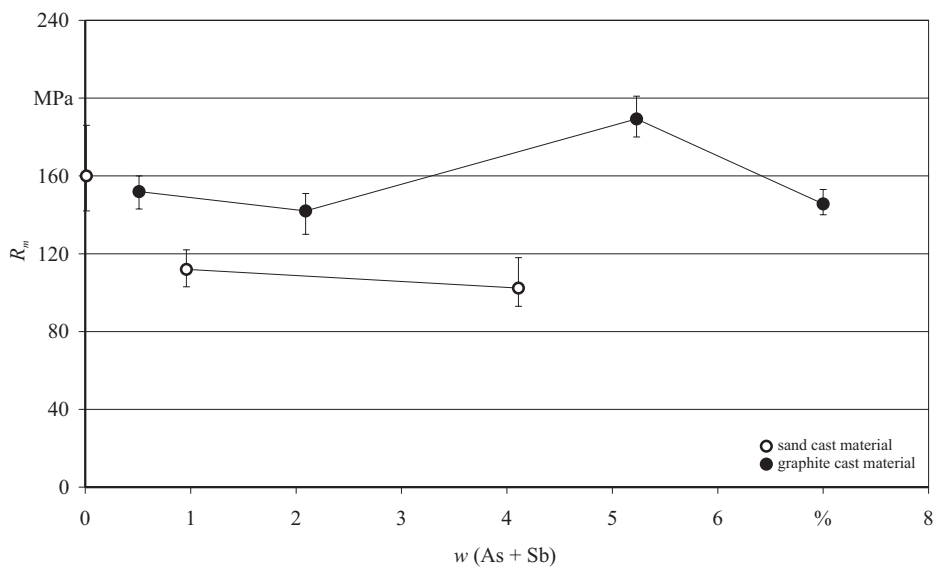


**Figure 7.18:** Tensile strength  $R_m$  of sand cast (circles) and graphite cast (black dots) reference material. Given are the average, maximum and minimum values. The points are connected in order to show trends.

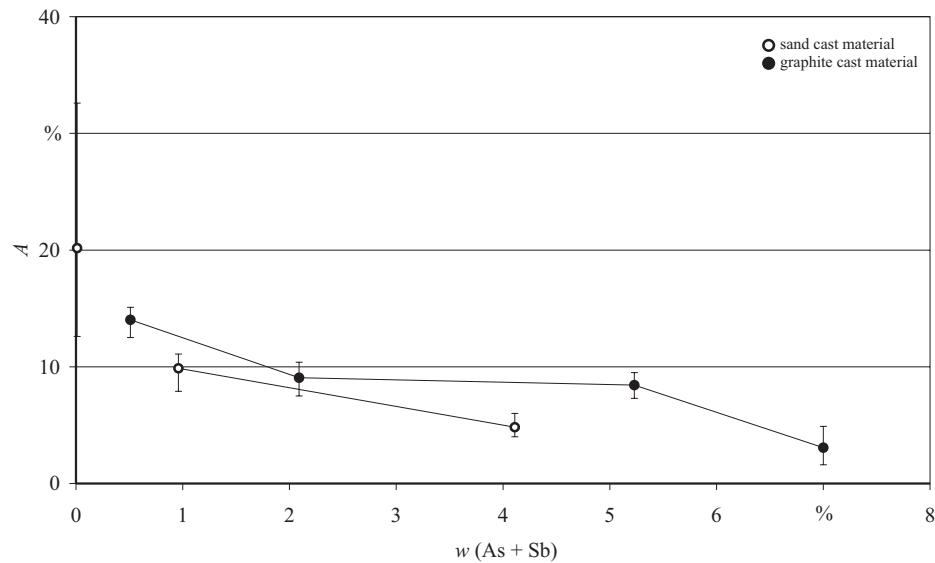


**Figure 7.19:** Percentage elongation after fracture *A* of sand cast (circles) and graphite cast (black dots) reference material. Given are the average, maximum and minimum values. The points are connected in order to show trends.

The fracture appearance changes considerably (Fig. C.14, p. 249). The pure copper specimens show ductile fractures. Both sand cast alloys have mixed fractures. The lower alloyed graphite cast materials Cu As<sub>0.25</sub> Sb<sub>0.25</sub> Bi<sub>0.1</sub> and Cu As<sub>1</sub> Sb<sub>1</sub> Bi<sub>0.1</sub> have funnel-shaped mixed fractures, whereas the high alloyed graphite cast materials Cu As<sub>3</sub> Sb<sub>3</sub> Bi<sub>0.1</sub> and Cu As<sub>4</sub> Sb<sub>4</sub> Bi<sub>0.1</sub> are broken brittle. Two of the Cu As<sub>4</sub> Sb<sub>4</sub> Bi<sub>0.1</sub> specimen had a porous fracture.

### 7.3.3 Notched bar impact test

The notch impact work  $A_v$ , markedly decreases if copper is alloyed with arsenic, antimony and bismuth (Fig. 7.20, p. 149 and Table C.10, p. 250). The pure copper specimens have an average notch impact work of 60 J, which decreases to 12 J for the reference alloy Cu As<sub>0.5</sub> Sb<sub>0.2</sub> Bi<sub>0.1</sub>. The graphite cast alloys show higher values for the notch impact work compared to the sand cast alloys. For the Cu As<sub>0.25</sub> Sb<sub>0.25</sub> Bi<sub>0.1</sub> reference alloy a notch impact work of about 28 J was determined, which decreases to 6.5 J for Cu As<sub>4</sub> Sb<sub>4</sub> Bi<sub>0.1</sub>.

The lateral spreading shows similar trends. It decreases substantially with the transition from copper to the alloyed material. While the copper specimens have



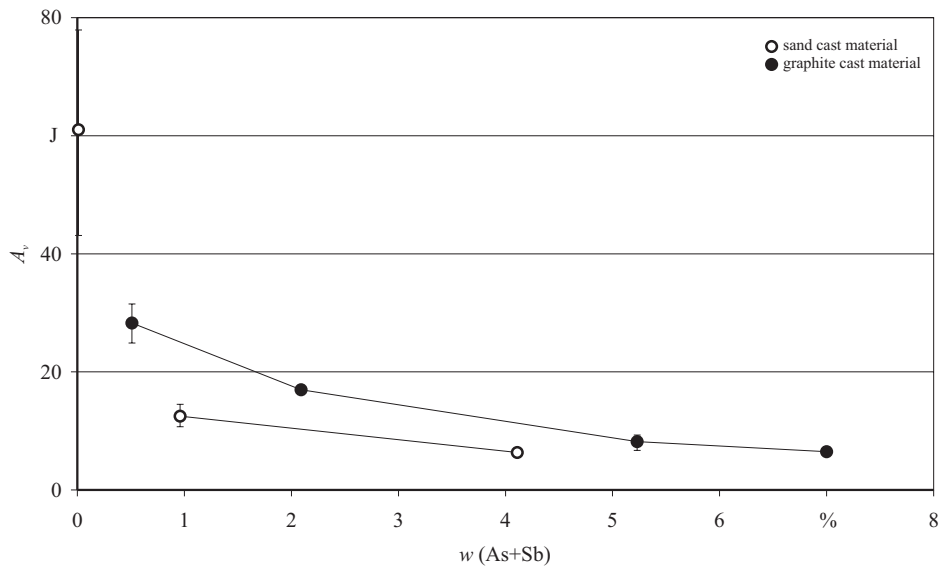


**Figure 7.20:** Notch impact work  $A_v$  of sand cast (circles) and graphite cast (black dots) reference material. Shown are the average values, the maximum and minimum values. The points are connected in order to show trends.

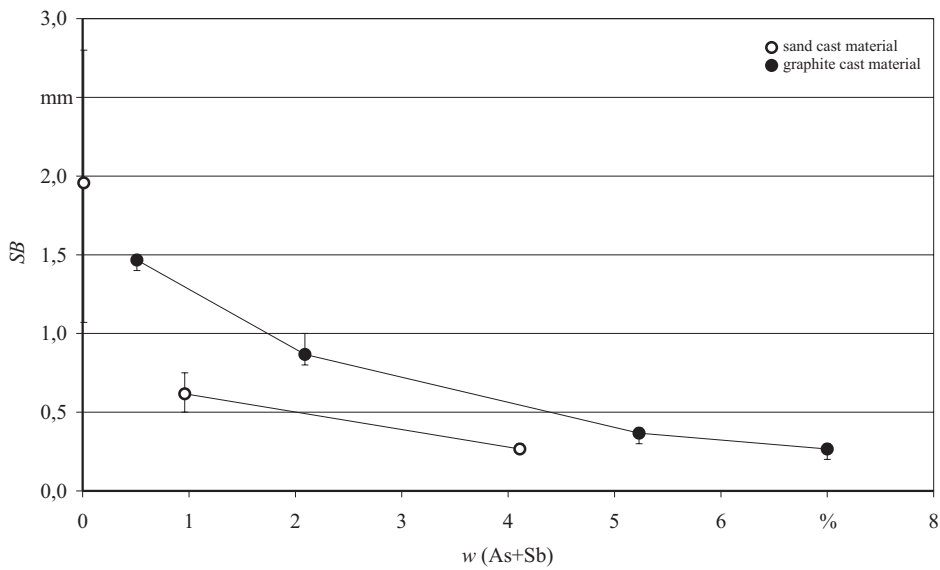


**Figure 7.21:** Lateral spreading  $SB$  of sand cast (circles) and graphite cast (black dots) reference material. Shown are the average values, the maximum and minimum values. The points are connected in order to show trends.

an average lateral spreading of about 2 mm, the specimens of the sand cast alloy Cu As0.5 Sb0.5 Bi0.1 were only spread 0.6 mm. Similar to the notch impact work the graphite cast alloys show higher values. The lateral spreading decreased from 1.5 mm (Cu As0.25 Sb0.25 Bi0.1) to 0.3 mm (Cu As4 Sb4 Bi0.1).

As for the tensile specimen the fracture appearance of the impact specimens changes with the alloying content from ductile to brittle (Fig. C.15, p. 251). The copper and Cu As0.25 Sb0.25 Bi0.1 specimen show ductile fractures. The sand cast alloy Cu As0.5 Sb0.5 Bi0.1 and the graphite cast reference material Cu As1 Sb1 Bi0.1 have mixed fractures with ductile and brittle parts. The higher alloyed materials have brittle fractures.

### 7.3.4 Torsion test

The maximum reference amount of deformation  $\phi_{v,max}$  decreases substantially between the copper specimens and the alloyed material (Fig. 7.22, p. 151 and Table C.11, p. 252). The copper specimens have a maximum reference amount of deformation of about 0.94. This value decreases to  $\phi_{v,max}=0.27$  for the sand cast reference alloy Cu As0.5 Sb0.5 Bi0.1 and  $\phi_{v,max}=0.22$  for Cu As2 Sb2 Bi0.1. Although there is a slight increase in the maximum reference amount of deformation for Cu As1 Sb1 Bi0.1, the graphite cast alloys show trends similar to those of the sand cast material. For the reference alloy Cu As0.25 Sb0.25 Bi0.1 an average  $\phi_{v,max}$  of 0.28 was determined, which drops to 0.16 for Cu As4 Sb4 Bi0.1.

For a defined reference amount of deformation  $\phi_v=0.1$  the reference stress  $\sigma_v$  was determined (Table C.11, p. 252). The stress which is needed to obtain a certain amount of deformation increases with the alloying content (Fig. 7.23, p. 151). For the sand cast material the reference stress for  $\phi_v=0.1$  increases from 133 MPa (Cu) to 153 MPa (Cu As2 Sb2 Bi0.1). The specimen of the graphite cast material show values which are about 50 MPa higher compared to the sand cast material. For the Cu As0.25 Sb0.25 Bi0.1 reference alloy an average reference stress for  $\phi_v=0.1$  of 162 MPa was determined. It increases up to 216 MPa for Cu As4 Sb4 Bi0.1.

The hardening exponent  $P$  shows no significant change with increasing alloying content, except for the Cu As0.5 Sb0.5 Bi0.1 reference alloy (Fig. 7.24, p. 152). This alloy has an average hardening exponent of 0.53, while the hardening exponent slightly decreases from 0.42 (Cu As0.25 Sb0.25 Bi0.1) to 0.37 (Cu As4 Sb4 Bi0.1). There is no detectable difference between the sand cast and the graphite cast material.

The copper torsion specimen show distinctive ductile fractures with regular

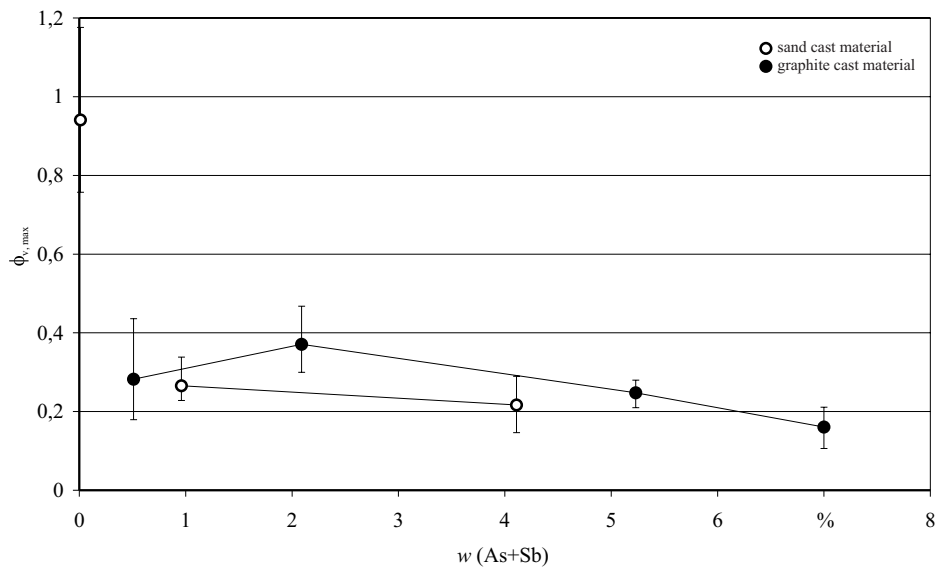


**Figure 7.22:** Maximum reference amount of deformation  $\phi_{v,max}$  of sand cast (circles) and graphite cast (black dots) material. Given are the average, maximum and minimum values. The points are connected in order to show trends.

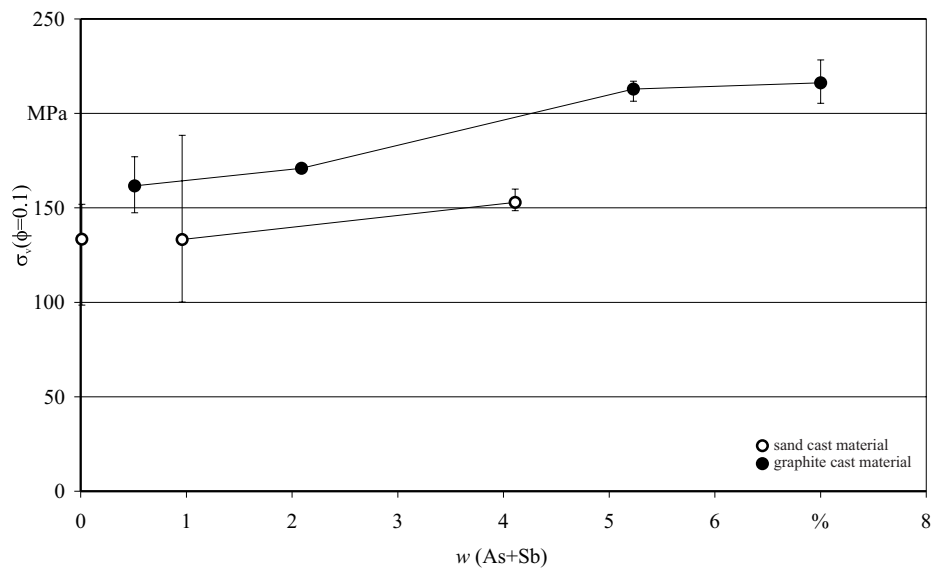


**Figure 7.23:** Reference stress  $\sigma_v$  for  $\phi_v=0.1$  of sand cast (circles) and graphite cast (black dots) reference material. Given are the average, maximum and minimum values. The points are connected in order to show trends.

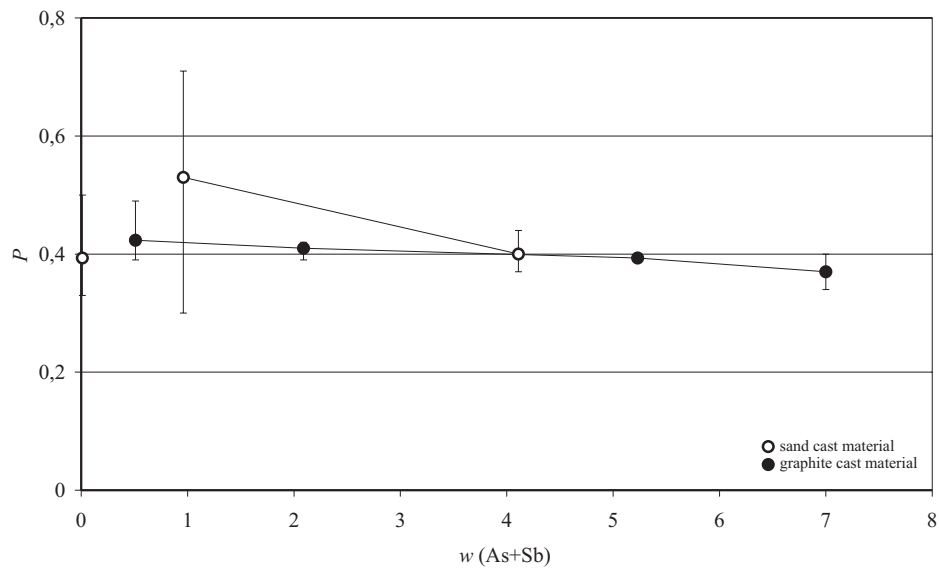


**Figure 7.24:** Hardening exponent  $P$  of sand cast (circles) and graphite cast (black dots) reference material. Shown are the average values, the maximum and minimum values. The points are connected in order to show trends.

displacements at the surface. With an increasing alloying content the brittle, intercrystalline amount of fractures increases. The surfaces of the specimen show a regular displacements with fine cracks. These cracks are more distinctive at the alloy Cu As<sub>2</sub> Sb<sub>2</sub> Bi<sub>0.1</sub> than at Cu As<sub>0.5</sub> Sb<sub>0.5</sub> Bi<sub>0.1</sub>.

### 7.3.5 Interpretation of the material tests

The Vickers low load hardness test has shown, that the copper specimen had a higher hardness than the other sand cast alloys. This may be explained by the copper-copper oxide eutectic in the sample. For the alloyed material there is a hardness increase with increasing amount of arsenic and antimony. The hardening may be caused by two effects, the grain size and the solid solution strengthening. While the effect of solid solution strengthening could not be determined with certainty, the influence of the grain size is obvious. The sand cast alloys have secondary dendrite arm spacings of about  $50 \mu\text{m}$ , that of the graphite cast material ranges between  $20$  and  $10 \mu\text{m}$ . The latter has a low load hardness which is about  $15$  to  $20 \text{HV}_{0.2}$  higher.

Similar to the hardness, the  $0.2\%$  offset yield strength  $R_{p0.2}$  increases with the

alloying content. This may be explained with the Hall-Petch equation (Askeland, 1994) which relates the grain size to the yield strength:

$$\sigma_y = \sigma_0 + \frac{K}{\sqrt{d}} \quad (7.1)$$

In this equation  $\sigma_y$  is the yield stress at which point the material is deformed permanently,  $d$  is the grain size,  $\sigma_0$  and  $K$  are constants. With decreasing grain size, the yield strength increases. The reference stress  $\sigma_v$  for a defined reference amount of deformation  $\phi_v$  in the torsion test shows the same tendency. The graphite cast material with the smaller grain size shows higher values compared to the sand cast material. With increasing alloying content both the 0.2% offset yield strength and the reference stress increase. This means that for plastic, permanent deformation of higher alloyed materials higher stresses are needed. For workpieces of similar size this means higher applied forces.

The tensile strength  $R_m$ , the notch impact strength  $A_v$  and the maximum reference amount of deformation in the torsion test  $\phi_{v,max}$  decrease distinctly from copper to the alloys. With increasing contents of alloying elements the values decrease further. The percentage elongation after fracture  $A$ , the percentage reduction in area after fracture  $Z$  in the tensile test, the lateral spreading  $SB$  in the notched bar impact test, and the fracture appearance all show that the alloys become more brittle with increasing arsenic and antimony contents.

Similar to the hardness and 0.2% offset yield strength, the graphite cast alloys show higher values for tensile strength and notch impact strength compared to the sand cast alloys. The maximum reference amounts of deformation  $\phi_{v,max}$  seem to be independent of the secondary dendrite arm spacings.

Within the investigated compositional range the hardening exponent seems to be nearly independent of the alloying content and the grain size, except the Cu As0.5 Sb0.5 Bi0.1 reference alloy.

The conclusions concerning the mechanical properties were made on the basis of the bulk analyses. As shown in the previous section (see Fig. 7.15, p. 145) only a part of the alloying elements is dissolved in the matrix, thus contributing to the main mechanical properties. Since the amount of arsenic and antimony dissolved in the matrix is proportional to their total amount, the general interpretation is still valid.

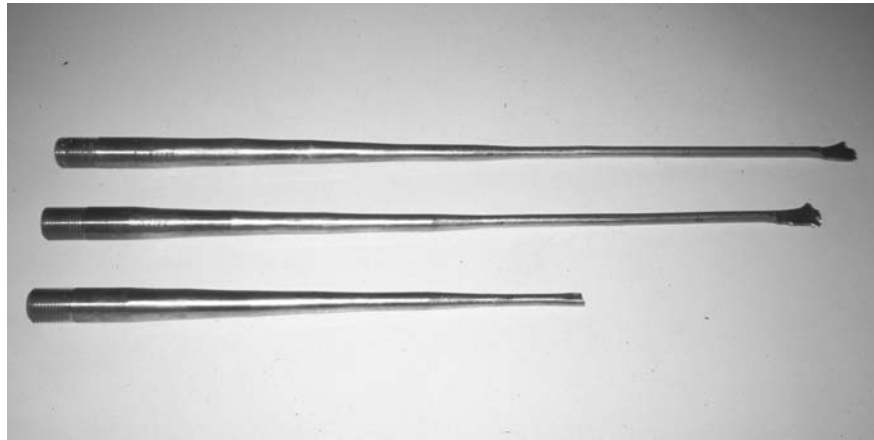


**Figure 7.25:** Stepwise cold worked (round forged) reference material. From the top: Cu, Cu As0.25 Sb0.25 Bi0.1 and Cu As2 Sb2 Bi0.1

## 7.4 Cold working properties

### 7.4.1 Cold working

The experiments of cold working were carried out by stepwise deformation of the material, similar to the experiments by Böhne (1965). In contrast to his experiments rods with rounded cross-sections were used.

Rods with an initial diameter of 16 mm were stepwise forged round in a forging press with a rotating head (Table 7.2, p. 155 and Fig. 7.25, p. 154). The sand cast material (Cu, Cu As0.5 Sb0.5 Bi0.1 and Cu As2 Sb2 Bi0.1) was further hammered flat until cracking occurred.

After deformation the exact diameters of the rods were determined. The deformation  $\phi$  can be calculated from the original cross-sectional area  $A_o$  and the final cross-sectional area  $A_f$  (Askeland, 1994):

$$\phi = \frac{A_o - A_f}{A_o} \cdot 100 \quad (7.2)$$

For rods with round cross-section the percentage of cold work can be calculated from the original diameter  $d_o$  and the final diameter  $d_f$ :

$$\phi = \frac{d_o^2 - d_f^2}{d_o^2} \cdot 100 \quad (7.3)$$

**Table 7.2:** Deformation steps for cold working. Given are the changes in diameter.

	deformation step
(1)	16 mm → 14 mm
(2)	14 mm → 12 mm
(3)	11 mm → 10 mm
(4)	10 mm → 9 mm
(5)	9 mm → 8 mm
(6)	8 mm → 7 mm
(7)	7 mm → 6 mm
(8)	6 mm → 5 mm

Samples for longitudinal metallographic sections were taken from the undeformed material, from parts with approximately 20 %, 55 %, 70 %, 83 %, and 86 % cold deformation, and from the flattened end.

#### 7.4.2 Vickers hardness

The Vickers low load hardness HV0.2 increases with the amount of cold working (Fig. 7.26, p. 156 and Table C.12, p.253f). The pure copper specimen, cold worked about 30 % shows a hardness which is comparable to that of the highest alloyed material Cu As4 Sb4 Bi0.1 in the cast state. With the alloying content, the initial hardness and, hence, the hardness in the cold worked state increase.

More meaningful for the cold working behaviour of the alloys is the hardness increase with the amount of cold deformation compared to the initial hardness. The percentage hardness increase  $\Delta(HV0.2)$  was determined from the Vickers low load hardness HV0.2 at a certain amount of cold work compared to the Vickers low load hardness of the cast material HV0.2( $\phi=0$ ):

$$\Delta(HV0.2) = \frac{HV0.2 - HV0.2(\phi = 0)}{HV0.2(\phi = 0)} \cdot 100 \quad (7.4)$$

The main increase in hardness occurs at cold working rates of up to 20 % (Fig. 7.27, p. 157). Pure copper shows at about 20 % cold deformation an average hardness of 86 HV0.2, which is an increase of about 40 % compared to the cast state. The total hardness increase of the copper specimen is about 84 % for a cold deformation of 86 %. The graphite cast alloys Cu As0.25 Sb0.25 Bi0.1, Cu As1 Sb1 Bi0.1 and Cu As3 Sb3 Bi0.1 have a very similar work hardening

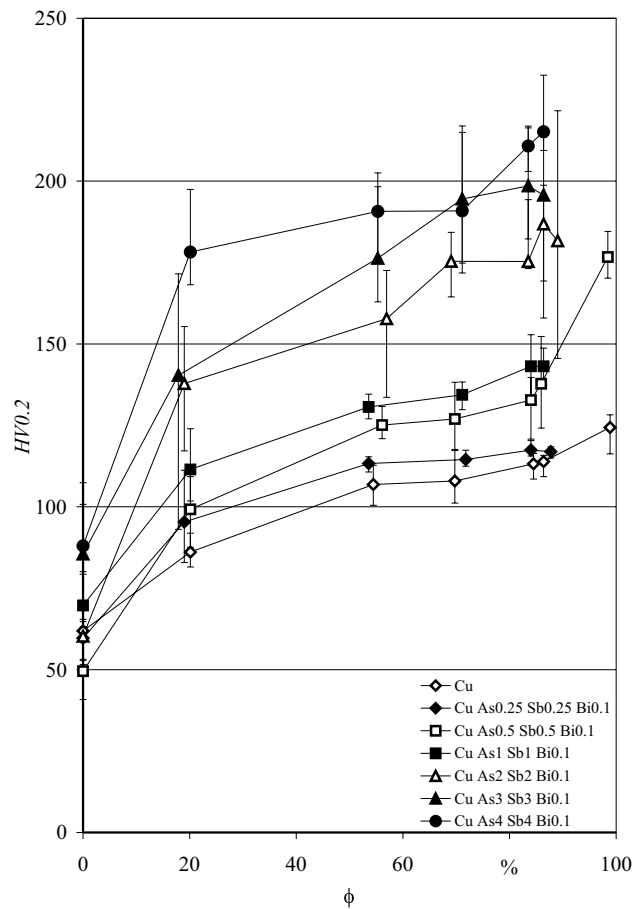


**Figure 7.26:** Work hardening of reference material. Given are the average values, the maximum and minimum values of low load Vickers hardness HV0.2 for sand cast material (white symbols) and graphite cast alloys (black symbols). The points are connected in order to show trends.

behaviour at cold deformation rates of 20 %. Until this deformation the hardness increase is about 60 %. At higher deformation rates of 86 % the lower alloyed material shows an hardness increase of 100 % compared to the cast state. The Cu As3 Sb3 Bi0.1 reference alloy work hardens up to 196 HV0.2, i.e. about 130 % of the initial hardness. The highest alloyed graphite cast material Cu As4 Sb4 Bi0.1 shows a hardness increase of 100 % in the first deformation step of 20 %. At 86 % deformation a hardness increase of about 144 % compared to its initial hardness is reached.



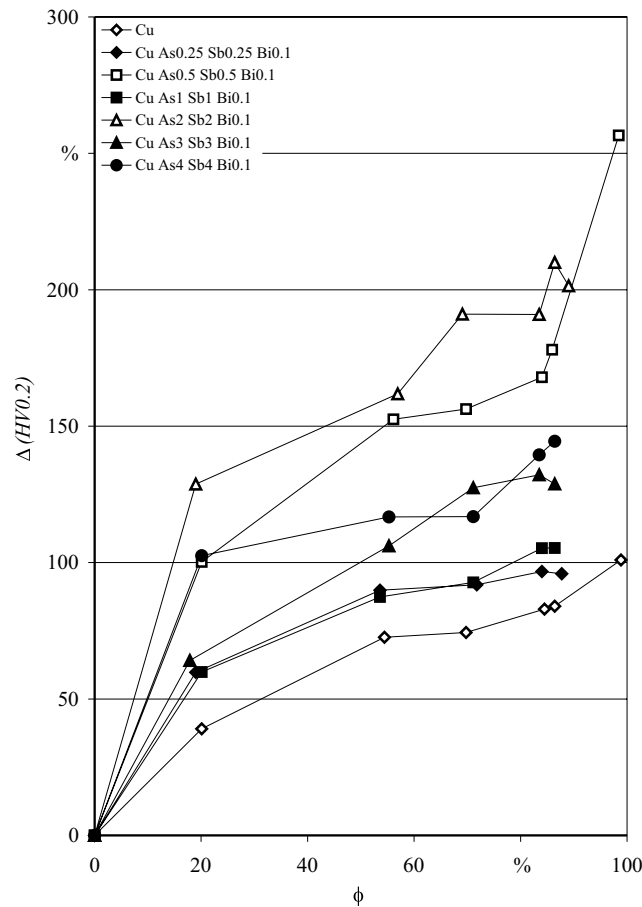


**Figure 7.27:** Work hardening of reference material. Given is the hardness increase  $\Delta(HV_{0.2})$  compared to the initial Vickers low load hardness  $HV_{0.2}(\phi=0)$  of the cast material for sand cast material (white symbols) and graphite cast alloys (black symbols). The points are connected in order to show trends.

The sand cast reference alloys Cu As0.5 Sb0.5 Bi0.1 and Cu As2 Sb2 Bi0.1 show a very pronounced work hardening behaviour. At a cold deformation rate of 20 % the hardness increase is about 100 % for Cu As0.5 Sb0.5 Bi0.1 and 130 % for Cu As2 Sb2 Bi0.1. Further deformation of up to 86 % leads to a hardness increase of 187 % and 210 % respectively. The flattened end of the Cu As0.5 Sb0.5 Bi0.1 reference alloy has an average hardness of 177 HV0.2, which means a hardness increase of 257 % compared to its initial hardness.

### 7.4.3 Metallographic investigation of cold worked material

#### Copper

With increasing amount of deformation the copper-copper oxide eutectic in the centre of the specimen is deformed. At a deformation rate of 23 % the microstructure is only slightly deformed (Fig. 7.28, p. 159; cf Fig. 7.2, p. 133). A cold deformation of more than 45 % leads to a stretched, fibrous structure of the copper-copper oxide eutectic (Fig. 7.29, p. 159). The flattened end of the rod shows some internal cracking parallel to the direction of deformation.

The sulfur containing inclusions are stretched in the direction of deformation, while the oxides within the eutectic structure retain their globular shapes.

#### **Cu As<sub>0.25</sub> Sb<sub>0.25</sub> Bi<sub>0.1</sub>**

At about 23 % cold working the Cu As<sub>0.25</sub> Sb<sub>0.25</sub> Bi<sub>0.1</sub> reference alloy shows slightly stretched grains, marked by the small, globular oxide inclusions (Fig. 7.30, p. 160). Towards the centre of the specimen the length to width-ratio of the deformed grains increases.

At a cold deformation of about 50 % the microstructure is markedly stretched. At 83 % cold working the specimen shows a fibrous microstructure, marked by small, globular oxide inclusions at the grain boundaries. (Fig. 7.31, p. 160). The two-phase inclusion in the centre of the specimen are stretched parallel to the deformation sense, the bluish grey internal structures retain their globular shapes.

#### **Cu As<sub>0.5</sub> Sb<sub>0.5</sub> Bi<sub>0.1</sub>**

The specimen, cold worked about 23 % shows an almost pristine dendritic microstructure with a slightly stretched second phase (Fig. 7.32, p. 161). At a deformation exceeding 30 % the dendrites are markedly deformed and the second phase is elongated. The oxide inclusions are undeformed.

The 83 % cold worked specimen has a highly distorted structure with alternating bands of arsenic- and antimony-rich and copper-rich material (Fig. 7.33, p. 161). At about 90 % cold deformation the specimen shows intergranular cracking.

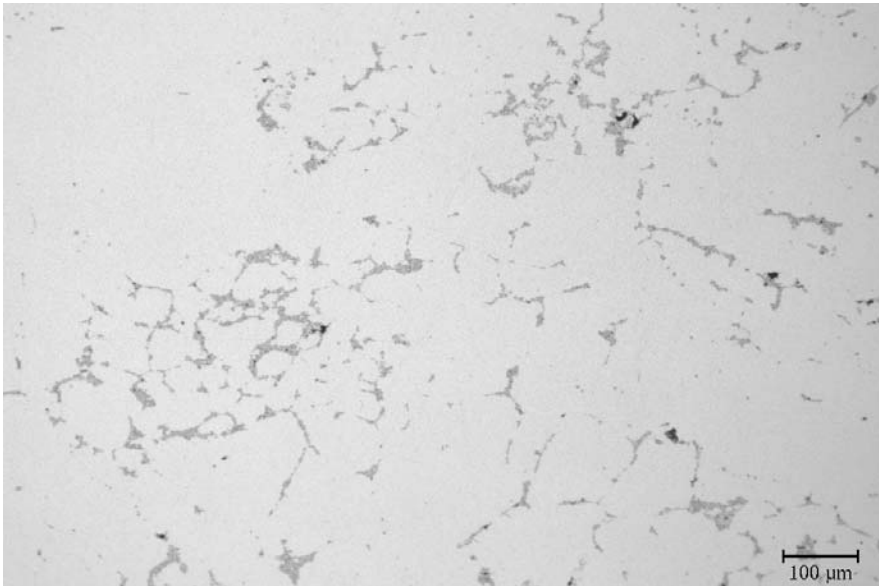


**Figure 7.28:** Cu, 23 % cold worked, metallographic section. Shown is the centre of the specimen with a slightly deformed copper-copper oxide eutectic.



**Figure 7.29:** Cu, 86 % cold worked, metallographic section. Shown is the centre of the specimen with an elongated copper-copper oxide eutectic.

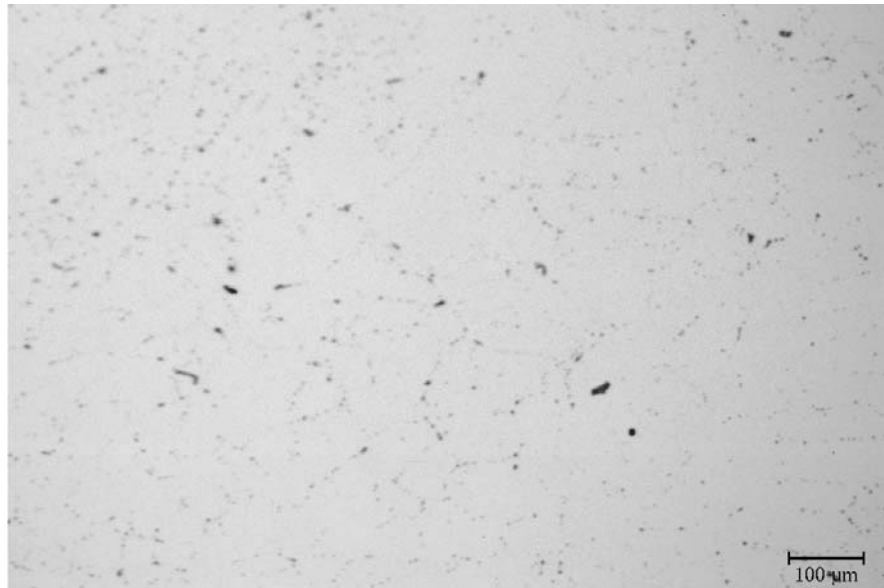


**Figure 7.30:** Cu As<sub>0.25</sub> Sb<sub>0.25</sub> Bi<sub>0.1</sub>, 20 % cold worked, metallographic section. Shown is a slightly stretched microstructure in the centre of the specimen.



**Figure 7.31:** Cu As<sub>0.25</sub> Sb<sub>0.25</sub> Bi<sub>0.1</sub>, 83 % cold worked, metallographic section. Shown is the centre of the specimen with a microstructure, that has been stretched parallel to the deformation.

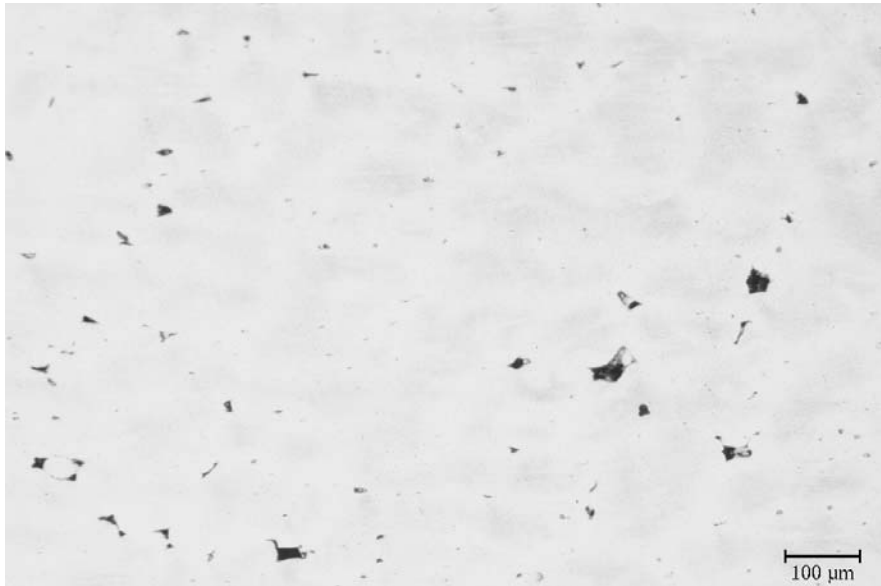


**Figure 7.32:** Cu As<sub>0.5</sub> Sb<sub>0.5</sub> Bi<sub>0.1</sub>, 23 % cold worked, metallographic section etched with NH<sub>3</sub>/H<sub>2</sub>O<sub>2</sub>. The dendritic microstructure is almost completely preserved.



**Figure 7.33:** Cu As<sub>0.5</sub> Sb<sub>0.5</sub> Bi<sub>0.1</sub>, 83 % cold worked, metallographic section etched with NH<sub>3</sub>/H<sub>2</sub>O<sub>2</sub>. Shown is the fibrous microstructure at the edge.

**Cu As1 Sb1 Bi0.1**

Up to a deformation of 23 % the dendritic microstructure of the Cu As1 Sb1 Bi0.1 reference alloy is almost completely preserved (Fig. 7.34, p. 163). The oxidic inclusions along the grain boundaries retain their globular shapes.

Cold working of more than 50 % leads to a microstructure stretched in the direction of the deformation. At higher amounts of deformation the fibrous structure with bands of arsenic- and antimony-rich and copper-rich material is more pronounced (Fig. 7.35, p. 163). Some deformation lines are visible. Independent of the deformation the small oxide inclusions are undeformed, while the two-phase inclusions are stretched.

**Cu As2 Sb2 Bi0.1**

The dendritic microstructure of the Cu As2 Sb2 Bi0.1 reference alloy is not visibly distorted by cold working of about 20 % (Fig. 7.36, p. 164).

At cold working of about 50 % the dendrites are markedly distorted. Further cold working of up to 83 % leads to a fibrous microstructure with alternating bands of copper solid solution and the second copper-arsenic-antimony phase (Fig. 7.37, p. 164). The few oxidic inclusions remained globular.

At about 90 % cold working the material fails, i.e. the first intergranular cracks occur in the centre of the specimen.

**Cu As3 Sb3 Bi0.1**

At cold working of about 20 % the Cu As3 Sb3 Bi0.1 reference alloy shows a dendritic cast structure which is not noticeably distorted (Fig. 7.38, p. 165).

A deformation of the ternary phase was observed at about 50 % cold working. The fibrous structure is not pronounced until about 80 % cold deformation. Cold working the material of about 83 % leads to a fine fibrous microstructure with alternating bands of copper solid solution and ternary phase (Fig. 7.39, p. 165). The small oxide inclusions retain their globular shape independent of the degree of deformation.

**Cu As4 Sb4 Bi0.1**

The 23 % cold worked specimen of Cu As4 Sb4 Bi0.1 shows an almost pristine dendritic microstructure (Fig. 7.40, p. 166).

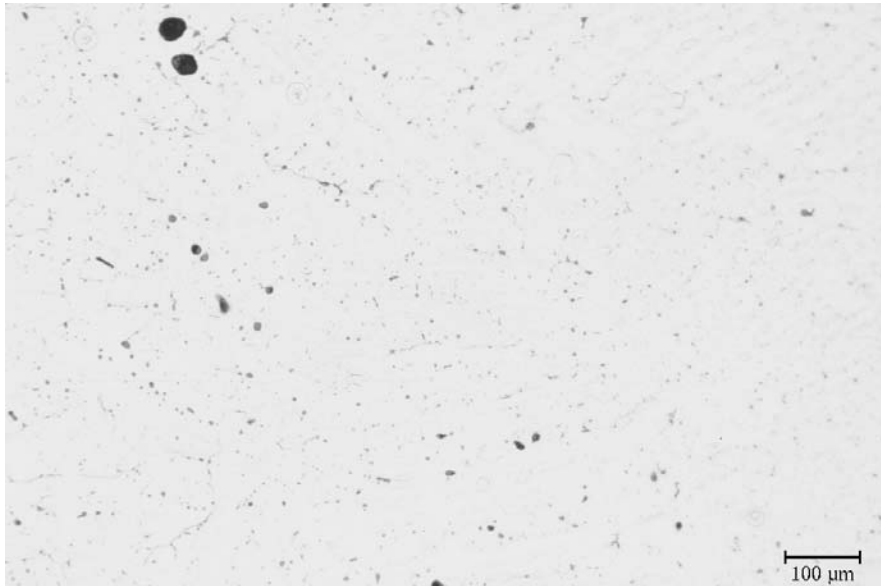


**Figure 7.34:** Cu As1 Sb1 Bi0.1, 23 % cold worked, metallographic section etched with  $\text{NH}_3/\text{H}_2\text{O}_2$ . The dendritic microstructure is almost undistorted.



**Figure 7.35:** Cu As1 Sb1 Bi0.1, 83 % cold worked, metallographic section etched with  $\text{NH}_3/\text{H}_2\text{O}_2$ . Shown is the fibrous microstructure in the centre of the specimen.

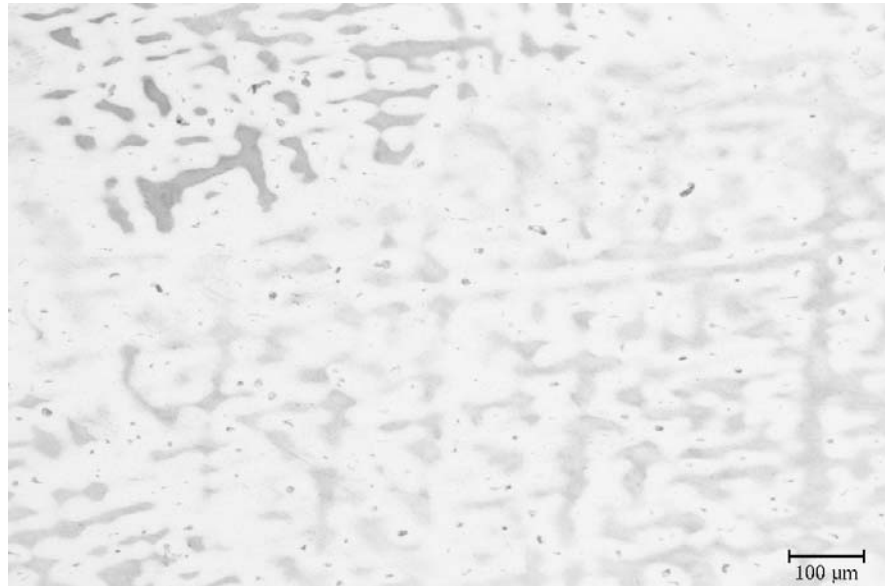


**Figure 7.36:** Cu As<sub>2</sub> Sb<sub>2</sub> Bi<sub>0.1</sub>, 20 % cold worked, metallographic section etched with NH<sub>3</sub>/H<sub>2</sub>O<sub>2</sub>. The dendritic microstructure near the edge is almost undistorted.



**Figure 7.37:** Cu As<sub>2</sub> Sb<sub>2</sub> Bi<sub>0.1</sub>, 83 % cold worked, metallographic section etched with NH<sub>3</sub>/H<sub>2</sub>O<sub>2</sub>. Visible is the fibrous microstructure in the centre of the sample.



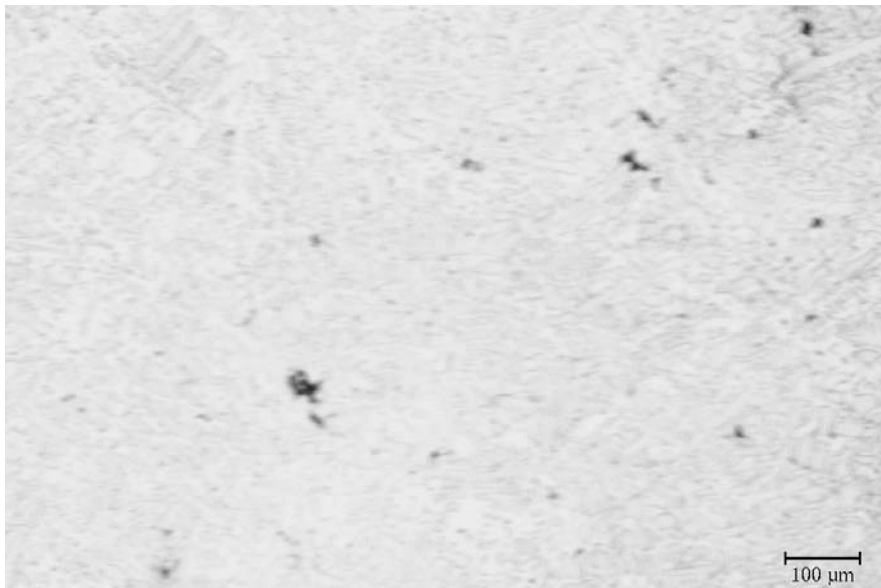


**Figure 7.38:** Cu As<sub>3</sub> Sb<sub>3</sub> Bi<sub>0.1</sub>, 20 % cold worked, metallographic section etched with NH<sub>3</sub>/H<sub>2</sub>O<sub>2</sub>. The dendritic microstructure in the centre of the specimen is almost completely preserved.



**Figure 7.39:** Cu As<sub>3</sub> Sb<sub>3</sub> Bi<sub>0.1</sub>, 83 % cold worked, metallographic section etched with NH<sub>3</sub>/H<sub>2</sub>O<sub>2</sub>. Visible is the fibrous microstructure at the edge of the sample.

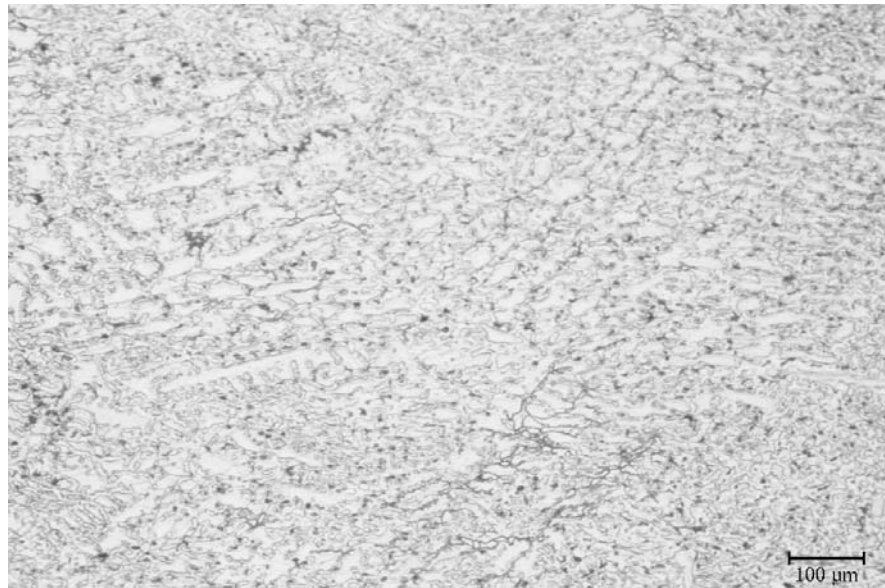


**Figure 7.40:** Cu As<sub>4</sub> Sb<sub>4</sub> Bi<sub>0.1</sub>, 23 % cold worked, metallographic section etched with NH<sub>3</sub>/H<sub>2</sub>O<sub>2</sub>. The dendritic microstructure in the centre of the specimen is not visibly distorted.



**Figure 7.41:** Cu As<sub>4</sub> Sb<sub>4</sub> Bi<sub>0.1</sub>, 83 % cold worked, metallographic section etched with NH<sub>3</sub>/H<sub>2</sub>O<sub>2</sub>. Visible is the fibrous microstructure near the sample edge.

At about 50 % cold deformation the microstructure is stretched and alternating bands of copper solid solution and ternary phase are visible. A deformation of about 83 % leads to a fine fibrous microstructure (Fig. 7.41, p. 166). The inclusions of copper arsenate and antimonate are slightly stretched, while the copper oxide inclusions remained globular.

#### 7.4.4 Summary

The copper alloyed with arsenic, antimony and bismuth work hardens to a greater extent than pure copper. Although the influence of the alloying content cannot be neglected, the working behaviour seems to depend more on the grain size, i.e. the casting technology (sand casting in preheated mould or graphite casting).

About 50 % of the recorded hardness increase took place until 23 % cold working. Above 50 % cold deformation the work hardening has comparably small effects. The comparably large initial increase in work hardening was reported already by Lechtman (1996), who explained it as a result of the intrinsic nature of plastic deformation in face-centred cubic material.

For all reference alloys cold working rates of more than 20 % were necessary to deform the dendritic cast microstructure. At about 50 % cold working the structure is distorted in the deformation sense and shows a fibrous structure. With increasing amount of arsenic and antimony the mixed oxide inclusions become more ductile. They are stretched at high deformation rates. In contrast, the small copper oxide inclusions retain their globular shapes.

The highly deformed sand cast material shows intergranular cracks, which are absent in the graphite cast alloys.



# Chapter 8

## Discussion

Large scale investigations like those by Junghans et al. (1960, 1968b) and new analyses in this work have shown that ingot torques were made mainly of two materials, low-impurity copper and ingot torque metal, containing appreciable amounts of arsenic, antimony, and silver. Since both materials have a very different composition which can be related to the smelting of different ore types, it was presumed that both copper types could be distinguished by the ancient metal-worker.

The hoards of Valley and Piding, which were investigated in this work, do not only contain both material types but additionally show a correlation between typology and material. In both finds, ingot torques with forging seams consist mainly of the ingot torque metal, while the other rings were made of low-impurity copper. The composition of the metals used is different in both hoards so that it is unlikely that they derive from the same workshop. The forging seam, interpreted by Menke (1982) as an intermediate manufacturing stage, can also be seen as a kind of 'label', marking the material. If the cast rod has a more or less flat surface, forging towards a round cross-section tends to result in facets rather than in a forging seam. But many ingot torques show dents, casting grooves or partly concave cross-sections (see e.g. Müh1 in Fig. B.2, p. 211). The cross-sections of such ingots are more difficult to rework and chamfering the edges would lead to a forging seam.

Longitudinal depressions in the cast surface were also observed by Greaves (1912) for arsenical and antimonial copper containing more than 0.1 % oxygen. Johnson noted that the 'set', i.e. the surface appearance of the bar, depended entirely on the percentage of oxygen and gases present (discussion on Greaves (1912)). He further stated that some ingots would have a flat surface because

they were cooled very rapidly. The dependence of the surface appearance both on oxygen content and on melting and casting technology, would explain why dents, casting grooves, and forging seams seem to be characteristic for the ingot torque metal, but are not found on all ingots made of this material. For the ancient metalworker, such a depression in the cast rod and the forging seam of the reworked rod could have been an indicator for ingot torque metal. The strong correlation between forging seam and ingot torque metal and the sorting of different materials in different bundles as it was observed at Valley, implies that copper and ingot torque metal could be and were distinguished.

Despite the different compositions the production technology of ingot torques, as deduced from the metallographic investigations, is very similar. The initial shape was a rod, cast in an open mould (Fig. 8.1, p. 171). The secondary dendrite arm spacings determined from metallographic sections of several ingot torque samples indicate sand casting. Nevertheless, the use of stone moulds cannot be completely excluded, since preheating of such moulds may lead to cooling rates and secondary dendrite arm spacings comparable with those of sand moulds.

The D-shaped or triangular cross-section of the rough cast rod was reworked to a more rounded, sometimes faceted one. Nevertheless, in some cases the rod remained unworked. The ends of the bar were flattened and curled more or less into loops. Finally, the rod was bent into a ring shape (Fig. 8.1, p.171). Most ingot torques were found in an annealed state, which would suggest, that the final deformation was hot working. It might be carried out subsequently after the last annealing in the hot state. But the amount of deformation for bending the ring is comparatively low, so that also cold deformation would leave only few traces like slip lines if any. An EPMA line-scan over a sample cross section (Fig. B.11, p. 219) did not reveal any differences in arsenic or antimony contents between the surface of the ingot and its core. In combination with the residual coring this suggests, that annealing took place under non-oxidising conditions in a short time process. Extensive hot working can be excluded.

The amount of deformation for rounding the cross-section can be estimated from partly reworked ingot torques like fragment Gam1. Depending on the initial cross-section, the rods were deformed by about 10 to 20 %. Comparisons with reference materials show that the main work hardening occurs in this deformation range (Fig. 8.2, p. 172). After this working stage the material may have been annealed for the first time. Flattening the ends requires more than 70 % deformation. In this range intergranular cracking was observed for the sand cast reference alloys. Similar cracking was found within the looped end of fragment Val1b. In order to avoid breaking, an intermediate annealing was necessary.

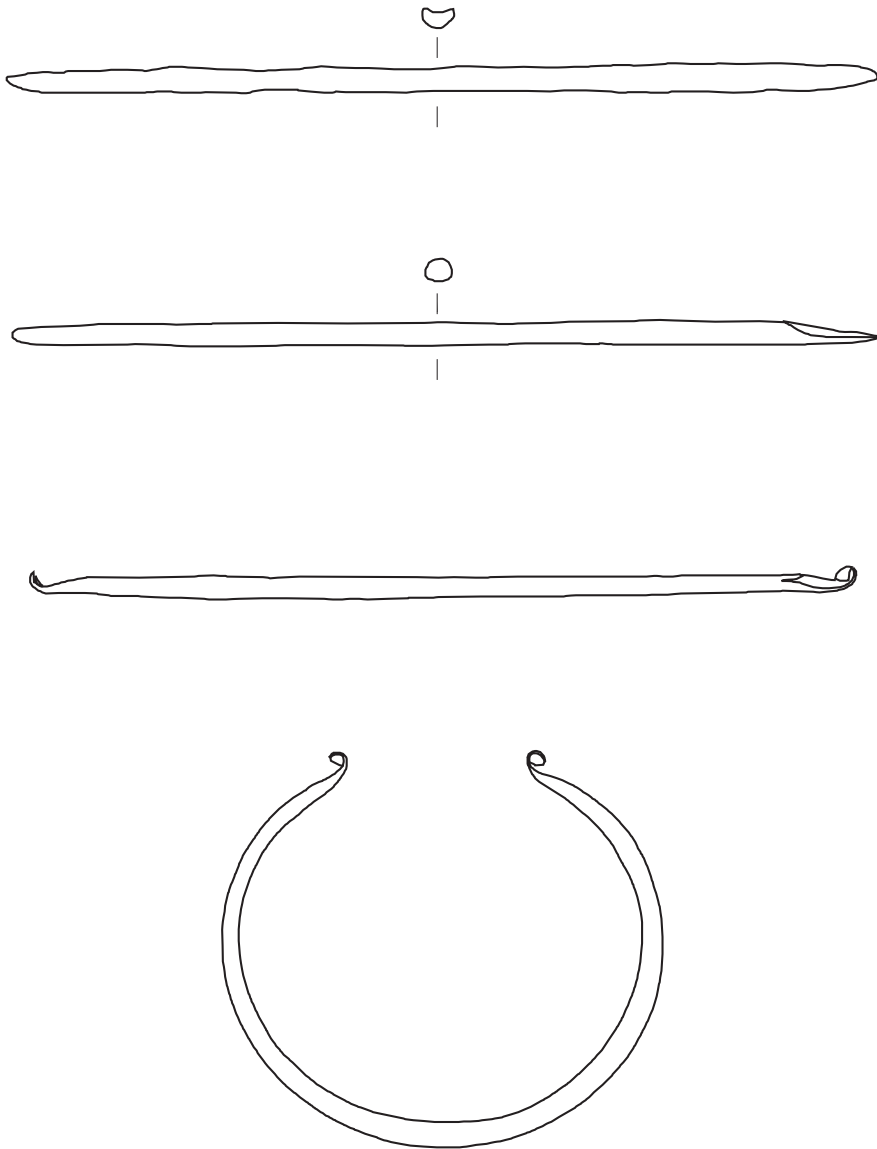


**Figure 8.1:** Manufacturing stages of ingot torques. From the top: initial cast shape, rod with rounded cross section and one end flattened, rod with bent and curled ends, finished ingot torque.

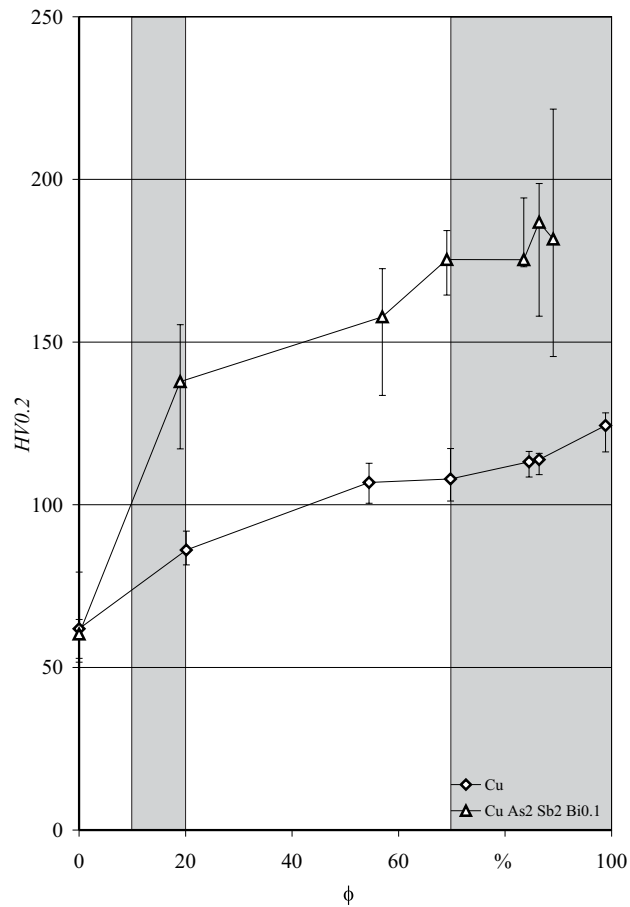


**Figure 8.2:** Work hardening of reference material. Given are the average, the maximum and minimum values of low load Vickers hardness HV0.2 for sand cast material (cf. Fig. 7.26, p. 156). The grey parts in the diagram show the amount of deformation for rounding the cross section of ingot torques (10 to 20 %) and for flattening and rolling the ends (above 70 %).

In the range of 10 to 20 % cold deformation, the differences in working behaviour of copper and a copper alloy with 2 % arsenic and antimony each, comparable to ingot torque metal, are very pronounced. While the hardness increases by about 40 % for copper, the alloy shows an increase in hardness of more than 100 % compared to the initial hardness (Fig. 8.2, p. 172, cf. Fig. 7.27, p. 157). After flattening the ends, the hardness of copper increased by about 100 %, that of Cu As<sub>2</sub> Sb<sub>2</sub> Bi<sub>0.1</sub> by about 200 %. Such differences in workability must have



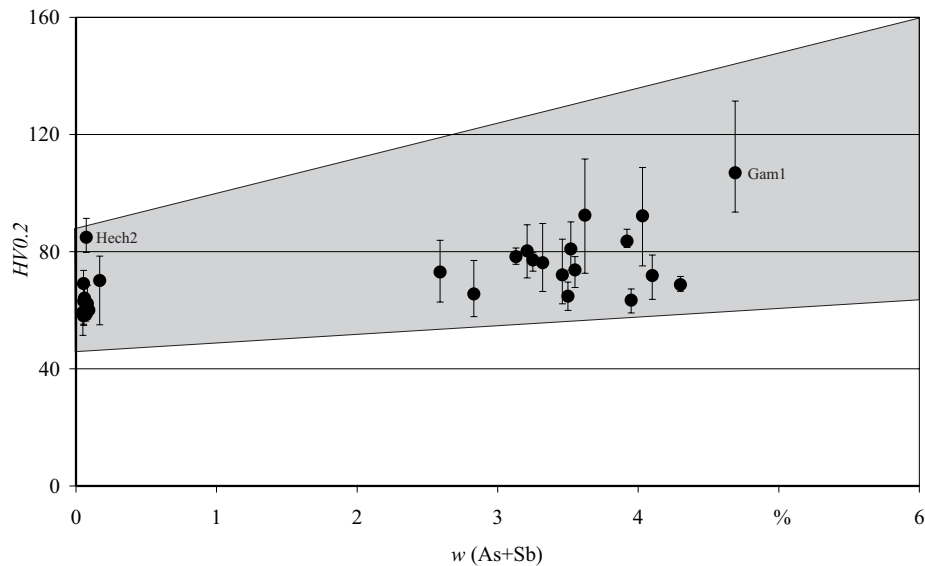


**Figure 8.3:** Vickers low load hardness HV0.2 of ingot torques. Given are the average, the maximum and minimum values. The grey area shows the range between the hardness of reference alloys in the cast state and about 20 % cold deformed.

been noticed by the Bronze Age metalworker.

Vickers low load hardness measurements reveal that the differences in the hardness of the ingot torques are smaller than expected from the composition (Fig. 8.3, p. 173). The metallographic sections of the ingot torques and comparisons of their hardness values with those of reference alloys show that the material was not annealed to full recrystallisation. It seems that both low-impurity copper and ingot torque metal were worked to a similar hardness level.

Two of the investigated ingot torques have significantly higher hardness values than the samples of comparable composition. The ingot torque fragment Hech2 consists of low-impurity copper. In contrast to the other ingots made of this material, the metallographic section of sample Hech2 (Fig. 6.22, p. 80) shows a pronounced eutectic structure of copper-copper sulfide. The second sample with a higher hardness, Gam1, consists of bismuth-rich fahlore metal. Compared to other samples, in Gam1, the fraction of arsenic and antimony in the matrix is higher (Fig. 6.82, p. 127). Both examples, Hech2 and Gam1, show that the material properties are influenced not only by the composition but also by the microstructure and the distribution of the alloying elements.

The material testing of reference alloys has shown that the copper-arsenic-

antimony alloys cast in graphite moulds had higher hardness, strength and toughness values compared to their sand cast counterparts. This means that the ingot torque metal, cast in stone moulds as used e.g. for axes, would show a very different behaviour from the material as it is found in the ingot torques.

The technology of ingot torque production appears standardised and independent of the material. But this independence especially helps to assess the worked material. The appearance of the cast rod, its colour and surface appearance are the first criteria for testing the material. Pores, shrinkage and slag inclusions near the surface will be noticed while reworking the cross-section. The flattening of the ends and their curling demonstrates how deformable the material is. A skilled metalworker was certainly able to compare the workability of different materials and relate it to their composition.

Smith (1988) stated that the fracture character of defective material must have been noticed at the very beginning of the Bronze Age and an observant artisan would soon have related the appearance of specific fracture characteristics to variables in smelting or melting procedures. So it is probably no coincidence that ingot torques, broken in antiquity, are found. Most of the fragments investigated are halves of ingot torques showing mixed bending fractures (Figs. B.1 and B.2, p. 210f.). Such a fracture appearance was characteristic also for the low alloyed reference material, whereas the alloys with more than 2 % arsenic and 2 % antimony show brittle fractures (Fig. C.15, p. 251). Even if the ingot torques have higher total amounts of arsenic and antimony, their matrix composition is comparable with that of the lower alloyed reference material. This suggests, that alloys which were too brittle, were not used for ingot torques. In order to increase the toughness of the material, the amount of arsenic and antimony in the matrix had to be lowered. It is, however, not necessary to remove the alloying elements by evaporation, or to add copper. Binding the alloying elements in oxidic inclusions would result in the same effect.

In summary, it is possible to distinguish the composition of the Early Bronze Age alloys by their mechanical and technological properties. The prerequisite for a material choice on the basis of mechanical and technological properties is a standardised technology, which was found for ingot torques. The shape of these rings may derive from aesthetic tradition but it is also well-suited to material testing. Hoards with two separate types of ingot torques imply that the differences between the material were noted. A choice of materials by composition or properties was surely possible for the Early Bronze Age metalworker. Whether he or she has deliberately made use of these skills can only be presumed at present.

Understanding the history of material means understanding the history of  
mankind and civilization (Hummel, 1997).



# Bibliography

Altwicker, H. (1925). Über den Einfluß von Kupferoxydul auf Elektrolyt- und Raffinadekupfer. *Metall und Erz*, XXII(23):583–594.

Archbutt, S. and Prytherch, W. (1937a). Investigation of the effects of impurities on copper. Part VII – The effect of antimony on copper. *Journal of the Institute of Metals*, 57:265–282.

Archbutt, S. and Prytherch, W. (1937b). Investigation of the effects of impurities on copper. Part VIII – The combined effect of antimony and arsenic on copper. *Journal of the Institute of Metals*, 57:282–297.

Askeland, D. R. (1994). *The science and engineering of materials*. PWS Publishing Company, Boston.

Bartelheim, M. (1998). *Studien zur Böhmisches Aunjetitzer Kultur - Chronologische und chorologische Untersuchungen*. Number 46 in Universitätsforschungen zur prähistorischen Archäologie. Dr. Rudolf Habelt GmbH, Bonn.

Bath-Bílková, B. (1973). K problému původu hřiven. *Památky Archeologické*, 64:24–41.

Böcker, J. (1997). *Spektroskopie*. LaborPraxis. Vogel, Würzburg.

Böhne, C. (1965). Zur Frage der Härtung von Kupferwaffen und Geräten. *Technische Beiträge zur Archäologie*, 2:126–130.

Böhne, C. (1968). Über die Kupferverhüttung der Bronzezeit. *Archaeologia Austriaca*, 44:49–60.

Blumenauer, H., editor (1994). *Werkstoffprüfung*. Deutscher Verlag für Grundstoffindustrie, Leipzig and Stuttgart.

- Budd, P. (1990). Eneolithic arsenical copper: heat treatment and the metallographic interpretation of manufacturing processes. In *Proceedings of the International Symposium on Archaeometry, Heidelberg 1990*, pages 35–44, Basel. Birkhäuser Verlag.
- Budd, P. (1991). *A metallographic investigation of Eneolithic arsenical copper*. PhD thesis, University of Bradford, Dep. of Archaeological Science, Bradford.
- Budd, P., Haggerty, R., Pollard, A., Scaife, B., and Thomas, R. (1996). Rethinking the quest for provenance. *Antiquity*, 70:168–174.
- Budd, P. and Ottaway, B. (1991). The properties of arsenical copper alloys: implications for the development of Eneolithic metallurgy. In Budd, P., Chapman, B., Jackson, C., Janaway, R., and Ottaway, B., editors, *Archaeological Sciences 1989*, pages 132–142, Oxford. Oxbow Books.
- Budd, P. and Taylor, T. (1995). The faerie smith meets the bronze industry: magic versus science in the interpretation of prehistoric metal making. *World Archaeology*, 27(1):133–143.
- Butler, J. J. (1978). Rings and ribs: The copper types of ingot hoards of the Central European Early Bronze Age. In Ryan, M., editor, *The origins of metallurgy in Atlantic Europe*, pages 345–362, Dublin.
- Chakrabarti, D. J. and Laughlin, D. E. (1994). Bi-Cu (Bismuth-Copper). In Subramanian, P. R., editor, *Phase diagrams of binary copper alloys*, Monograph Series on Alloy Phase Diagrams, pages 99–105. The Materials Information Society, Materials Park. Ohio.
- Charles, J. A. (1967). Early arsenical bronzes – a metallurgical view. *American Journal of Archaeology*, (1):21–26.
- Christoforidis, A., Pernicka, E., and Schickler, H. (1988). Ostalpine Kupferlagerstätten und ihre Bedeutung für die prähistorische Metallgewinnung in Mitteleuropa. In *Symposion Archäometallurgie von Kupfer und Eisen in Westeuropa*, volume 35 of *Jahrbuch des Römisch-Germanischen Zentralmuseums*, pages 533–536. Römisch-Germanisches Zentralmuseum, Mainz.
- Coghlan, H. H. (1960). Prehistorical working of bronze and arsenical copper. *Sibirium*, 5:145–152.

- Dies, K. (1967). *Kupfer und Kupferlegierungen in der Technik*. Springer, Berlin, Heidelberg, New York.
- DIN 50 115 (1991). Prüfung metallischer Werkstoffe; Kerbschlagbiegeversuch; Besondere Probenform und Auswerteverfahren.
- DIN 50 125 (1991). Prüfung metallischer Werkstoffe; Zugproben.
- DIN 50 133 (1985). Prüfung metallischer Werkstoffe; Härteprüfung nach Vickers; Bereich HV 0,2 bis HV 100.
- DIN 50 145 (1975). Prüfung metallischer Werkstoffe; Zugversuch.
- Earl, B. and Adriaens, A. (2000). Initial experiments on arsenical bronze production. *JOM*, (3):14–16.
- Eckel, F. (1992). *Studien zur Form- und Materialtypologie von Spangenbarren und Ösenringbarren*. Number 54 in Saarbrücker Beiträge zur Altertumskunde. Dr. Rudolf Habelt, Bonn.
- Eibisch, J. (1992). Die werkstoffkundliche Klassifizierung von frühen Bronze- Werkzeugen mit mathematisch-statistischen Methoden. *Berliner Beiträge zur Archäometrie*, 11:67–91.
- Falbe, J. and Regitz, M., editors (1995). *Römpp Chemie Lexikon*. Georg Thieme Verlag, Stuttgart.
- Freiser, H. and Nancollas, G. H., editors (1987). *Compendium of analytical nomenclature*. Blackwell Scientific Publ., Oxford.
- GMA (1994). Härteprüfung an metallischen Werkstoffen. VDI/VDE-Richtlinien 2616, VDI/VDE-Gesellschaft Meß- und Automatisierungstechnik (GMA) Fachausschuß Härteprüfung, Berlin.
- Goldmann, K. (1981). Guß in verlorener Sandform - das Hauptverfahren alt-europäischer Bronze gießer? *Archäologisches Korrespondenzblatt*, (11):109–116.
- Gowland, W. (1912). Copper and its alloys in early times. *Journal of the Institute of Metals*, 7:23–48.

Greaves, R. H. (1912). The influence of oxygen on copper containing arsenic or antimony. *Journal of the Institute of Metals*, 7:218–245.

Gräfen, H., editor (1991). *Lexikon Werkstofftechnik*. VDI-Verlag, Düsseldorf.

Grimm, J. and Grimm, W. (1905). *Deutsches Wörterbuch*, volume 10. S. Hirzel, Leipzig.

Hahn-Weinheimer, P., Hirner, A., and Weber-Diefenbach, K. (1984). *Grundlagen und praktische Anwendung der Röntgenfluoreszenzanalyse (RFA)*. Vieweg, Braunschweig, Wiesbaden.

Hamilton, E. (1991). Metallurgical Analysis and the Bronze Age of Bohemia: or, Are Cultural Alloys Real? *Archeomaterials*, 5(1):75–89.

Hanson, D. and Ford, G. W. (1927). Investigation of the effects of impurities on copper. Part V – The effect of bismuth on copper. *Journal of the Institute of Metals*, 37:169–178.

Hanson, D. and Marryat, C. (1927). Investigation of the effects of impurities on copper. Part III – The effect of arsenic on copper. *Journal of the Institute of Metals*, 37:121–148.

Hauptmann, A. (1991). Die Kupfer- und die Bronzezeit. *Ferrum*, 63(7):12–17.

Hein, K. and Bombach, H. (1980). On the electrochemical behavior of ternary copper-arsenic-antimony alloys in sulfuric acid copper electrolytes. *Neue Hütte*, 25(10):391–393.

Hell, M. (1952). Zur Verbreitung der altbronzezeitlichen Spangen- und Halsringbarren. *Germania*, 30:90.

Härke, H. (1978). Probleme der optischen Spektralanalyse in der Urgeschichtsforschung. *Prähistorische Zeitschrift*, 53(2):165–276.

Hummel, R. E. (1997). *Understanding material science*. Springer, New York.

Hunger, H.-J., editor (1995). *Werkstoffanalytische Verfahren*. Deutscher Verlag für Grundstoffindustrie, Leipzig, Stuttgart.



Innerhofer, F. (1997). Frühbronzezeitliche Barrenhortfunde – Die Schätze aus dem Boden kehren zurück. In Hänsel, A. and Hänsel, B., editors, *Gaben an die Götter*, number 4 in Bestandskataloge, pages 53–59. Staatliche Museen Berlin, Berlin.

Johnson, F. (1910). The effect of silver, bismuth, and aluminum upon the mechanical properties of “tough-pitch” copper containing arsenic. *Journal of the Institute of Metals*, 4(2):163–234.

Junghans, S., Klein, S., and Scheufele, E. (1954). Untersuchungen zur Kupfer- und Frühbronzezeit Süddeutschlands. *Berichte der Römisch-Germanischen Kommission*, 34:77–114.

Junghans, S., Sangmeister, E., and Schröder, M. (1960). *Metallanalysen kupferzeitlicher und frühbronzezeitlicher Bodenfunde aus Europa*, volume 1 of *Studien zu den Anfängen der Metallurgie*. Gebr. Mann, Berlin.

Junghans, S., Sangmeister, E., and Schröder, M. (1968a). *Kupfer und Bronze in der frühen Metallzeit Europas. Die Materialgruppen beim Stand von 12000 Analysen*, volume 2,1 of *Studien zu den Anfängen der Metallurgie*. Gebr. Mann, Berlin.

Junghans, S., Sangmeister, E., and Schröder, M. (1968b). *Kupfer und Bronze in der frühen Metallzeit Europas. Tafeln, Tabellen, Diagramme, Karten*, volume 2,2 of *Studien zu den Anfängen der Metallurgie*. Gebr. Mann, Berlin.

Junk, M., Krause, R., and Pernicka, E. (2001). Ösenringbarren and the classical Ösenring copper. In Metz, W. H., van Beek, B. L., and Steegstra, H., editors, *Patina*, pages 353–366. private publishing, Groningen.

Keesmann, I. and Moreno Onorato, A. (1999). Naturwissenschaftliche Untersuchungen zur frühen Technologie von Kupfer und Kupfer-Arsen-Bronze. In Hauptmann, A., Pernicka, E., Rehren, T., and Yalçın, Ü., editors, *The Beginnings of Metallurgy*, Der Anschnitt: Beiheft 9, pages 317–332. Deutsches Bergbaumuseum Bochum, Bochum.

Keesmann, I., Moreno Onorato, A., and Kronz, A. (1997). Investigaciones científicas de la metalurgia de El Malagón y Los Millares en el Sureste de España. *Cuadernos de Prehistoria de la Universidad de Granada*, (16–17):247–302.

- Krause, R. (1988). Der Beginn der Metallzeiten. In Planck, D., editor, *Archäologie in Württemberg*, pages 111–139. Theiss, Stuttgart.
- Krause, R. (1996). Deponiert und vergraben: Ein frühbronzezeitliches Ösenringdepot von Pfedelbach, Hohenlohekreis. *Archäologische Ausgrabungen in Baden-Württemberg*, 16:60–63.
- Krause, R. and Pernicka, E. (1996). Das neue Stuttgarter Metallanalysenprojekt “SMAP”. *Archäologisches Nachrichtenblatt*, (1):274–291.
- Krause, R. and Pernicka, E. (1998a). Frühbronzezeitliche Kupfersorten im Alpenvorland und ihr archäologischer Kontext. In *L’atelier du bronzier en europe du XXe au VIII siècle avant notre ère*, volume I, pages 191–202.
- Krause, R. and Pernicka, E. (1998b). The function of ingot torques and their relation with Early Bronze Age copper trade. In *L’atelier du bronzier en europe du XXe au VIII siècle avant notre ère*, volume II, pages 219–226.
- Lechtman, H. (1985). The manufacture of copper-arsenic alloys in prehistory. *Historical Metallurgy*, 19(1):141–142.
- Lechtman, H. (1996). Arsenic bronze: Dirty copper or chosen alloy? A view from the Americas. *Journal of Field Archaeology*, 23(4):477–514.
- Lechtman, H. and Klein, S. (1999). The production of copper-arsenic alloys (arsenic bronze) by cosmelting. *Journal of Archaeological Science*, 26:497–526.
- Lenerz-deWilde, M. (1995). Premonetäre Zahlungsmittel in der Kupfer- und Bronzezeit Europas. *Fundberichte aus Baden-Württemberg*, (20):229–327.
- Liversage, D. and Liversage, M. (1991). Early Bronze Age impurity patterns. In Mohen, J.-P., editor, *Découverte du métal*, volume 2 of *Millénaires*, pages 167–177. Picard, Paris.
- Lutz, J. and Pernicka, E. (1996). Energy dispersive x-ray fluorescence analysis of ancient copper alloys: empirical values for precision and accuracy. *Archaeometry*, 38:313–323.
- Lutz, J. and Pernicka, E. (1998). Analytische Untersuchungen zur frühen Kupfer- und Bronzemetallurgie in Mittel- und Osteuropa. manuscript to be published in *Römisch-Germanische Forschungen*.

- McKerrell, H. and Tylecote, R. F. (1972). The working of copper-arsenic alloys in the Early Bronze Age and the effect of the determination of provenance. *Proceedings of the Prehistoric Society*, (38):209–218.
- Menke, M. (1982). Studien zu den frühbronzezeitlichen Metalldepots Bayerns. *Jahresbericht der Bayerischen Bodendenkmalpflege*, (19/20).
- Moorey, P. R. S. (1985). *Materials and manufacture in ancient Mesopotamia*. Number 237 in BAR International Series. Archaeopress, Oxford.
- Möslein, S. (1998). Überlegungen zur Bedeutung der Metallurgie in der Frühbronzezeit anlässlich des Ringbarrendepotfundes von Piding. *Das archäologische Jahr in Bayern*, pages 73–74.
- Möslein, S. (1999). Neue Depotfunde der älteren Bronzezeit aus dem oberbayerischen Voralpenland. *Archäologie Österreichs*, 9/10:69–77.
- Neugebauer, J.-W., Blesl, C., Lochner, M., and Neugebauer-Maresch, C. (1999). Zu Metall- und Keramikdepots der Bronzezeit aus dem Zentralraum Niederösterreichs. *Archäologie Österreichs*, 9/10:5–45.
- Neuninger, H. and Pittioni, R. (1962). Das Kupfer vom Typ Unterwölbling. *Archaeologia Austriaca*, 32:105–120.
- Neuninger, H., Pittioni, R., and Preuschen, E. (1960). Das Kupfer der Nordtiroler Urnenfelderkultur. *Archaeologia Austriaca Beiheft*, 5.
- Neuninger, H., Pittioni, R., and Preuschen, E. (1969). Salzburgs Kupferlagerstätten und Bronzefunde aus dem Lande Salzburg. *Archaeologia Austriaca Beiheft*, 9.
- Northover, P. (1988). Alloy design in the Bronze Age. In Jones, J. E., editor, *Aspects of Ancient Mining and Metallurgy*, Acta of the British School in Athens, pages 44–54. University College of North Wales, Bangor, Wales.
- Northover, P. (1989). Properties and use of arsenic-copper alloys. In Hauptmann, A., Pernicka, E., and Wagner, G. A., editors, *Archäometallurgie der Alten Welt*, Der Anschnitt: Beiheft 7, pages 111–118. Deutsches Bergbaumuseum Bochum, Bochum.

- Northover, P. (1998). Exotic alloys in antiquity. In Rehren, T., Hauptmann, A., and Muhly, J. D., editors, *Metallurgia Antiqua*, Der Anschnitt: Beiheft 8, pages 113–121. Deutsches Bergbaumuseum Bochum, Bochum.
- Ottaway, B. (1994). *Prähistorische Archäometallurgie*. Verlag Marie L. Leidorf, Espelkamp.
- Otto, H. (1949). Typologische und technologische Bronzezeit. *Forschungen und Fortschritte*, (7/9):73–76.
- Otto, H. and Witter, W. (1952). *Handbuch der ältesten vorgeschichtlichen Metallurgie in Mitteleuropa*. Barth, Leipzig.
- Paret, O. (1954). Ein Sammelfund von steinernen Bronzegußformen aus der späten Bronzezeit. *Germania*, 32:7–11.
- Pazuchin, V. A. (1964). O proischoždenii drevnej myš'jakovistoj medi (on the origin of ancient copper containing arsenic). *Izvestija Akademii Nauk SSSR - Metallurgija i Gorneo Delo (Transactions of the Academy of Sciences of the USSR - Metallurgy and Mining)*, (1):151–165.
- Pernicka, E. (1984). Instrumentelle Multi-Elementanalyse archäologischer Kupfer- und Bronzeartefakte: Ein Methodenvergleich. *Jahrbuch des Römisch-Germanischen Nationalmuseums Mainz*, pages 517–531.
- Pernicka, E. (1990). Gewinnung und Verbreitung der Metalle in prähistorischer Zeit. *Jahrbuch des Römisch-Germanischen Nationalmuseums Mainz*, pages 21–129.
- Pernicka, E. (1995). review of: Franz Eckel, Studien zur Form- und Materialtypologie von Spangenbarren und Ösenringbarren. *Germania*, 73(1):174–183.
- Pernicka, E. (1999). Trace element fingerprint of ancient copper: a guide to technology or provenance? In Young, S. M., Pollard, A. M., Budd, P., and Ixer, R. A., editors, *Metals in antiquity*, number 792 in BAR International Series, pages 163–171. Archaeopress, Oxford.
- Pietsch, A. (1964). *Zur Technik der Wendelringe*. Number 4 in Arbeits- und Forschungsberichte zur sächsischen Bodendenkmalpflege. VEB Deutscher Verlag der Wissenschaften, Berlin.

- Pittioni, R. (1957). Urzeitlicher Bergbau auf Kupfererz und Spurenanalyse. *Archaeologia Austriaca, Beiheft*, 1.
- Pollard, A. M., Thomas, R. G., Ware, D., and William, P. (1990). Experimental smelting of secondary copper minerals: implications for Early Bronze Age metallurgy in Britain. In Pernicka, E. and Wagner, G. A., editors, *Archaeometry '90*, pages 127–136, Basel. Birkhäuser.
- Pollard, A. M., Thomas, R. G., and William, P. (1989). Some experiments concerning smelting of arsenical copper. In Budd, P., Chapman, B., Jackson, C., Janaway, R., and Ottaway, B., editors, *Archaeological Sciences 1989*, Oxford. Oxbow Books.
- Preßlinger, H. and Eibner, C. (1989). Bronzezeitliche Kupferverhüttung im Paltental. In Hauptmann, A., Pernicka, E., and Wagner, G. A., editors, *Archäometallurgie der Alten Welt, Der Anschnitt: Beiheft 7*, pages 235–240. Deutsches Bergbaumuseum Bochum, Bochum.
- Ravič, I. G. and Ryndina, N. V. (1984). Izučenie svojstv i mikrostrukturny splavov med'-myš'jak v svjazi s ich ispol'zovanijem v drevnosti (On the investigation of the properties and microstructure of the copper-arsenic alloys in conjunction with their use in antiquity). *Chudožestvennoe nasledie (Art Heritage)*, 39(9):114–124.
- Rittershofer, K.-F. (1983). Der Hortfund von Bühl und seine Beziehungen. *Berichte der Römisch-Germanischen Kommission*, 64:139–416.
- Rostoker, W. and Dvorak, J. (1991). Some experiments with cosmelting to copper alloys. *Archaeomaterials*, 5(1):5–20.
- Rostoker, W., Pigott, V., and Dvorak, J. (1989). Direct reduction to copper metal by oxide-sulfide mineral interaction. *Archaeomaterials*, 3(1):69–87.
- Rösler, H. J. (1991). *Lehrbuch der Mineralogie*. Deutscher Verlag für Grundstoffindustrie, Leipzig.
- Ruhrmann, J. (1925). Über Arsen und Nickel sowie deren Sauerstoffverbindungen im Kupfer und ihren Einfluß in geringen Mengen auf seine mechanischen Eigenschaften. *Metall und Erz*, XXII(14):339–348.
- Sangmeister, E. (1971). Aufkommen der Arsenbronze in SO-Europa. In Novak, G., editor, *Actes du VIIIe Congrès International des Sciences Préhistoriques et protohistoriques, Beograd, 9 - 15 Septembre 1971*, pages 109–129, Beograd.

- Sangmeister, E. (1998). Metallanalysen in der Archäologie: Erfahrungen aus 45 Jahren Forschung. In Mordant, C., Pernot, M., and Rychner, V., editors, *L'atelier du bronzier en europe du XXe au VII siècle avant notre ère*, pages 9–18, Paris. cths.
- Schimmel, A. (1930). *Metallographie der technischen Kupferlegierungen*. Springer, Berlin.
- Schubert, E. (1981). Zur Frage der Arsenlegierungen in der Kupfer- und Frühbronzezeit Südosteuropas. In Lorenz, H., editor, *Studien zur Bronzezeit: Festschrift für Wilhelm Albert v. Brunn*, pages 447–459. von Zabern, Mainz.
- Schumann, H., editor (1991). *Metallographie*. Deutscher Verlag für Grundstoffindustrie, Leipzig.
- Scott, D. A. (1991). *Metallography and microstructure of ancient and historic metals*. Getty Conservation Inst., J. Paul Getty Museum, Malibu, Calif.
- Selimchanov, I. R. (1982). Arsenical copper in H.H. Coghlan's works and investigations in the laboratory of the Institute of History at the Academie of Sciences at Azerbaijan SSR. *Historical Metallurgy*, 16(2):50–57.
- Slater, E. A. and Charles, J. A. (1970). Archaeological classification by metal analysis. *Antiquity*, 44:207–213.
- SMAP database (1999). smap-01-99.mdb; database including the analyses published in (Junghans et al., 1960) and (Junghans et al., 1968b).
- Smith, C. S. (1968). The early history of casting, molds and the science of solidification. In *Metal transformations. Informal proceedings of the second Buhl International conference on materials, 1966*, pages 3–52, New York.
- Smith, C. S. (1988). *A history of metallography*. MIT Press, Cambridge, Massachusetts.
- Sperl, G. (1970). *Die Aussagekraft der chemischen Analysen antiker Kupferlegierungen*. PhD thesis, Montanuniversität Leoben, Leoben.
- Sperl, G. (1975). Metallurgische Unterscheidungskriterien metallischer Funde der Kupfer- und Bronzezeit Europas. *Fortschritte in der Metallographie. Praktische Metallographie Sonderband*, (4).

- Spirgatis, H. (1876). Ueber das Vorkommen von Arsen in antiken Bronzen. *Justus Liebig's Annalen der Chemie*, 181:394–396.
- Spiridonov, A. A. (1986). *Kupfer in der Geschichte der Menschheit*. VEB Deutscher Verlag für Grundstoffindustrie, Leipzig.
- Spittel, M., Spittel, T., and Teichert, H. (1994). Deformation properties of aluminium and aluminium alloys. Brochure: Mannesmann Demag Sack, Düsseldorf.
- Stahl, W. (1918). Erörterung und Ergänzung der Angaben über den Einfluß des Antimons auf die mechanischen Eigenschaften des Kupfers. *Metall und Erz*, XV(21):395–396.
- Stahl, W. (1925). Über wismuthaltiges Kupfer. *Metall und Erz*, XXII(17):421–422.
- Stan, M., Mihaiu, S., Crisan, D., and Zaharescu, M. (1998). Subsolidus phase equilibrium in the Cu-Sb-O system. *European Journal of Solid State and Inorganic Chemistry*, 35(3):243–254.
- Stein, F. (1976a). *Bronzezeitliche Hortfunde in Süddeutschland. Beiträge zur Interpretation einer Quellengattung*. Number 23 in Saarbrücker Beiträge zur Altertumskunde. Rudolf Habelt, Bonn.
- Stein, F. (1976b). *Katalog der vorgeschichtlichen Hortfunde in Süddeutschland*. Number 24 in Saarbrücker Beiträge zur Altertumskunde. Rudolf Habelt, Bonn.
- Subramanian, P. R. and Laughlin, D. E. (1994a). As-Cu (Arsenic-Copper). In Subramanian, P. R., editor, *Phase diagrams of binary copper alloys*, Monograph Series on Alloy Phase Diagrams, pages 43–52. The Materials Information Society, Materials Park, Ohio.
- Subramanian, P. R. and Laughlin, D. E. (1994b). Cu-Sb (Copper-Antimony). In Subramanian, P. R., editor, *Phase diagrams of binary copper alloys*, Monograph Series on Alloy Phase Diagrams, pages 372–383. The Materials Information Society, Materials Park, Ohio.
- Tedenac, J.-C. (1994). Arsenic-copper-antimony. In Petzow, G., editor, *Ternary alloys: a comprehensive compendium of evaluated constitutional data and phase diagrams*, volume 10, page 128. VCH, Weinheim.

Voce, E. (1961). Scientific evidence concerning metal-working techniques. *Man*, 61:68–71.

Winghart, S. (1990). Ein frühbronzezeitliches Ösenringdepot von Grub. *Das archäologische Jahr in Bayern*, pages 42–44.

Witter, W. (1953). Neues zu den Barrenring-Hortfunden im Vorlande der Ostalpen. *Prähistorische Zeitschrift*, 34/35:179–190.

Zwicker, U. (1991). Natural copper-arsenic alloys and smelted arsenic bronzes in early metal production. In Mohen, J.-P., editor, *Découverte du métal*, volume 2 of *Millénaires*, pages 331–340. Picard, Paris.

Zwicker, U., Greiner, H., Hofmann, K.-H., and Reithinger, M. (1992). Smelting, refining and alloying of copper and copper alloys in crucible furnaces during prehistoric up to Roman times. In Craddock, P. T. and Hughes, M., editors, *Furnaces and smelting technology in antiquity*, number 48 in Occasional Paper, pages 103–115. British Museum, London.



## **Appendix A**

### **X-ray fluorescence analyses of ingot torques**

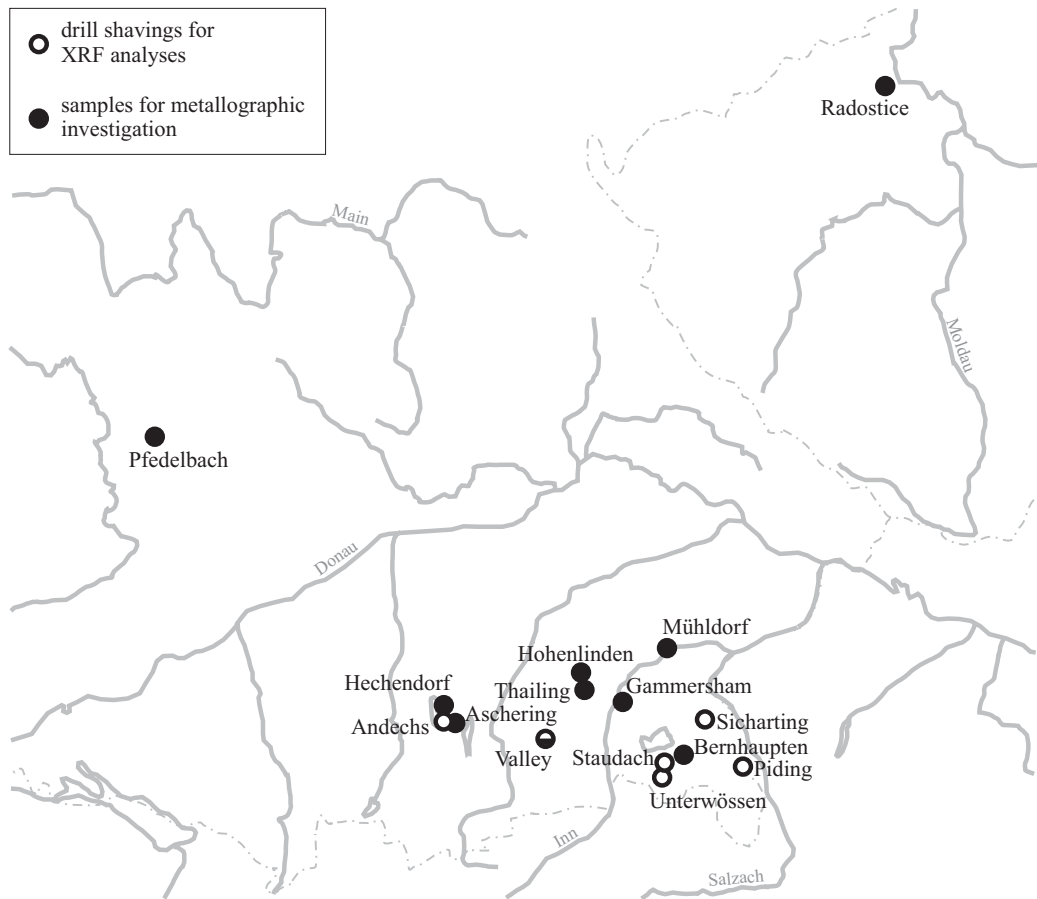


**Figure A.1:** Locations of the investigated hoards. The circles mark the hoards from which samples for XRF-analyses were available, the black dots mark the finds used for metallographic investigations.

**Table A.1:** X-ray fluorescence analyses of ingot torques from Andechs-Erling, Sickingarting and Unterwössen. Given are the mass fractions of the elements  $w$  and the material class according to Junghans et al. (1968b) (Fig. 2.1, p. 8).

Lab.-No.	original name	w(Cu) [%]	w(As) [%]	w(Sb) [%]	w(Ag) [%]	w(Bi) [%]	w(Fe) [%]	w(Co) [%]	w(Ni) [%]	w(Sn) [%]	w(Pb) [%]	mat. class
FG-990274	Andechs-E. I/1	95.5	2.20	1.12	0.98	0.065	< 0.05	0.007	< 0.010	< 0.005	< 0.01	C2
FG-990275	Andechs-E. I/2	95.3	1.70	1.74	0.97	0.052	< 0.05	< 0.005	0.048	< 0.005	0.01	C2D
FG-990276	Andechs-E. I/3	94.7	2.12	1.57	1.05	0.050	< 0.05	< 0.005	< 0.010	< 0.005	0.04	C2
FG-990277	Andechs-E. I/4	94.8	2.15	1.47	1.11	0.065	< 0.05	< 0.005	< 0.010	< 0.005	< 0.01	C2
FG-990278	Andechs-E. I/5	95.0	1.92	1.47	1.10	0.064	< 0.05	< 0.005	< 0.010	< 0.005	< 0.01	C2
FG-990279	Andechs-E. I/6	95.0	2.14	1.42	1.14	0.067	< 0.05	< 0.005	0.016	< 0.005	< 0.01	C2
FG-990280	Andechs-E. I/7	95.4	2.09	1.29	1.10	0.064	< 0.05	0.006	0.032	< 0.005	< 0.01	C2D
FG-990281	Andechs-E. I/8	95.2	2.05	1.12	1.11	0.056	< 0.05	< 0.005	< 0.010	< 0.005	0.01	C2
FG-990282	Andechs-E. I/9	96.1	1.88	0.96	0.80	0.050	< 0.05	< 0.005	0.012	< 0.005	< 0.01	C2
FG-990283	Andechs-E. II/1	94.6	2.80	1.22	1.08	0.076	< 0.05	< 0.005	0.015	< 0.005	< 0.01	C2
FG-990284	Andechs-E. II/2	94.4	2.30	1.30	1.19	0.202	< 0.05	< 0.005	0.014	< 0.005	< 0.01	C2C
FG-990285	Andechs-E. II/3	94.1	2.19	1.87	1.10	0.148	< 0.05	< 0.005	< 0.010	< 0.005	< 0.01	C2
FG-990286	Andechs-E. II/4	95.3	0.81	2.21	1.04	0.040	< 0.05	< 0.005	0.025	< 0.005	< 0.01	C2D
FG-990287	Andechs-E. II/5	94.7	2.90	0.80	1.13	0.069	< 0.05	< 0.005	0.014	< 0.005	< 0.01	C2
FG-990326	Sickingarting 1	94.9	2.04	1.63	1.19	0.043	< 0.05	< 0.005	< 0.010	< 0.005	< 0.01	C2
FG-990327	Sickingarting 2	95.3	1.31	2.04	0.91	0.035	< 0.05	< 0.005	< 0.010	0.005	< 0.01	C2
FG-010446	Unterwössen 1	99.6	0.075	0.012	0.012	< 0.005	0.10	< 0.005	0.064	0.015	0.02	FA
FG-010447	Unterwössen 2	99.7	0.053	0.007	0.005	< 0.005	0.10	< 0.005	0.059	0.011	0.01	FA
FG-010448	Unterwössen 3	99.7	0.047	0.009	0.014	< 0.005	< 0.05	0.009	0.047	0.013	0.03	FA
FG-010449	Unterwössen 4	99.8	0.030	0.008	0.007	< 0.005	< 0.05	0.012	0.039	0.006	0.02	FA
FG-010450	Unterwössen 5	99.8	0.046	0.007	< 0.005	< 0.005	< 0.05	0.010	0.040	< 0.005	0.03	FA

**Table A.2:** X-ray fluorescence analyses of ingot torques from Piding, continued on p.193. Given are the mass fractions of the elements  $w$  and the material class according to Junghans et al. (1968b) (Fig. 2.1, p. 8). The material classes printed in *italic* are analyses close to classification limits.

Lab-No.	original name	$w(\text{Cu})$ [%]	$w(\text{As})$ [%]	$w(\text{Sb})$ [%]	$w(\text{Ag})$ [%]	$w(\text{Bi})$ [%]	$w(\text{Fe})$ [%]	$w(\text{Co})$ [%]	$w(\text{Ni})$ [%]	$w(\text{Sn})$ [%]	$w(\text{Pb})$ [%]	mat. class
FG-990172	Piding 1	98.1	0.90	1.07	0.158	0.025	< 0.05	< 0.005	0.059	< 0.005	< 0.01	C6A
FG-990173	Piding 2	95.4	2.79	0.87	0.95	0.121	0.10	0.005	< 0.010	< 0.005	< 0.01	C2
FG-990174	Piding 3	95.1	2.87	1.05	1.05	0.179	< 0.05	< 0.005	0.012	0.010	< 0.01	C2C
FG-990175	Piding 4	95.5	2.63	1.05	0.99	0.127	< 0.05	< 0.005	< 0.010	< 0.005	< 0.01	C2
FG-990176	Piding 5	99.9	< 0.005	< 0.005	0.006	< 0.005	< 0.05	< 0.005	0.017	0.008	< 0.01	<i>E00FC</i>
FG-990177	Piding 6	99.3	0.054	< 0.005	0.015	< 0.005	0.12	0.008	0.079	0.35	< 0.01	FA
FG-990178	Piding 7	99.6	0.042	0.007	0.007	< 0.005	0.12	0.009	0.061	0.100	< 0.01	FA
FG-990179	Piding 8	95.6	2.62	0.86	0.94	0.125	< 0.05	< 0.005	< 0.010	< 0.005	< 0.01	C2
FG-990180	Piding 9	99.6	0.026	0.011	0.014	0.125	0.11	0.009	0.021	0.124	< 0.01	FA
FG-990181	Piding 10	95.8	2.46	0.82	0.89	0.132	< 0.05	< 0.005	< 0.010	0.012	0.01	C2
FG-990182	Piding 11	95.7	1.82	1.99	0.44	0.076	< 0.05	< 0.005	0.053	< 0.005	< 0.01	C2D
FG-990183	Piding 12	96.6	1.36	1.88	0.73	0.073	< 0.05	< 0.005	< 0.010	< 0.005	< 0.01	C2
FG-990184	Piding 13	99.6	0.086	0.017	0.009	< 0.005	< 0.05	< 0.005	0.162	0.010	< 0.01	FA
FG-990185	Piding 14	99.6	0.146	0.012	0.005	< 0.005	0.08	0.005	0.055	0.026	< 0.01	FA
FG-990186	Piding 15	99.7	0.029	0.008	0.005	< 0.005	0.09	0.012	0.022	0.022	< 0.01	FA
FG-990187	Piding 16	99.7	0.027	< 0.005	0.007	< 0.005	0.09	< 0.005	0.015	0.024	0.01	E01A
FG-990188	Piding 17	99.7	0.020	< 0.005	0.005	< 0.005	0.11	< 0.005	0.011	< 0.005	< 0.01	<i>E00FC</i>
FG-990189	Piding 18	99.7	0.023	< 0.005	< 0.005	< 0.005	0.09	0.007	0.017	0.012	< 0.01	<i>E00FC</i>
FG-990190	Piding 19	99.6	0.011	0.005	< 0.005	< 0.005	0.25	< 0.005	0.024	0.010	0.01	<i>FC</i>
FG-990191	Piding 20	99.8	0.009	< 0.005	< 0.005	< 0.005	< 0.05	< 0.005	0.028	< 0.005	< 0.01	<i>FCC2</i>
FG-990192	Piding 21	99.8	0.027	< 0.005	< 0.005	< 0.005	0.09	< 0.005	0.024	0.013	< 0.01	FA
FG-990193	Piding 22	95.8	2.40	0.90	1.03	0.104	< 0.05	< 0.005	< 0.010	< 0.005	< 0.01	C2
FG-990194	Piding 22A	94.6	3.00	1.07	1.14	0.155	< 0.05	< 0.005	< 0.010	< 0.005	< 0.01	C2
FG-990195	Piding 23	96.2	2.05	1.13	0.70	0.077	< 0.05	< 0.005	< 0.010	< 0.005	< 0.01	C2
FG-990196	Piding 24	99.8	0.018	< 0.005	0.010	< 0.005	0.10	< 0.005	< 0.010	0.011	< 0.01	<i>E00</i>

Table A.2: continued from p.192

Lab.-No.	original name	w(Cu) [%]	w(As) [%]	w(Sb) [%]	w(Ag) [%]	w(Bi) [%]	w(Fe) [%]	w(Co) [%]	w(Ni) [%]	w(Sn) [%]	w(Pb) [%]	mat. class
FG-990197	Piding 25	99.7	0.012	< 0.005	< 0.005	< 0.005	0.13	< 0.005	0.018	0.005	< 0.01	E00FC
FG-990198	Piding 26	96.0	1.95	1.01	1.06	0.132	< 0.05	< 0.005	< 0.010	< 0.005	< 0.01	C2
FG-990199	Piding 27	99.7	0.026	< 0.005	0.008	0.005	0.13	< 0.005	0.032	0.015	< 0.01	FA
FG-990200	Piding 28	94.8	2.43	1.28	1.21	0.091	< 0.05	0.007	0.019	< 0.005	< 0.01	C2
FG-990201	Piding 29	95.5	2.38	1.11	0.95	0.140	< 0.05	< 0.005	< 0.010	< 0.005	< 0.01	C2
FG-990202	Piding 31	99.8	0.03	< 0.005	< 0.005	< 0.005	0.09	< 0.005	< 0.010	0.009	< 0.01	E01A
FG-990203	Piding 32	99.8	0.019	< 0.005	< 0.005	< 0.005	0.09	< 0.005	0.018	0.009	< 0.01	E00FC
FG-990204	Piding 33	99.7	0.023	0.005	0.006	< 0.005	0.13	0.013	0.037	0.035	< 0.01	FC
FG-990205	Piding 34	95.7	2.32	1.22	0.97	0.109	< 0.05	< 0.005	< 0.010	0.016	< 0.01	C2
FG-990206	Piding 35	95.7	1.99	1.14	0.89	0.110	< 0.05	< 0.005	< 0.010	0.005	< 0.01	C2
FG-990207	Piding 36	95.3	2.80	1.50	1.00	0.129	< 0.05	0.006	< 0.010	< 0.005	< 0.01	C2
FG-990208	Piding 37	99.4	0.117	< 0.005	0.017	< 0.005	0.24	0.020	0.033	< 0.005	0.04	FA
FG-990209	Piding 38	99.7	0.022	0.012	< 0.005	< 0.005	0.08	0.022	0.052	0.011	< 0.01	FC
FG-990210	Piding 39	94.7	2.70	1.34	1.04	0.110	0.08	0.005	< 0.010	< 0.005	< 0.01	C2
FG-990211	Piding 40	99.6	0.105	0.016	0.012	< 0.005	0.10	0.008	0.089	0.01	< 0.01	FA
FG-990212	Piding 41	96.1	2.11	1.95	0.63	0.073	< 0.05	< 0.005	< 0.010	< 0.005	< 0.01	C2
FG-990213	Piding 42	99.3	0.085	< 0.005	0.012	< 0.005	0.34	0.012	0.025	0.141	< 0.01	FA
FG-990214	Piding 42A	99.4	0.074	0.019	0.021	< 0.005	0.24	0.006	0.026	0.143	< 0.01	FA
FG-990215	Piding 43	99.5	0.143	0.079	0.079	0.008	< 0.05	0.009	0.053	0.04	< 0.01	C5
FG-990216	Piding 44	96.3	2.28	1.58	0.39	0.026	< 0.05	< 0.005	< 0.010	< 0.005	< 0.01	C2
FG-990217	Piding 45	99.4	0.028	0.015	0.015	< 0.005	0.16	< 0.005	0.053	0.192	0.02	FA
FG-990218	Piding 46	99.8	0.008	< 0.005	< 0.005	< 0.005	< 0.05	0.005	< 0.010	< 0.005	< 0.01	E00
FG-990219	Piding 47	95.4	2.58	1.12	1.07	0.140	< 0.05	< 0.005	< 0.010	0.008	< 0.01	C2
FG-990220	Piding 48	96.1	1.57	1.50	0.97	0.116	< 0.05	< 0.005	< 0.010	< 0.005	0.02	C2
FG-990221	Piding 49	95.7	2.33	1.54	0.96	0.125	< 0.05	< 0.005	< 0.010	0.011	< 0.01	C2

Table A.2: continued from p.193

Lab.-No.	original name	w(Cu) [%]	w(As) [%]	w(Sb) [%]	w(Ag) [%]	w(Bi) [%]	w(Fe) [%]	w(Co) [%]	w(Ni) [%]	w(Sn) [%]	w(Pb) [%]	mat. class
FG-990222	Piding 50	99.8	< 0.005	0.007	0.010	< 0.005	0.06	< 0.005	0.023	< 0.005	< 0.01	FC
FG-990223	Piding 51	96.6	1.52	0.75	1.14	0.071	< 0.05	0.006	< 0.010	< 0.005	< 0.01	C2
FG-990224	Piding 52	96.2	1.66	0.78	1.31	0.077	< 0.05	< 0.005	0.016	< 0.005	< 0.01	C2
FG-990225	Piding 53	99.7	0.012	< 0.005	0.009	0.005	0.11	< 0.005	0.027	< 0.005	0.02	C1A
FG-990226	Piding 54	99.6	0.069	0.014	< 0.005	< 0.005	0.16	< 0.005	0.052	0.012	< 0.01	FA
FG-990227	Piding 55	99.7	0.008	< 0.005	0.005	< 0.005	0.12	0.005	0.031	0.015	< 0.01	FC
FG-990228	Piding 56	99.4	0.056	0.005	0.011	< 0.005	0.29	0.016	0.032	< 0.005	< 0.01	FA
FG-990229	Piding 57	97.8	0.85	0.70	0.60	0.059	< 0.05	< 0.005	0.026	0.022	< 0.01	C2D
FG-990230	Piding 58	99.8	0.036	0.008	0.005	< 0.005	< 0.05	< 0.005	0.032	0.015	< 0.01	FA
FG-990231	Piding 59	95.8	1.74	1.04	1.29	0.172	< 0.05	< 0.005	< 0.010	0.011	0.02	C2C
FG-990232	Piding 59A	95.9	1.82	1.11	1.41	0.169	0.08	< 0.005	< 0.010	< 0.005	< 0.01	C2C
FG-990233	Piding 60	95.6	2.08	1.31	1.17	0.125	0.09	< 0.005	< 0.010	0.020	< 0.01	C2

**Table A.3:** X-ray fluorescence analyses of ingot torques from Staudach-Egerndach. Given are the mass fractions of the elements  $w$  and the material class according to Junghans et al. (1968b) (Fig. 2.1, p. 8). The material classes printed in *italic* are analyses close to classification limits.

Lab.-No.	original name	w(Cu) [%]	w(As) [%]	w(Sb) [%]	w(Ag) [%]	w(Bi) [%]	w(Fe) [%]	w(Co) [%]	w(Ni) [%]	w(Sn) [%]	w(Pb) [%]	mat. class
FG-990250	Staudach-E. 1	94.6	2.34	1.70	0.99	0.061	< 0.05	< 0.005	< 0.010	< 0.005	0.02	C2
FG-990251	Staudach-E. 2	94.0	2.37	1.75	1.21	0.208	< 0.05	< 0.005	< 0.010	< 0.005	< 0.01	C2C
FG-990252	Staudach-E. 3	95.1	2.44	1.06	1.30	0.053	< 0.05	< 0.005	< 0.010	< 0.005	< 0.01	C2
FG-990253	Staudach-E. 4	94.0	2.49	2.17	1.04	0.124	< 0.05	< 0.005	< 0.010	< 0.005	< 0.01	C2
FG-990254	Staudach-E. 5	94.9	2.27	1.55	0.95	0.090	< 0.05	< 0.005	0.021	< 0.005	< 0.01	C2D
FG-990255	Staudach-E. 6	94.5	2.98	0.97	1.14	0.116	< 0.05	< 0.005	0.015	0.005	< 0.01	C2
FG-990256	Staudach-E. 7	94.6	2.60	1.32	1.21	0.162	< 0.05	< 0.005	< 0.010	< 0.005	< 0.01	C2C
FG-990257	Staudach-E. 8	94.8	2.06	1.36	1.27	0.191	< 0.05	< 0.005	0.021	0.006	< 0.01	C2D
FG-990258	Staudach-E. 9	94.5	1.88	1.99	1.18	0.163	< 0.05	< 0.005	< 0.010	< 0.005	< 0.01	C2C
FG-990259	Staudach-E. 10	95.6	2.01	0.94	1.20	0.076	< 0.05	< 0.005	< 0.010	0.006	< 0.01	C2
FG-990260	Staudach-E. 11	95.7	1.83	1.44	0.85	0.067	< 0.05	< 0.005	< 0.010	< 0.005	0.05	C2
FG-990261	Staudach-E. 12	95.2	2.16	1.41	1.00	0.043	< 0.05	< 0.005	0.016	< 0.005	0.04	C2
FG-990262	Staudach-E. 13	95.6	1.64	1.42	1.05	0.067	< 0.05	0.009	0.015	0.030	< 0.01	C2
FG-990263	Staudach-E. 14	95.1	1.96	1.45	1.00	0.076	< 0.05	< 0.005	< 0.010	< 0.005	< 0.01	C2
FG-990264	Staudach-E. 15	95.0	2.10	1.66	1.05	0.073	< 0.05	< 0.005	< 0.010	0.006	< 0.01	C2
FG-990265	Staudach-E. 16	96.3	1.73	0.81	0.82	0.045	< 0.05	< 0.005	< 0.010	< 0.005	< 0.01	C2
FG-990266	Staudach-E. 17	95.2	2.12	1.32	0.99	0.072	< 0.05	0.005	< 0.010	< 0.005	< 0.01	C2
FG-990267	Staudach-E. 18	95.8	1.62	1.27	0.97	0.076	< 0.05	< 0.005	< 0.010	< 0.005	< 0.01	C2
FG-990268	Staudach-E. 19	95.6	1.87	1.12	0.91	0.088	< 0.05	0.008	0.017	< 0.005	< 0.01	C2
FG-990269	Staudach-E. 20	94.4	2.09	1.75	0.98	0.094	< 0.05	< 0.005	< 0.010	< 0.005	< 0.01	C2
FG-990270	Staudach-E. I	95.2	1.96	1.47	1.05	0.057	< 0.05	< 0.005	< 0.010	< 0.005	< 0.01	C2
FG-990271	Staudach-E. II	95.1	1.68	1.80	0.94	0.068	< 0.05	< 0.005	< 0.010	< 0.005	0.02	C2
FG-990272	Staudach-E. III	96.5	1.50	0.93	0.72	0.029	< 0.05	< 0.005	0.031	0.005	< 0.01	C2D
FG-990273	Staudach-E. IV	94.7	2.44	1.54	0.95	0.056	< 0.05	< 0.005	0.027	< 0.005	< 0.01	C2D

**Table A.4:** X-ray fluorescence analyses of ingot torques from Valley, continued on p.197. Given are the mass fractions of the elements  $w$  and the material class according to Junghans et al. (1968b) (Fig. 2.1, p. 8). The material classes printed in italic are analyses close to classification limits.

Lab.-No.	original name	$w(\text{Cu})$ [%]	$w(\text{As})$ [%]	$w(\text{Sb})$ [%]	$w(\text{Ag})$ [%]	$w(\text{Bi})$ [%]	$w(\text{Fe})$ [%]	$w(\text{Co})$ [%]	$w(\text{Ni})$ [%]	$w(\text{Sn})$ [%]	$w(\text{Pb})$ [%]	mat. class
FG-990069	Valley V/1	95.7	2.05	1.28	0.49	0.018	< 0.05	< 0.005	0.030	< 0.005	< 0.01	C5
FG-990070	Valley II/1	95.0	2.15	1.33	0.86	0.075	< 0.05	0.005	0.020	< 0.005	< 0.01	C2
FG-990071	Valley II/2	95.1	2.05	1.26	1.34	0.082	< 0.05	< 0.005	0.023	0.009	< 0.01	C2D
FG-990072	Valley II/3	95.2	2.22	1.30	0.53	0.017	< 0.05	< 0.005	0.039	< 0.005	< 0.01	C5
FG-990073	Valley II/4	99.4	0.065	0.012	0.007	< 0.005	0.09	0.039	0.256	< 0.005	0.05	FA
FG-990074	Valley II/5	95.2	1.84	1.12	1.11	0.074	< 0.05	< 0.005	0.034	0.014	< 0.01	C2D
FG-990075	Valley III/1	94.3	2.05	1.75	1.00	0.053	< 0.05	< 0.005	< 0.010	< 0.005	< 0.01	C2
FG-990076	Valley III/2	95.9	2.08	1.17	0.51	0.034	< 0.05	< 0.005	0.039	< 0.005	< 0.01	C2D
FG-990077	Valley III/3	94.9	1.93	1.58	0.99	0.046	< 0.05	< 0.005	0.023	< 0.005	< 0.01	C2D
FG-990078	Valley III/4	95.9	1.57	1.14	1.00	0.059	< 0.05	< 0.005	0.031	< 0.005	< 0.01	C2D
FG-990079	Valley III/5	94.1	2.35	1.71	1.21	0.069	< 0.05	< 0.005	< 0.010	< 0.005	< 0.01	C2
FG-990080	Valley IV/1	95.7	1.82	1.15	1.01	0.057	< 0.05	< 0.005	0.015	< 0.005	< 0.01	C2
FG-990081	Valley IV/2	95.0	1.83	1.46	0.92	0.046	< 0.05	< 0.005	0.020	< 0.005	< 0.01	C2
FG-990082	Valley IV/3	95.0	2.04	1.40	1.05	0.065	< 0.05	< 0.005	0.026	< 0.005	< 0.01	C2D
FG-990083	Valley IV/4	95.2	1.80	1.49	0.89	0.049	< 0.05	< 0.005	0.032	< 0.005	< 0.01	C2D
FG-990084	Valley IV/5	95.4	1.84	1.19	0.96	0.049	< 0.05	< 0.005	0.033	< 0.005	< 0.01	C2D
FG-990085	Valley V/1	94.8	2.19	1.43	1.06	0.056	< 0.05	< 0.005	0.013	< 0.005	< 0.01	C2
FG-990086	Valley V/2	95.2	1.84	1.33	0.97	0.058	< 0.05	< 0.005	0.036	< 0.005	< 0.01	C2D
FG-990087	Valley V/3	94.8	1.91	1.44	0.94	0.054	< 0.05	< 0.005	0.056	< 0.005	< 0.01	C2D
FG-990088	Valley V/4	95.5	1.79	1.36	0.87	0.051	< 0.05	< 0.005	0.018	< 0.005	< 0.01	C2
FG-990089	Valley V/5	94.5	1.96	1.64	1.10	0.058	< 0.05	< 0.005	0.019	< 0.005	< 0.01	C2
FG-990090	Valley VI/1	95.3	2.33	1.42	0.52	0.030	< 0.05	< 0.005	0.034	< 0.005	< 0.01	C2D
FG-990091	Valley VI/2	94.5	2.36	1.50	0.62	0.032	< 0.05	< 0.005	0.040	0.005	< 0.01	C2D
FG-990092	Valley VI/3	94.8	2.38	1.37	0.75	0.035	< 0.05	< 0.005	0.011	< 0.005	< 0.01	C2
FG-990093	Valley VI/4	95.8	2.06	1.17	0.67	0.040	< 0.05	< 0.005	0.033	< 0.005	< 0.01	C2D
FG-990094	Valley VI/5	95.1	2.40	1.40	0.57	0.029	< 0.05	< 0.005	< 0.010	< 0.005	< 0.01	C2



Table A.4: continued from p.196

Lab.-No.	original name	w(Cu) [%]	w(As) [%]	w(Sb) [%]	w(Ag) [%]	w(Bi) [%]	w(Fe) [%]	w(Co) [%]	w(Ni) [%]	w(Sn) [%]	w(Pb) [%]	mat. class
FG-990095	Valley VII/1	95.2	1.87	1.44	0.95	0.060	< 0.05	< 0.005	0.040	< 0.005	< 0.01	C2D
FG-990096	Valley VII/2	95.0	1.97	1.50	1.03	0.064	< 0.05	0.006	0.034	< 0.005	< 0.01	C2D
FG-990097	Valley VII/3	95.1	1.96	1.46	0.97	0.053	< 0.05	< 0.005	0.016	< 0.005	< 0.01	C2
FG-990098	Valley VII/4	95.1	1.96	1.40	0.99	0.067	< 0.05	< 0.005	0.022	< 0.005	< 0.01	C2D
FG-990099	Valley VII/5	95.7	1.88	1.15	1.00	0.058	< 0.05	< 0.005	0.025	< 0.005	< 0.01	C2D
FG-990100	Valley VIII/1	99.5	0.087	0.018	0.008	< 0.005	0.07	0.042	0.213	0.006	< 0.01	FA
FG-990101	Valley VIII/2	99.6	0.076	0.020	0.012	< 0.005	< 0.05	< 0.005	0.119	0.009	< 0.01	FA
FG-990102	Valley VIII/3	99.4	0.095	0.011	0.011	< 0.005	0.08	0.028	0.251	0.009	< 0.01	FA
FG-990103	Valley VIII/4	99.4	0.126	0.011	< 0.005	< 0.005	0.12	0.024	0.199	0.017	< 0.01	FA
FG-990104	Valley VIII/5	99.4	0.179	0.016	0.013	< 0.005	0.05	0.032	0.181	0.010	< 0.01	FA
FG-990105	Valley IX/1	95.5	2.12	1.43	0.49	0.024	< 0.05	< 0.005	0.022	< 0.005	< 0.01	C2D
FG-990106	Valley IX/2	95.7	2.13	1.29	0.53	0.023	< 0.05	< 0.005	0.018	< 0.005	< 0.01	C2
FG-990107	Valley IX/3	95.1	2.32	1.47	0.56	0.027	< 0.05	0.005	< 0.010	< 0.005	0.02	C2
FG-990108	Valley IX/4	95.7	2.18	1.35	0.48	0.019	< 0.05	0.005	0.016	< 0.005	< 0.01	G
FG-990109	Valley IX/5	95.3	2.24	1.42	0.55	0.028	< 0.05	0.009	0.035	< 0.005	< 0.01	C2D
FG-990110	Valley X/1	99.6	0.150	< 0.005	0.005	< 0.005	0.06	0.012	0.112	< 0.005	< 0.01	FA
FG-990111	Valley X/2	99.4	0.055	0.010	0.006	0.006	0.13	0.047	0.239	0.005	0.01	FA
FG-990112	Valley X/3	99.2	0.277	0.014	0.019	< 0.005	0.08	0.045	0.268	0.026	< 0.01	FA
FG-990113	Valley X/4	99.4	0.093	0.008	0.008	< 0.005	0.14	0.039	0.212	< 0.005	< 0.01	FA
FG-990114	Valley X/5	99.3	0.049	0.005	0.015	< 0.005	0.24	0.049	0.218	< 0.005	< 0.01	FA
FG-990115	Valley XI/1	99.2	0.089	< 0.005	0.009	< 0.005	0.13	0.009	0.400	0.012	< 0.01	FA
FG-990116	Valley XI/2	99.5	0.054	< 0.005	0.011	< 0.005	0.06	0.039	0.251	0.009	0.0	FAI
FG-990117	Valley XI/3	99.5	0.043	< 0.005	0.009	< 0.005	0.09	0.038	0.222	0.006	< 0.01	FA
FG-990118	Valley XI/4	99.5	0.094	< 0.005	0.008	< 0.005	0.07	0.034	0.162	0.008	< 0.01	FA
FG-990119	Valley XI/5	99.6	0.085	< 0.005	0.010	0.005	< 0.05	0.013	0.161	0.008	0.01	FA

**Table A.5:** Composition of material class FA (low-impurity copper). Given are the average mass fractions of the elements  $\bar{w}$  and the standard deviations.

hoard find	$\bar{w}(\text{Cu})$ [%]	$\bar{w}(\text{As})$ [%]	$\bar{w}(\text{Sb})$ [%]	$\bar{w}(\text{Ag})$ [%]	$\bar{w}(\text{Bi})$ [%]	$\bar{w}(\text{Fe})$ [%]	$\bar{w}(\text{Co})$ [%]	$\bar{w}(\text{Ni})$ [%]	$\bar{w}(\text{Sn})$ [%]	$\bar{w}(\text{Pb})$ [%]
Piding	99.6	0.063	0.008	0.010	< 0.005	0.14	0.007	0.050	0.073	< 0.01
	$\pm 0.2$	$\pm 0.037$	$\pm 0.007$	$\pm 0.006$		$\pm 0.10$	$\pm 0.006$	$\pm 0.036$	$\pm 0.097$	
Unterwössen	99.7	0.050	0.009	0.008	< 0.005	< 0.05	0.006	0.050	0.009	0.02
	$\pm 0.1$	$\pm 0.016$	$\pm 0.002$	$\pm 0.006$			$\pm 0.006$	$\pm 0.011$	$\pm 0.006$	$\pm 0.01$
Valley	99.4	0.101	0.008	0.009	< 0.005	0.09	0.031	0.217	0.008	< 0.01
	$\pm 0.1$	$\pm 0.060$	$\pm 0.007$	$\pm 0.004$		$\pm 0.06$	$\pm 0.015$	$\pm 0.068$	$\pm 0.007$	

**Table A.6:** Composition of material class C2 (ingot torque metal). Given are the average mass fractions of the elements  $\bar{w}$  and the standard deviations.

hoard find	$\bar{w}(\text{Cu})$ [%]	$\bar{w}(\text{As})$ [%]	$\bar{w}(\text{Sb})$ [%]	$\bar{w}(\text{Ag})$ [%]	$\bar{w}(\text{Bi})$ [%]	$\bar{w}(\text{Fe})$ [%]	$\bar{w}(\text{Co})$ [%]	$\bar{w}(\text{Ni})$ [%]	$\bar{w}(\text{Sn})$ [%]	$\bar{w}(\text{Pb})$ [%]
Andechs- Erling	95.0	2.24	1.30	1.06	0.071	< 0.05	< 0.005	< 0.010	< 0.005	< 0.01
	$\pm 0.5$	$\pm 0.34$	$\pm 0.32$	$\pm 0.10$	$\pm 0.028$					
Piding	95.7	2.26	1.21	0.96	0.108	< 0.05	< 0.005	< 0.010	< 0.005	< 0.01
	$\pm 0.5$	$\pm 0.44$	$\pm 0.33$	$\pm 0.20$	$\pm 0.030$					
Staudach- Egerndach	95.2	2.06	1.40	1.02	0.074	< 0.05	< 0.005	< 0.010	< 0.005	< 0.01
	$\pm 0.6$	$\pm 0.35$	$\pm 0.35$	$\pm 0.12$	$\pm 0.022$					
Valley	95.0	2.10	1.45	0.88	0.049	< 0.05	< 0.005	0.012	< 0.005	< 0.01
	$\pm 0.5$	$\pm 0.22$	$\pm 0.17$	$\pm 0.22$	$\pm 0.016$			$\pm 0.008$		

**Table A.7:** Correlation of typological features (priv. comm. S. Möslein) and composition of the ingot torques from Piding, Lkr. Berchtesgadener Land. Ingot torques marked with ‘?’ were poorly preserved or the features were not clearly visible, features marked with a circle are not certain. Continued on p. 200

ingot torque		reworked	forging seam	ingot torque metal	low impurity copper
bundle 1	36	●		●	
	37	●			●
	38	?			●
	39	●	●	●	
	40	●	●		●
bundle 2	41	●	●	●	
	42	●			●
	43	?	○		●
	44	●	●	●	
	45	●			●
bundle 3	1	●	●	●	
	2	●	○	●	
	3	?	?	●	
	4	●		●	
	5	●	●		●
bundle 4	56	●			●
	57	●		●	
	58	●			●
	59	●	●	●	
	60	●	●	●	
bundle 5	6	●			●
	7	●	●		●
	8	●	●	●	
	9	●			●

**Table A.7:** continued from p. 199

ingot torque		reworked	forging seam	ingot torque metal	low impurity copper
bundle 6	10	●	●	●	
	11	●	●	●	
	12	●	●	●	
	13	●			●
	14	?			●
	15	●			●
bundle 7	31	●			●
	32				●
	33	●			●
	34	●	●	●	
	35	●	●	●	
bundle 8	25	●			●
	26	●		●	
	27	●			●
	28=30	●	●	●	
	29	●	●	●	
bundle 9	21	●	○		●
	22	●	●	●	
	22A	●		●	
	23	●	●	●	
	24	●			●
bundle 10	16	?			●
	17	●			●
	18	●			●
	19	?			●
	20	●			●

**Table A.7:** continued from p. 200

ingot torque		reworked	forging seam	ingot torque metal	low impurity copper
bundle 11	46	●			●
	47	●	●	●	
	48	●		●	
	49	●	●	●	
	50	●			●
	51	●	●	●	
	52	●	●	●	
	53	●			●
	54	●			●
	55	●			●

**Table A.8:** Correlation of typological features (priv. comm. S. Möslein) and composition of the ingot torques from Valley, Lkr. Miesbach. Continued on p. 203

ingot torque	reworked	forging seam	ingot torque metal	low impurity copper
bundle I I/1	•	•	•	
bundle II II/1	•	•	•	
II/2	•	•	•	
II/3	•	•	•	
II/4				•
II/5	•	•	•	
bundle III III/1	•	•	•	
III/2	•	•	•	
III/3	•	•	•	
III/4	•	•	•	
III/5	•	•	•	
bundle IV IV/1	•	•	•	
IV/2	•	•	•	
IV/3	•	•	•	
IV/4	•	•	•	
IV/5	•	•	•	
bundle V V/1	•	•	•	
V/2	•	•	•	
V/3	•	•	•	
V/4	•	•	•	
V/5	•	•	•	
bundle VI VI/1	•	•	•	
VI/2	•	•	•	
VI/3	•	•	•	
VI/4	•	•	•	
VI/5	•	•	•	

Table A.8: continued from p. 202

ingot torque		reworked	forging seam	ingot torque metal	low impurity copper
bundle VII	VII/1	●	●	●	
	VII/2	●	●	●	
	VII/3	●	●	●	
	VII/4	●	●	●	
	VII/5	●	●	●	
bundle VIII	VIII/1				●
	VIII/2				●
	VIII/3				●
	VIII/4				●
	VIII/5				●
bundle IX	IX/1	●	●	●	
	IX/2	●	●	●	
	IX/3	●	●	●	
	IX/4	●	●	●	
	IX/5	●	●	●	
bundle X	X/1				●
	X/2				●
	X/3				●
	X/4				●
	X/5				●
bundle XI	XI/1				●
	XI/2				●
	XI/3				●
	XI/4				●
	XI/5				●





## **Appendix B**

### **Metallographic investigations of ingot torques**

Table B.1: Provenance of investigated ingot torques and fragments

ingot torque/ fragment	provenance	museum	inventory number
Asch1	Aschering, Kr. Starnberg	Prähistorische Staatssammlung München	1921.8
Asch2	Aschering, Kr. Starnberg	Prähistorische Staatssammlung München	1921.8
Ber1	Bernhaupten, Kr. Traunstein	Prähistorische Staatssammlung München	A 521
Ber3	Bernhaupten, Kr. Traunstein	Prähistorische Staatssammlung München	A 521
Gam1	Gammersham, Kr. Wasserburg am Inn	Prähistorische Staatssammlung München	1910.143
Gam2	Gammersham, Kr. Wasserburg am Inn	Prähistorische Staatssammlung München	1910.143
Hech1	Hechendorf am Pilsensee, Kr. Starnberg	Prähistorische Staatssammlung München	1939.2
Hech2	Hechendorf am Pilsensee, Kr. Starnberg	Prähistorische Staatssammlung München	1939.2
Hohl1	Hohenlinden-Mühlhausen, Kr. Ebersberg	Prähistorische Staatssammlung München	H. V. 32
Mühl1	Mühlendorf am Inn, Kr. Mühlhof	Prähistorische Staatssammlung München	1890.420
Pfe10	Pfedelbach-Untersteinbach, Hohenlohekreis	Landesdenkmalamt Baden-Württemberg, Stuttgart	
Pfe14	Pfedelbach-Untersteinbach, Hohenlohekreis	Landesdenkmalamt Baden-Württemberg, Stuttgart	
Rad2	Radosvice, okr. Litomeřice	Okresní vlastivědné muzeum Litomeřice	275
Rad4	Radosvice, okr. Litomeřice	Okresní vlastivědné muzeum Litomeřice	303
Thal1	Thalting, Kr. Ebersberg	Prähistorische Staatssammlung München	1954/10i
Val1	Valley, Kr. Miesbach	private owner	
Val2	Valley, Kr. Miesbach	private owner	
Val3	Valley, Kr. Miesbach	private owner	
Val4	Valley, Kr. Miesbach	private owner	
Val5	Valley, Kr. Miesbach	private owner	
Val6	Valley, Kr. Miesbach	private owner	

**Table B-2:** X-ray fluorescence analyses of metallographic sections from ingot torques and fragments. Given are the mass fractions of the elements  $w$  and the material class according to Junghans et al. (1968b) (Fig. 2.1, p. 8). The material classes printed in *italic* are analyses close to classification limits.

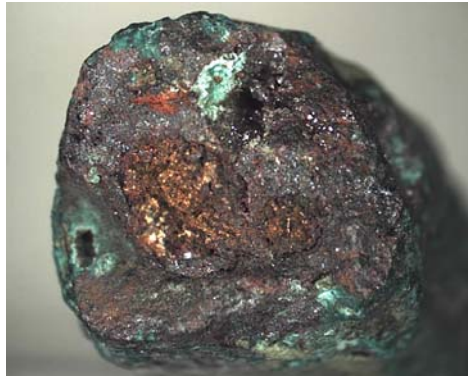
Lab.- No.	provenance	$w(\text{Cu})$ [%]	$w(\text{As})$ [%]	$w(\text{Sb})$ [%]	$w(\text{Ag})$ [%]	$w(\text{Bi})$ [%]	$w(\text{Fe})$ [%]	$w(\text{Co})$ [%]	$w(\text{Ni})$ [%]	$w(\text{Sn})$ [%]	$w(\text{Pb})$ [%]	mat.
Asch1	Aschering	94.9	1.88	1.25	1.71	0.118	< 0.05	< 0.005	0.014	0.049	< 0.01	C2
Asch2	Aschering	94.3	2.72	1.31	0.92	0.127	0.06	< 0.005	0.019	0.400	< 0.01	C2
Ber1	Bernhaupten	99.7	0.10	0.03	0.02	< 0.005	0.07	< 0.005	< 0.010	0.020	< 0.01	G
Ber3	Bernhaupten	94.3	2.49	1.87	1.02	0.240	< 0.05	< 0.005	0.010	< 0.005	< 0.01	C2C
Gam1	Gammersham	93.6	2.93	1.76	1.22	0.170	< 0.05	< 0.005	0.048	0.182	< 0.01	C2D
Gam2	Gammersham	94.0	2.52	1.58	1.56	0.166	< 0.05	< 0.005	0.017	0.064	< 0.01	C2C
Hech1	Hechendorf	99.7	0.041	0.008	0.106	< 0.005	< 0.05	0.006	0.021	0.035	< 0.01	FA
Hech2	Hechendorf	99.7	0.039	0.034	0.009	< 0.005	0.07	< 0.005	0.076	0.007	< 0.01	FG
Hohl1	Hohenlinden- Mühlhausen	94.6	2.06	1.56	1.28	0.126	< 0.05	0.005	0.032	0.152	0.01	C2D
Müh1	Mühldorf	94.1	2.37	1.58	1.05	0.237	0.14	0.011	0.035	0.320	< 0.01	C2D
Pfe10	Pfedelbach- Untersteinbach	95.5	1.95	1.23	0.98	0.211	< 0.05	0.006	< 0.010	< 0.005	< 0.01	C2C
Pfe14	Pfedelbach- Untersteinbach	95.2	2.05	1.30	1.22	0.108	< 0.05	< 0.005	< 0.010	< 0.005	< 0.01	C2
Rad2	Radostice	94.5	2.06	1.86	1.11	0.293	< 0.05	< 0.005	0.022	0.045	< 0.01	C2D
Rad4	Radostice	95.2	2.16	1.30	1.00	0.177	< 0.05	< 0.005	0.029	0.052	< 0.01	C2D
Tha1	Thailing	95.0	1.82	1.50	1.26	0.310	< 0.05	< 0.005	< 0.010	0.018	0.02	C2C

Table B.2: continued from p.207

Lab.- No.	provenance	w(Cu) [%]	w(As) [%]	w(Sb) [%]	w(Ag) [%]	w(Bi) [%]	w(Fe) [%]	w(Co) [%]	w(Ni) [%]	w(Sn) [%]	w(Pb) [%]	mat. class
Val1a	Valley	99.5	0.049	0.005	< 0.005	< 0.005	0.07	0.036	0.203	< 0.005	0.02	FA
Val1b	Valley	99.4	0.082	0.009	0.007	< 0.005	0.15	0.034	0.165	0.009	0.01	FA
Val2a	Valley	95.6	1.82	1.43	0.92	0.081	< 0.05	0.007	0.020	< 0.005	< 0.01	C2
Val2b	Valley	95.3	1.97	1.53	0.99	0.090	< 0.05	0.010	0.012	< 0.005	< 0.01	C2
Val2c	Valley	94.4	1.92	1.60	1.43	0.102	0.17	< 0.005	< 0.010	< 0.005	0.23	C2
Val3a	Valley	99.3	0.055	< 0.005	0.01	< 0.005	0.22	0.064	0.215	< 0.005	< 0.01	FA
Val3b	Valley	99.3	0.054	< 0.005	0.007	< 0.005	0.28	0.057	0.231	< 0.005	< 0.01	FA
Val3c	Valley	99.0	0.071	0.01	0.034	0.006	0.41	0.065	0.204	< 0.005	0.04	FA
Val4a	Valley	99.5	0.06	< 0.005	0.01	< 0.005	0.06	0.032	0.205	< 0.005	< 0.01	FA
Val4b	Valley	99.5	0.062	0.008	0.016	< 0.005	0.08	0.043	0.182	< 0.005	< 0.01	FA
Val5a	Valley	95.2	2.08	1.47	1.02	0.105	< 0.05	0.007	0.022	< 0.005	< 0.01	C2D
Val5b	Valley	95.6	1.87	1.34	0.98	0.094	< 0.05	< 0.005	0.014	< 0.005	< 0.01	C2
Val6a	Valley	96.6	1.55	1.28	0.45	0.023	< 0.05	0.007	0.047	< 0.005	< 0.01	C2D
Val6b	Valley	96.9	1.42	1.17	0.38	0.027	< 0.05	< 0.005	0.068	< 0.005	< 0.01	C2D

**Table B.3:** Low load Vickers hardness values HV0.2 for the investigated samples from ingot torques and fragments. The hardness was measured from the surface towards the centre of the sample.

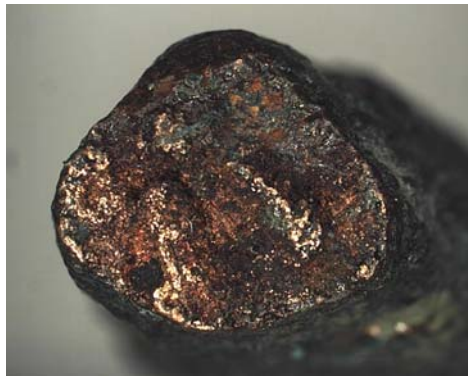
Lab.-No.	HV0.2		
	surface → centre		
Asch1	81.28	75.66	77.90
Asch2	108.72	92.91	75.13
Ber1	77.10	78.46	55.01
Ber3	71.52	68.32	66.43
Gam1	131.44	93.49	95.93
Gam2	78.85	73.06	63.73
Hech1	63.98	62.71	51.40
Hech2	91.36	79.73	83.73
Hoh1	111.62	93.08	72.64
Müh1	63.94	67.28	59.05
Pfe10	73.40	70.80	63.20
Pfe14	80.40	68.10	59.60
Rad2	87.67	81.41	81.77
Rad4	84.26	69.85	62.17
Tha1	89.61	72.61	66.42
VAL1a	73.58	69.60	64.14
VAL1b	61.35	60.95	57.81
VAL2a	79.61	78.56	73.35
VAL2b	69.63	64.75	59.97
VAL2c	90.16	78.91	73.66
VAL3a	68.25	66.31	54.80
VAL3b	61.13	57.83	55.23
VAL3c	68.51	61.43	57.00
VAL4a	67.71	65.03	59.78
VAL4b	60.96	58.25	56.30
VAL5a	78.33	75.27	67.78
VAL5b	89.20	80.65	71.03
VAL6a	76.97	61.92	57.84
VAL6b	83.87	72.52	62.77



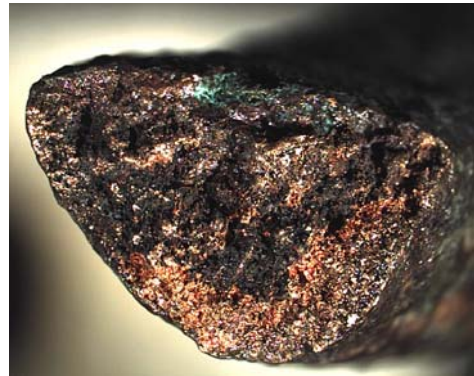
Ber1  
mixed bending fracture with pores



Ber3  
brittle fracture with patinated crack  
and copper-coloured residual fracture

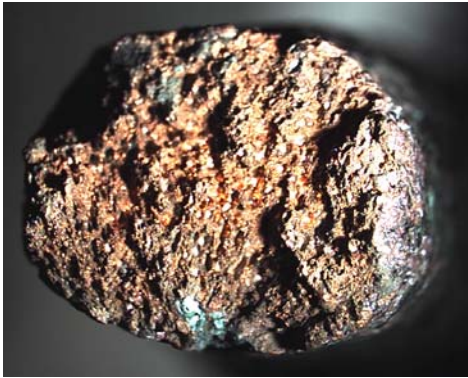


Gam1  
mixed fracture, slightly notched



Gam2  
mixed fracture with patinated crack  
and copper-coloured residual fracture

**Figure B.1:** Fracture appearance of ingot torque fragments from Bernhaupten (Ber1 and Ber3) and Gammersham (Gam1 and Gam2) .



Hech1  
fissured, porous fracture



Hech2  
mixed bending fracture



Hoh1  
low deformation bending fracture  
with patinated crack and copper-  
coloured residual fracture



Müh1  
mixed bending fracture

**Figure B.2:** Fracture appearance of ingot torque fragments from Hechendorf (Hech1 and Hech2), Hohenlinden-Mühlhausen (Hoh1), and Mühdorf am Inn (Müh1).

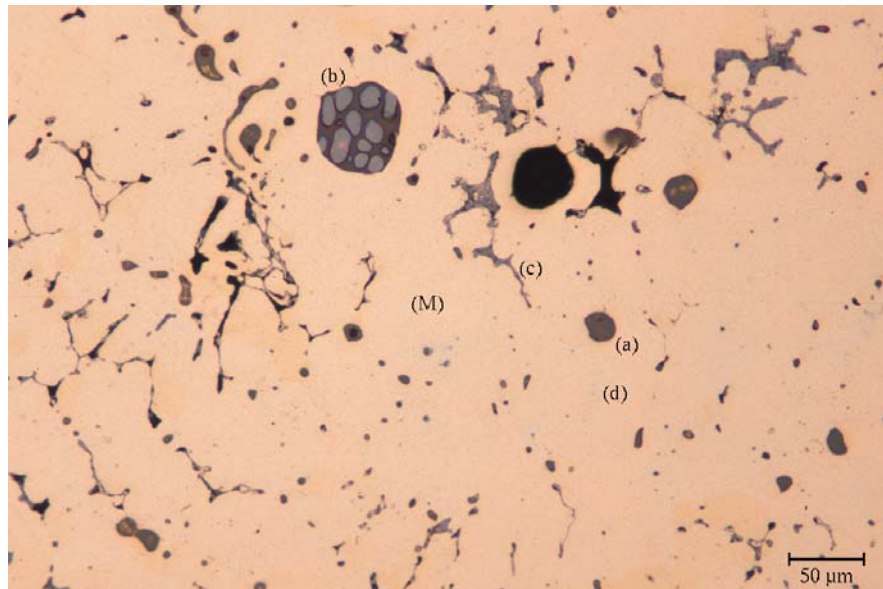


**Figure B.3:** Asch1, metallographic section with inclusion types.

**Table B.4:** Asch1, electron microprobe analyses of inclusions. Given are the mass fractions  $w$  of the determined elements. For inclusion types see Fig. B.3.

inclusion type/phase	$w(\text{As})$ [%]	$w(\text{Sb})$ [%]	$w(\text{Ag})$ [%]	$w(\text{Bi})$ [%]	$w(\text{Cu})$ [%]	$w(\text{O})$ [%]	$w(\text{S})$ [%]
(a) grey, globular	17.57	40.95	0.37	1.53	26.72	23.92	0.23
(b) bluish grey, globular	0.02	0.02	0.03	0.03	87.28	13.25	0.02
(c) bluish grey; at the grain boundary	0.28	0.73	1.03	0.05	86.36	7.73	0.02
(d) light bluish	1.01	11.89	26.98	40.82	18.47	0.68	0.02
(M) matrix, bright material surrounding an inclusion	1.89	0.39	2.15	0.00	90.97	0.25	0.01
(M) matrix	0.45	0.17	0.58	0.08	96.83	0.13	0.03



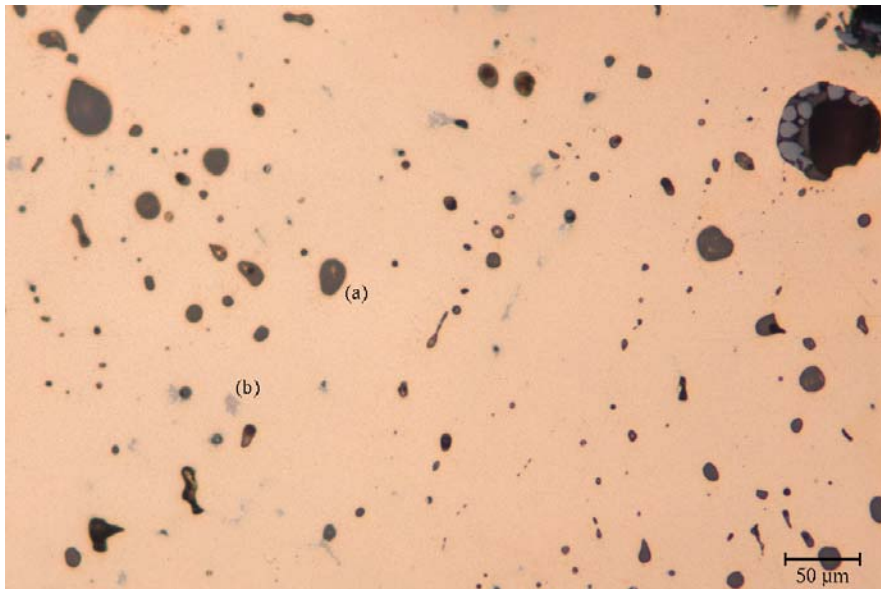


**Figure B.4:** Asch2, metallographic section with inclusion types.

**Table B.5:** Asch2, electron microprobe analyses of inclusions. Given are the mass fractions  $w$  of the determined elements. For inclusion types see Fig. B.4.

inclusion type/phase	$w(\text{As})$ [%]	$w(\text{Sb})$ [%]	$w(\text{Ag})$ [%]	$w(\text{Bi})$ [%]	$w(\text{Cu})$ [%]	$w(\text{O})$ [%]	$w(\text{S})$ [%]
(a) grey, globular	20.55	41.80	0.36	2.08	19.68	24.56	0.18
(b) pale blue	20.33	10.20	0.47	1.04	68.70	0.33	0.19
(b) pale blue	18.65	12.77	0.34	0.82	67.81	0.34	0.12

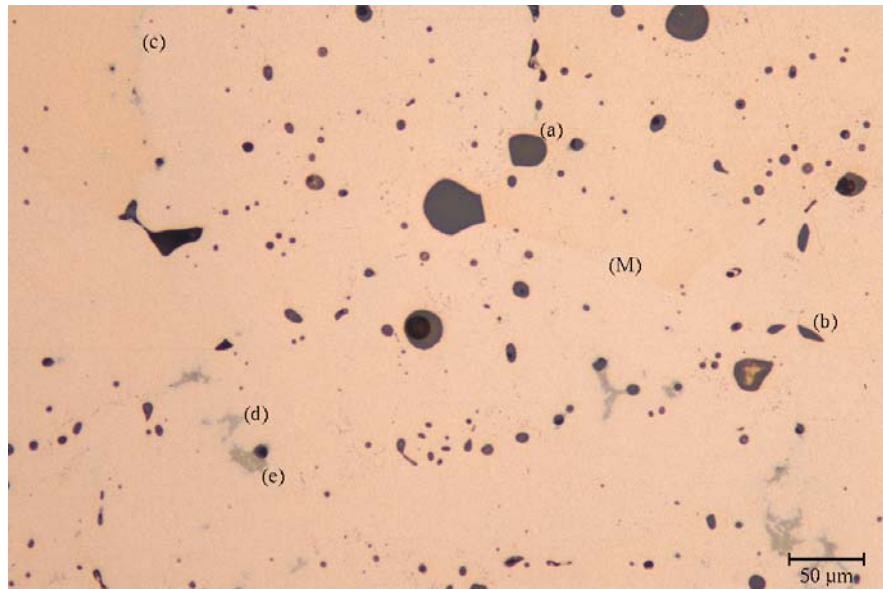


**Figure B.5:** Gam1, metallographic section with inclusion types.

**Table B.6:** Gam1, electron microprobe analyses of inclusions. Given are the mass fractions  $w$  of the determined elements. For inclusion types see Fig. B.5.

inclusion type/phase	$w(\text{As})$ [%]	$w(\text{Sb})$ [%]	$w(\text{Ag})$ [%]	$w(\text{Bi})$ [%]	$w(\text{Cu})$ [%]	$w(\text{O})$ [%]	$w(\text{S})$ [%]
(a) grey, globular	18.74	51.27	0.21	1.94	15.97	26.22	0.28
(b) grey, elongated	1.79	0.44	0.80	0.00	60.50	3.46	0.12
(c) light blue, globular, at the grain boundary	3.86	10.90	28.30	17.01	43.57	0.32	0.00
(d) pale blue	14.65	7.88	2.04	2.62	76.59	0.43	0.01
(e) pale blue	14.19	18.02	6.36	7.43	55.72	0.55	0.04
(M) matrix	2.24	0.56	1.22	0.03	94.62	0.14	0.00

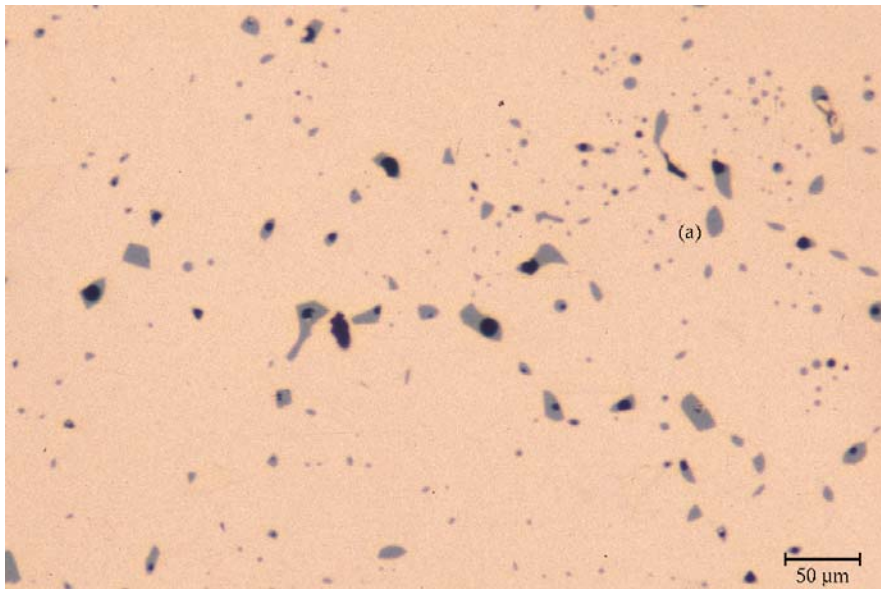


**Figure B.6:** Hech1, metallographic section with inclusion types, detail from Fig. 6.20, p. 79.

**Table B.7:** Hech1, electron microprobe analyses of inclusions. Given are the mass fractions  $w$  of the determined elements. For inclusion types see Fig. B.6.

inclusion type/phase	$w(\text{As})$ [%]	$w(\text{Sb})$ [%]	$w(\text{Ag})$ [%]	$w(\text{Bi})$ [%]	$w(\text{Cu})$ [%]	$w(\text{O})$ [%]	$w(\text{S})$ [%]
(a) light blue, globular	0.00	0.02	0.01	0.14	77.95	1.01	19.48

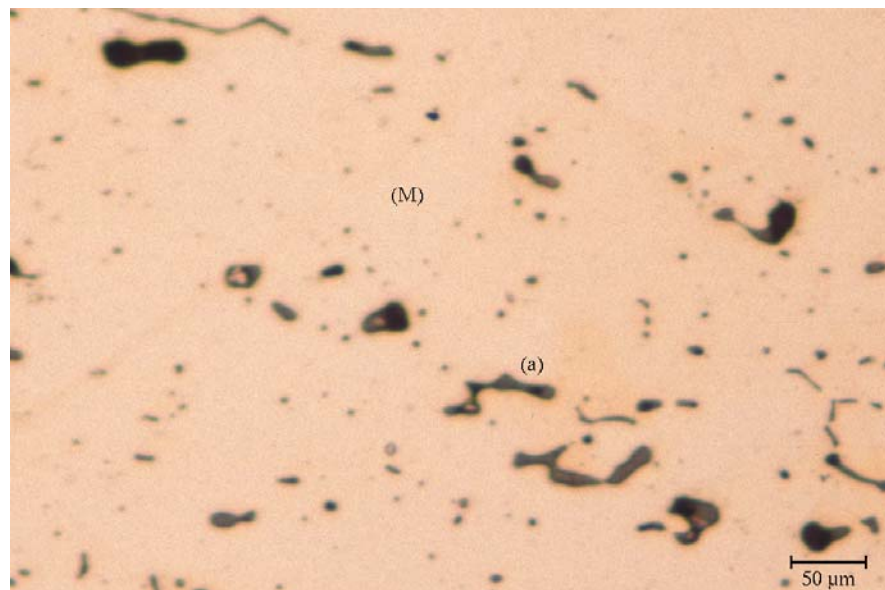


**Figure B.7:** Hoh1, metallographic section with inclusion types.

**Table B.8:** Hoh1, electron microprobe analyses of inclusions. Given are the mass fractions  $w$  of the determined elements. For inclusion types see Fig. B.7.

inclusion type/phase	$w(\text{As})$ [%]	$w(\text{Sb})$ [%]	$w(\text{Ag})$ [%]	$w(\text{Bi})$ [%]	$w(\text{Cu})$ [%]	$w(\text{O})$ [%]	$w(\text{S})$ [%]
(a) grey, elongated	4.81	11.39	0.91	2.07	71.23	5.53	0.05
(M) matrix, bright material surrounding an inclusion	1.79	0.69	1.55	0.00	94.20	0.29	0.08
(M) matrix	1.98	0.71	1.42	0.00	90.57	0.32	0.09

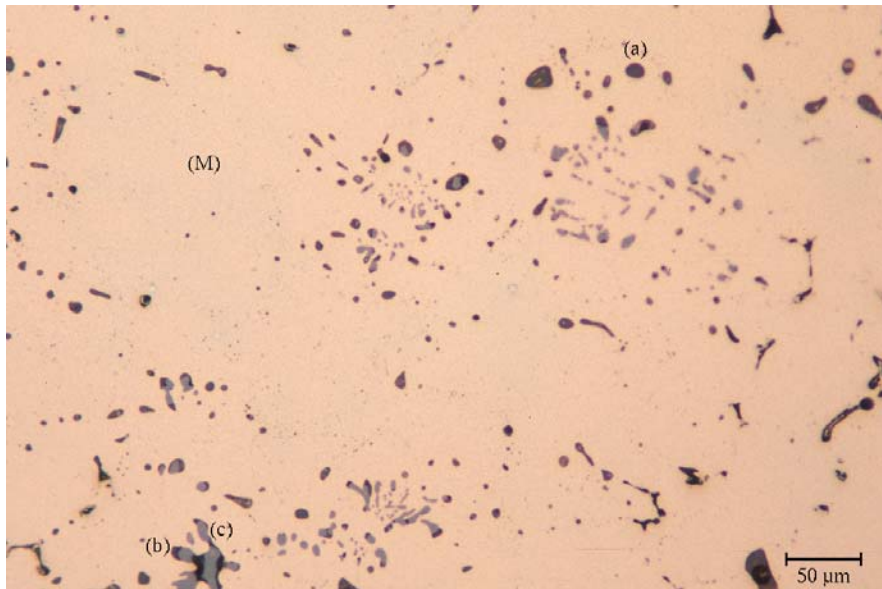


**Figure B.8:** PFe10, metallographic section with inclusion types.

**Table B.9:** PFe10, electron microprobe analyses of inclusions. Given are the mass fractions  $w$  of the determined elements. For inclusion types see Fig. B.8.

inclusion type/phase	$w(\text{As})$ [%]	$w(\text{Sb})$ [%]	$w(\text{Cu})$ [%]	$w(\text{O})$ [%]
(a) grey, globular	16.60	25.07	25.85	12.76
(b) dual phase inclusion, grey part	24.02	29.02	21.20	13.00
(b) dual phase inclusion, grey part	22.76	34.74	13.28	10.70
(c) dual phase inclusion, bluish grey part	4.29	13.48	55.55	7.08
(c) dual phase inclusion, bluish grey part	16.75	4.38	64.30	10.64
(M) matrix (average of the line scan)	1.24	0.24	97.31	0.12

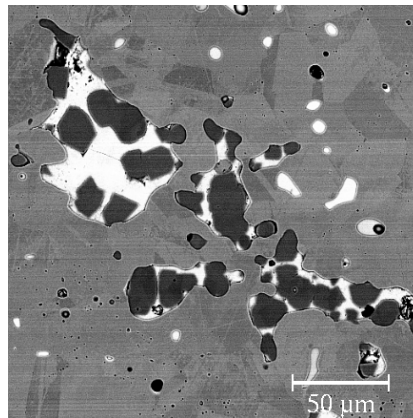


**Figure B.9:** Pfe10, SEM back scatter electron image (element contrast) of a two phase inclusion. The grey part of the inclusion appears white in the SEM element contrast, the bluish grey part appears dark grey.

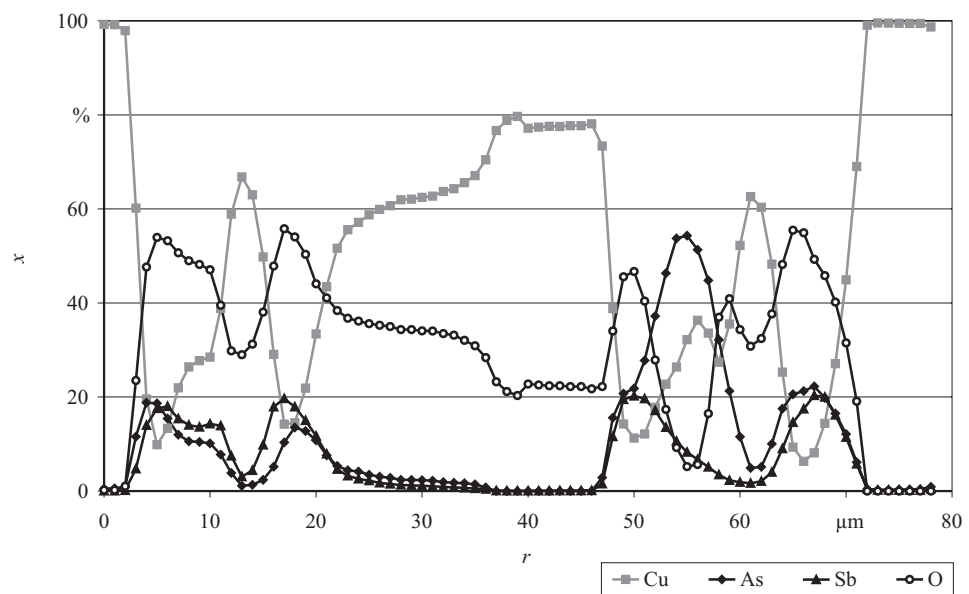


**Figure B.10:** Pfe10, electron microprobe analysis (line scan) of a two phase inclusion. Shown are the amount fractions  $x$  of copper, arsenic, antimony and oxygen. Between 13 and 20  $\mu\text{m}$  and 60 and 70  $\mu\text{m}$  there is a grey part of the inclusion, between 25 and 45  $\mu\text{m}$  a bluish grey part.

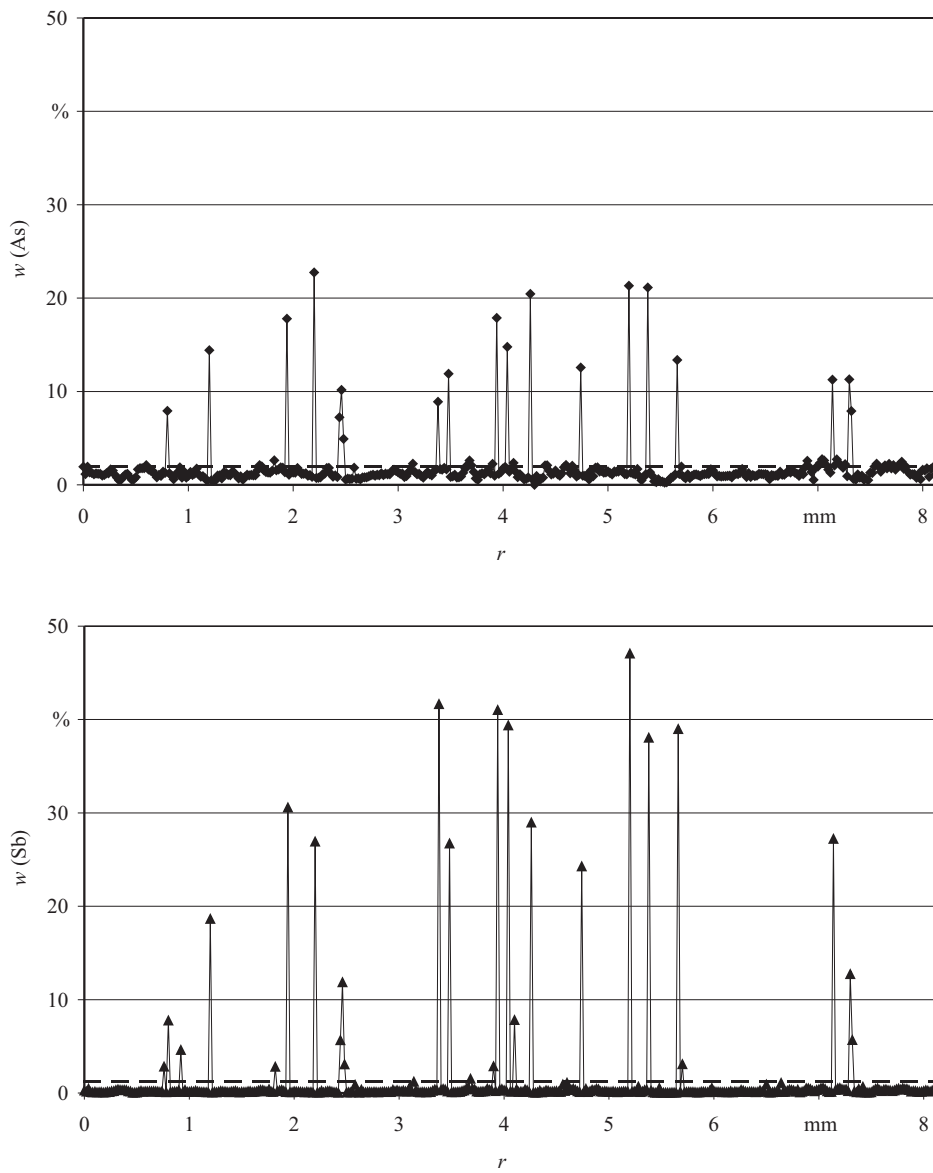


**Figure B.11:** Pfe10, electron microprobe analysis (line scan) of the sample cross-section. Shown are the mass fractions  $w$  of arsenic and antimony. The broken line marks the total mass fraction of the elements from the EDXRF analysis.

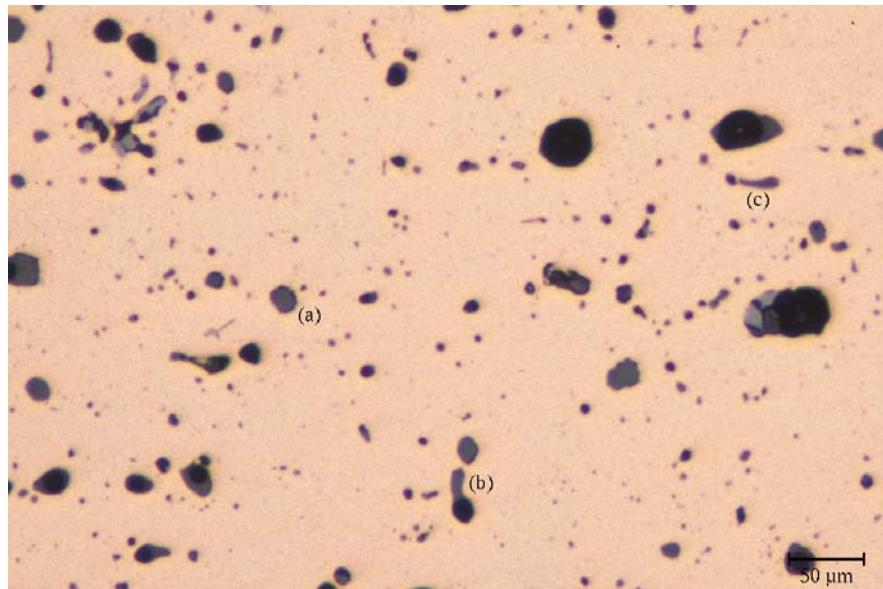


**Figure B.12:** PFe14, metallographic section with inclusion types, detail from Fig. 6.36, p. 92.

**Table B.10:** PFe14, electron microprobe analyses of inclusions. Given are the mass fractions  $w$  of the determined elements. For inclusion types see Fig. B.12.

inclusion type/phase		$w(\text{As})$ [%]	$w(\text{Sb})$ [%]	$w(\text{Cu})$ [%]	$w(\text{O})$ [%]
(a)	grey, globular	23.82	35.98	28.48	9.23
(b)	grey, elongated	21.47	50.07	14.67	9.17
(c)	grey, stretched	22.13	42.51	21.50	7.62



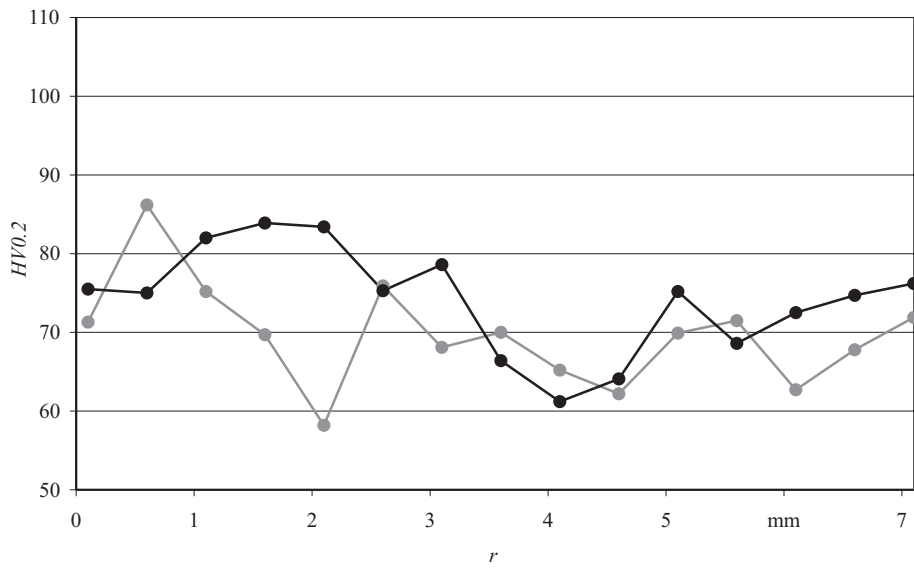


**Figure B.13:** Pfe10, Vickers low load hardness HV0.2 measured over the cross-section of the sample. Shown are two measurement series. The large differences in hardness result from the two phase structure of sample Pfe10.

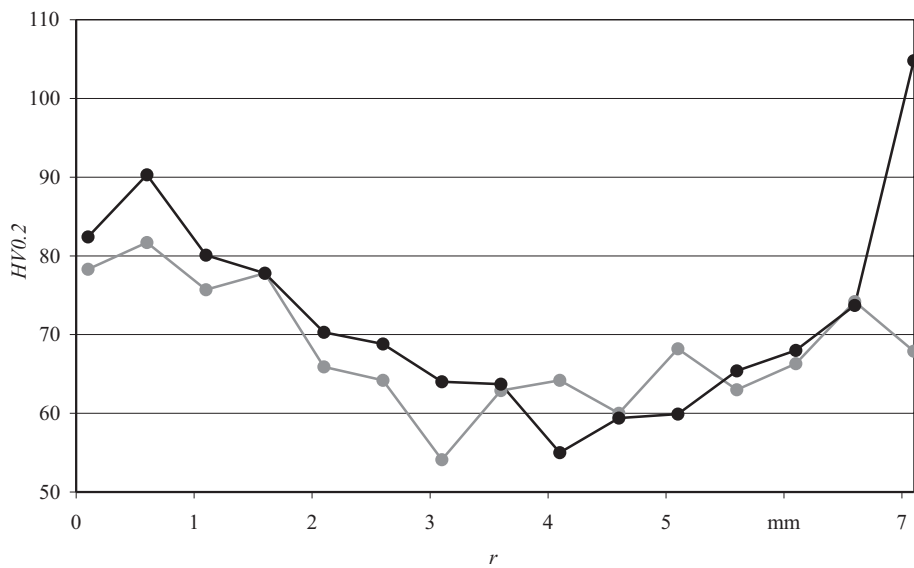


**Figure B.14:** Pfe14, Vickers low load hardness HV0.2 measured over the cross-section of the sample. Shown are two measurement series.

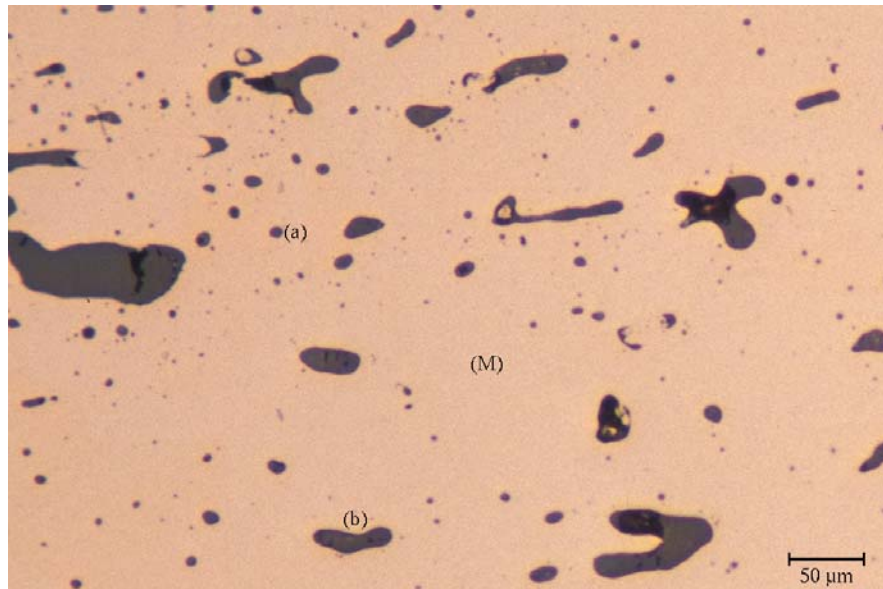


**Figure B.15:** Rad4, metallographic section with inclusion types.

**Table B.11:** Rad4, electron microprobe analyses of inclusions. Given are the mass fractions  $w$  of the determined elements. For inclusion types see Fig. B.15.

inclusion type/phase		$w(\text{As})$ [%]	$w(\text{Sb})$ [%]	$w(\text{Ag})$ [%]	$w(\text{Bi})$ [%]	$w(\text{Cu})$ [%]	$w(\text{O})$ [%]	$w(\text{S})$ [%]
(a)	grey, globular	16.90	51.77	0.21	4.66	12.45	27.31	0.05
(b)	grey, elongated	12.32	60.48	0.07	8.94	7.49	22.44	0.02
(M)	matrix	1.52	0.24	1.03	0.02	98.66	0.05	0.01

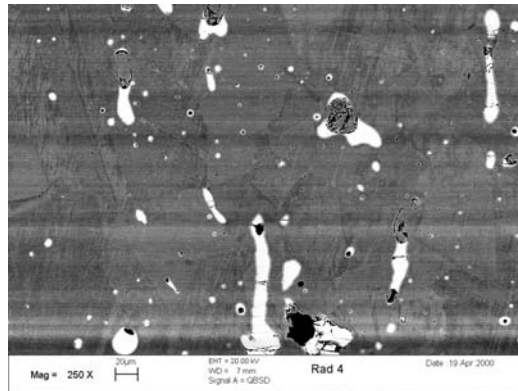


**Figure B.16:** Rad4, SEM back scatter electron image. The grey inclusions in the metallographic section (Fig. B.15, p. 222) appear white in the element contrast.

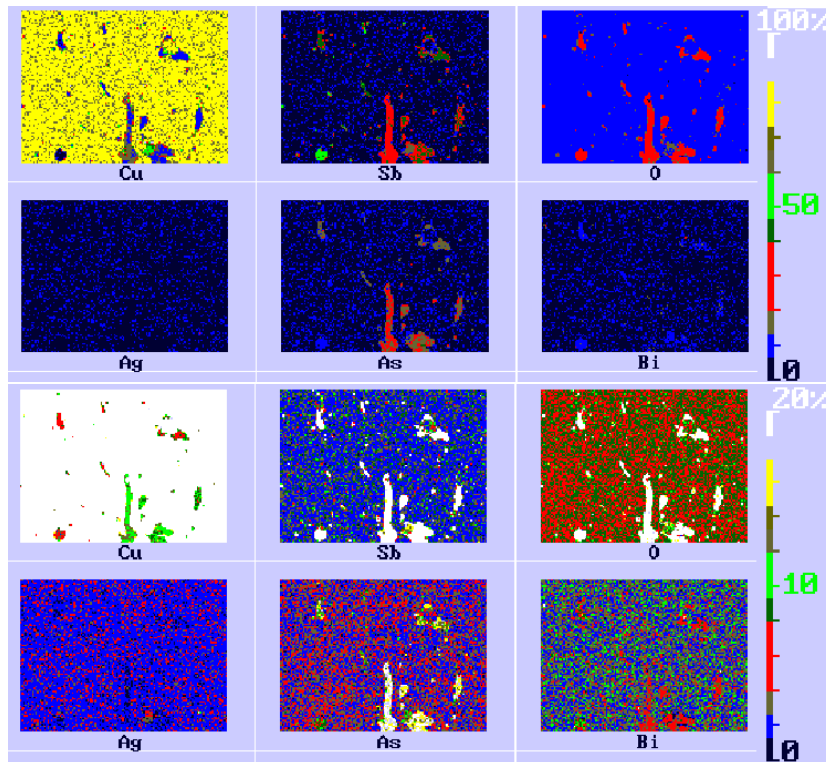


**Figure B.17:** Rad4, distribution of elements analysed by EDX in the scanning electron microscope. The mass fractions  $w$  of the elements are given by the colour bar on the right side.

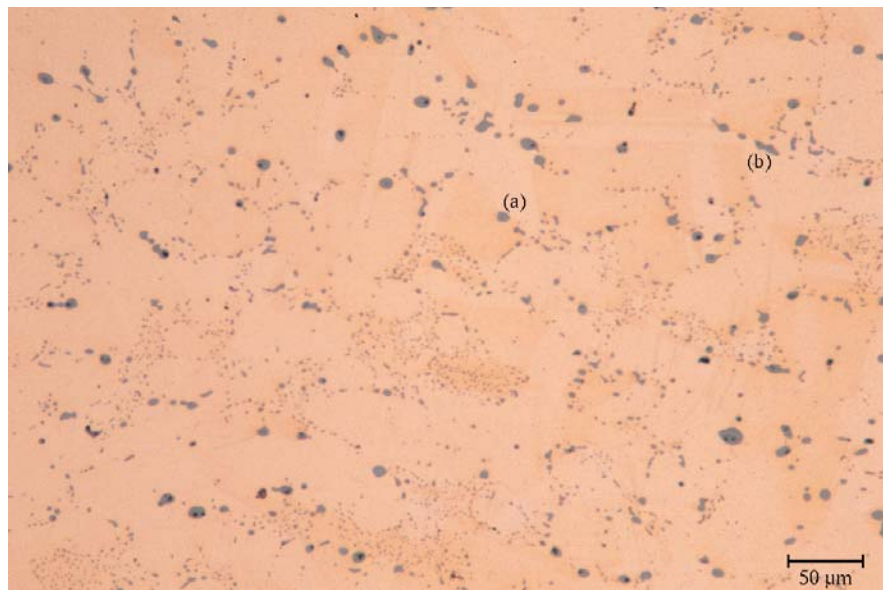


**Figure B.18:** Val1b, metallographic section with inclusion types.

**Table B.12:** Val1b, electron microprobe analyses of inclusions. Given are the mass fractions  $w$  of the determined elements. Since there was a drift of the sample in the microprobe during the first and second run, the analysed spot has changed. Therefore, the sum of the elements differs significantly from the ideal total of 100 %. For inclusion types see Fig. B.18.

inclusion type/phase		$w(\text{As})$ [%]	$w(\text{Sb})$ [%]	$w(\text{Ag})$ [%]	$w(\text{Bi})$ [%]	$w(\text{Cu})$ [%]	$w(\text{O})$ [%]	$w(\text{S})$ [%]
(a)	light blue, globular	0.00	0.02	0.00	0.06	66.05	0.70	4.91
(b)	light blue, elongated	0.00	0.00	0.00	0.00	85.37	0.60	18.06
(c)	light blue (corrosion product?)	0.01	0.00	0.05	0.30	84.24	11.52	0.00



**Figure B.19:** Val2b, metallographic section with inclusion types.

**Table B.13:** Val2b, electron microprobe analyses of inclusions. Given are the mass fractions  $w$  of the determined elements. Since there was a drift of the sample in the microprobe during the first and second run, the analysed spot has changed. Therefore, the sum of the elements differs significantly from the ideal total of 100 %. For inclusion types see Fig. B.19.

inclusion type/phase	$w(\text{As})$ [%]	$w(\text{Sb})$ [%]	$w(\text{Ag})$ [%]	$w(\text{Bi})$ [%]	$w(\text{Cu})$ [%]	$w(\text{O})$ [%]	$w(\text{S})$ [%]
(a) grey, globular	33.80	26.93	0.61	0.43	66.77	21.42	0.08
(a) grey, globular	33.27	40.47	0.34	2.04	15.10	22.57	0.20
(b) dual phase inclusion, grey part	33.92	24.65	0.07	0.54	21.95	9.26	0.12

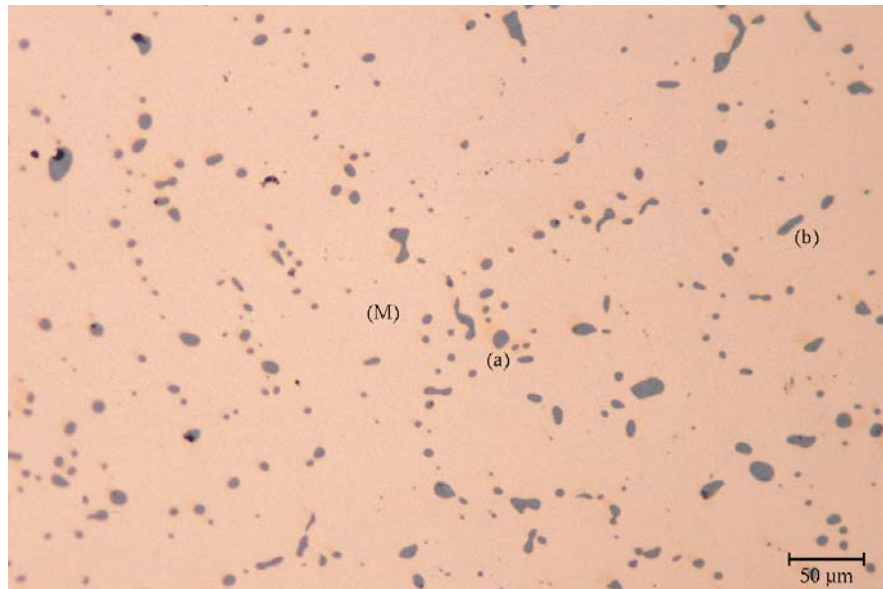


**Figure B.20:** Val3b, metallographic section with inclusion types.

**Table B.14:** Val3b, electron microprobe analyses of inclusions. Given are the mass fractions  $w$  of the determined elements. Since there was a drift of the sample in the microprobe during the first and second run, the analysed spot has changed. Therefore, the sum of the elements differs significantly from the ideal total of 100 %. For inclusion types see Fig. B.20.

inclusion type/phase		$w(\text{As})$ [%]	$w(\text{Sb})$ [%]	$w(\text{Ag})$ [%]	$w(\text{Bi})$ [%]	$w(\text{Cu})$ [%]	$w(\text{O})$ [%]	$w(\text{S})$ [%]
(a)	light blue	0.00	0.00	0.02	0.00	80.83	0.17	15.32
(b)	light blue, elongated	0.00	0.01	0.03	0.00	74.61	0.26	17.59
(M)	matrix	0.00	0.00	0.03	0.00	97.67	0.07	0.00

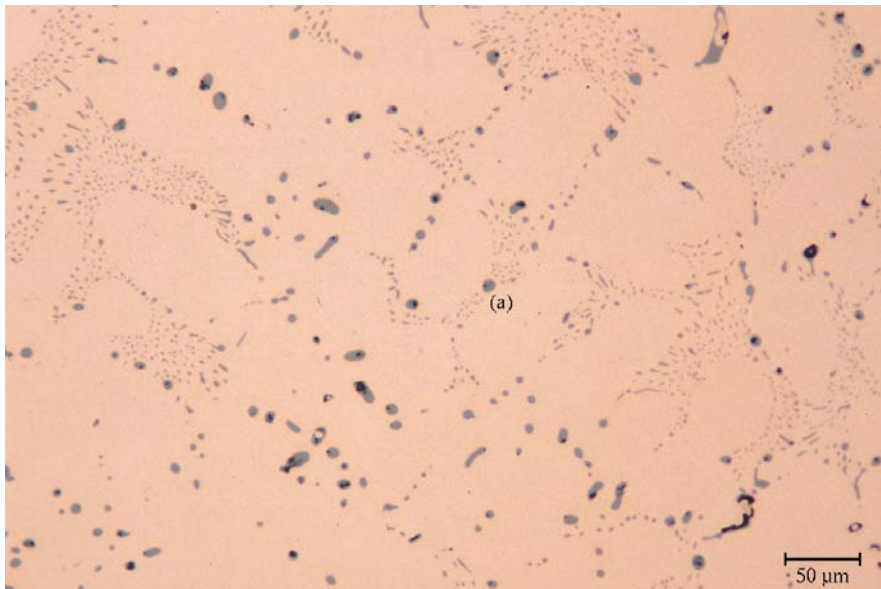


**Figure B.21:** Val4a, metallographic section with inclusion types.

**Table B.15:** Val4a, electron microprobe analyses of inclusion. Given are the mass fractions  $w$  of the determined elements. Since there was a drift of the sample in the microprobe during the first and second run, the analysed spot has changed. Therefore, the sum of the elements differs significantly from the ideal total of 100 %. For inclusion types see Fig. B.21.

inclusion type/phase	$w(\text{As})$ [%]	$w(\text{Sb})$ [%]	$w(\text{Ag})$ [%]	$w(\text{Bi})$ [%]	$w(\text{Cu})$ [%]	$w(\text{O})$ [%]	$w(\text{S})$ [%]
(a) light blue, globular	0.00	0.06	0.00	0.07	102.77	0.37	10.05

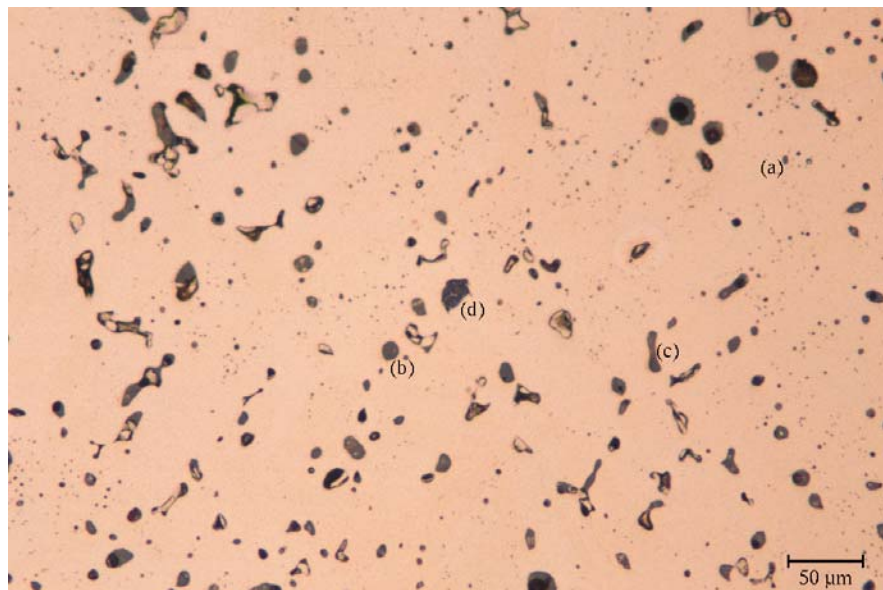


**Figure B.22:** Val5b, metallographic section with inclusion types.

**Table B.16:** Val5b, electron microprobe analyses of inclusions. Given are the mass fractions  $w$  of the determined elements. Since there was a drift of the sample in the microprobe during the first and second run, the analysed spot has changed. Therefore, the sum of the elements differs significantly from the ideal total of 100 %. For inclusion types see Fig. B.22.

inclusion type/phase	$w(\text{As})$ [%]	$w(\text{Sb})$ [%]	$w(\text{Ag})$ [%]	$w(\text{Bi})$ [%]	$w(\text{Cu})$ [%]	$w(\text{O})$ [%]	$w(\text{S})$ [%]
(a) bluish grey, globular	27.02	50.93	0.13	3.08	11.58	20.46	0.10
(b) grey, globular	3.65	1.32	0.12	0.34	59.81	6.79	0.16
(c) grey, elongated	27.55	40.78	0.28	3.26	15.44	22.48	0.11
(d) dual phase inclusion, luish grey part	0.38	0.31	0.21	0.03	75.82	6.17	0.09



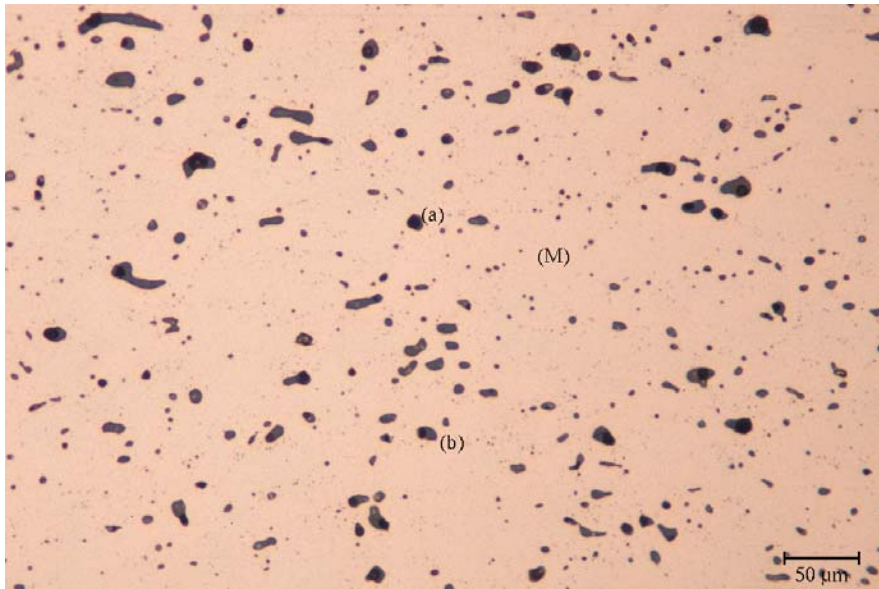


**Figure B.23:** Val6a, metallographic section with inclusion types.

**Table B.17:** Val6a, electron microprobe analyses of inclusions. Given are the mass fractions  $w$  of the determined elements. Since there was a drift of the sample in the microprobe during the first and second run, the analysed spot has changed. Therefore, the sum of the elements differs significantly from the ideal total of 100 %. For inclusion types see Fig. B.23.

inclusion type/phase		w(As) [%]	w(Sb) [%]	w(Ag) [%]	w(Bi) [%]	w(Cu) [%]	w(O) [%]	w(S) [%]
(a)	grey, globular	36.87	42.01	0.19	0.55	16.05	22.03	0.24
(b)	grey, globular	31.26	44.59	0.15	1.46	30.20	21.67	0.08
(M)	matrix	1.09	0.21	0.30	0.00	91.02	0.05	0.01

**Table B.18:** Metallographic investigation of ingot torques. The material classes printed in *italic* are analyses close to classification limits, features marked with a circle are not certain.

Lab.- No.	mat. class	cross section	typology			inclusion types				structure		
			casting groove	forging seam	copper sulphide	copper oxide	mixed oxides	two-phase inclusions	ternary phase	dendrites	annealing twins	
ASCH1	C2	triangular	○			●	●	●	●	●	●	●
ASCH2	<i>C2</i>	triangular	○			●			●		●	●
BER1	<i>G</i>	D-shaped			●							●
BER3	C2C	round		●				●	●			●
GAM1	C2D	triangular	○			●	●	●	●	●	●	
GAM2	<i>C2C</i>	triangular				●		●	●	●	●	●
HECH1	<i>FA</i>	oval			●							●
HECH2	<i>FG</i>	triangular			●							●
HOH1	C2D	round						●				●
MÜH1	C2D	D-shaped	●					●				●
PFE10	C2C	round		●		●	●	●	●	●	●	●
PFE14	C2	round				●	●	●	●	●	●	●
RAD2	<i>C2D</i>	round				●	●	●	●			●
RAD4	C2D	round					●		●			●
THA1	C2C	round						●				●

Table B.18: continued from p. 230

Lab.- No.	mat. class	cross section	typology		forging seam	copper sulphide	inclusion types			two-phase inclusions	ternary phase	structure	
			casting groove				copper oxide	mixed oxides	dendrites			annealing twins	
VAL1A	FA	D-shaped	●			●						●	●
VAL1B	FA	D-shaped	●			●						●	●
VAL2A	C2	round			●		●	●	●	●		●	●
VAL2B	C2	round			●		●	●	●	●		●	●
VAL2C	C2	round			●		●	●	●	●		●	●
VAL3A	FA	round	●			●							●
VAL3B	FA	round	●			●							●
VAL3C	FA	round	●			●							●
VAL4A	FA	triangular	●			●						●	●
VAL4B	FA	triangular	●			●							●
VAL5A	C2D	round			●		●		●	●		●	●
VAL5B	C2	round			●		●		●	●		●	●
VAL6A	C2D	round			●		●		●	●		●	●
VAL6B	C2D	round			●		●		●	●		●	●



# **Appendix C**

## **Material Testing**

**Table C.1:** Reference material, charge numbers and casting parameters. The charges marked with ‘\*’ were used for material testing

reference material/charge number		casting technology	temperature
Cu	1	sand mould; bottom cast	1200°C
Cu	2	sand mould; bottom cast	1200°C
Cu	3	sand mould; bottom cast	1200°C
Cu	4	sand mould; bottom cast	1160°C
Cu*	5	sand mould; bottom cast	1165°C
Cu As0.25 Sb0.25 Bi0.1*	1	graphite tubes; top cast	1180°C
Cu As0.5 Sb0.5 Bi0.1	1	sand mould; bottom cast	1150°C
Cu As0.5 Sb0.5 Bi0.1	2	sand mould; bottom cast	1170°C
Cu As0.5 Sb0.5 Bi0.1*	3	sand mould; bottom cast	1180°C
Cu As1 Sb1 Bi0.1	1	graphite mould; top cast	1160°C
Cu As1 Sb1 Bi0.1	2	graphite mould; top cast	1180°C
Cu As1 Sb1 Bi0.1*	3	graphite tubes; top cast	1200°C
Cu As2 Sb2 Bi0.1	1	sand mould; bottom cast	1175°C
Cu As2 Sb2 Bi0.1*	2	sand mould; bottom cast	1160°C
Cu As3 Sb3 Bi0.1*	1	graphite mould; top cast	1160°C
Cu As4 Sb4 Bi0.1	1	sand mould; bottom cast	1150°C
Cu As4 Sb4 Bi0.1	2	sand mould; bottom cast	1150°C
Cu As4 Sb4 Bi0.1	3	sand mould; bottom cast	1150°C
Cu As4 Sb4 Bi0.1	4	sand mould; bottom cast	1160°C
Cu As4 Sb4 Bi0.1*	5	graphite mould; top cast	1160°C

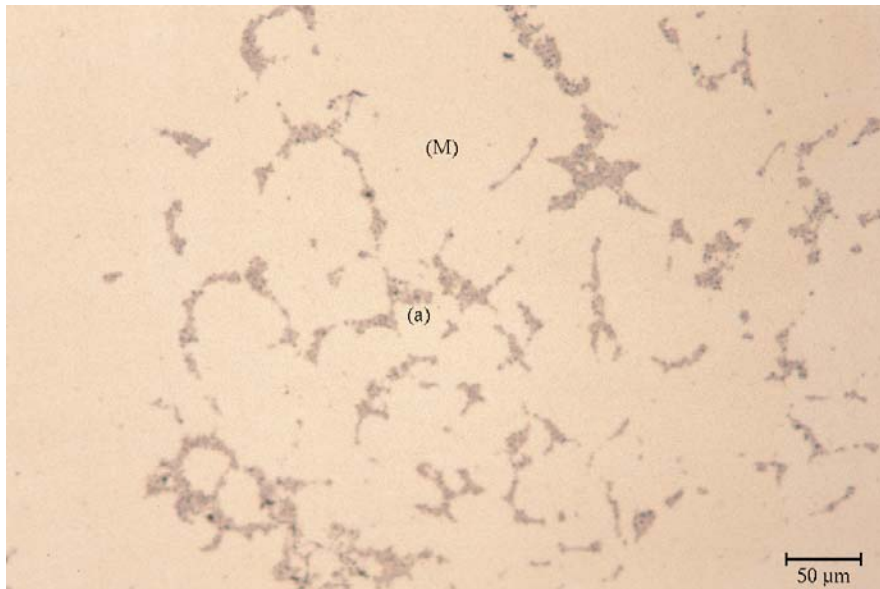


**Figure C.1:** Cu, metallographic section with inclusion types.

**Table C.2:** Cu, electron microprobe analyses of inclusions. Given are the mass fractions  $w$  of the determined elements. For inclusion types see Fig. C.1.

inclusion type/phase	$w(\text{As})$ [%]	$w(\text{Sb})$ [%]	$w(\text{Ag})$ [%]	$w(\text{Bi})$ [%]	$w(\text{Fe})$ [%]	$w(\text{Cu})$ [%]	$w(\text{O})$ [%]	$w(\text{S})$ [%]
(a) bluish grey, un-evenly shaped	0.00	0.00	0.03	0.00	0.51	65.19	14.94	0.87
(a) bluish grey, un-evenly shaped	0.00	0.00	0.03	0.00	0.48	72.30	10.58	0.91
(a) bluish grey, un-evenly shaped	0.00	0.04	0.01	0.04	0.49	75.83	3.28	1.43
(a) bluish grey, un-evenly shaped	0.00	0.03	0.08	0.01	0.38	80.30	3.67	1.39
(M) matrix (average of linescan)	0.01	0.01	0.04	0.01	0.05	99.51	0.16	0.00

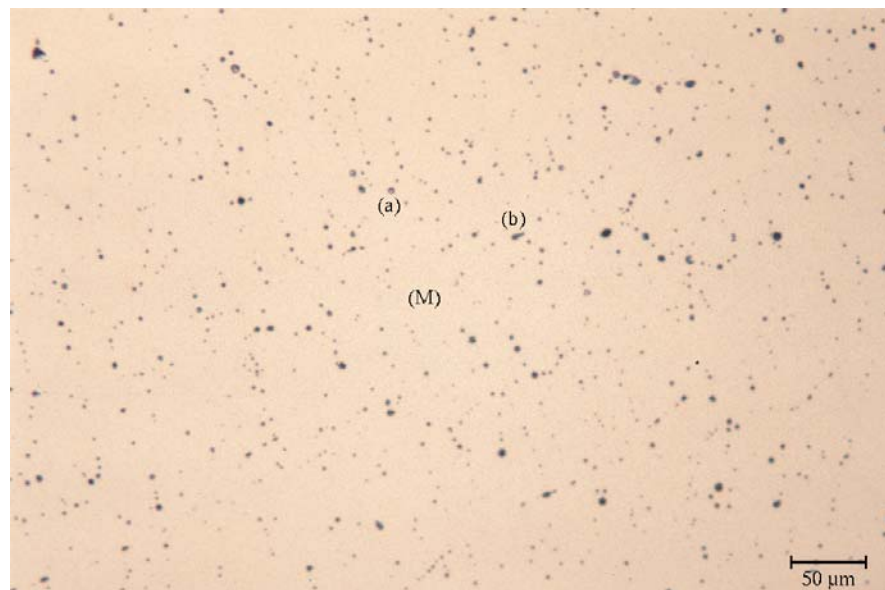


**Figure C.2:** CuAs<sub>0.25</sub> Sb<sub>0.25</sub> Bi<sub>0.1</sub>, metallographic section with inclusion types.

**Table C.3:** CuAs<sub>0.25</sub> Sb<sub>0.25</sub> Bi<sub>0.1</sub>, electron microprobe analyses of inclusions. Given are the mass fractions  $w$  of the determined elements. For inclusion types see Fig. C.2.

inclusion type/phase	$w(\text{As})$ [%]	$w(\text{Sb})$ [%]	$w(\text{Ag})$ [%]	$w(\text{Bi})$ [%]	$w(\text{Fe})$ [%]	$w(\text{Cu})$ [%]	$w(\text{O})$ [%]	$w(\text{S})$ [%]
(a) grey, globular	2.05	3.76	0.02	0.18	0.00	83.04	17.67	0.01
(a) grey, globular	2.66	4.21	0.02	0.27	0.05	79.15	16.51	0.01
(a) grey, globular	1.59	7.50	0.03	0.12	0.01	50.86	1.63	0.00
(b) grey, elongated	0.06	0.22	0.01	0.01	0.01	79.13	1.07	0.00
(M) matrix (average of linescan)	0.06	0.03	0.03	0.01	0.00	98.67	0.29	0.00



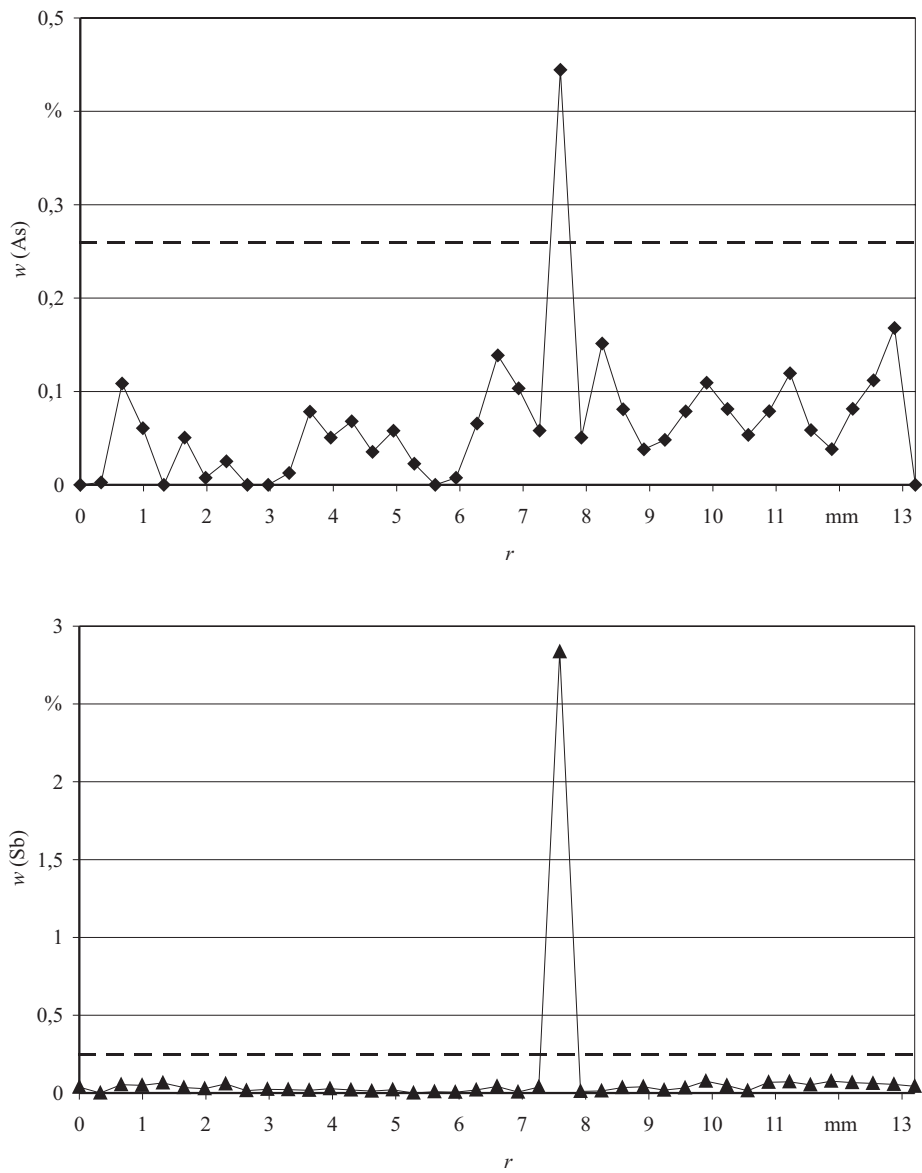


**Figure C.3:**  $\text{CuAs}_{0.25}\text{Sb}_{0.25}\text{Bi}_{0.1}$ , electron microprobe analysis (line scan) of the sample cross-section. Shown are the mass fractions  $w$  of arsenic and antimony. The broken line marks the total mass fractions of the elements as determined by EDXRF analysis.

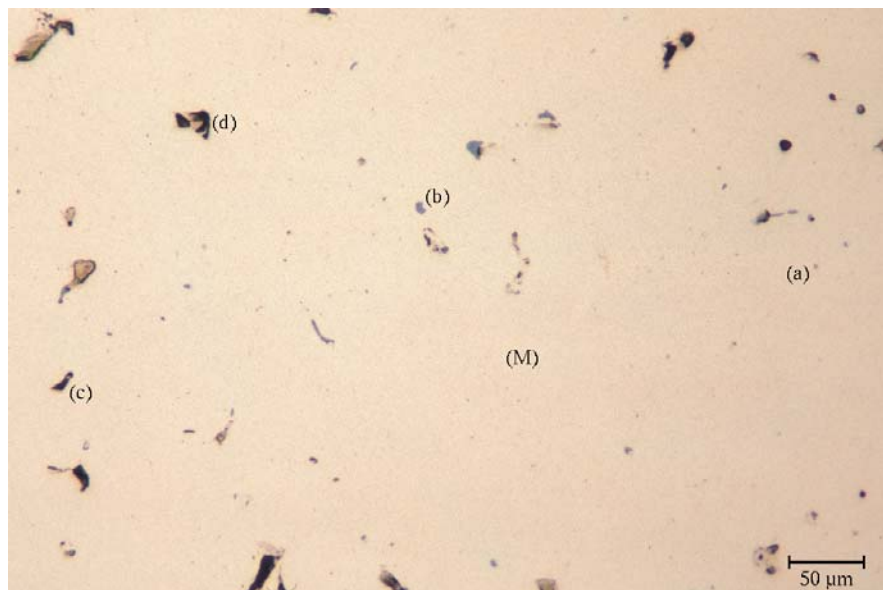


**Figure C.4:** CuAs<sub>0.5</sub> Sb<sub>0.5</sub> Bi<sub>0.1</sub>, metallographic section with inclusion types.

**Table C.4:** CuAs<sub>0.5</sub> Sb<sub>0.5</sub> Bi<sub>0.1</sub>, electron microprobe analyses of inclusions. Given are the mass fractions  $w$  of the determined elements. For inclusion types see Fig. C.4.

inclusion type/phase	$w(\text{As})$ [%]	$w(\text{Sb})$ [%]	$w(\text{Ag})$ [%]	$w(\text{Bi})$ [%]	$w(\text{Fe})$ [%]	$w(\text{Cu})$ [%]	$w(\text{O})$ [%]	$w(\text{S})$ [%]
(a) bluish-grey, globular	0.00	0.49	0.04	0.01	0.72	85.74	0.47	1.36
(b) bluish-grey, unevenly shaped	0.00	0.00	0.02	0.08	1.48	74.90	1.18	2.04
(c) dark grey, elongated	0.28	0.27	0.06	0.00	0.09	74.68	0.72	0.01
(c) dark grey, unevenly shaped	0.47	0.87	0.01	4.69	0.05	84.87	0.82	0.00
(M) matrix (average of linescan)	0.18	0.34	0.05	0.01	0.10	99.40	0.12	0.00

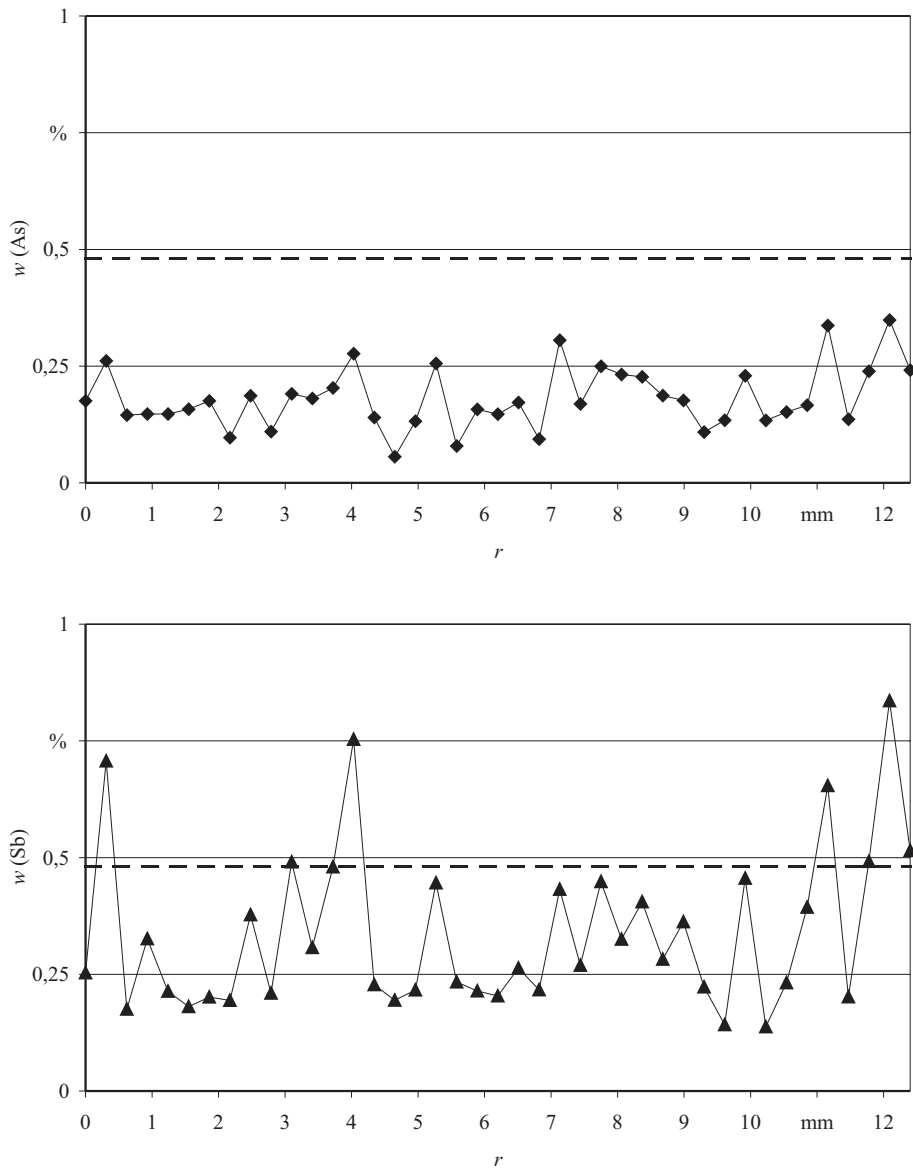


**Figure C.5:**  $\text{CuAs}_{0.5}\text{Sb}_{0.5}\text{Bi}_{0.1}$ , electron microprobe analysis (line scan) of the sample cross-section. Shown are the mass fractions  $w$  of arsenic and antimony. The broken line marks the total mass fractions of the elements as determined by EDXRF analysis.

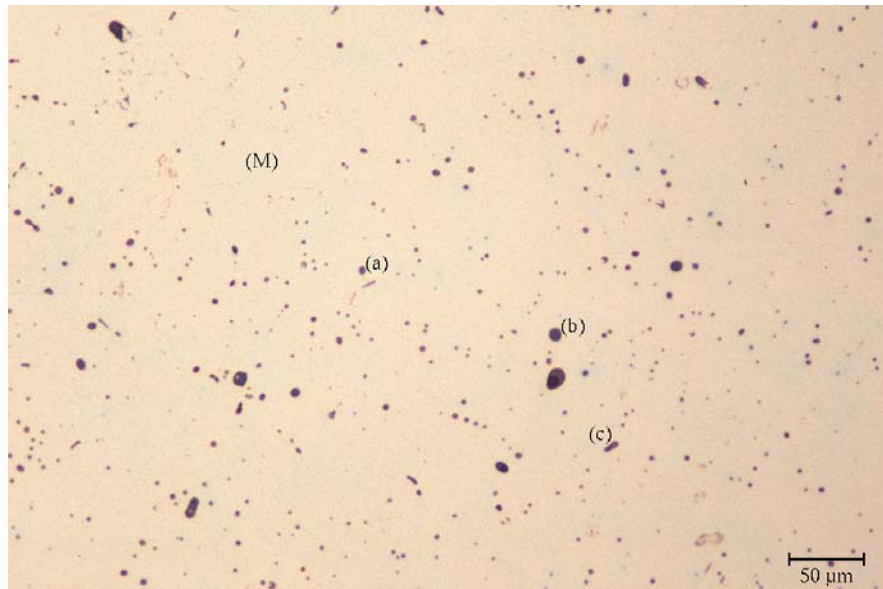


**Figure C.6:** Cu As1 Sb1 Bi0.1, metallographic section with inclusion types.

**Table C.5:** Cu As1 Sb1 Bi0.1, electron microprobe analyses of inclusions. Given are the mass fractions  $w$  of the determined elements. For inclusion types see Fig. C.6.

inclusion type/phase	$w(\text{As})$ [%]	$w(\text{Sb})$ [%]	$w(\text{Ag})$ [%]	$w(\text{Bi})$ [%]	$w(\text{Fe})$ [%]	$w(\text{Cu})$ [%]	$w(\text{O})$ [%]	$w(\text{S})$ [%]
(a) grey, globular	3.10	48.79	0.01	1.04	0.03	21.15	24.20	0.00
(b) dark grey, globular	10.74	39.15	0.01	0.52	0.03	19.02	29.33	0.03
(c) dark grey, elongated	15.19	38.84	0.01	0.96	0.34	11.54	30.39	0.04
(M) matrix (average of linescan)	0.50	0.24	0.06	0.00	0.01	99.47	0.83	0.00

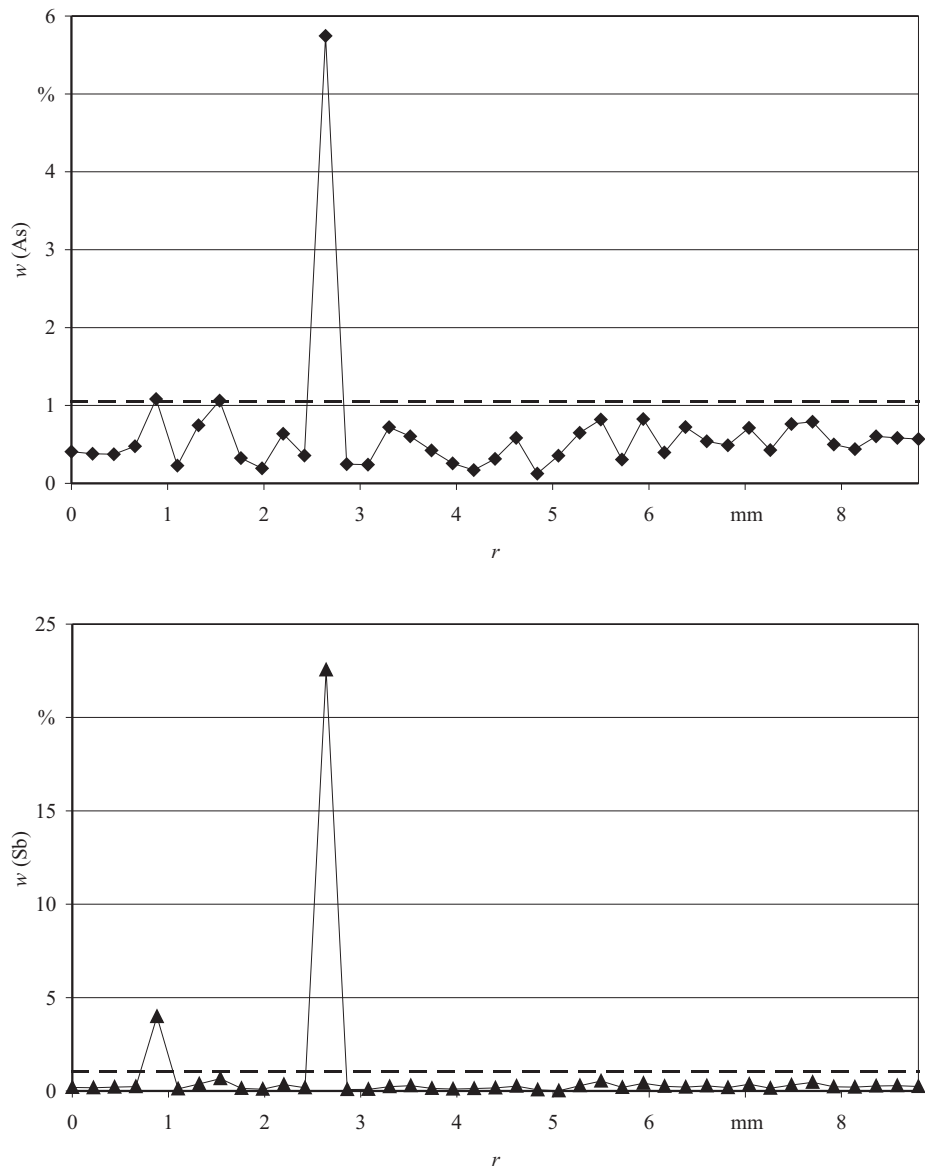


**Figure C.7:** Cu As<sub>1</sub> Sb<sub>1</sub> Bi<sub>0.1</sub>, electron microprobe analysis (line scan) of the sample cross-section. Shown are the mass fractions  $w$  of arsenic and antimony. The broken line marks the total mass fractions of the elements as determined by EDXRF analysis.

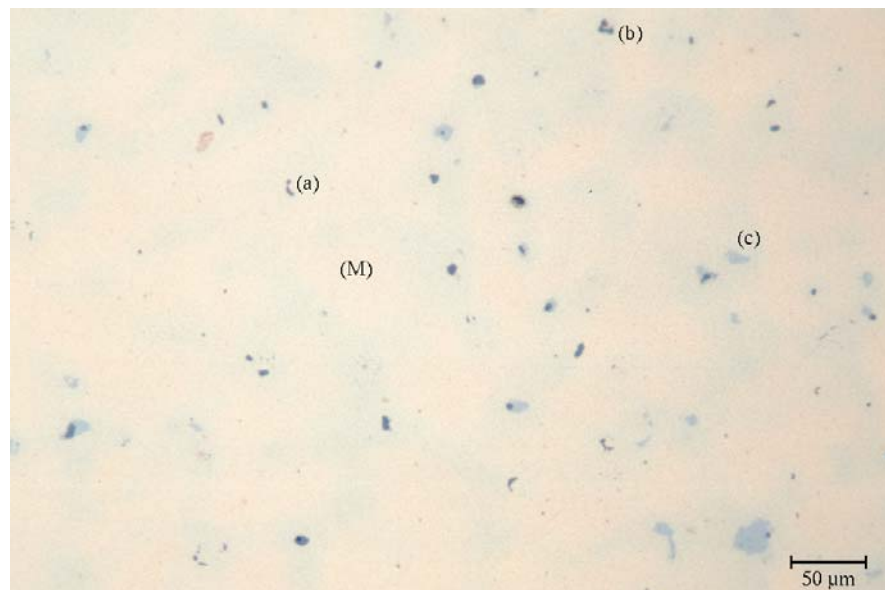


**Figure C.8:** Cu As<sub>2</sub> Sb<sub>2</sub> Bi<sub>0.1</sub>, metallographic section with inclusion types.

**Table C.6:** Cu As<sub>2</sub> Sb<sub>2</sub> Bi<sub>0.1</sub>, electron microprobe analyses of inclusions. Given are the mass fractions  $w$  of the determined elements. For inclusion types see Fig. C.8.

inclusion type/phase	$w(\text{As})$ [%]	$w(\text{Sb})$ [%]	$w(\text{Ag})$ [%]	$w(\text{Bi})$ [%]	$w(\text{Fe})$ [%]	$w(\text{Cu})$ [%]	$w(\text{O})$ [%]	$w(\text{S})$ [%]
(a) grey, elongated	0.00	0.08	0.04	0.00	0.81	72.21	0.38	1.84
(b) grey, unevenly shaped	0.00	0.03	0.01	0.02	4.40	70.28	2.63	1.95
(b) grey, unevenly shaped	0.00	0.11	0.02	0.04	3.10	73.01	1.86	2.00
(c) pale blue phase	1.72	22.55	0.07	0.06	0.08	69.72	0.22	0.04
(c) pale blue phase	1.54	24.64	0.04	0.00	0.06	69.01	0.19	0.00
(M) matrix (average of linescan)	0.78	1.29	0.02	0.02	0.05	97.10	0.28	0.00

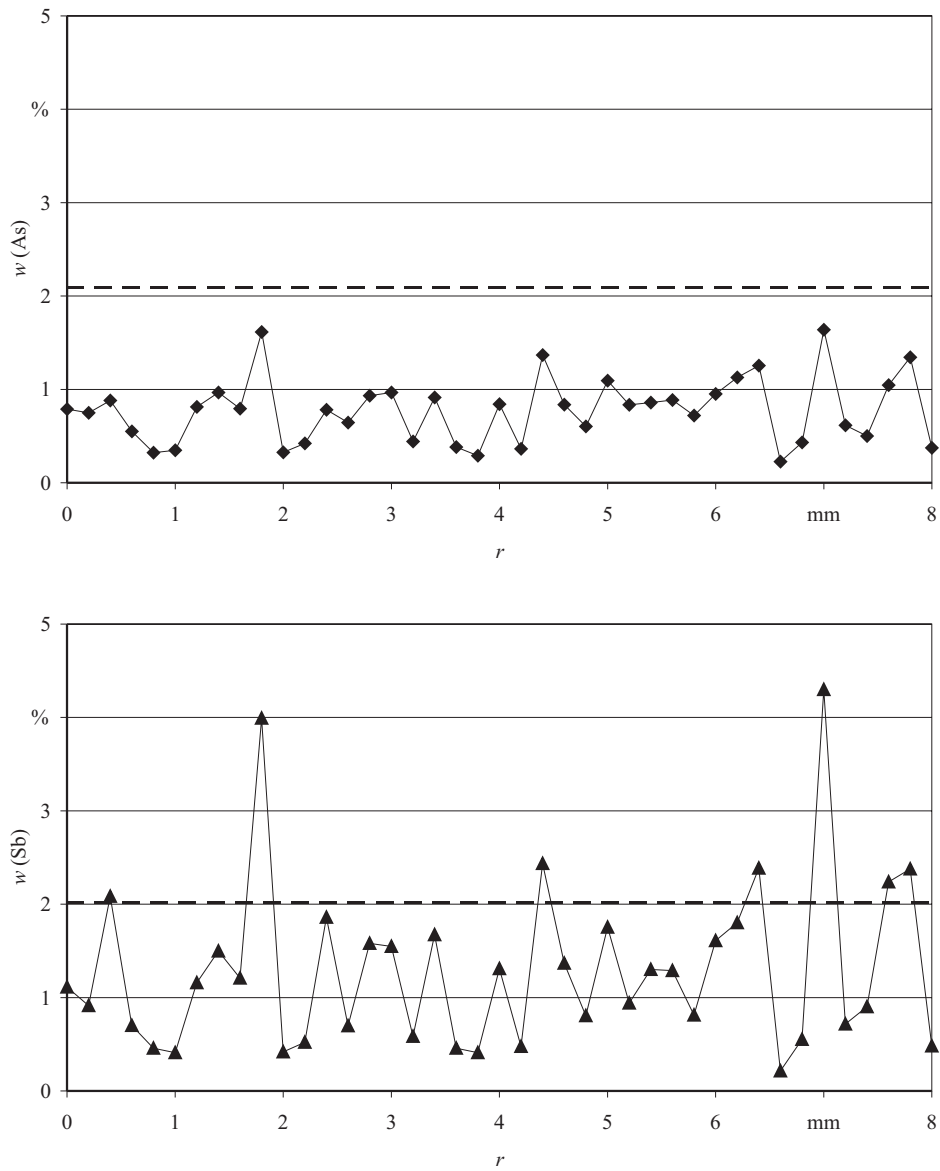


**Figure C.9:** Cu As<sub>2</sub> Sb<sub>2</sub> Bi<sub>0.1</sub>, electron microprobe analysis (line scan) of the sample cross-section. Shown are the mass fractions  $w$  of arsenic and antimony. The broken line marks the total mass fractions of the elements as determined by EDXRF analysis.

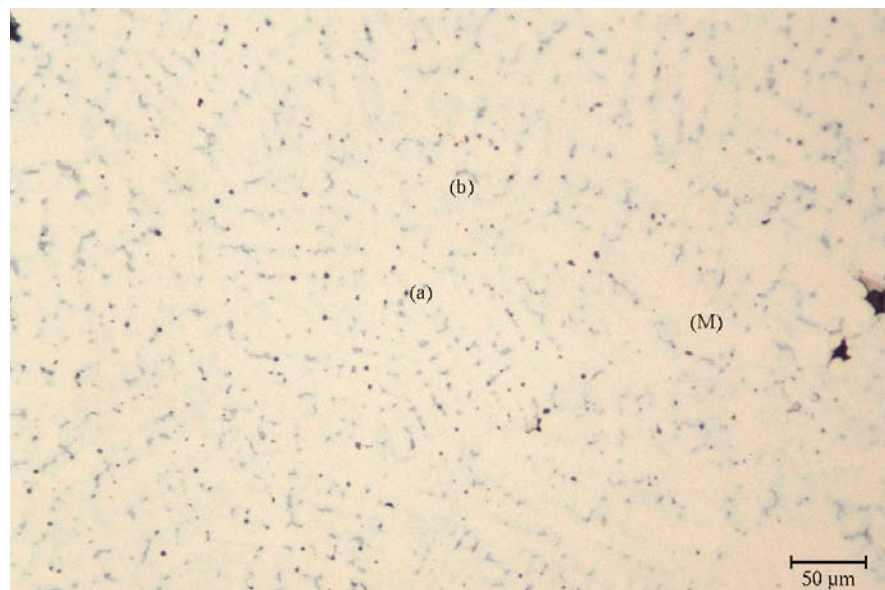


**Figure C.10:** Cu As<sub>3</sub> Sb<sub>3</sub> Bi<sub>0.1</sub>, metallographic section with inclusion types.

**Table C.7:** Cu As<sub>3</sub> Sb<sub>3</sub> Bi<sub>0.1</sub>, electron microprobe analyses of inclusions. Given are the mass fractions  $w$  of the determined elements. For inclusion types see Fig. C.10.

inclusion type/phase	$w(\text{As})$ [%]	$w(\text{Sb})$ [%]	$w(\text{Ag})$ [%]	$w(\text{Bi})$ [%]	$w(\text{Fe})$ [%]	$w(\text{Cu})$ [%]	$w(\text{O})$ [%]	$w(\text{S})$ [%]
(a) grey, globular	1.98	45.04	0.00	0.21	0.20	28.34	17.91	0.01
(a) grey, globular	2.51	10.65	0.02	0.42	0.01	72.69	1.55	0.00
(b) pale blue phase	6.20	20.33	0.04	0.30	0.01	66.06	0.22	0.00
(b) pale blue phase	3.95	15.95	0.02	0.40	0.01	72.07	0.12	0.01
(M) matrix (average of linescan)	1.71	1.41	0.01	0.01	0.01	63.50	0.14	0.00



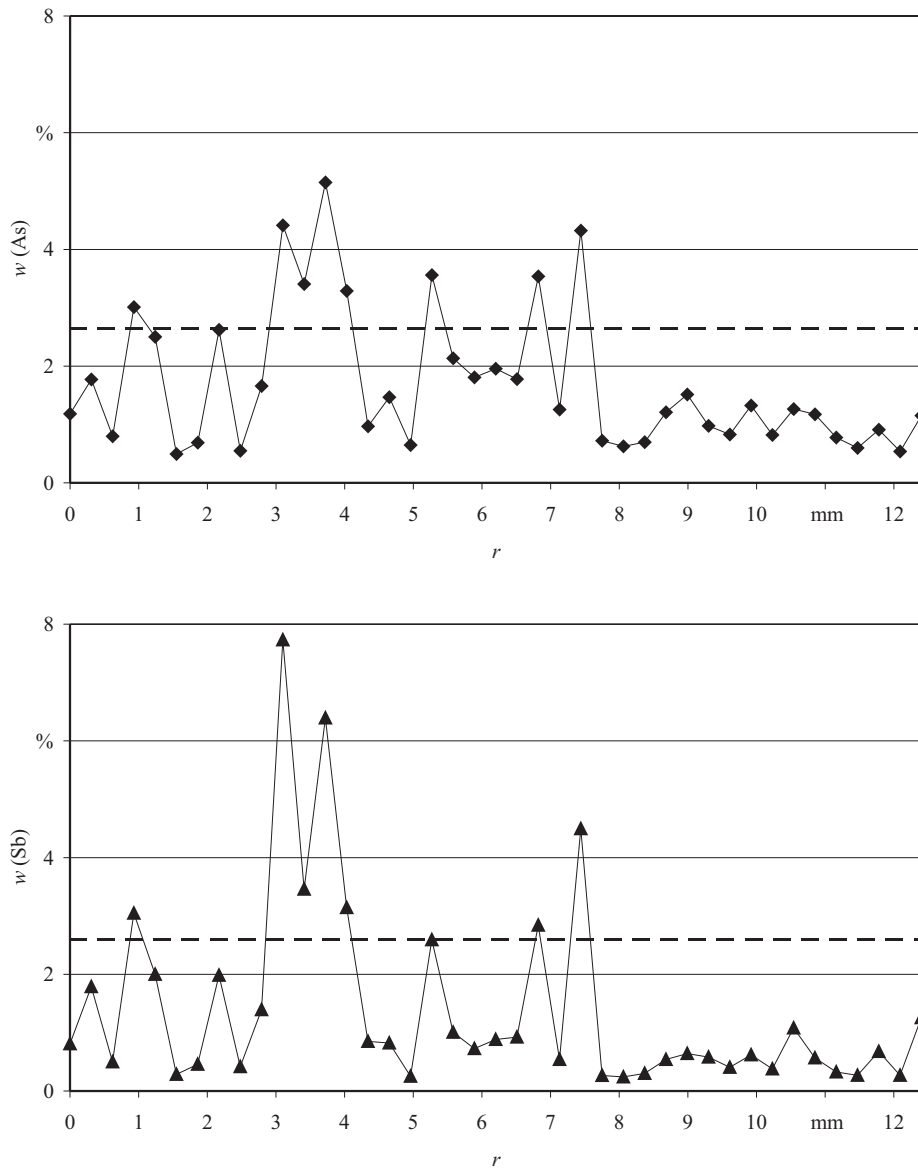


**Figure C.11:** Cu As<sub>3</sub> Sb<sub>3</sub> Bi<sub>0.1</sub>, electron microprobe analysis (line scan) of the sample cross-section. Shown are the mass fractions  $w$  of arsenic and antimony. The broken line marks the total mass fractions of the elements as determined by EDXRF analysis.

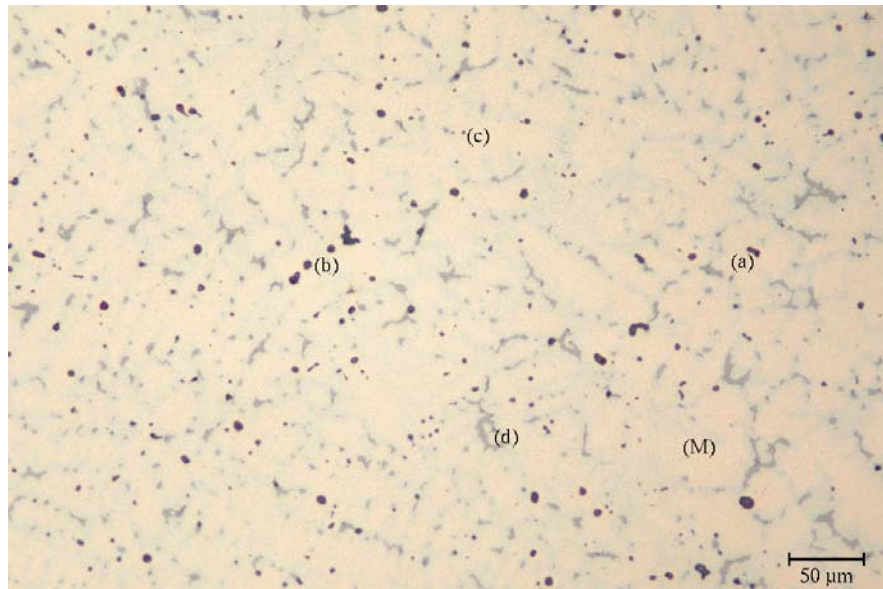


**Figure C.12:** Cu As<sub>4</sub> Sb<sub>4</sub> Bi<sub>0.1</sub>, metallographic section with inclusion types.

**Table C.8:** Cu As<sub>4</sub> Sb<sub>4</sub> Bi<sub>0.1</sub>, electron microprobe analyses of inclusions. Given are the mass fractions  $w$  of the determined elements. For inclusion types see Fig. C.12.

inclusion type/phase	$w(\text{As})$ [%]	$w(\text{Sb})$ [%]	$w(\text{Ag})$ [%]	$w(\text{Bi})$ [%]	$w(\text{Fe})$ [%]	$w(\text{Cu})$ [%]	$w(\text{O})$ [%]	$w(\text{S})$ [%]
(a) dark grey, elongated	1.56	61.31	0.00	0.08	3.36	5.79	28.80	0.00
(a) dark grey, elongated	1.61	55.48	0.01	0.12	5.66	8.25	26.81	0.00
(b) dark grey, globular	6.90	27.99	0.00	0.01	2.43	41.16	36.87	0.01
(c) bluish grey, globular	9.82	17.31	0.00	0.27	0.01	66.11	0.16	0.01
(d) pale blue phase	8.35	19.76	0.00	0.33	0.03	64.96	0.21	0.01
(d) pale blue phase	9.49	16.82	0.00	0.09	0.02	67.96	0.47	0.01
(M) matrix (average of linescan)	1.98	1.80	0.01	0.02	0.00	93.33	0.19	0.02

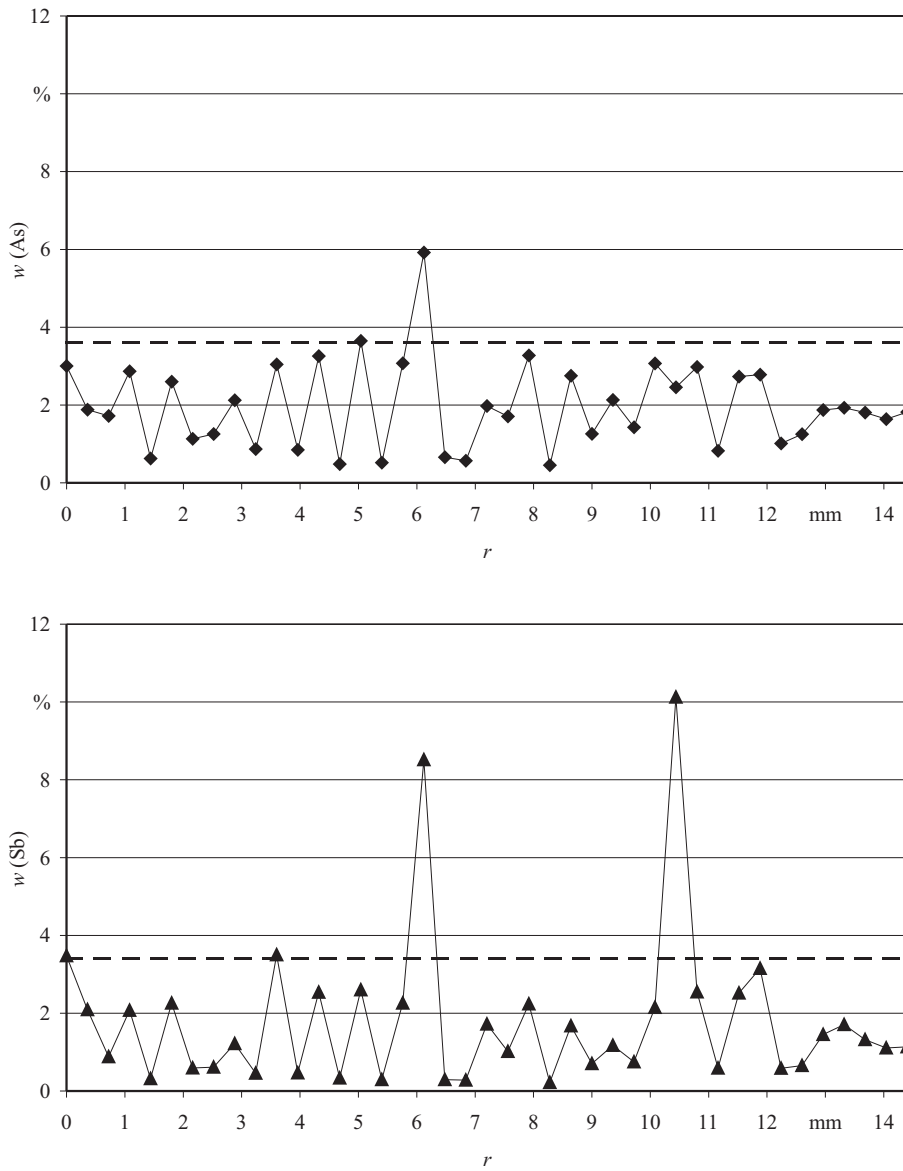
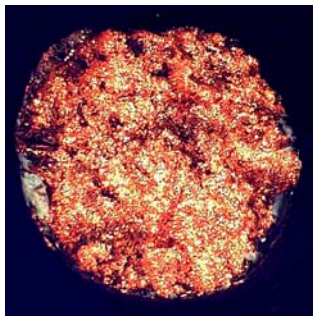


**Figure C.13:** Cu As<sub>4</sub> Sb<sub>4</sub> Bi<sub>0.1</sub>, electron microprobe analysis (line scan) of the sample cross-section. Shown are the mass fractions  $w$  of arsenic and antimony. The broken line marks the total mass fractions of the elements as determined by EDXRF analysis.

**Table C.9:** Tensile test. Given are the 0.2% offset yield strength  $R_{p0.2}$ , the tensile strength  $R_m$ , the percentage elongation after fracture  $A$ , and the percentage reduction of area after fracture  $Z$ . The samples marked with ‘\*’ were broken near the head of the sample, so that  $Z$  could not be determined.

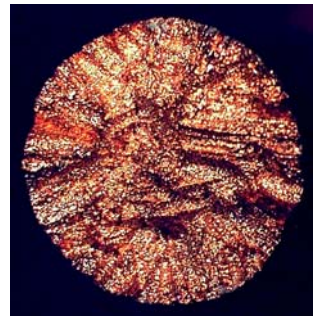
Reference material	sample	$R_{p0.2}$ [MPa]	$R_m$ [MPa]	$A$ [%]	$Z$ [%]
Cu	A-Z1	56	152	15.3	24.0
	A-Z2	50	186	32.6	38.0
	A-Z3	52	142	12.6	16.0
Cu As0.25 Sb0.25 Bi0.1	D-Z1	60	160	15.1	8.7
	D-Z2	60	143	12.5	8.6
	D-Z3	50	153	14.5	11.0
Cu As0.5 Sb0.5 Bi0.1	B-Z1	48	103	7.9	8.0
	B-Z2	52	122	11.1	9.0
	B-Z3	48	111	10.6	9.0
Cu As1 Sb1 Bi0.1	E-Z1	84	130	7.5	4.4
	E-Z2	66	145	10.4	7.4
	E-Z3	55	151	9.3	9.8
Cu As2 Sb2 Bi0.1	C-Z1*	67	118	6.0	
	C-Z2*	64	96	4.0	
	C-Z3	62	93	4.5	3.2
Cu As3 Sb3 Bi0.1	F-Z1	94	180	7.3	3.4
	F-Z2	94	187	8.5	5.4
	F-Z3	96	201	9.5	4.8
Cu As4 Sb4 Bi0.1	G-Z1	90	153	4.9	2.4
	G-Z2	92	144	2.7	2.0
	G-Z3	122	140	1.6	1.1



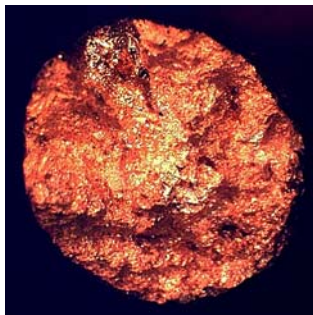
Cu  
(A-Z1) ductile fracture,  
funnel shaped



Cu As<sub>0.25</sub> Sb<sub>0.25</sub> Bi<sub>0.1</sub>  
(D-Z2) mixed fracture,  
funnel shaped to tapered



Cu As<sub>0.5</sub> Sb<sub>0.5</sub> Bi<sub>0.1</sub>  
(B-Z1) mixed fracture,  
cutter shaped



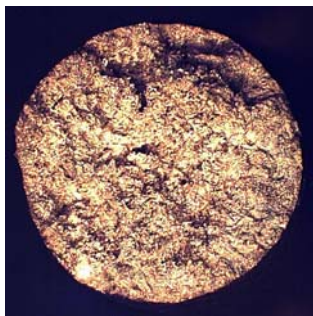
Cu As<sub>1</sub> Sb<sub>1</sub> Bi<sub>0.1</sub>  
(E-Z2) mixed fracture,  
funnel shaped to tapered



Cu As<sub>2</sub> Sb<sub>2</sub> Bi<sub>0.1</sub>  
(C-Z1) mixed fracture,  
fissured



Cu As<sub>3</sub> Sb<sub>3</sub> Bi<sub>0.1</sub>  
(F-Z2) brittle fracture,  
funnel shaped to fissured

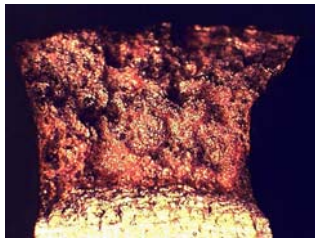


Cu As<sub>4</sub> Sb<sub>4</sub> Bi<sub>0.1</sub>  
(G-Z1) brittle fracture,  
funnel shaped to fissured

**Figure C.14:** Fracture appearance of tensile test specimens

**Table C.10:** Notched bar impact test. Given are the notch impact work  $A_v$ , the notch impact strength  $a_k$ , and the lateral spreading  $SB$ . The samples marked with ‘\*’ were not broken.

Reference material	sample	$A_v$ [J]	$a_k$ [J/cm <sup>-2</sup> ]	$SB$ [mm]
Cu	A-K1*	43.1	53.9	(1.7)
	A-K2*	77.9	97.4	(2.8)
	A-K3	62.1	77.6	2.0
Cu As0.25 Sb0.25 Bi0.1	D-K1	31.5	39.4	1.5
	D-K2	24.9	31.1	1.4
	D-K3	28.4	35.5	1.5
Cu As0.5 Sb0.5 Bi0.1	B-K1	10.7	13.4	0.5
	B-K2	14.5	18.1	0.8
	B-K3	12.3	15.4	0.6
Cu As1 Sb1 Bi0.1	E-K1	17.4	21.8	1.0
	E-K1	16.5	20.6	0.8
	E-K3	17.0	21.3	0.8
Cu As2 Sb2 Bi0.1	C-K1	6.2	7.8	0.3
	C-K2	6.3	7.9	0.3
	C-K3	6.5	8.1	0.3
Cu As3 Sb3 Bi0.1	F-K1	6.7	8.4	0.3
	F-K2	8.6	10.8	0.4
	F-K3	9.3	11.6	0.4
Cu As4 Sb4 Bi0.1	G-K1	7.3	9.1	0.3
	G-K2	5.9	7.4	0.2
	G-K3	6.2	7.8	0.3



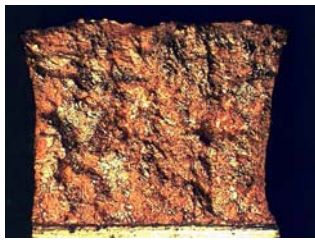
Cu  
(A-K3) ductile fracture,  
fissured



Cu As<sub>0.25</sub> Sb<sub>0.25</sub> Bi<sub>0.1</sub>  
(D-K2) ductile fracture,  
fissured



Cu As<sub>0.5</sub> Sb<sub>0.5</sub> Bi<sub>0.1</sub>  
(B-K3) mixed fracture,  
fissured



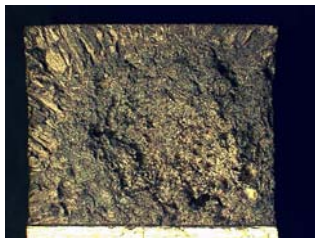
Cu As<sub>1</sub> Sb<sub>1</sub> Bi<sub>0.1</sub>  
(E-K1) mixed fracture,  
fissured to crystalline



Cu As<sub>2</sub> Sb<sub>2</sub> Bi<sub>0.1</sub>  
(C-K3) brittle fracture,  
fissured



Cu As<sub>3</sub> Sb<sub>3</sub> Bi<sub>0.1</sub>  
(F-K1) brittle fracture,  
fissured to crystalline



Cu As<sub>4</sub> Sb<sub>4</sub> Bi<sub>0.1</sub>  
(G-K3) brittle fracture,  
crystalline

**Figure C.15:** Fracture appearance of notched bar impact specimens

**Table C.11:** Torsion test. Given are the maximum reference amounts of deformation  $\phi_{v,max}$ , the reference stress for a reference amount of deformation  $\sigma_v(\phi = 0.1)$ , the maximum reference stress  $\sigma_{v,max}$ , and the hardening exponent  $P$ .

Reference material	sample	$\phi_{v,max}$	$\sigma_v(\phi = 0.1)$ [MPa]	$\sigma_{v,max}$ [MPa]	$P$
Cu	A-T1	0.76	98.54	256.67	0.50
	A-T2	0.89	149.92	287.56	0.35
	A-T3	1.18	151.89	335.92	0.33
Cu As0.25 Sb0.25 Bi0.1	D-T1	0.44	160.55	277.26	0.39
	D-T2	0.18	177.04	211.24	0.39
	D-T3	0.23	147.41	214.90	0.49
Cu As0.5 Sb0.5 Bi0.1	B-T1	0.23	100.14	158.25	0.71
	B-T2	0.34	111.35	212.27	0.58
	B-T3	0.23	188.41	238.13	0.30
Cu As1 Sb1 Bi0.1	E-T1	0.35	171.74	281.96	0.42
	E-T2	0.30	171.64	256.29	0.39
	E-T3	0.47	169.40	308.45	0.42
Cu As2 Sb2 Bi0.1	C-T1	0.29	150.33	239.28	0.44
	C-T2	0.15	148.52	174.13	0.37
	C-T3	0.22	159.92	218.50	0.39
Cu As3 Sb3 Bi0.1	F-T1	0.28	215.23	319.62	0.39
	F-T2	0.21	206.43	274.19	0.40
	F-T3	0.25	217.08	308.92	0.39
Cu As4 Sb4 Bi0.1	G-T1	0.21	205.39	278.72	0.40
	G-T2	0.16	215.00	250.69	0.37
	G-T3	0.11	228.32	230.29	0.34



**Table C.12:** Vickers hardness test. Given is the low load hardness HV0.2 depending on the amount of cold deformation  $\phi$ . For the flattened end of Cu and Cu As0.5 Sb0.5 Bi0.1 the amount of cold deformation is 99%, for Cu As2 Sb2 Bi0.1 it is 89%. The hardness was measured over the sample cross section. Continued on p. 254

Reference material	HV0.2 at a cold deformation $\phi$ of						flattened end
	0%	20%	55%	70%	84%	86%	
Cu							
	70.81	83.67	111.44	101.14	110.90	114.35	125.48
	56.11	84.40	100.45	105.84	115.63	115.36	127.57
	51.60	81.50	108.36	117.30	114.61	115.80	128.25
	51.62	88.92	101.16	106.32	116.41	109.28	116.22
	79.31	91.90	112.74	109.03	108.52	114.56	
Cu As0.25 Sb0.25 Bi0.1							
	71.28	101.26	114.71	112.46	120.33	118.43	
	54.26	82.88	113.16	115.66	117.01	118.21	
	57.79	85.41	112.67	114.35	115.58	116.10	
	53.17	96.00	110.70	112.67	117.80	114.95	
	61.90	111.25	115.34	117.36	116.29	116.96	
Cu As0.5 Sb0.5 Bi0.1							
	52.29	109.25	120.90	125.84	135.61	152.30	184.59
	40.81	91.25	121.79	117.60	120.77	143.59	173.51
	42.27	87.54	130.82	128.65	135.12	124.17	178.45
	52.10	100.27	123.41	124.60	132.57	128.08	170.20
	60.28	107.87	128.68	138.22	139.73	140.77	
Cu As1 Sb1 Bi0.1							
	84.26	116.61	127.01	134.51	140.12	148.72	
	66.73	104.16	133.08	138.34	131.56	141.79	
	64.22	101.78	134.57	135.70	152.82	145.02	
	63.15	110.79	131.41	129.80	147.06	136.98	
	70.23	123.98	127.20	133.56	144.17	143.26	

**Table C.12:** continued from p. 253

Reference material	HV0.2 at a cold deformation $\phi$ of						flattened end
	0%	20%	55%	70%	84%	86%	
<b>Cu As2 Sb2 Bi0.1</b>							
	64.76	155.33	172.58	164.89	194.29	196.98	221.61
	63.14	147.66	159.39	164.43	173.16	183.08	145.57
	56.09	123.52	133.59	182.69	157.86	197.36	173.25
	64.53	117.16	153.78	184.30	176.88	157.94	167.75
	52.78	145.60	169.55	180.67	174.41	198.72	200.16
<b>Cu As3 Sb3 Bi0.1</b>							
	107.40	163.94	198.28	214.97	216.34	202.17	
	65.44	135.12	162.92	187.63	182.25	187.97	
	77.91	93.05	171.82	174.82	194.56	169.33	
	76.57	138.09	168.18	188.18	187.73	205.59	
	100.27	171.52	180.24	206.87	211.86	213.44	
<b>Cu As4 Sb4 Bi0.1</b>							
	91.01	197.46	202.51	196.92	216.90	208.81	
	82.02	168.78	187.77	182.25	202.96	206.29	
	80.09	173.25	186.92	171.78	212.89	218.73	
	86.11	168.18	175.64	186.32	206.81	209.40	
	100.76	183.47	200.71	216.96	214.30	232.54	